Laser Annealing of Carrier-Selective Layers in High-Efficiency Photovoltaic Devices

A Ph.D. thesis dissertation
presented to the faculty advisory committee
at the School of Engineering and Applied Science of the
University of Virginia

In partial fulfillment
of the requirements for the degree of
Doctor of Philosophy
Charles L. Brown Department of Electrical and Computer Engineering

By

George C. Wilkes

December 2020

APPROVAL SHEET

This Ph.D. dissertation is submitted in partial fulfillment of the requirements

for the degree of

Doctor of Philosophy (Electrical and Computer Engineering)

George C. Wilkes

This Ph.D. dissertation has been read and approved by the Examining Committee:

Professor Mool C. Gupta, Advisor (ECE)

Professor Andreas Beling, Committee Chair (ECE)

Professor Joshua J. Choi (ChE)

Professor Jon F. Ihlefeld (ECE & MSE)

Professor Kyusang Lee (ECE & MSE)

Accepted for the School of Engineering and Applied Science:

Professor Craig H. Benson, Dean, School of Engineering and Applied Science

December 2020

To my parents, Angela and Brent, brother, John, and the love of my life, Kendall

ACKNOWLEDGEMENTS

I would like to express my sincere gratitude to all of those who have supported me during my time in doctoral study — this dissertation would not have been possible without your support. Your adoration and encouragement have helped me through thick and thin in pursuit of my academic career, and I will always hold your support and help along the way near and dear to my heart.

I am grateful to my advisor and mentor, Professor Mool Gupta, for taking a chance on a young, inexperienced, and fresh-from-undergraduate student in May of 2015 and helping me become the scientist I am today. Through his guidance and support, I was given the opportunity to pursue research which I truly valued and found interesting, and that I hope will someday improve our world. His enthusiasm and passion for the beauty in scientific research has inspired me and will continue to guide me throughout the rest of my career.

I would also like to thank my committee: Professor Andreas Beling, for serving as my committee chair and discussing my research at the end-of-summer graduate research symposiums; Professor Joshua Choi, for co-advising me on my early research in perovskite solar cells and empowering me to collaborate with your students; Professor Jon Ihlefeld, for training me in atomic layer deposition and your fruitful discussions on its applications; and Professor Kyusang Lee, for your support and advice on the NASA Big Idea competition.

I acknowledge the support of the NASA Langley Professor Program, National Institute of Aerospace and specifically Dr. Douglas Stanley, NASA IRAD, and the NSF I/UCRC program. I would also like to thank my inter-university collaborators and colleagues: Ajay Upadhyaya and Professor Ajeet Rohatgi at Georgia Tech; Professor Steven Hegedus, Dr. Ujjwal Das, Dr. Kevin Dobson, and Anish Soman at IEC; and Professor Zach Holman and Kate Fisher at ASU.

I would like to extend thanks to the staff and administrators that answered my questions, supported me, and endured my shenanigans throughout my graduate experience: MC, Doug, and Suzanne at NIA; Crystal, Dan, Beth, David, and Susan in the UVa ECE department, and Richard, Joe T., Cathy, Alex, Mike and Joe B. of the NMCF and Cleanroom staff. Thank you for your guidance and helping me with the impossible.

In addition, my gratitude extends to my friends and colleagues that have helped me along the way: Jacob and Nick who showed me the ropes at NIA and were excellent roommates; Matt, Kim, Harold and Raj who I first met when starting at NIA and helped guide my research progress; Xiaoyu, Alex, Matt, Ben, Scott, Lucy, and Kate who collaborated and helped me with perovskite solar cell fabrication when I first started traveling to UVa for research; Zeming, Elisa, Alan, Kai, Moon, Peixun, Adrian, Arpan, Joel, Chris D, and Raju for their companionship and fruitful discussions throughout my time at UVa; and the numerous other colleagues who helped me throughout graduate school.

To all my friends that I met in McLean, Harrisonburg, Hampton Roads, and Charlottesville — thank you for your consolation during the hard times, your shared excitement during the good, and reminding me that life is not just about research. Without your friendship, I never would have finished.

I would be remiss if I did not acknowledge the immense love, sacrifice, and encouragement of my family. Thank you to my parents, Angela and Brent, my brother John, my grandparents, my aunts and uncles, and my cousins. You have all helped and encouraged me throughout my life, and your love remains dear to my heart.

Finally, I am forever grateful to Kendall. Her love, support, and sacrifice were immeasurable throughout this lengthy process which has finally ended. I love you, always.

ABSTRACT

To realize efficient photovoltaic devices, charge carrier-selective layers are utilized to effectively separate and collect them at the electrodes. These layers allow the transport of one type of charge carrier while presenting a barrier to the other, preventing recombination within the layer. Typically, in both high-efficiency perovskite and silicon solar cells, carrier-selective layers require high-temperature treatments to achieve enhanced efficiency, which hinders scalability, increases thermal budgets, and causes other detrimental effects to the underlying layers. Traditionally, furnace annealing processes have been used for high-temperature treatment. This thesis investigates high-temperature treatment using short-pulse laser heating to improve photovoltaic device performance, overcome some of the limitations of the furnace annealing process, and generate a fundamental understanding of the laser annealing process.

By utilizing pulsed laser annealing, energy can be injected at short timespans (nanoseconds) with localized energy deposition due to the shallow absorption depth (10s of nanometers) of the laser light wavelength. This prevents the detrimental effects by having selective energy deposition, lower thermal budget, higher throughput, and by increasing the overall device efficiencies. In addition, laser processing is advantageous due to the ability to control the laser fluence, repetition rate, scan speed, pulse overlap, beam shape, and pulse width, allowing for fine-tuning of laser-material interaction.

This work has investigated: (1) the laser annealing of low-temperature TiO_2 electron transport layers (ETLs) used in flexible perovskite solar cells; (2) laser annealing for selective activation of dopants and crystallization of a/poly-Si carrier-selective passivating contacts (CSPC) for high-efficiency; (3) laser annealing of Al_2O_3, MoO_x, and TiO_x passivating and carrier-selective layers for Si solar cell devices; (4) laser-induced defects on a well-passivated silicon solar cell to

evaluate the impact of laser annealing and high fluence laser processing on defect formation; and (5) the use of lasers to bond well-passivated wafers of opposite doping type to form a p-n junction and solar cell device by transmitting a focused beam through one of the wafers.

The main results demonstrate the use of laser annealing of the thin layers that enables (1) conversion of chemical solution-deposited film to an efficient TiO_2 electron transporting layer without damaging underlying flexible substrates; (2) partial crystallization and dopant activation of n^+ doped a-Si:H thin films without detrimental effects to the underlying tunnel oxide or bulk wafer; (3) improved performance of passivating and carrier-selective metal oxides for silicon solar cells through interface improvements and changes in stoichiometry. The results also demonstrate (4) the impact of laser fluence and the percentage of laser process area on defect formation and subsequent impact on device performance; and (5) that wafer bonding of well-passivated Si wafers is feasible and shows promise for future high-efficiency devices.

This work is of widespread interest to the photovoltaic community and essential to improving efficiency and reducing the fabrication cost of photovoltaic devices. By demonstrating laser annealing methods for various carrier-selective layers and demonstrating an innovative method for p-n junction formation, this work provides viable avenues for further improvements to device efficiency and fabrication cost reduction.

TABLE OF CONTENTS

LIST OF FIGURES

LIST OF TABLES

CHAPTER 1: Introduction and Motivation

Photovoltaics (PVs) convert solar radiation into electricity by exploiting the photovoltaic effect discovered by A. E. Becquerel in 1839. Photovoltaics have several unique advantages: their operation produces no emissions, their operation is passive in nature, the materials required for fabrication are abundant on earth, and they are easily and entirely scalable. Photovoltaic energy generation is one of the most rapidly growing industries, yet accounts for only a small portion of the overall energy production market. To increase their share of the energy market, photovoltaics must produce as much electricity as possible for as low a price as possible, evaluated in terms of their cost per kilowatt-hour or $/kWh. To compare the costs of various sources of electricity production at the utility scale, the Levelized Cost of Energy (LCOE) is used, which sums the cost of the investment, operations and maintenance, and fuel expenditures (not applicable for photovoltaics) for a given year and divides it by the total electrical energy generated in that same

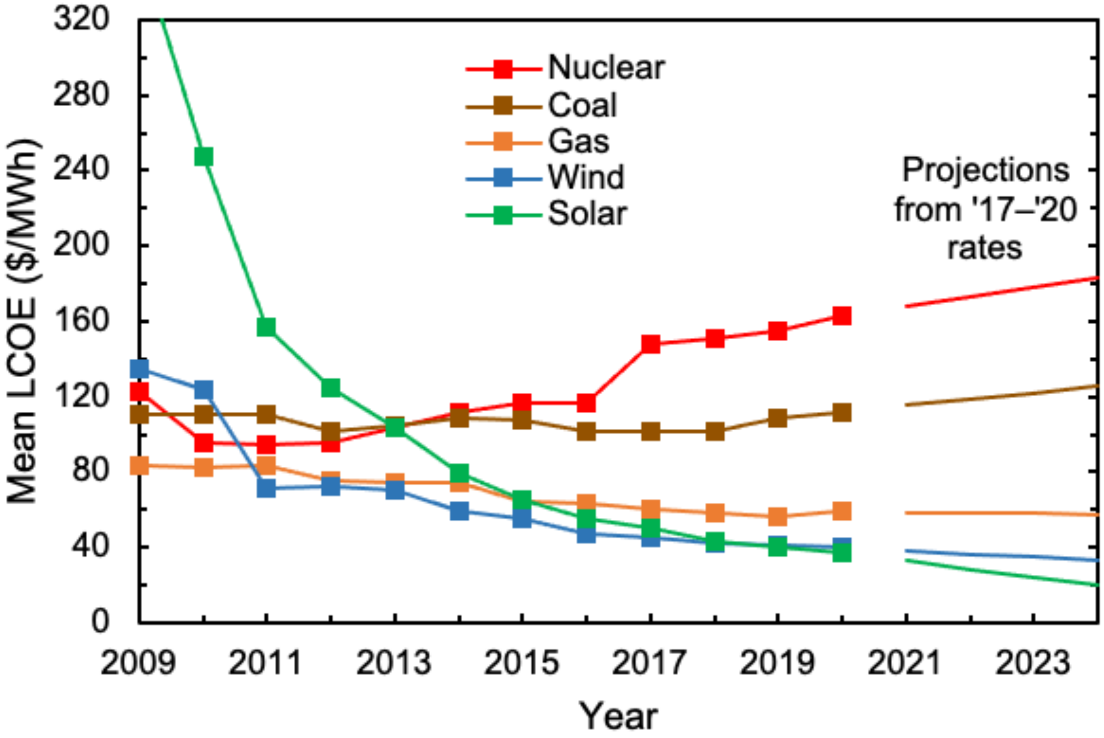

Fig. 1 Unsubsidized levelized cost of energy and projected cost for electricity production technologies. Data taken from Lazard Levelized Cost of Energy Analysis–V14.0 [1].

year. The expected lifetime of the system and any discounts can also be included in the calculation. Figure 1 shows the unsubsidized LCOE and projected LCOE for various electricity production technologies [1]. Solar photovoltaics have seen a rapid decrease in LCOE in recent years, with projections indicating a further decrease in cost. The two primary approaches for reducing the cost per kilowatt-hour or LCOE are to reduce the cost of fabrication and to increase the power conversion efficiency of the device.

To reduce manufacturing costs, researchers have looked into replacing high-temperature, high-vacuum, and other complex fabrication steps as they can hinder scalability and throughput. In addition, high-temperature processes can cause unwanted damage or diffusion to the underlying layers in a photovoltaic device. By reducing the temperature of key steps in the photovoltaic fabrication process, the thermal budget is reduced, saving cost. Also, if the complexity and duration of these steps are reduced, the manufacturing throughput is increased, providing more production volume in less time. Both of these goals can be obtained using pulsed laser processing, decreasing the cost per kilowatt-hour of photovoltaics, and potentially increasing the device efficiency.

A promising method for enhancing photovoltaic efficiency is to employ carrier-selective layers on opposite sides of the absorber to efficiently extract the photogenerated charge carriers and minimize unwanted charge-carrier recombination. These layers selectively allow one type of charge carrier, either electrons or holes, to pass through the layer, while preventing the other from entering, based on the layer energy alignment with the absorber. By separating these charge carriers, the recombination of the electron-hole pair is prevented, enabling the device to extract them to produce current and enhancing the overall device efficiency. However, these layers

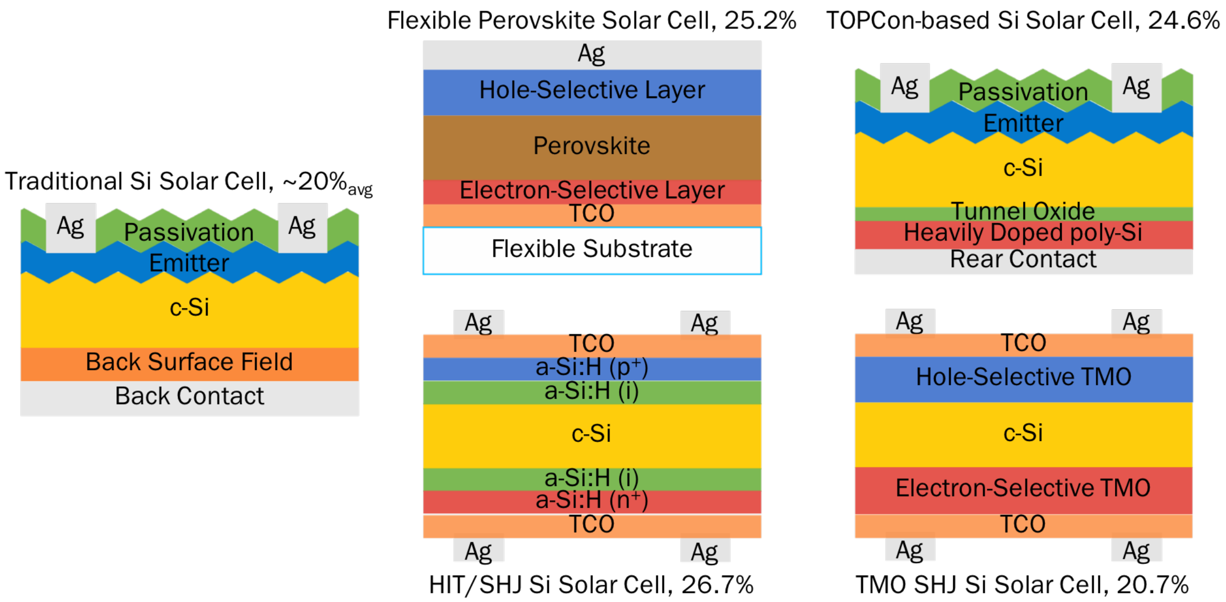

Fig. 2 Device structures of traditional Si Al-BSF cells, which do not make use of carrier-selective layers, compared to the next generation of high-efficiency devices, which all employ carrier-selective layers.

commonly require high-temperature thermal treatment or complex deposition methods, hindering scalability and throughput. Therefore, innovative approaches, such as laser annealing, are needed to make device fabrication with these layers cost-effective.

Perovskite solar cells are one of the most rapidly developing photovoltaic technologies to date and have power conversion efficiencies comparable to or exceeding traditional photovoltaics [2]. They are solution-processable and can be deposited on flexible substrates for high-throughput roll-to-roll manufacturing. Thin, lightweight, and flexible solar cells are of expanding interest in the aerospace industry for providing power to lightweight aircraft and balloons or as deployable arrays for satellites and extraterrestrial missions, where conventional photovoltaics are too rigid and heavy. The active area of perovskite solar cells is hundreds of times thinner than that of silicon solar cells, enabling substantially higher specific power. However, the electron selective layers in this perovskite solar cells, commonly composed of TiO_2, require high-temperature thermal annealing, which is unusable with the flexible plastic substrates needed for roll-to-roll manufacturing [3]. Therefore, a low-temperature annealing method is required in order to use this layer with flexible plastic substrates.

Silicon solar cells are currently the most widely used in the photovoltaics market, accounting for 90% of photovoltaic manufacturing production [4]. The materials used in their fabrication are earth-abundant, the modules have greater than 20-year reliability, and silicon cell design has received the most extensive study of any photovoltaic technology. The most commonly manufactured crystalline Si cell structure is the passivated-emitter rear contact (PERC)/Al-back surface field (Al-BSF), which has metal directly contacting doped regions in the absorber [4]. Carrier-selective layers are needed between the contact and the absorber for the aforementioned reasons, but the most promising carrier-selective layers require high-temperature annealing or complex deposition methods, raising the thermal budget and slowing throughput. A variety of state-of-the-art, high-efficiency solar cell concepts that employ carrier selective contacts are shown in Figure 2. This work explores state-of-the-art tunnel oxide passivated contacts and dopant-free transition metal oxide contacts for Si solar cells.

Conventional p–n and solar cell junctions as well as heavily doped areas near the contacts are formed using dopants and diffusion processes. High levels of doping can cause unwanted Auger recombination and ultimately limit the device efficiency, and undesirable dopant diffusion from highly doped areas can occur with high-temperature annealing. Dopant-free carrier-selective contacts are of interest because they avoid these issues while still maintaining carrier selectivity. Transition metal oxides are a novel group of materials for forming carrier-selective layers that is gaining increased interest because they reduce fabrication complexity, temperature, and cost. However, these materials have not yet reached the performance of heterojunction with intrinsic layer (HIT) contacts for Si, and more research is needed to improve their band alignment and process temperature. In addition, an innovative method for forming p–n junctions for solar cells is demonstrated by using laser bonding of wafers with opposite dopant types. This avoids the need to form heavily doped emitters using traditional ion-implanted dopant and thermal diffusion techniques. Carrier selectivity is needed to reduce recombination at the interfaces of the wafers and to effectively separate the photogenerated charge.

Carrier-selective contacts play an important role in high-efficiency perovskite and silicon solar cells. Therefore, an in-depth investigation of the complexities inherent in their fabrication, annealing, and functionality will have a large impact on improving the creation of high-efficiency perovskite and silicon solar cells. To address this important issue, this dissertation investigates high-temperature annealing using short-pulse laser heating to improve photovoltaic device performance, overcome some of the limitations of the furnace annealing process, and generate a fundamental understanding of the laser annealing process. A fundamental understanding of laser-induced defects generated from short-pulse laser heating is critically important in the quest to improve carrier-selective contacts.

CHAPTER 2: Solar Cell Operating Principle

Solar cells, and in particular silicon photovoltaics, are an increasingly widespread form of energy generation due to their sustainability, ability to generate power passively, and their potential for low-cost development. The two important functions of a solar cell are to convert absorbed photons into electron-hole pairs and to separate and extract the electrons and holes before they recombine. By absorbing incoming photon energy from the sun, electrons in the active layer's valence band become excited into the conduction band, creating an electron-hole pair which can be extracted and used to produce electricity. Extraction is achieved by having regions that are conductive to one type of carrier but not the other on opposite sides of the device. The basic process is shown in Figure 3. By measuring the current-voltage characteristics of the photovoltaic device under a 1-sun-calibrated illumination, its open-circuit voltage (V_{OC}), short-circuit current (I_{SC}), fill factor (FF), and power conversion efficiency (η) can be extracted and used to evaluate the device's performance. Silicon solar cells have achieved a record efficiency of 26.7% [5], roughly 3% shy of the theoretical Shockley-Queisser efficiency limit for crystalline silicon solar cells of 29.4% [6]. An overview of the champion efficiencies of various solar cell structures is shown in Figure 2.

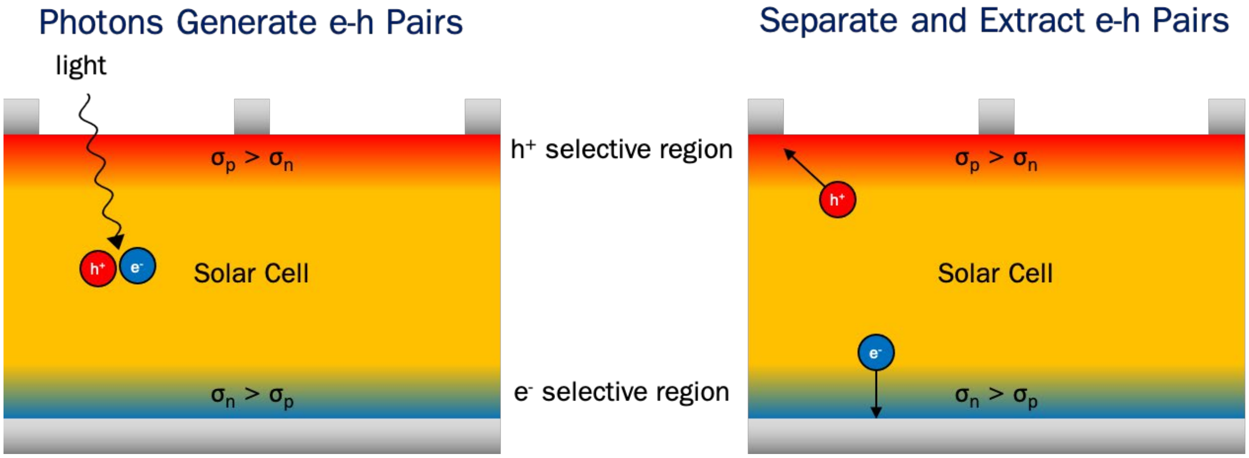

Fig. 3 The two important functions of solar cells: e-h pair photogeneration and e-h pair separation and extraction.

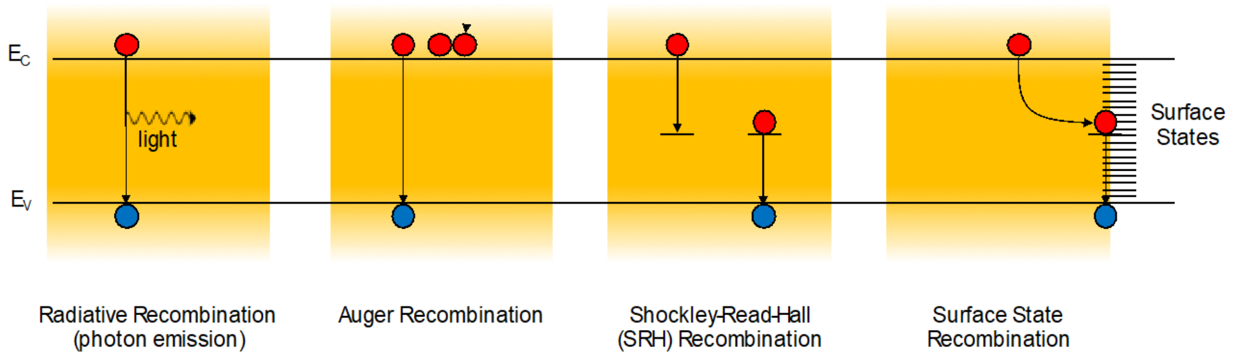

Fig. 4 Overview of the different types of recombination in solar cells.

Two primary loss mechanisms prevent solar cells from reaching the theoretical limit: optical losses and electrical losses. Optical losses usually result from reflection from the front of the cell surface, reflection from the front contact, or front contact shadowing loss, and affects the short-circuit current primarily. Steps have been taken to reduce these optical losses including the introduction of back contact cells [7], surface microtextures [8], and anti-reflective coatings [9], reducing its impact on the overall device loss. Electrical losses such as electron-hole pair recombination and contact resistances decrease the open-circuit voltage primarily. All photo-excited electrons in the conduction band (E_C) will eventually shift back to the valence band (E_V) via one of three possible mechanisms, if it they are not extracted. These mechanisms for recombination are shown in Figure 4. For traditional crystalline silicon photovoltaics, Shockley-Read-Hall and Auger recombination dominate, and are driven by defects and high dopant concentrations, respectively. Surface-state recombination is present in all solar cells because the surface is terminated at the surface of the solar cell, producing dangling bonds which provide additional defect states for charge carriers to recombine. These states can be passivated using dielectrics such as oxides, and hydrogenation can further passivate remaining bonds. An overview of dangling bonds and surface passivation is shown in Figure 5.

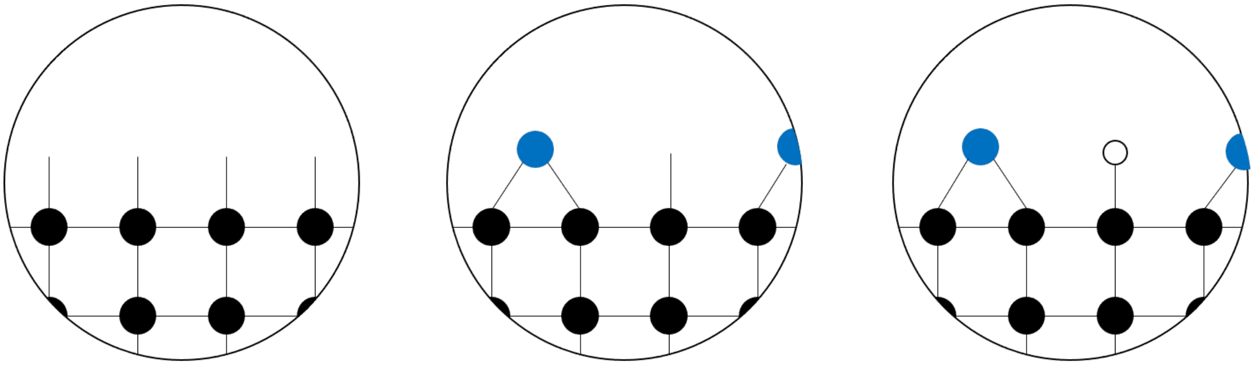

Dangling bonds at the surface result in a high number of defects.

Surface passivation caps the majority of dangling bonds, reducing defects.

Hydrogenation can passivate the remaining dangling surface bonds.

Fig. 5 Dangling bonds at the absorber surface and methods for passivating them.

In order to reduce voltage and efficiency losses from recombination, the causes for that particular type of recombination need to be addressed. In order for minority carriers to be captured before recombining, a high carrier diffusion length is required. Diffusion length is improved by superior material properties, while increased doping can reduce the diffusion length. Generally, amorphous materials have a high number of defects due to the variety of bond lengths and dangling bonds, leading to increased recombination. Crystalline materials will have a more discrete distribution of bond lengths, leading to a low number of defects and low recombination. Dopants in amorphous materials are typically un-activated, as they will occupy interstitial sites and may not share bonds with the bulk material, leading to low conductivity and poor band bending if used as heterojunction layer. Once the material becomes crystallized, these materials become activated, swapping with atoms in the lattice, increasing the conductivity and band bending of these materials. A summary of crystallization and dopant activation is shown in Figure 6. However, increasing the doping can reduce the minority equilibrium carrier concentration at the junction, which reduces recombination at the junction, introducing a delicate balance between the two. Lastly, passivating surfaces can reduce the surface recombination or interface recombination by

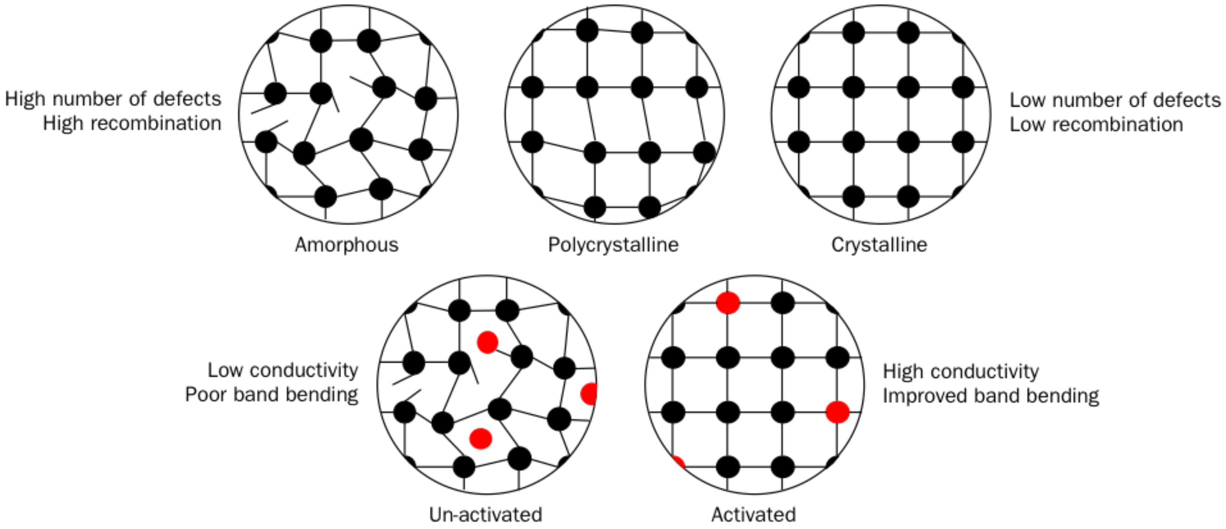

Fig. 6 Material crystallinity and dopant activation and the effects of defect quantity on recombination, conductivity, and band bending.

reducing the number of recombination locations and even providing electric field passivation to repel unwanted carriers. Since the passivating layers used to prevent surface recombination are generally thin insulators, ohmic contact with the device cannot be made, so a heavily doped region is typically employed near the patterned contacts, and the passivating layers are employed where the contacts are absent. This heavily doped region degrades the diffusion length of the carriers but was previously the best option to reduce recombination at the surface [10].

However, this heavy doping limits the efficiency of front junction silicon solar cells due to the carrier recombination in those areas, especially in the contact region. Carrier-selective passivating contacts eliminate the need for heavily doped regions near the contacts and diffused regions to separate the carriers, reducing Auger recombination and increasing the carrier lifetime. A comparison of the various methods for forming carrier-selective contacts is shown in Figure 7. The conduction and valence bands are denoted by E_C and E_V, respectively, while the quasi-Fermi levels for the electrons and holes are denoted by E_{FC} and E_{FV}. E_F denotes the Fermi level in the contact. When the Fermi energy of the structure more closely matches the quasi-Fermi energy for electrons, the electron drift current density, denoted by J_n, indicates that electrons will more readily

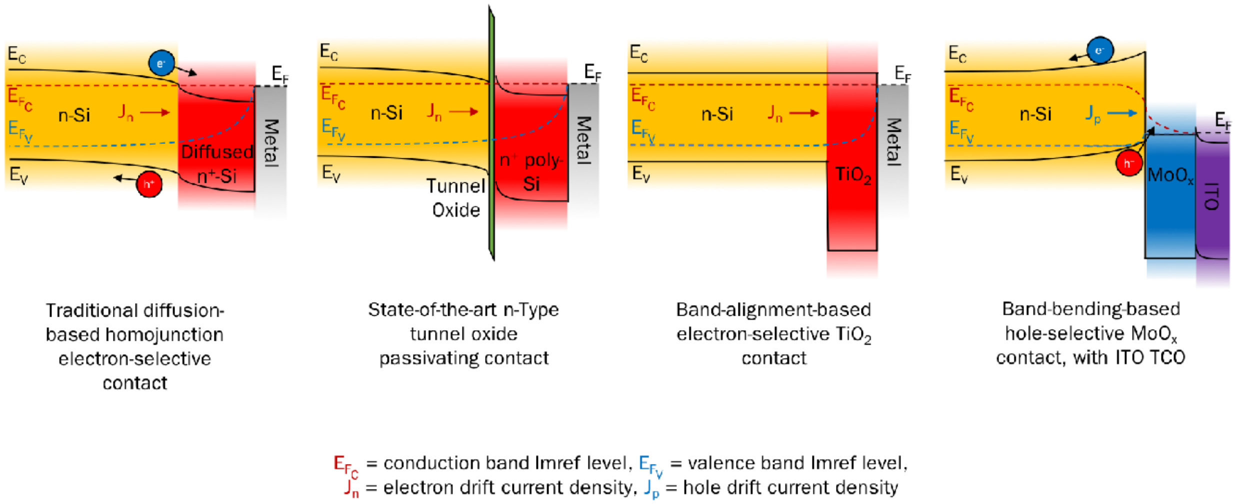

Traditional diffusion-based homojunction electron-selective contact

State-of-the-art n-Type tunnel oxide passivating contact

Band-alignment-based electron-selective TiO_2 contact

Band-bending-based hole-selective MoO_x contact, with ITO TCO

E_{F_C} = conduction band Imref level, E_{F_V} = valence band Imref level, J_n = electron drift current density, J_p = hole drift current density

Fig. 7 Overview of carrier-selective contacting methods: Traditional diffusion-based homojunction electron-selective contact; state of the art n-type tunnel oxide passivating contact; band-alignment-based electron-selective TiO_2 contact; and band-bending-based hole-selective MoO_x contact, with ITO transparent conductive oxide.

flow toward the metal contact, and vice versa for holes, denoted by the hole drift current density J_p. The Fermi energy must remain constant through the device, which causes the shifts and subsequent band bending in the conduction and valence bands of the materials at their interfaces. Carrier-selective contacts move the interface defects away from the metal contact, reducing recombination, while traditional diffusion-based homojunction contacts do not. The work function

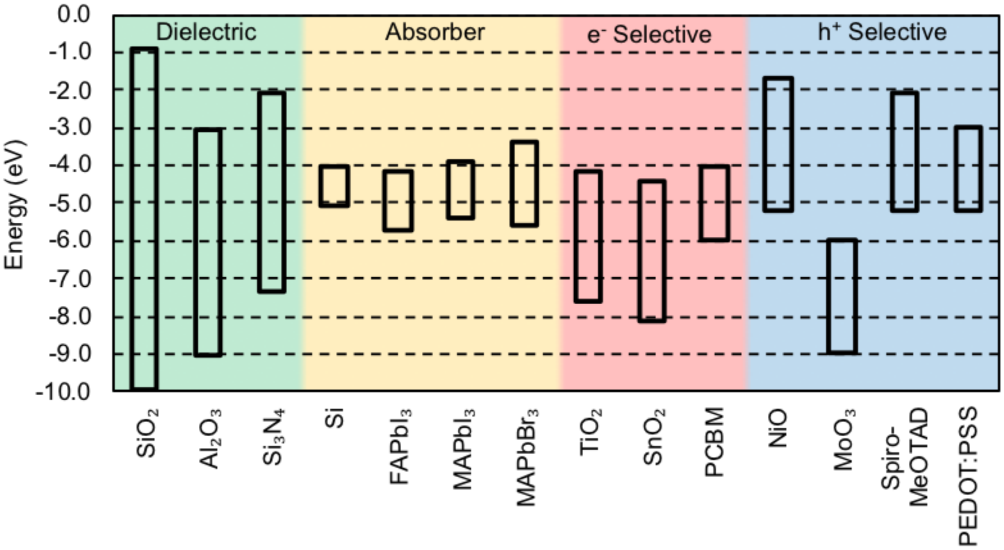

Fig. 8 Energy alignment chart of dielectrics and carrier-selective layers used and considered in this work. The chart is separated into passivating dielectrics, light absorbers, electron-selective contacts, and hole selective contacts. The conduction band minima and valence band maxima are defined by the materials work function and band gap from the vacuum level energy (0.0 eV).

of a particular layer will also affect where its conduction and valence bands will be in an energy diagram. For example, while MoO_3 has a smaller band gap than TiO_2, it has a much higher work function, making it useful for hole selective contacts as shown in Figure 7. A variety of dielectrics and carrier-selective layers were considered and used for this work, and their energy alignment compared to silicon and perovskite absorbers is shown in Figure 8. The values shown in Figure 8 were taken from the literature [11]–[13].

CHAPTER 3: Background on Laser Annealing and Experimental Setup

High-temperature thermal treatments are commonly employed during solar cell fabrication and for annealing the various layers in a device. From start to finish of solar cell fabrication, these thermal treatments are used for growing crystalline silicon boules (≥1400 °C), gettering (1100 °C), driving in and activating dopants (800–1200 °C), annealing crystal defects (400–900 °C), layer interface adhesion (100–900 °C), and contact firing (750 °C). For carrier-selective layers, these temperatures can range from 400–900 °C and the anneal time can be anywhere from 5–60 minutes, depending on the purpose of the anneal. However, there is a need to replace these high-temperature, long-duration anneals which increase the thermal budget of manufacturing and decrease the throughput. In addition, high-temperature, long-duration anneals can potentially cause damage or unwanted diffusion to other layers in the device. Rapid thermal annealing (RTA) can bring the device to even higher temperatures (≥1000 °C) and reduce the anneal time to minutes or seconds, but can only process a single wafer at a time. A comparison of these annealing techniques is shown in Figure 9.

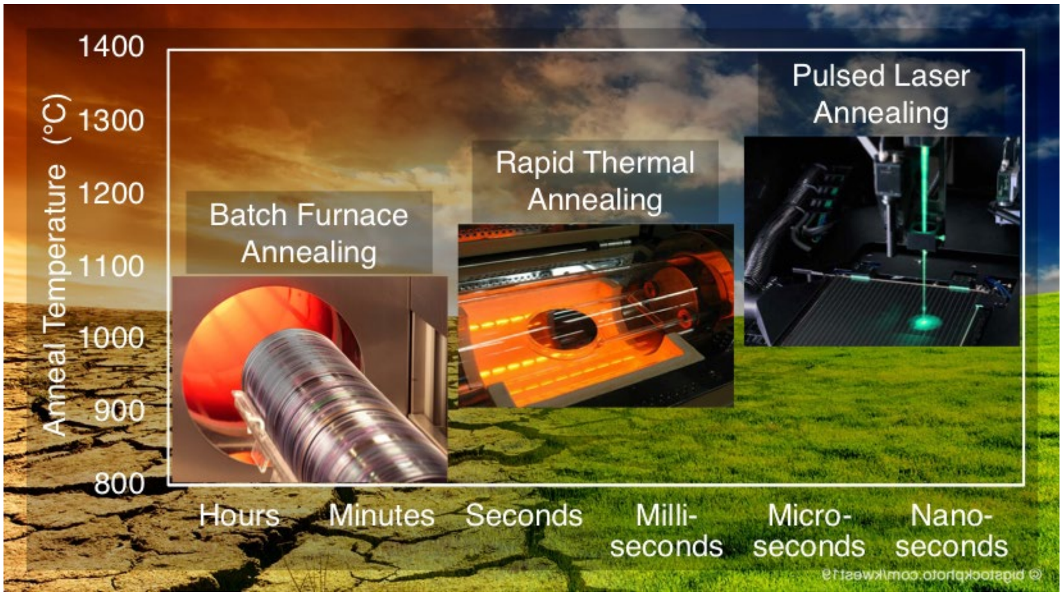

Fig. 9 Comparison of the annealing times and temperatures for traditional batch furnace annealing, rapid thermal annealing, and pulsed laser annealing.

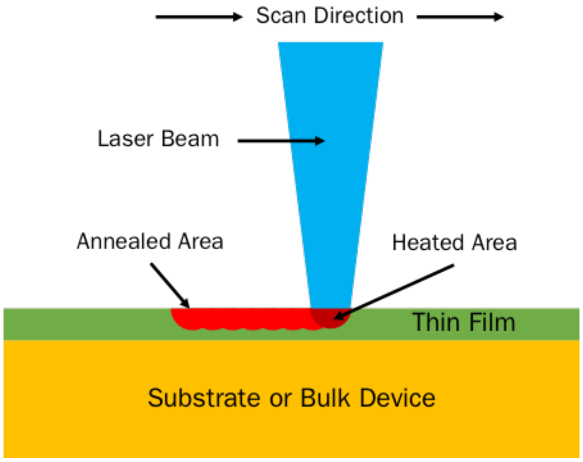

Fig. 10 Schematic of pulsed laser annealing of thin films on a substrate or bulk device indicating the localized heating of the film due to short absorption depth and short pulse width.

Pulsed laser processing for solar cells has gained increased interest over the years due to its potential for replacing furnace heating techniques [14]. Due to the shallow laser absorption depths and short laser pulse lengths, lasers grant additional control over heat application to localized regions while preventing damage to the bulk of the device or substrate. A schematic of the pulsed laser annealing process is shown in Figure 10. The laser wavelength, laser fluence, pulse width, pulse repetition rate, pulse overlap, scan speed, and spot size are tunable, allowing for precise control over laser-material interaction and kinetics. In addition, laser techniques are entirely scalable for industrial applications, with a variety of processes available for PV manufacturing, and they enable high-throughput solar cell fabrication at a reduced thermal budget.

The majority of the completed work described in this thesis made use of a Coherent, Inc. MATRIX 355-8-50, diode-pumped solid state, Q-switched laser. This laser operates at 355 nm ultraviolet wavelength, at pulse durations between 8–33 ns, at repetition frequencies between 20 kHz and 150 kHz, and a maximum average power of 8 W at 50 kHz. The output beam passes through a beam expander and then through a collimator, reducing beam divergence and allowing for a smaller spot size after focusing the beam. The collimated beam passes through a mirrored galvanometric scan head with an f-theta lens. The scan head uses a series of galvanometric mirrors

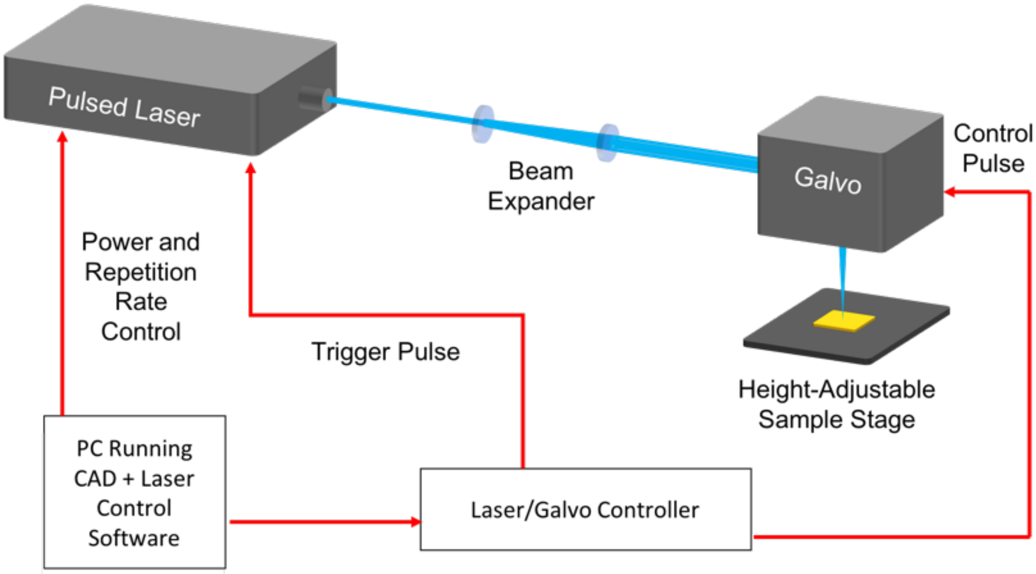

Fig. 11 Computer-controlled pulsed laser processing schematic showing laser, beam expander, galvanometer scanner, laser/galvo controller, and computer interface.

to direct the beam at scan speeds up to 15,000 mm/s at a resolution of 0.1 μm while the f-theta lens produces a linear displacement to reduce distortion at angles far from the normal. This focused beam is directed down onto the height-adjustable sample stage to account for varying sample thicknesses with a fixed laser focus. In certain applications, the sample stage height was adjusted in order to obtain a defocused beam that reduces high intensity at the Gaussian peak, smoothing out the profile to obtain reduced temperature gradients in the material. The galvo scan head is interfaced with a controller that connects to the laser system, galvo scan head, and computer and sends a trigger pulse and control pulse to the laser and galvo, respectively, at a precisely calibrated time. The computer sets the laser power and repetition rate, and sends a signal to the controller to begin laser firing and scanning. This system can be modified to have gas flow over the sample or with a vacuum chamber placed under the scan head to control the laser processing environment. An x-y stage can also be incorporated to allow for large-area sample processing. A schematic of this setup is shown in Figure 11.

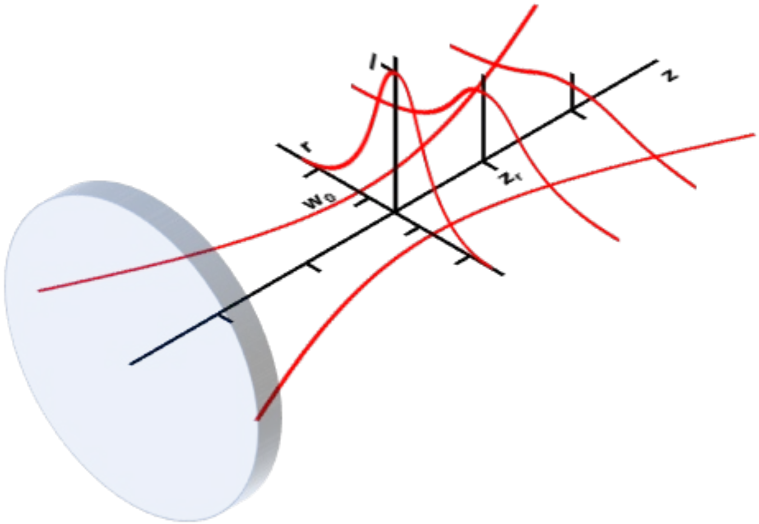

Fig. 12 Propagation of Gaussian beam with increased distance from focus and change of beam profile.

For certain experiments, the beam focus location can be changed using a height-adjustable z-stage. This is particularly advantageous for positive out-of-focus laser processing in order to reduce the intensity gradient of a Gaussian beam, resulting in a more uniform and smooth temperature profile in the material being processed. Figure 12 shows how the Gaussian beam intensity changes with respect to increased distance from the focus. Negative defocusing is necessary for thru-wafer laser processing of the rear surface of the wafer, particularly for wafer bonding, where keeping the front surface un-damaged is desired. A general comparison of intensity gradients versus the location of the beam focus relative to sample depth is shown in Figure 13.

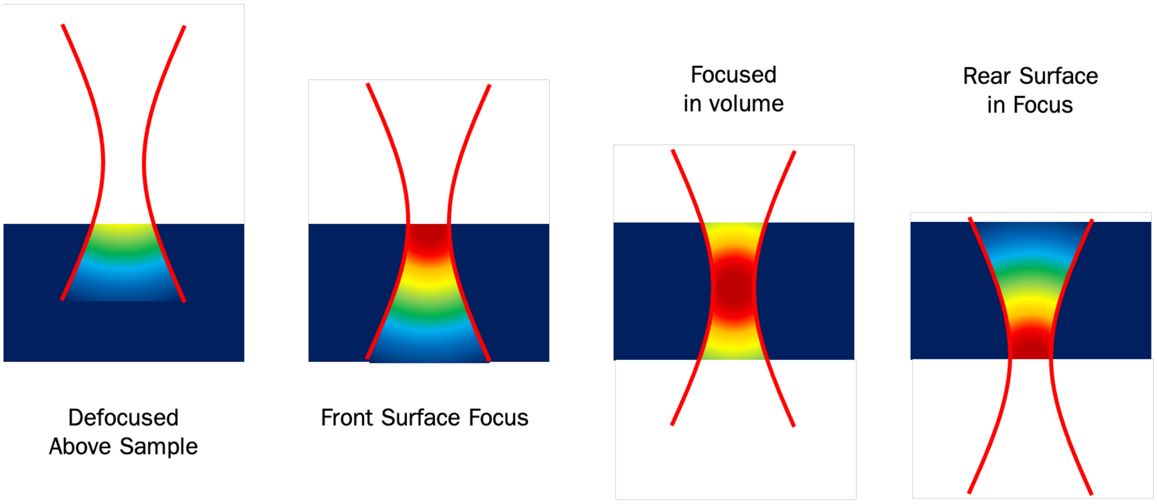

Defocused Above Sample

Front Surface Focus

Focused in volume

Rear Surface in Focus

Fig. 13 Intensity profile of the beam relative to beam focus depth in a material.

CHAPTER 4: Laser Annealing of TiO_2 Electron Transporting Layers for Flexible Perovskite Solar Cells

4.1 Introduction

Hybrid organic-inorganic metal-halide perovskite solar cells are a relatively new photovoltaic technology that emerged from dye-sensitized solar cells in 2009. Initially, they were used by Kojima et al. as a photoactive dye to assist a TiO_2 structure collect more photogenerated electrons [15]. However, their power conversion efficiencies were low—around 3.8%. More recently, single-junction perovskite solar cells have perovskite featured as the primary photoactive layer and have recently reached efficiencies of 25.5% [2]. They have an advantage over traditional photovoltaics due to the wide variety of inexpensive methods used to fabricate them while retaining high efficiency. A basic device structure is shown in Figure 14 (a).

The TiO_2 layer in perovskite solar cells, initially used as scaffolding for a photoactive dye, commonly serves as the electron transport layer (ETL)—a nanoscale-thin film that transports photogenerated electrons from the perovskite active layer to a metal contact. Without the TiO_2 layer, device efficiencies are limited to ~14% [16], since that layer assists with electron extraction, prevents carrier recombination, and provides the most favorable conduction band mismatch (~0.2 eV) when compared to other metal oxides [17]. TiO_2 has high optical transmittance allowing for increased light capture by perovskite along with high durability and stability, allowing for long-lasting and highly efficient perovskite solar cells.

The greatest weakness of TiO_2 electron transport layers is that they require a high temperature (>450 °C) anneal to generate high efficiency, and they are the only layer within a perovskite device that requires temperatures above 150 °C. Temperatures above 190 °C can shrink

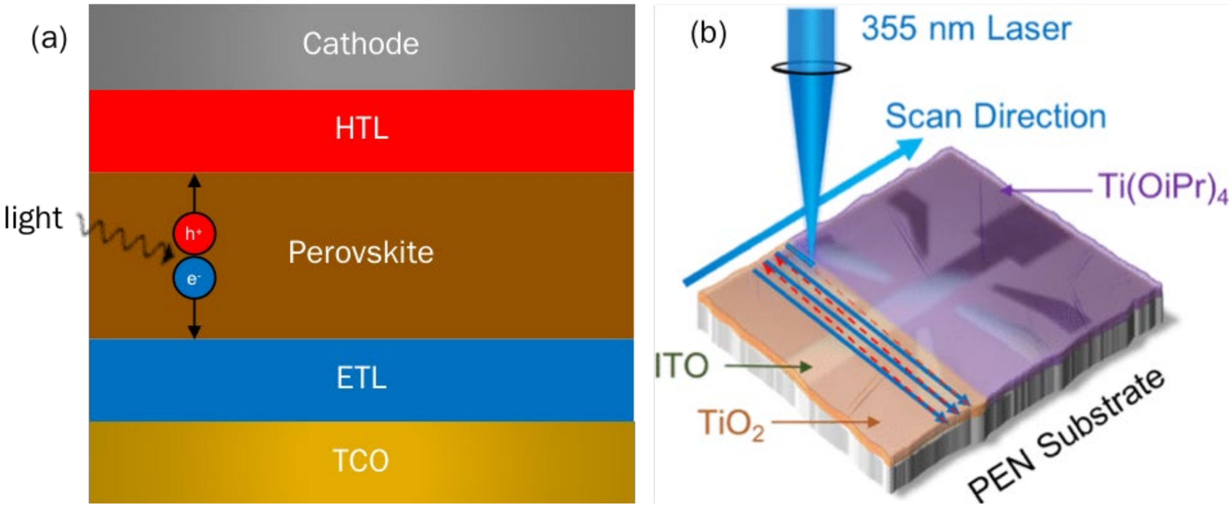

Fig. 14 (a) Basic perovskite solar cell structure. (b) Laser annealing concept for TiO_2 ETLs on flexible PEN substrates.

and degrade the polyethylene napthalate (PEN) substrate, decreasing surface wetting and preventing subsequent layer deposition. Temperatures above 200 °C can begin to melt polyethylene-based plastics. In addition, the transparent conductive oxide, Indium Tin Oxide (ITO), which is commonly used as a transparent cathode for perovskite solar cells, loses conductivity after annealing at temperatures exceeding 300 °C. At temperatures of 500 °C, the sheet resistance of ITO can increase by 500% mainly due to a filling of oxygen vacancies and consequent decrease in carrier current density [18], [19]. This causes an increase in series resistance, decreasing the ultimate device V_{OC}. A doubling in sheet resistance can negatively impact the normalized power conversion efficiency of a device by as much as 20%. Thermal annealing can also increase the roughness of ITO, decreasing its wettability for subsequent layer deposition.

The rest of the perovskite solar cell fabrication process typically only needs annealing temperatures of less than 150 °C, so there is significant interest in low-temperature fabrication techniques that are compatible with flexible substrates such as poly(ethylene terephthalate) (PET) and poly(ethylene naphthalate) (PEN). These substrates are low cost, flexible, lightweight, and roll-to-roll processable [20], making them financially attractive by decreasing the device weight while increasing manufacturing throughput [21]. The active layer of perovskite solar cells is less than 500 nm thick, hundreds of times thinner than that of traditional silicon counterparts, so thin PEN substrates enable perovskite solar cells to have 60 times the power-to-weight ratio of silicon solar cells [22]–[24]. This makes flexible perovskite solar cells of considerable interest to the aerospace industry, as the cells enable high specific power, flexibility, compact storage, and low weight when compared to traditional photovoltaics. It currently costs \$5k per kg for low-earth orbit, \$30k per kg for geostationary orbit, \$0.3M per kg for lunar orbit, \$1.8M per kg for the lunar surface, and \$2M per kg for delivery with the lunar rover [25].

Pulsed laser annealing provides an opportunity to anneal the TiO_2 ETL without damaging the ITO or underlying substrate. It also allows the use of the standard titanium diisopropoxide bis(acetylacetonate) in butanol sol-gel method for TiO_2 layer formation, capable of generating efficiencies of 15–18% with 450 °C anneals, on flexible substrates. A schematic of the laser annealing process for TiO_2 ETLs is shown in Figure 14 (b).

4.2 Fabrication, Optimization, and Device Results

The ITO film on the ITO-coated glass substrates has a thickness and roughness of ~100 nm and ~2.5 nm, respectively, characterized by spectroscopic ellipsometry and optical profilometry. Topographical scanning electron microscopy (SEM) gives good visual qualitative information about the film smoothness. The starting ITO sheet resistance was 19 Ω/sq, which began to rise at annealing temperatures above 300°C, and increased to 90 Ω/sq after a 500 °C 5 min anneal. The optical bandgap, determined from ellipsometry, shifted from 3.55 eV to 3.29 eV with the 500 °C anneal.

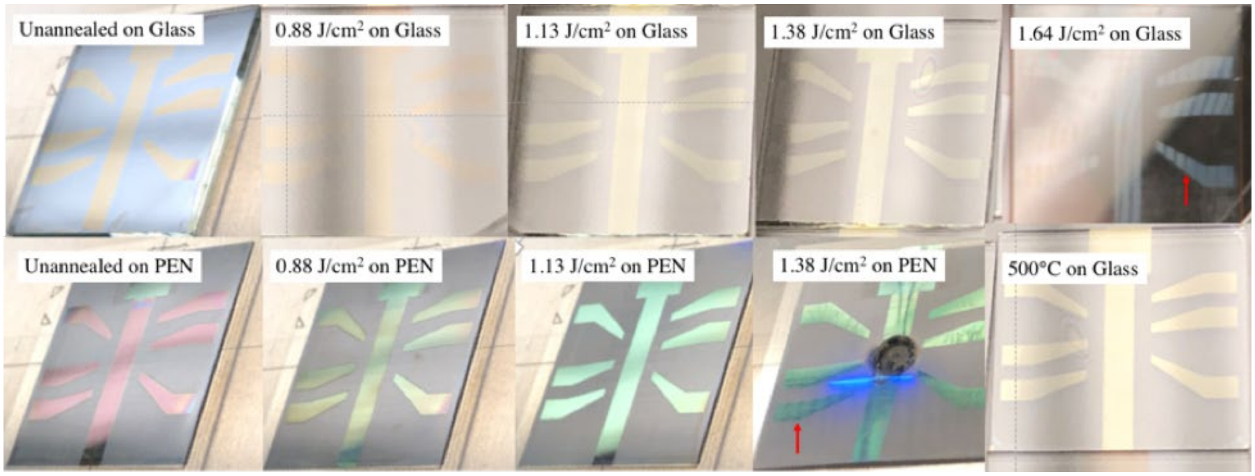

Fig. 15 Effect of laser fluence on film color shift for ITO-coated glass and PEN substrates with as-deposited, laser-annealed films, and thermally annealed films (glass).

The laser processing fluence was optimized by coating the ITO-coated glass and PEN substrates with sol-gel TiO_2 and annealing at increasing laser fluences. As-deposited films appear blue on ITO-coated glass and purple on ITO-coated PEN. The 5 min, 500 °C thermal anneal causes fading of the blue color of the sol-gel film indicating successful conversion to TiO_2. With increasing laser fluence, similar color shifts are observed on glass and PEN ITO-coated substrates. Above a threshold fluence, a moiré pattern begins to appear, suggesting periodic ablation damage to the underlying film, ITO, or potentially the substrate. This occurs at 1.64 J/cm^2 fluence for glass and 1.38 J/cm^2 for PEN coated-substrates, indicating a lower damage threshold for ITO-coated PEN. These results are summarized in Figure 15. SEM was used to inspect the laser-processed spots at increasing fluence on the stack to see the qualitative shift in contrast which is an indicator of conductivity, and the laser-induced damage. The dark regions represent unannealed film, while the lighter 20 μm diameter spots are regions annealed by a single laser pulse. The 0.88 J/cm^2 fluence, laser-processed films have poor spot uniformity and contrast, while spot uniformity and contrast for the 1.13 J/cm^2 and 1.38 J/cm^2 fluence-processed films are good. Above 1.64 J/cm^2, ablation damage appears which is unsuitable for subsequent device fabrication. SEM images are shown in Figure 16. A fluence of 1.13 J/cm^2 was selected as the optimal fluence, based on visual

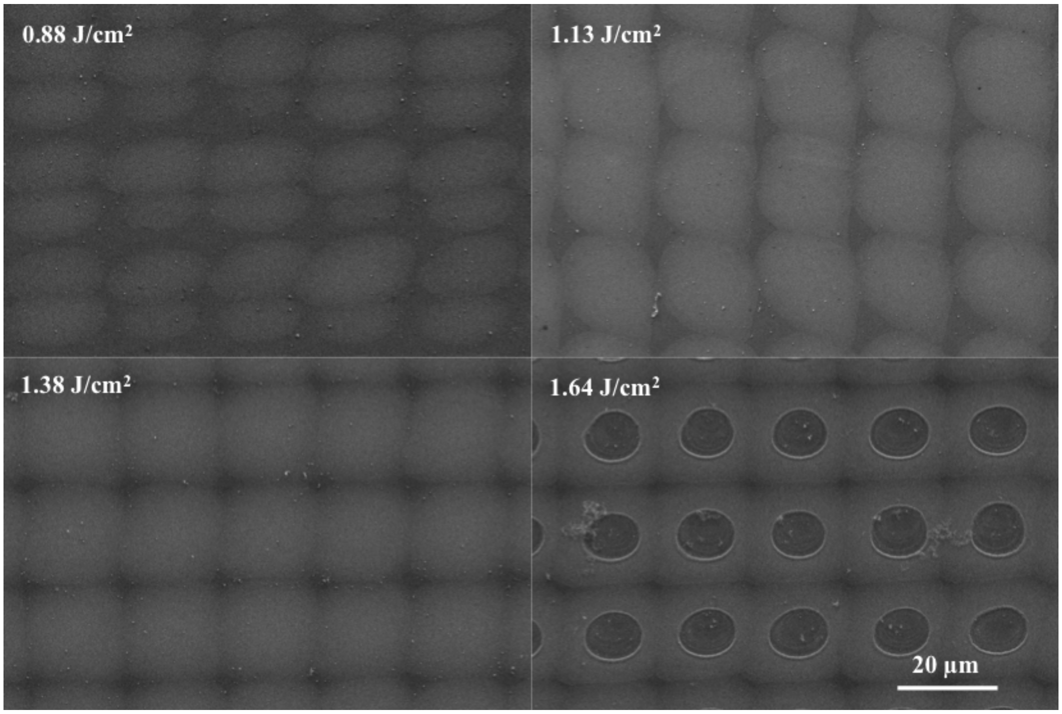

Fig. 16 SEM inspection of spot uniformity and laser-induced contrast at increasing laser fluence for TiO_2 films on ITO-coated glass.

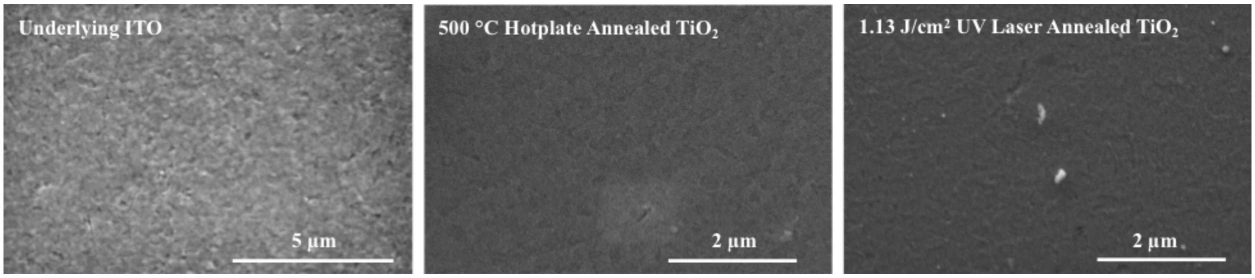

Fig. 17 SEM inspection of the topography of the underlying ITO, hot plate-annealed, and laser-annealed TiO_2 films on ITO-coated glass.

and SEM inspection as well as compatibility with flexible substrates. A comparison of the topography of the underlying ITO, 500 °C hot-plate annealed TiO_2, and laser-annealed TiO_2 is shown in Figure 17 for reference.

Next, perovskite solar cell devices consisting of glass or PEN/ITO/TiO_2/perovskite/Spiro-OMeTAD/Ag or Au were fabricated and tested under illumination for I–V data. Figure 18 shows (a) a schematic of the device structure and (b) a picture of the flexible perovskite device being bent by hand. The device area was defined by the overlap between the ITO top contact and the bottom Au contact which was 0.03 cm^2. For laser annealing of the TiO_2 film, a laser fluence of 1.13 J/cm^2,

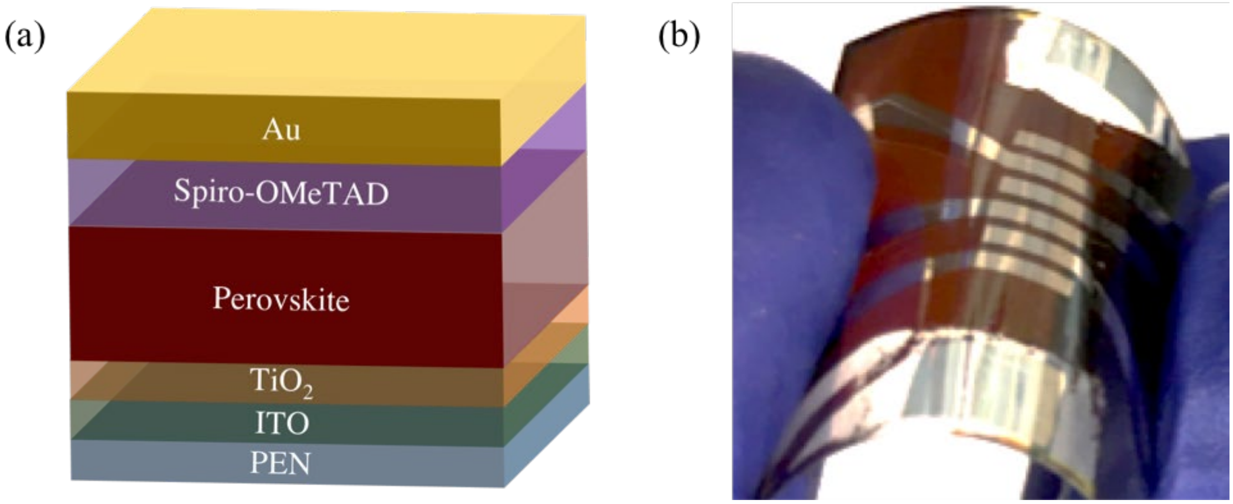

Fig. 18 (a) Perovskite solar cell structure and (b) picture of the flexible perovskite solar cell being bent by hand.

focal spot size of 20 µm, pulse width of 25 ns, pulse overlap of 25% (or a 15 µm spacing between pulses), scan speed of 750 mm/s, repetition rate of 50 kHz, and line overlap of 15 µm were used. Reference devices consisted of TiO_2 annealed thermally on a hot plate for 500 °C for 5 mins. On top of the TiO_2 films, a two-step mixed-halide alloyed perovskite ($FA_{0.85}MA_{0.15}PbI_{2.55}$-$Br_{0.45}$) layer (~300 nm), a 2,2′,7,7′-tetrakis(N,N-di-p-methoxyphenyl-a mine)-9,9′-spiro bifluorine (Spiro-OMeTAD) layer (100 nm), and a gold anode layer (60 nm) were deposited. Illuminated I-V and I-

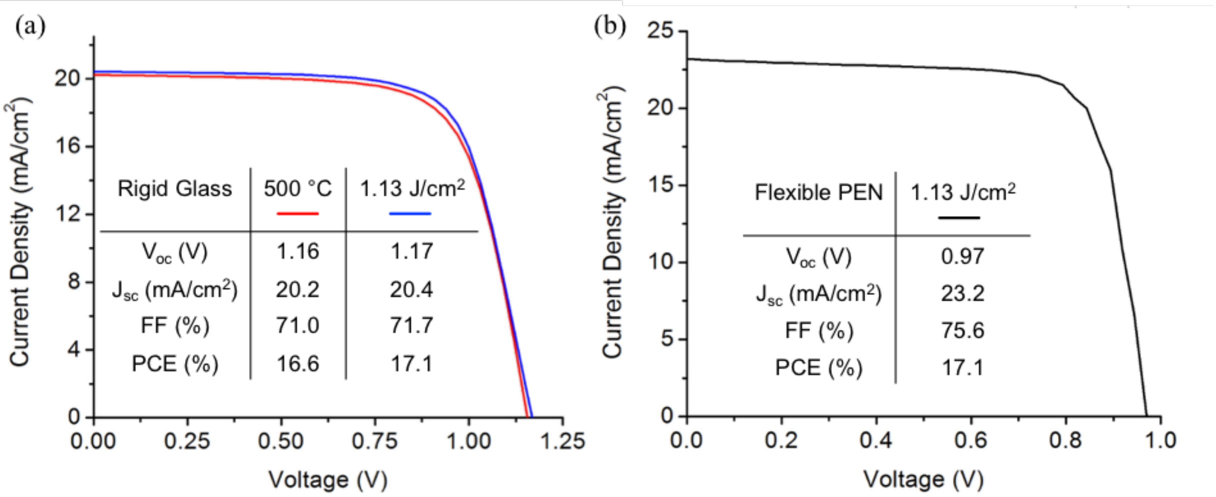

Rigid Glass	500 °C 🟥	1.13 J/cm^2 🟦
V_{oc} (V)	1.16	1.17
J_{sc} (mA/cm^2)	20.2	20.4
FF (%)	71.0	71.7
PCE (%)	16.6	17.1

Flexible PEN	1.13 J/cm^2 ▬
V_{oc} (V)	0.97
J_{sc} (mA/cm^2)	23.2
FF (%)	75.6
PCE (%)	17.1

Fig. 19 I-V curve and corresponding parameters for (a) reference hot plate-annealed device on glass and laser-annealed device on glass and (b) flexible laser-annealed device on PEN.

V parameters of the reference thermally-annealed device on glass, the laser-annealed device on glass, and the laser-annealed device on PEN are shown in Figure 19.

4.3 Characterization of Laser Annealed TiO_2

TiO_2 films were deposited on ITO-coated glass substrates and were stepwise annealed on a hotplate and their sheet resistance and 635 nm wavelength optical transmission were measured. The sheet resistance begins increasing at temperatures above 300 °C due to a filling of oxygen vacancies in the ITO, while the optical transmission begins decreasing. This decrease in optical transmission is caused by a reduced photon mean free path from increased light scattering at grain boundaries caused by morphological changes in the film due to the phase transition to crystalline TiO_2 and crystalline grainy boundary improvement from annealing [26], [27]. These results are summarized in Figure 20 (a). A similar experiment was done using pulsed laser annealing of the structure at a 1.13 J/cm^2 fluence with an increasing number of pulses. It is able to bring about similar decrease in optical transmission in the stack, indicating conversion to TiO_2, without increasing the sheet resistance at all. These results are shown in Figure 20 (b).

Additional TiO_2 films were prepared on glass via thermal and laser annealing for characterization. Variable-angle spectroscopic ellipsometry (VASE) was used to compare the peak

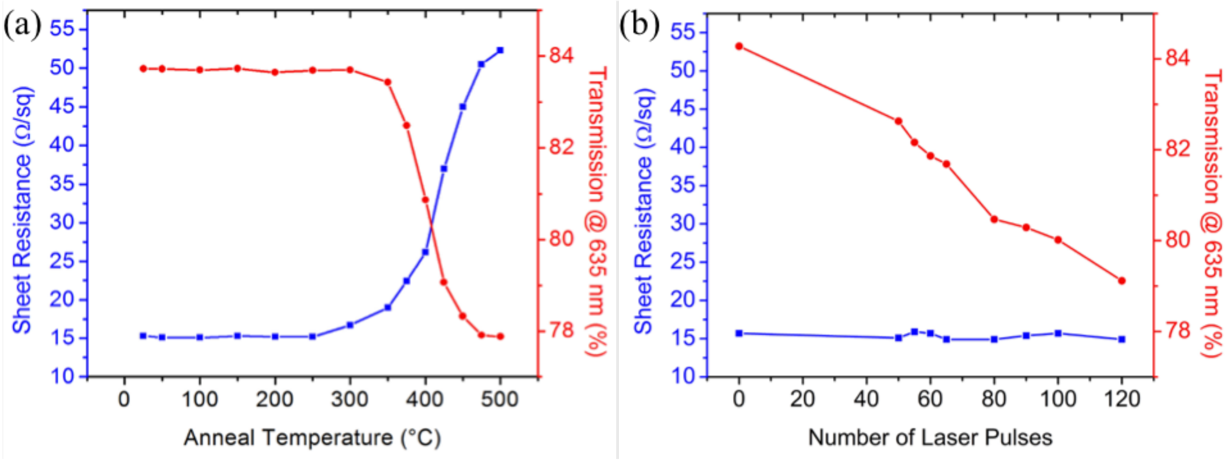

Fig. 20 Effect of (a) annealing temperature and (b) number of pulses on glass/ITO/TiO_2 sheet resistivity and light transmission at a 635 nm wavelength.

in refractive index of the various TiO_2 films to evaluate their crystallinity and band gap. TiO_2 has a refractive index peak between 2.0 and 3.3 at a wavelength of 300 nm. The band gap varies between 3.2 and 3.6 eV, with higher band gaps having more crystalline film phase [28] and higher density [29], [30]. This is due to the air voids in the film, which have a refractive index of 1.0, decreasing the overall refractive index in the film and signifying denser films will have fewer voids and therefore a higher refractive index. The as-deposited films have a band gap of 3.35 eV and refractive index peak value of 1.9. This increases to 3.51 eV and 2.05 after thermal annealing at 500 °C for 5 mins due to increasing film density and transition to a crystalline anatase phase. Similarly, laser processing of the as-deposited film increases the band gap to 3.56 eV and the peak refractive index to 2.1, suggesting improved film density and crystallinity. The refractive indices of these films are shown in Figure 21 (a). VASE can also be used to obtain film thickness which were found to be 45 nm, 24 nm, and 27 nm for as-deposited, hot plate-annealed, and laser-annealed TiO_2 films, respectively.

X-ray photoelectron spectroscopy was done to characterize the chemical composition and bonding of the TiO_2 films. Survey spectra for all films, shown in Figure 21 (b), reveal O 1s, Ti 2p, and C 1s peaks, which is consistent with the literature for titanium diisopropoxide bis(acetylacetonate) in butanol sol-gel prepared TiO_2 films by thermal annealing [31], [32]. High-resolution XPS spectra are shown for the Ti 2p and O 1s in Figure 21 (c) and (d), respectively. The thermal-annealed and laser-annealed Ti $2p_{3/2}$ and $2p_{1/2}$ are well aligned with each other and are consistent with values found in the literature for anatase TiO_2 [32], [33], while the as-deposited Ti 2p peaks have higher binding energies due to their structural and chemical difference from the annealed forms. Ti^{4+} 2p peaks correspond with predominately TiO_2 while Ti^{3+} can indicate suboxide TiO_x or even TiO. Both thermal and laser annealing reduce the intensity of the Ti^{3+} peaks,

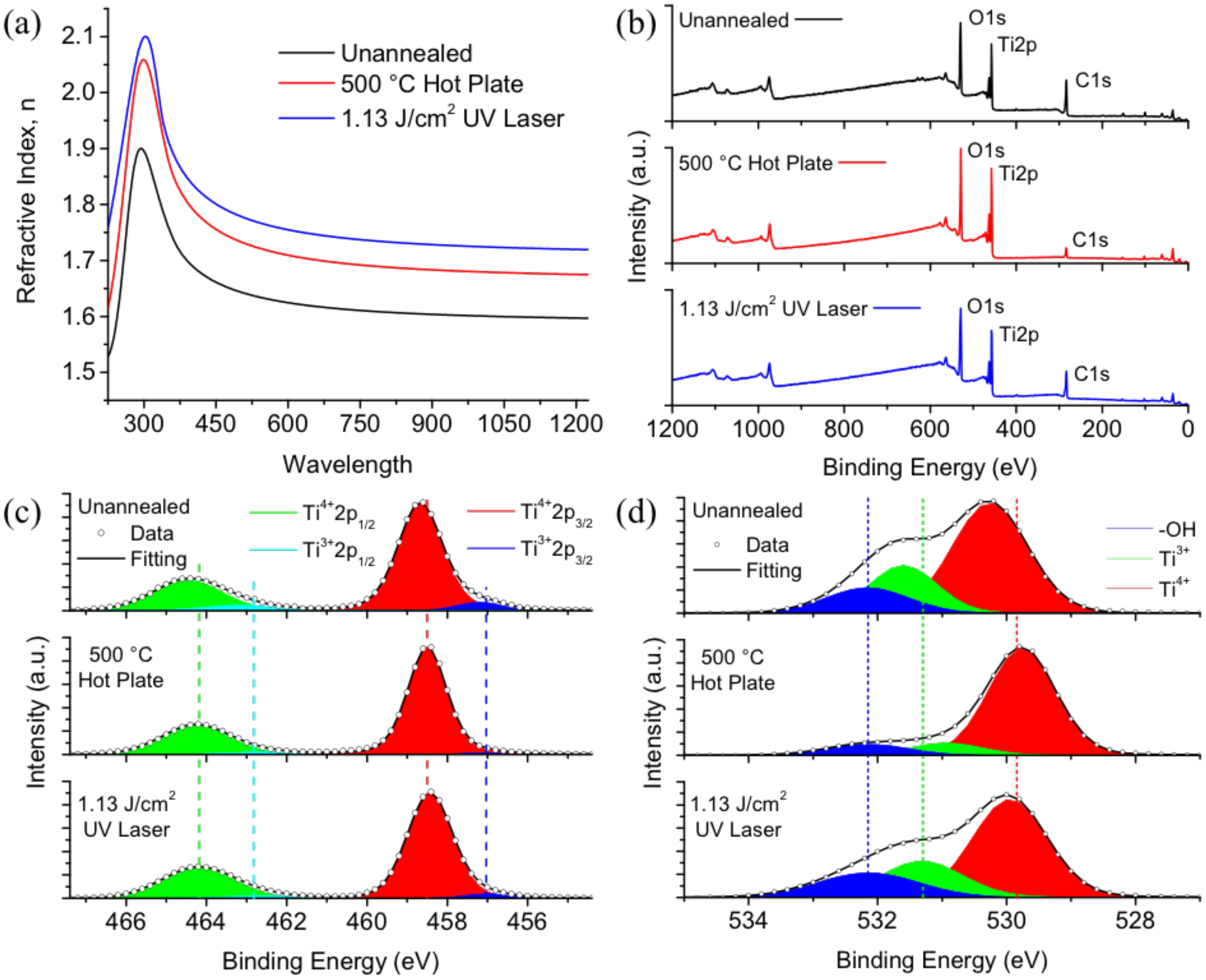

Fig. 21 (a) Spectral refractive index, (b) XPS survey spectra and high-resolution XPS spectra of the (c) Ti 2p and (d) O 1s peaks of unannealed, 500 °C thermally annealed, and 1.13 J/cm^2 laser-annealed TiO_2.

indicating the formation of stoichiometric TiO_2 with the Ti^{4+} peaks. The Ti^{4+}–O 1s peaks correspond with the Ti^{4+} 2p peaks, also indicating stoichiometric TiO_2. A similar binding energy shift with thermal and laser annealing from their as-deposited state was observed. Un-annealed sol-gel TiO_2 has an Ti^{4+}–O 1s peak at 529.85 eV, matching well with our as-deposited result [34]. Anatase TiO_2 has a Ti^{4+}–O 1s peak at 530.6 eV, and both the thermal and laser annealed TiO_2 have matching Ti^{4+}–O 1s binding energies for anatase [35]. The additional O 1s peaks are the result of from leftover organic compounds and hydroxyl groups, but do not affect device performance [21].

These XPS results demonstrate that hydrolysis and linkage of Ti-O-Ti groups can occur on the order of a 25 ns laser pulse, demonstrating nanosecond crystallization and formation of TiO_2 films.

4.4 Conclusions

This project successfully demonstrates a novel laser annealing method for sol-gel TiO_2 films for electron transporting layers in high-efficiency flexible perovskite solar cells. By utilizing laser annealing of TiO_2 on ITO-coated glass and flexible PEN substrates, a 17.1% device efficiency was obtained. Film characterization demonstrates that laser processing can successfully convert the as-deposited titanium diisopropoxide bis(acetylacetonate) into stoichiometric, dense, uniform, conductive, and crystalline anatase films of comparable quality to their traditional, 500 °C thermally annealed counterparts. This technique is compatible with flexible PEN substrates, unlike 500 °C thermal annealing. This chapter opens the door for high-throughput and low-temperature laser processing for high performance flexible perovskite solar cells and has the potential to bring the difference in efficiency between flexible and rigid devices to parity.

The results of this chapter were published in ACS Applied Materials & Interfaces, volume 10, issue 48, on pages 41312–41317 in November of 2018.

CHAPTER 5: Laser Annealing of Poly-Si for Tunnel-Oxide Passivated Carrier-Selective Contacts for Silicon Solar Cells

5.1 Introduction

Carrier recombination in silicon solar cells can be greatly reduced by using passivating and carrier-selective interlayers between the silicon absorber and its metal electrodes to enhance cell efficiency. Highly doped a-Si:H, well studied as an interlayer in various Si devices, is receiving increasing interest as a carrier-selective layer for high-efficiency Si solar cells [36]–[42]. When coupled with a thin (< 2 nm) passivating layer (such as SiO_2), surface passivation can be achieved without negatively impacting carrier transport. Additionally, tunnel-oxide passivating contacts are one of the few viable methods for eradicating diffusion and metal-contact-induced recombination because they relocate heavily doped diffused regions and metallized contacts outside of the absorbing base. The band alignment of the base, thin passivation layer, and carrier-selective layer work together to create a high barrier for one carrier and low barrier for the other, providing carrier selectivity for low minority carrier recombination and efficient majority carrier transport. The energy diagram of this system is shown in Figure 22.

Typically, the highly doped amorphous or nanocrystalline silicon layer is deposited via plasma-enhanced or low-pressure chemical vapor deposition (PECVD or LPCVD) at low temperatures between 200–600 °C and a subsequent 30-minute high-temperature anneal at 800–1000 °C is used to further crystallize the as-deposited layer [36]–[38], [40]–[42]; increase structural and electrical stability [37]–[39], [41], [42]; activate dopants within the layer [36], [41], [42]; reduce short wavelength parasitic absorption by increasing crystallinity [43]; and possibly generate pinholes in the interfacial oxide for carrier transport [38], [39]. Amorphous Si can reduce

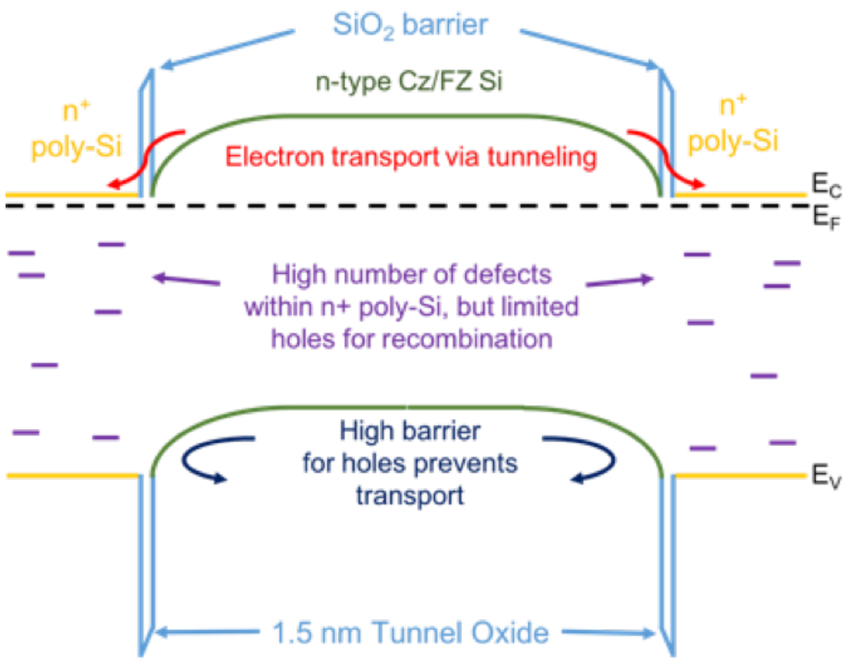

Fig. 22 TOPCon energy diagram showing carrier transport.

short-circuit current density values by as much as 9 mA/cm^2 for a 100 nm thick layer, which is reduced to 4 mA/cm^2 for poly-Si [43], emphasizing the need for layer crystallization. Dopant activation will decrease the sheet resistance of the poly-Si, enabling a low series resistance for subsequent metallization. However, high-temperature furnace anneals lead to several problems: (1) degradation of the tunnel oxide and its interfaces [38]; (2) dopant diffusion from the poly-Si into the base which increases Auger recombination; (3) incomplete dopant activation in the poly-Si; and (4) degradation of the absorber lifetime due to prolonged high-temperature exposure.

To alleviate these issues and grant further control over the processing, the use of ultraviolet pulsed-laser annealing was investigated to replace the secondary furnace-based high-temperature anneal. Laser-based solar cell manufacturing has gained increased interest in recent years, allowing for easy adoption [14], [44]. Pulsed laser annealing allows for selective control over dopant activation and crystallization of the poly-Si layer while preventing oxide degradation, absorber degradation, and excessive diffusion. This is due to the short laser pulse (25 ns) which can activate dopants and crystallize the poly-Si in nanoseconds, and the shallow absorption depth (10 nm for

Si) enabling the processing to only affect the desired layer. Coupled with the low thermal diffusivity of amorphous (0.10 cm^2/s) and polycrystalline silicon (0.14 cm^2/s) when compared to crystalline silicon (0.90 cm^2/s) [45], it is possible to reach the high temperatures required for activation and crystallization while preventing passivating oxide break-up (at 900 °C) [46] under nanosecond pulsed laser heating [47]. This provides a unique advantage in preventing oxide break-up while annealing the poly-Si layer.

In this chapter, the change in passivation, crystallization, and dopant concentration of laser processed a-Si:H, carrier-selective passivating contacts and the impact of subsequent SiN_x deposition to replace the furnace-based high-temperature anneal for TOPCon for high efficiency Si solar cells is described.

5.2 Modeling and Simulation

In order to understand the impact of the laser wavelength and fluence on the absorption and resultant temperature increase in the TOPCon structure, the spectral optical properties of amorphous and crystalline silicon were modeled and the laser-material interaction was simulated to provide a conceptual background for the study.

The optical properties of amorphous and crystalline silicon were modelled to assess an appropriate wavelength for laser annealing using Essential MacLeod optical modeling software. While laser wavelengths can vary greatly, high-powered lasers based on Nd:YAG are typically restricted to 1064, 532, 355, and 266 nm wavelengths based on the first, second, third, and fourth harmonic generation. The absorption properties of silicon with varying degrees of crystallinity from amorphous to single crystal were investigated using data from Sopra SA [48]. Throughout the visible spectrum, the absorption coefficient can shift by an order of magnitude across the

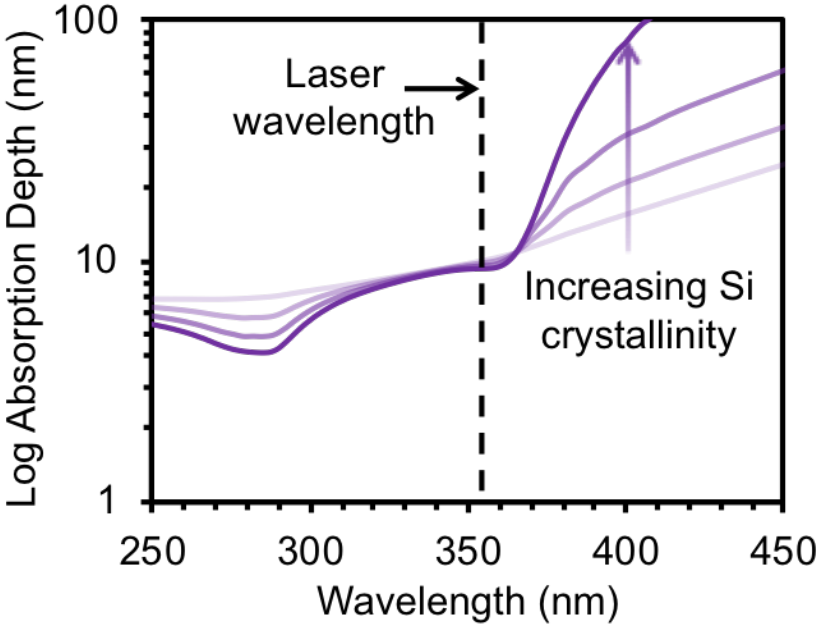

Fig. 23 Log plot of the ultraviolet absorption depth of silicon of various degrees of crystallinity from amorphous to single crystal. The arrow direction indicates the trend of increasing crystallinity. Dashed line indicates the selected laser wavelength, which will have identical absorption regardless of silicon degree of crystallinity.

aforementioned allotropes, but is relatively constant below 360 nm and above 940 nm. A constant absorption depth across allotropes ensures consistent laser energy absorption regardless of the crystallinity of the Si and is therefore desired to ensure film homogeneity. However, above 940 nm the absorption depth reaches 100 μm, indicating the majority of the laser energy will be absorbed in the bulk wafer and not in the film. Therefore, a laser wavelength of 355 nm was chosen to ensure sufficient energy absorption in the a-Si film without large amounts of c-Si substrate absorption. Figure 23 shows a log plot of the absorption depth of silicon with various states of crystallinity from amorphous to single crystal for ultraviolet wavelengths.

LCPSim, a finite differences code programmed in MATLAB and developed by Andreas Fell at Fraunhofer ISE, can simulate laser optical effects such as reflection and absorption as well as thermodynamic effects such as heat transport and phase change within various materials [49], [50]. This simulation was used to calculate the variation of temperature with silicon depth for various laser fluences to validate the experimental measurements. Only the laser interaction with crystalline silicon could be reliably modeled due to the varying film density of amorphous silicon, which does not have consistent thermal diffusivity or optical properties data. An enthalpy-based heat transfer model was used along with the laser wavelength set to 355 nm, pulse width to 25 ns, and pulse shape to Gaussian. Figure 24 shows the simulated temperature versus depth in crystalline silicon for single laser pulses of increasing fluence. In addition, the substrate temperature after times of 20, 10, and 7 µs, which correspond to the time between pulses for repetition rates of 50, 100, and 150 kHz, respectively, were investigated. The findings suggest that despite the high repetition rates (50–150 kHz) used in laser raster processing, substrate temperature returns to near 25°C between pulses for the fluences assessed, indicating that there is no thermally induced increase in absorption between pulses and each pulse has its own discrete, isolated effect on the sample. The thermal diffusivity for crystalline, polycrystalline, and amorphous Si are 0.90, 0.10–

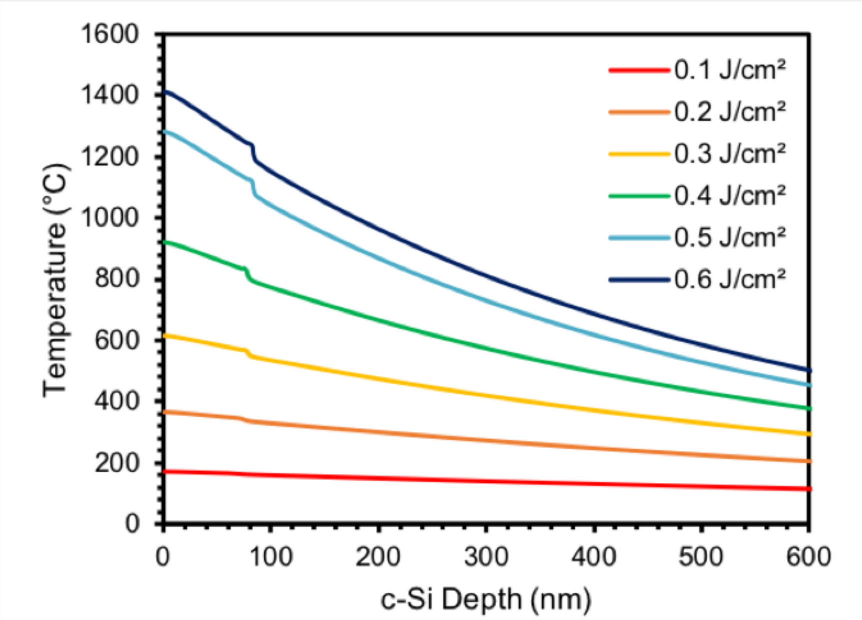

Fig. 24 Modeled results of temperature vs. crystalline silicon depth for increasing laser fluences of a single laser pulse. The simulated laser had a 355 nm wavelength and 25 ns pulse width and was modelled using LCPSim from Fraunhofer ISE with permission from A. Fell.

0.14, and <0.10 cm^2/s, respectively [45]. Therefore, the true temperatures at increasing depths in the a-Si may be lower.

5.3 Fabrication, Optimization, and Device Results

This study used high carrier lifetime, 100 mm, 500 Ω-cm resistivity, 298 μm thick, textured, n-type FZ wafers so that the variation in dark current density, J_0, better reflects the change in surface passivation and sheet resistance measurements reflect the change in film resistivity. The wafers are etched using a KOH solution and then cleaned in an RCA solution. Next, a 1.5 nm-thick tunnel oxide was grown symmetrically on both sides of the wafer using a HNO_3 solution at 100 °C. After this, a 12 nm-thick phosphorus-doped a-Si:H layer was deposited on both sides of the structure using PECVD by Prof. Rohatgi’s research group at the Georgia Institute of Technology. This layer is subjected to a furnace anneal at 875 °C for 30 minutes or pulsed laser annealing to further crystallize the layer, activate dopants, and improve its interface with SiO_2 [41].

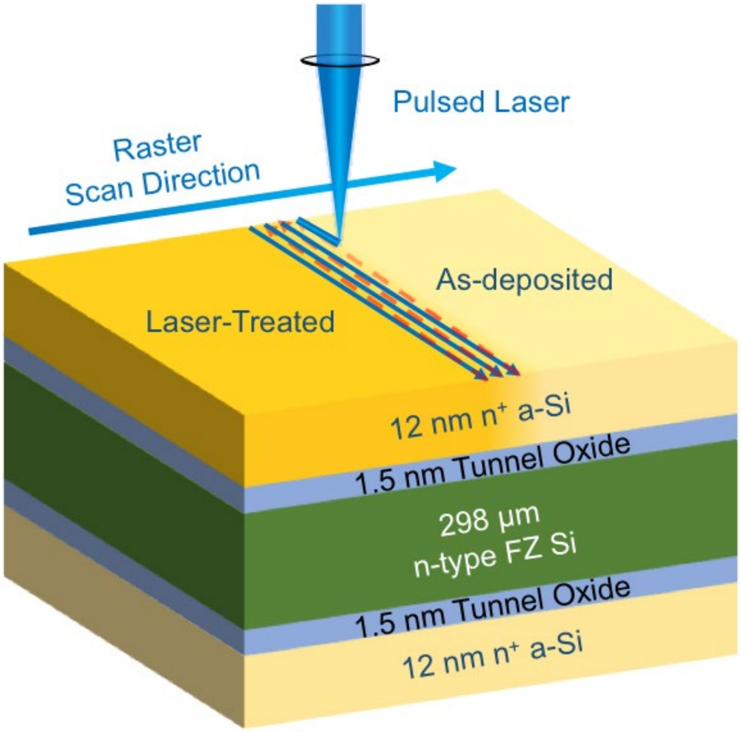

Fig. 25 Symmetric carrier-selective passivating-contact device structure for QSSPCD evaluation of passivation showing laser raster scan pattern.

Using a 355 nm wavelength, 25 ns pulse width laser with a spot size of 160 µm and a computer-controlled galvanometric scan head, the laser fluence and pulse overlap was optimized. The pulsed laser was raster scanned across the substrate with a repetition rate of 50 kHz, a scan speed between 2–8 m/s, and a raster line spacing between 40–160 µm. Figure 25 shows a schematic of the device structure and laser raster pattern.

To evaluate the passivation parameters of the symmetric structures shown in Figure 25, the method developed by Kane and Swanson [51] was employed, using a Sinton Instruments WCT-120 QSSPC at a specified minority carrier density of 1.0×10^{15} cm^{-3} in generalized (1/1) analysis mode. J_0 values are divided by two to reflect the saturation current of one of the two layers in the symmetric structure which is designated by $1\times J_0$. The sheet resistances of the deposited films were measured with a Jandel Multiposition Probe with a linear 1.00 mm probe spacing and a 25 µm tip radius.

After deposition of the 20 nm n^+ a-Si:H films but before any subsequent anneal, the as-deposited films had an average resistivity exceeding 12 mΩ·cm, active dopant concentration on the order of 10^{16} cm^{-3}, lifetime of 733 µs, implied open circuit voltage (iV_{OC}) of 679 mV, and $1\times J_0$ of 25.6 fA/cm^2. One sample was conventionally annealed in a furnace at 875 °C for 30 mins in inert nitrogen to activate the dopants, crystallize the a-Si, and improve the interface it shares with SiO_2. After annealing, the resistivity dropped to 0.7 mΩ·cm and the active dopant concentration increased to 7.7×10^{19} cm^{-3}, indicating phosphorus moving from interstitial to substitutional lattice sites and solid-phase crystallization of the n^+ a-Si. The lifetime and iV_{OC} increased to 3586 µs and 719 mV, respectively, while the $1\times J_0$ decreased to 5.2 fA/cm^2, indicating excellent surface passivation.

To reduce the thermal budget for this process and the amount of time at which the structure stays at elevated temperatures, as-deposited samples were laser processed across a variety of laser fluences and pulse overlap percentages on both sides of the symmetric structure. The process optimization results are shown in Figure 26. Initially, as the laser fluence increases, the film resistivity decreases and the iV_{OC} increases, suggesting simultaneous dopant activation and passivation improvement. The iV_{OC} peaks at 703 mV at a fluence of 0.34 J/cm^2, which corresponds to a temperature range near 800 °C from the simulation and coincides well with conventional furnace annealing temperatures for TOPCon. Above this fluence, the drop in resistivity flattens

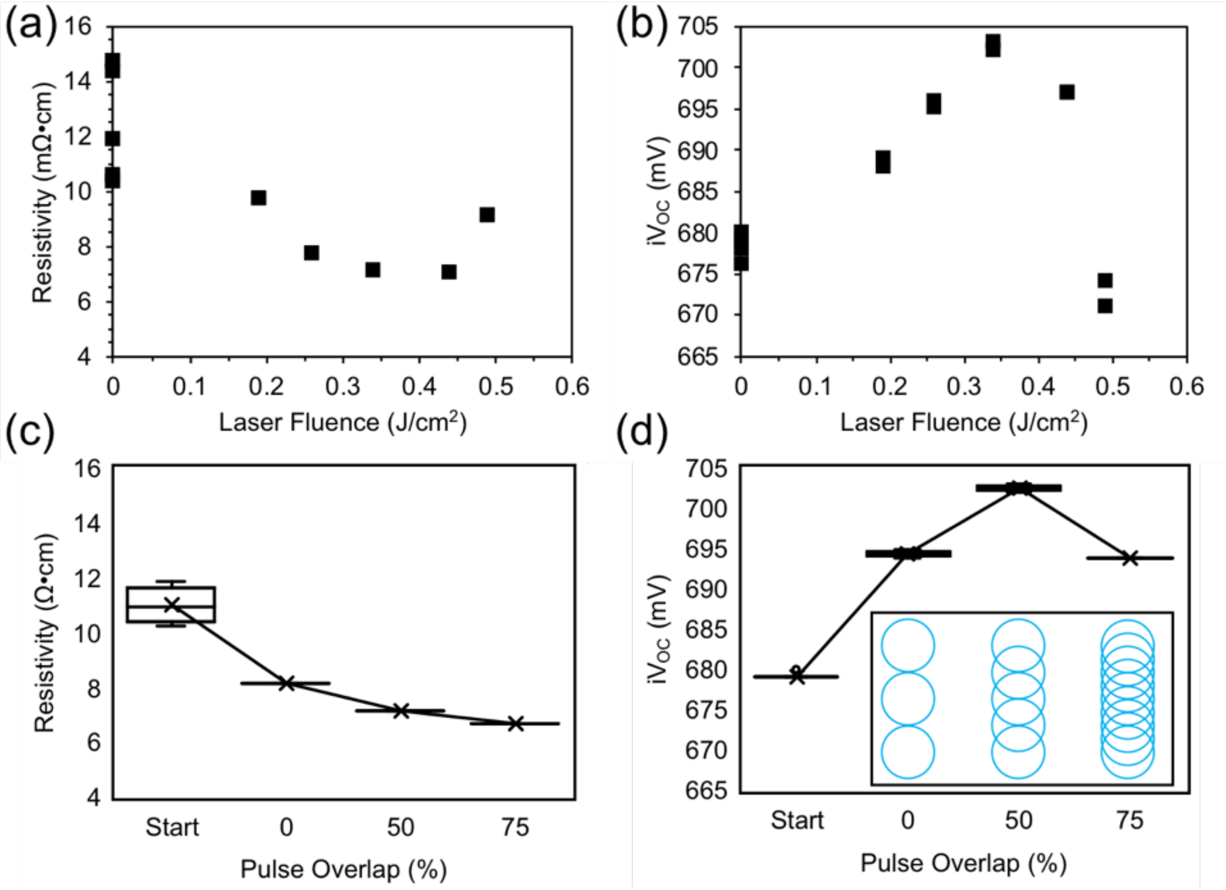

Fig. 26 Fluence of a single laser pulse vs. (a) film resistivity and (b) device iV_{OC}. The optimal fluence occurs at 0.34 J/cm^2 based on low film resistivity and high iV_{OC}. Percentage of pulse overlap at the optimal laser fluence vs. (c) film resistivity and (d) device iV_{OC}. While greater overlap resulted in a lower film resistivity, the peak device iV_{OC} occurred at a pulse overlap of 50%. The inset in (d) shows a top-down illustration of how pulse overlap of a Gaussian beam influences the number of pulses per area.

out with a minimum of 7.0 mΩ·cm and begins to increase again at higher fluences. This suggests that laser activation of dopants may saturate at this density for 12 nm n^+ poly-Si films, and the resistivity increase at fluences above 0.45 J/cm^2 may indicate dopant loss or a-Si film loss due to ablation. Similarly, the drop in iV_{OC} at higher fluences could indicate damage to the underlying tunnel oxide interfaces and reduced band-bending as a result of dopant or film loss. Therefore, the optimal fluence was chosen as 0.34 J/cm^2 for laser annealing and was used to optimize the pulse overlap. The pulse overlap was adjusted by changing the galvanometer scanning speed from 2–8 m/s and the scan line spacing between 40–160 µm at a fixed repetition rate of 50 kHz and laser spot size of 160 µm. The pulse and scan line spacing were kept identical for simplicity. The inset of Figure 26 (d) shows a top-down illustration of the pulse overlap. The film resistivity continued to decrease with increasing overlap, reaching a minimum value of 6.7 mΩ·cm at an overlap percentage of 75%. However, the iV_{OC} peaked at an overlap percentage of 50% and decreased at higher overlap percentages. This indicates that while a higher overlap percentage could grant increased dopant activation, it may cause minor damage to the tunnel oxide interfaces from photomechanical stress. Therefore, 50% (4000 mm/s scan speed and 80 µm scan line spacing) was selected as the optimal pulse overlap.

To examine how SiN_x further improves the passivation properties, 60 nm of SiN_x was deposited symmetrically on a pre-laser-processed sample with a Trion Orion PECVD system. Films were deposited at a substrate temperature of 350 °C and pressure of 600 mTorr using 600 sccm of 2% SiH_4 balanced with N_2 and 15 sccm of NH_3. The films were annealed at 350 °C for 30 minutes after deposition to ensure suitable film adhesion. Table I summarizes the data for dopant activation and passivation of the as-deposited, furnace-annealed, optimally laser-processed sample, and optimally laser-processed sample with 60 nm of SiN_x symmetrically deposited on both

TABLE I
TOPCON TEST STRUCTURES ELECTRICAL PARAMETERS

Sample	ρ (mΩ·cm)	N_D (cm^{-3})	τ_{fit} (µs)	iV_{OC} (mV)	$1\times J_0$ (fA/cm^2)
As-deposited, pre-annealing	> 12[a]	~10^{16}	733	679	25.6
875 °C, 30 min, N_2 furnace anneal	0.7	7.7×10^{19}	3586	719	5.2
Optimal laser-processed[b] sample	7.1	7.1×10^{18}	1333	703	15.5
Laser-processed sample with post-deposition of SiN_x	7.1	7.1×10^{18}	2001	718	8.6

Resistivity, active dopant concentration, lifetime, implied open-circuit voltage, and one side recombination current density for the starting as-deposited, furnace-annealed, champion laser-annealed, and laser-annealed with subsequent SiN_x deposition samples. All a-Si:H layers are 12 nm thick.

[a] Sheet resistance is unmeasurable above 10 kΩ/sq, corresponding to a resistivity 12 mΩcm.

[b] Optimal condition is at a laser fluence of 0.34 J/cm^2.

sides of the sample. Laser annealing of the TOPCon/SiN_x stack after SiN_x deposition resulted in a loss in passivation even at lower laser annealing fluences.

5.4 Characterization of Laser Annealed Poly-Si

Due to the 12 nm film thickness and sample roughness, characterization with Raman and Hall effect measurement becomes difficult because the majority of the Raman signal would come from the bulk Si substrate and Hall effect measurements on rough samples with ultra-thin films leads to inconsistent results. Therefore, 200 nm a-Si films were deposited and furnace- or laser-annealed to characterize the crystallization and dopant activation. Due to the increased film thickness, the ultraviolet laser wavelength was unable to reach the c-Si/SiO_2/a-Si interface and influence the passivation, but Raman and Hall effect characterization was simplified.

Raman spectra were taken with a Renishaw inVia confocal Raman microscope with an 1800 lines/mm grating (2.93 cm^{-1} resolution) at an excitation wavelength of 405 nm to reduce the signal coming from the substrate. Figure 27 shows the Si Raman peak for as-deposited, furnace-annealed, and laser-annealed samples at increasing laser fluence where each laser-annealed spectra

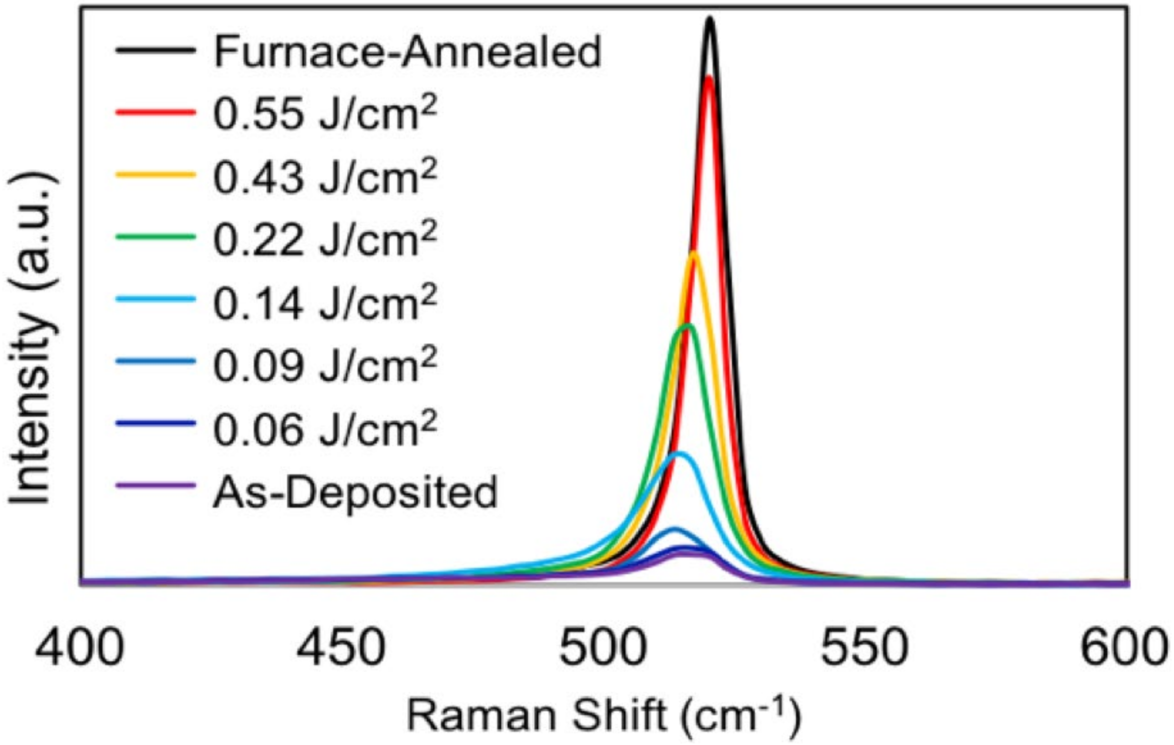

Fig. 27 Raman spectra of 200 nm thick as-deposited, furnace-annealed and a-Si films that were laser-processed under a single pulse at increasing laser fluence. As the laser fluence increases, the intensity of the 520 cm^{-1} Si peak increases, demonstrating increased crystallinity under increasing laser fluence. Thicker films were used to ensure Raman signal only comes from the deposited film and not the wafer.

is from a single laser pulse on an as-deposited sample. Amorphous Si has a broad Raman band based on the wide variety of different bond lengths in its amorphous state, while c-Si has a sharp Raman peak centered at 520.5 cm^{-1} corresponding to a high count of similar short length bonds. With increasing fluence, the peak intensity increases and the peak width decreases indicating increased crystallinity. Part of the signal intensity increase with crystallinity is the result of an increased interaction volume with an increased absorption depth of c-Si (100 nm) versus a-Si (11 nm) at 405 nm as shown in Figure 23. While the high 0.55 J/cm^2 fluence spectra shows crystallinity on par with that of the furnace-annealed poly-Si, that fluence is too high for thinner 12 nm a-Si samples as it caused a large drop in iV_{OC} from oxide interface disruption. The thickness of the

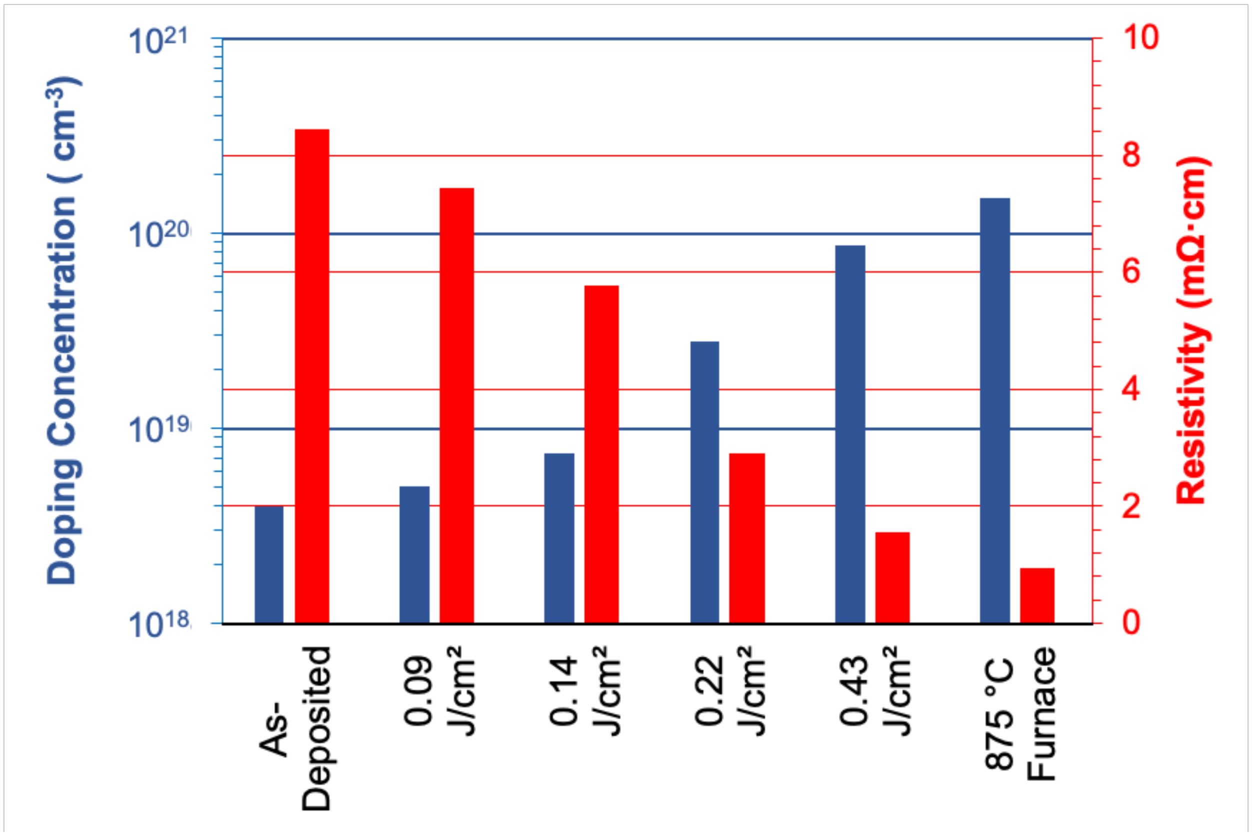

Fig. 28 Hall-effect measurement of doping concentration (left axis, blue bars) and resistivity (right axis, red bars) for 200 nm thick as-deposited, furnace-annealed, and laser-annealed a-Si films, showing an increase in doping concentration and decrease in resistivity with increasing laser fluence that is comparable to furnace annealing.

deposited a-Si layer could potentially be optimized to allow for a higher fluence without impacting the tunnel oxide interface.

Carrier concentration and resistivity were measured at room temperature with an Ecopia HMS-3000 Hall Measurement System using a 0.55 T permanent magnet and spring probes configured to the Van der Pauw arrangement on square samples. As-deposited samples had a carrier concentration of 4.0×10^{18} cm^{-3} and resistivity of 8.4 mΩ·cm. Since most of the phosphorus dopant is in interstitial sites and few lattice sites exist in the amorphous state, it contributes little to the electrical properties of the film. As the laser fluence increases, dopant activation continues to rise, increasing the measured dopant concentration and decreasing the film resistivity as the amorphous film crystalizes and the phosphorus dopant enters the crystalline lattice. The highest laser fluence evaluated, 0.43 J/cm^2, has a measured doping concentration of 8.7×10^{19} cm^{-3} and resistivity of 1.6 mΩ·cm comparable to the furnace-annealed 200 nm poly-Si sample's 1.5×10^{20} cm^{-3} concentration and 0.9 mΩ·cm resistivity, indicating successful activation of dopant and film crystallization with room for future improvement through laser annealing optimization. A summary of these results is shown in Figure 28.

The a-Si:H film thickness must be carefully chosen for improved performance at a given laser wavelength. Thicker a-Si:H films, in the range of 100–200 nm, will absorb the laser light in the upper part of the film and the thermal annealing of interface defects would not occur due to the temperature gradient in the film. If the a-Si:H film thickness is too low (~10 nm), then part of the laser light will be absorbed by the Si substrate, inducing defects. For a 355 nm wavelength laser, an optimum a-Si:H film thickness appears to be around 20–40 nm to achieve higher performance from laser annealing. This work demonstrates the feasibility of laser crystallization and dopant activation of a-Si:H in TOPCon carrier-selective contacts, and further improvements can be made by optimizing the layer thickness and corresponding annealing fluence.

5.5 Conclusions

This section demonstrated a novel laser processing concept to replace the high-temperature furnace anneal for n-type TOPCon carrier-selective passivating contacts for silicon solar cells. By utilizing laser processing, the polysilicon layer increases in crystallinity, electrical conductivity due to dopant activation, and passivation due to the shallow absorption depth of the laser wavelength and the nano-timescale from the laser pulse width, with minimal thermal impact on the interfacial oxide. Optical modeling and LCPSim simulations help shape the knowledge of the laser material interaction process and provide a foundation for experimental work. Combined with a SiN_x capping layer, this section demonstrates a passivating SiN_x/poly-Si/tunnel oxide/Si structure with a low 7.1 mΩ·cm poly-Si film resistivity, over 2001 µs effective carrier lifetime, 718 mV iV_{OC}, and 8.6 fA/cm^2 J_0 demonstrating the viability of the approach. Raman and Hall effect characterization of 200 nm laser-annealed a-Si films show that a high degree of crystallinity and dopant activation comparable to 875 °C furnace-annealed films can be achieved.

A thicker a-Si film, potentially in the range of 20–40 nm, would allow for a higher fluence to be used, granting increased crystallinity and dopant activation but reducing damage to the tunnel oxide interfaces due to the temperature decrease at increased thickness. By adapting the laser processing to a solar cell device, high-efficiency and well-passivated carrier selective silicon solar cells could be fabricated at a reduced thermal budget and without the heating of the entire wafer done under furnace annealing. Thicker a-Si films and use in a full device structure will be the subject of future study.

The results of this chapter were published in the IEEE Journal of Photovoltaics, volume 10, issue 5, pages 1283–1289 in September of 2020. The publication was proceeded by similar work in a published conference proceeding at the 46th IEEE Photovoltaics Specialist Conference on pages 2708–2712, in July 2019.

CHAPTER 6: Laser Annealing of Carrier-Selective MoO_x and TiO_x layers for Silicon Solar Cells

6.1 Introduction

Efficient photovoltaics have two important functions: (1) converting light into electron-hole pairs, and (2) effectively separating these pairs and extracting them at the electrodes before they recombine. Carrier-selective contacts have received increased interest in recent years because of their ability to collect one type of carrier (e.g. holes) while blocking the other (e.g. electrons). Additionally, these layers also provide passivation of the absorber surfaces making them the most promising method for reducing recombination at the interfaces of crystalline-Si (c-Si) photovoltaics while enabling effective carrier transport.

Current top candidates include solar cells with heterojunction with intrinsic thin layer (HIT)-based contacts and tunnel-oxide passivating contacts (TOPCon) and have achieved power conversion efficiencies of 26.7% [52] and 25.8% [53], respectively, however they require costly deposition techniques like PECVD or high-temperature (>800 °C) thermal treatments. To reduce fabrication complexity, temperature, and cost, transition metal oxides (TMO) carrier-selective contacts have garnered expanding intrigue and demonstrated device efficiencies of 20.7% [54] with simulated device structures reaching efficiencies of 25.3%–27.95% [55], [56]. TMO contacts can be deposited with simple techniques like thermal evaporation [54], [57] or sol-gel processes [58] at low temperatures and without dopants while retaining ideal optical characteristics, carrier-selectivity, and passivation. Removal of hydrogenated amorphous silicon (a-Si:H) entirely would reduce fabrication complexity by reducing the amount of toxic and flammable process gases used.

Due to a-Si low band gap of 1.7 eV, there is also considerable interest in removing them entirely to reduce parasitic absorption.

High-work function transition metal oxides, such as sub-stoichiometric molybdenum trioxide (MoO_x, x <3), have shown promise in recent years as hole-selective layers [54], [55], [57], [59], [60]. Depending on the exact stoichiometry, MoO_x has a high band gap of ~3 eV [61], reducing parasitic absorption, and a high work function 5.5–6.8 eV [62], enabling effective hole selectivity. The high work function induces upward band-bending at the Si surface causing inversion, reducing the electron surface concentration and increasing the hole current density to the contact [12]. Similarly, a low work-function metal oxide, such as TiO_2, can induce electron-selectivity through band alignment. TiO_2 has a wide band gap of 3.2–3.6 eV [3] with work functions roughly equivalent to the c-Si absorber. Therefore, carrier selectivity is obtained, not from induced band-bending, but by the minimal valence band offset and high conduction band offset with c-Si. The energy band diagram for these TMO-based carrier-selective contacts is shown in Figure 29. These layers can be used with thin tunnel oxides consisting of SiO_2 or Al_2O_3 sandwiched between the layer and the c-Si absorber for enhanced passivation.

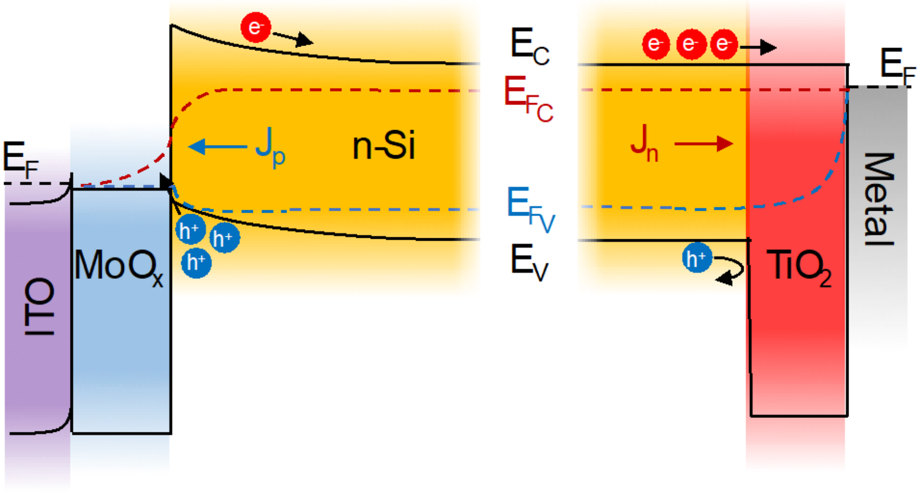

Fig. 29. Energy diagram showing carrier transport in MoO_x hole-selective contact and TiO_2 electron-selective contact, based on induced band bending and energy band alignment, respectively.

Commonly, moderate temperature (250–350 °C) annealing is needed to improve layer interface properties and cure low-temperature screen printed contacts in heterojunction silicon solar cells (standard screen printed contacts need temperatures of 500–700 °C). Bullock et al. noted that conventional annealing of TiO_2 up to 300 °C improved the V_{OC} and contact resistivity [54]. Neusel et al. noted that MoO_x, irrespective of the presence of an a-Si:H (i) buffer layer, has a loss in carrier selectivity and fill factor with annealing temperatures above 150°C [63]. Therefore, there is a need to accomplish annealing without detrimental impact to the MoO_x layer carrier-selectivity and passivation ability, and potentially improve those properties. In this chapter, a description of pulsed laser annealing of Al_2O_3, MoO_x and TiO_x is described. Although the carrier-selectivity was not studied, Sun et al. used laser annealing of sol-gel TiO_x for superior Si passivation layers, obtaining carrier lifetimes of 1000 μs and a surface recombination velocity of 6.25 cm/s [58]. With laser annealing, the duration of time the layer of interest is heated is exceedingly low and the laser wavelength can be selected to anneal only the layer of interest without bulk heating. This prevents

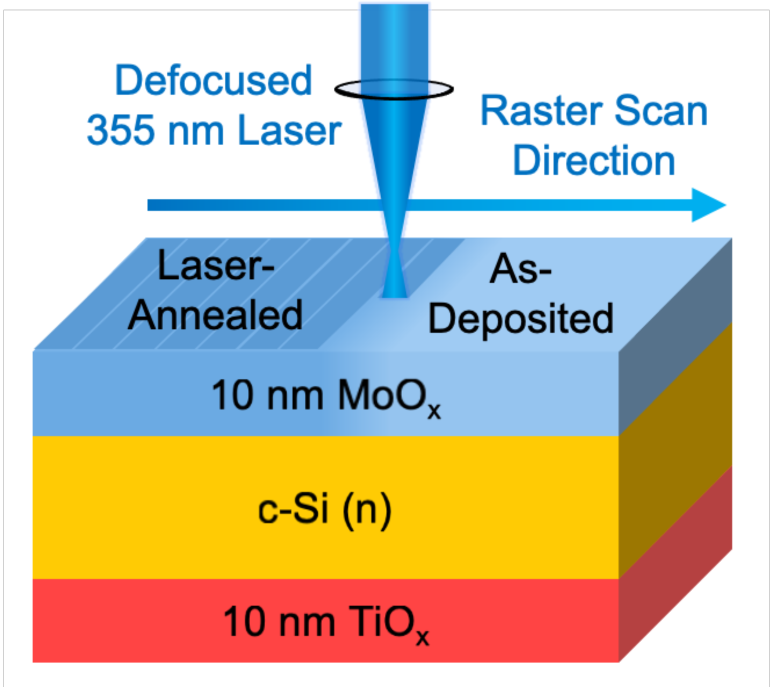

Fig. 30 Defocus beam laser annealing method for MoO_x hole selective contacts. The beam focus position is above the sample surface.

the detrimental effects experienced from conventional thermal annealing. Figure 30 shows the annealing concept.

6.2 Fabrication and Optimization of Furnace and Laser Annealing

Double-side polished, 1–5 Ω·cm resistivity, high-lifetime silicon wafers of both p- and n-type were dipped in HF to remove any native oxide and rinsed with DI water. The native oxide on some samples was left intact to study the impact. Additionally, some samples had 1.2 nm of Al_2O_3 deposited as a tunnel oxide using a plasma process at 200°C with a trimethylaluminum precursor in an atomic layer deposition (ALD) tool (Oxford, FlexAL). Samples were then placed in a thermal evaporator with a molybdenum boat containing either stoichiometric MoO_3 or TiO_2 pellets. The chamber is brought down to a pressure of 1×10^{-5} mbar, and 5–10 nm of MoO_x or TiO_x is evaporated at a rate of 0.1–0.2 Å/s by monitoring the deposition rate with a quartz crystal monitor. Afterwards, the wafers are flipped and a symmetric or asymmetric layer is deposited on the opposite side. For reference, thermal annealing was also done in an ambient air-filled furnace at increasing temperatures for 10 mins. A 10 nm, single-side MoO_x and TiO_x film was also coated on glass substrates to monitor the change in optical transmission with increasing annealing temperature and for additional characterization. TiO_2 films were also deposited via a plasma ALD process with a Tetrakis(dimethylamino)titanium(IV) (TDMAT) precursor to compare with thermally evaporated films.

The optical transmission of MoO_x at first increases at increasing annealing temperatures up to 300°C but then rapidly degrades when annealing at higher temperatures. The as-deposited MoO_x passivates the n-Si wafer modestly, with a lifetime of 230 μs, iV_{OC} of 635 mV, and J_0 of 68 fA/cm^2. However, upon annealing at any temperature in air, the passivation performance degrades, likely due to shift in stoichiometry and loss of carrier-selectivity. This indicates that thermal

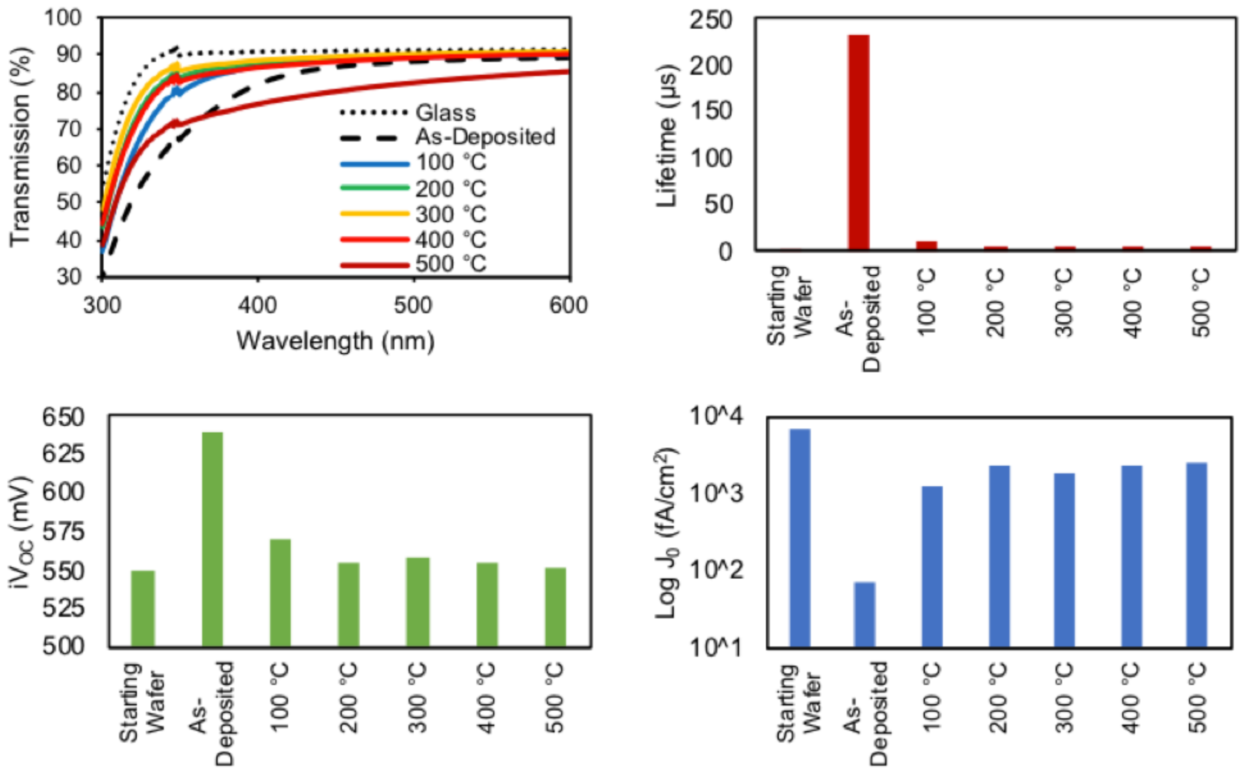

Fig. 31 The effect of ambient air annealing temperature on the optical transmission of MoO_x-coated glass, and the lifetime, iV_{OC}, and J_0 of n-type silicon symmetrically coated by MoO_x. The starting wafer was measured with the native oxide still intact.

annealing in air of MoO_x is not an effective process for fabrication of high-efficiency transition metal oxide-based heterojunction solar cells. The ambient air thermal annealing results for thermally evaporated MoO_x are shown in Figure 31.

Similarly, the optical transmission of TiO_x increases at temperatures up to 400 °C, but then becomes opaque and blisters are formed at temperatures of 500 °C. In contrast, the as-deposited TiO_x does not grant a substantial improvement to the passivation. Subsequent annealing in ambient air increases the passivation, with the peak passivation occurring at an annealing temperature of 200 °C with a lifetime of 461 µs, iV_{OC} of 668 mV and J_0 of 205 fA/cm^2. Above this temperature the passivation moderately decreases, but still remains higher than the measured as-deposited passivation parameters. This decrease is likely due to crystallization of the TiO_2, leading to restructuring of the film on the Si surface and potentially leaving partial regions un-passivated

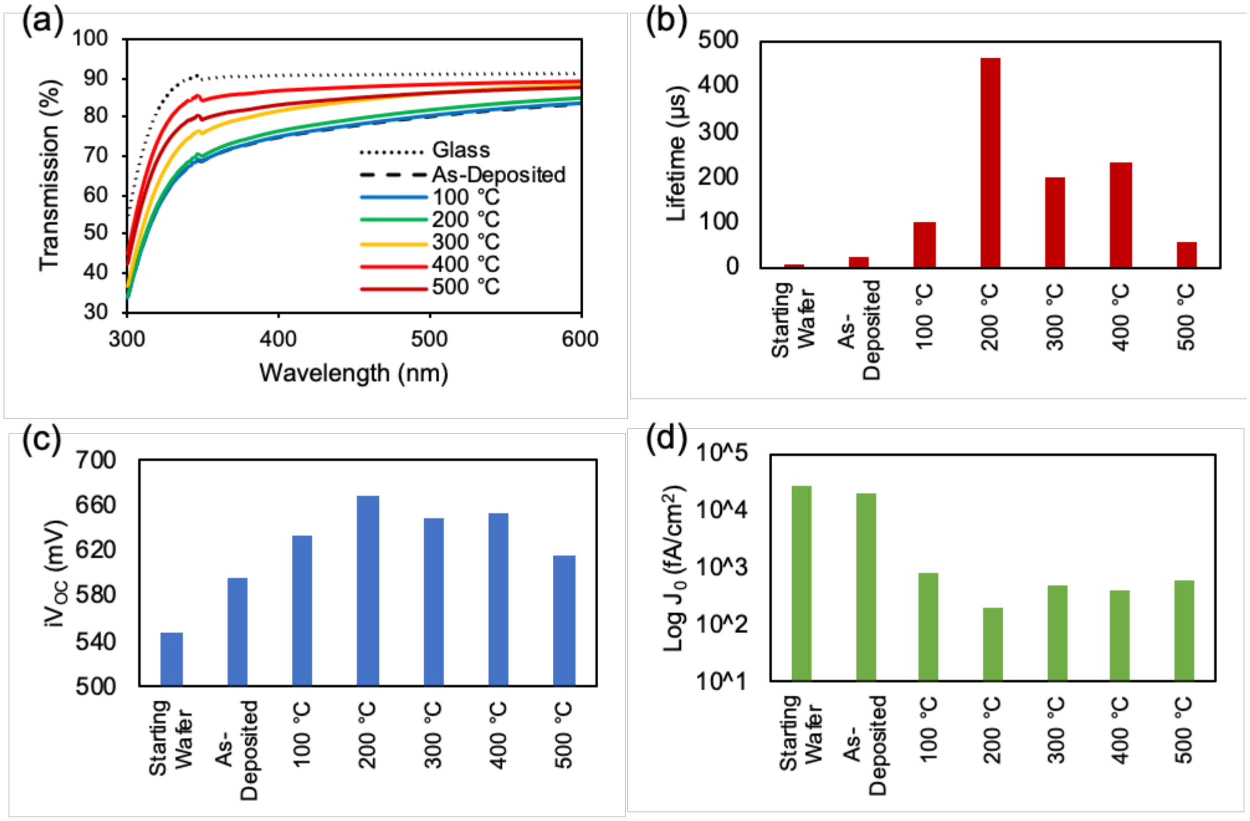

Fig. 32 The effect of ambient air annealing temperature on the optical transmission of TiO_x-coated glass, and the lifetime, iV_{OC}, and J_0 of n-type silicon symmetrically coated by TiO_x. The starting wafer was measured with the native oxide still intact.

[54]. The observed blistering and opaqueness of the film at 500 °C confirms that this is occurring. This demonstrates that moderate temperature annealing of the TiO_2 is necessary for improved passivation and these results are shown in Figure 32.

Laser annealing with a defocused laser beam was utilized to more evenly distribute energy across the beam waist and to avoid reach the ablation threshold near the Gaussian peak of the beam [64]. Defocused laser annealing can improve the interface properties and modify the stoichiometry of the as-deposited MoO_x or TiO_x. A schematic of this process for the MoO_x film is shown in Figure 30. The short pulse (25 ns) and shallow absorption depth (10 nm) ensures that there is minimal substrate heating during annealing and that most of the energy is absorbed by the film. In contrast to thermal annealing, laser annealing has a large fluence window in which MoO_x

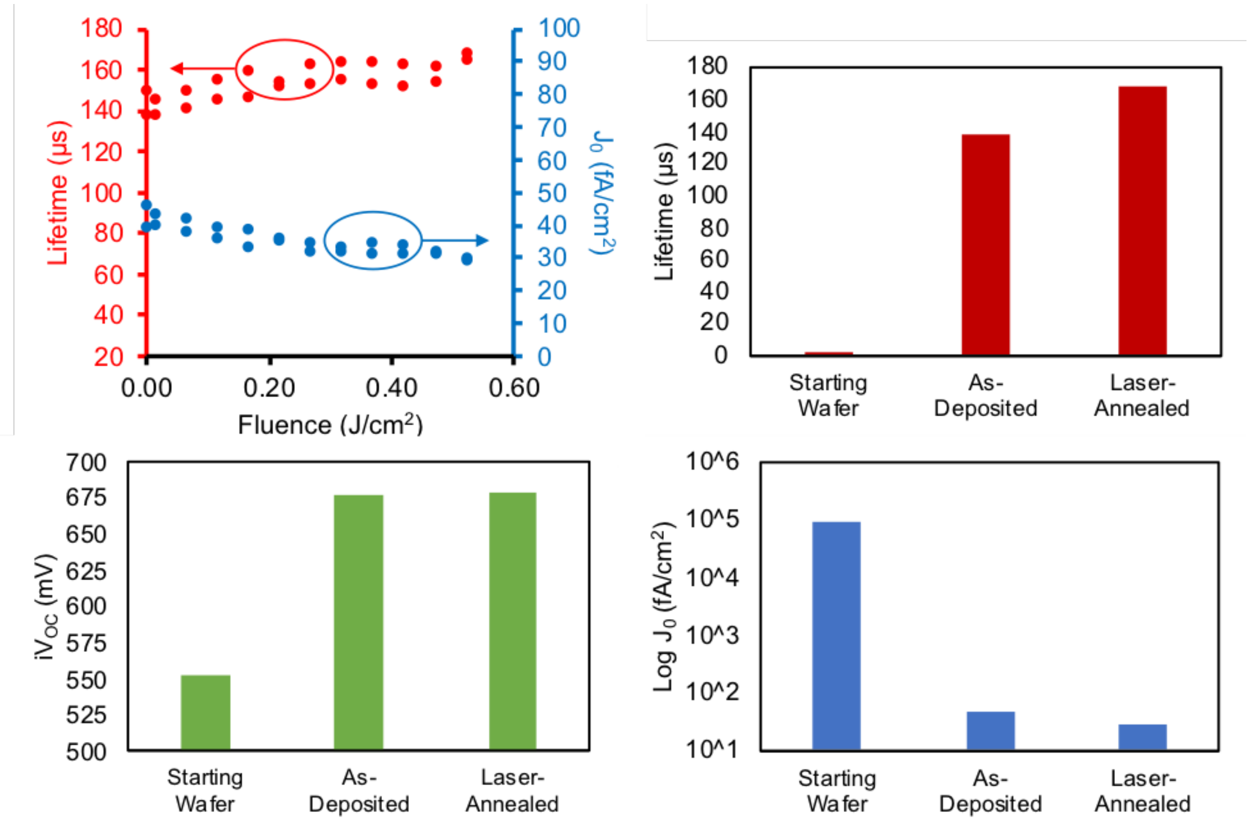

Fig. 33 Optimization of laser annealing fluence on MoO_x device lifetime and J_0 and comparison of the lifetime, iV_{OC} and J_0 for the starting wafer, as-deposited 10 nm MoO_x on p-type Si, and laser annealed MoO_x on p-type Si.

passivation of Si experiences increased lifetime and decreased recombination current density, J_0. This indicates there is a wide range of laser parameters which could be used to improve the device passivation. The optimized annealing condition improved the lifetime by 30 µs (21 $\%_{rel}$) and decreased the J_0 by 17 fA/cm^2 (38 $\%_{rel}$) of the as-deposited film, with marginal improvement in the iV_{OC} (2 mV, <1 $\%_{rel}$). Laser annealing results for MoO_x are shown in Figure 33. Laser annealing has already shown to be beneficial over even low temperature furnace annealing. With further optimization, this method could potentially generate an improved passivation in a transition metal oxide contacted carrier-selective devices.

Similarly, TiO_2 layers were prepared by thermal evaporation and were similarly laser annealed at a defocused condition. These results are shown in Figure 34. Unfortunately, laser

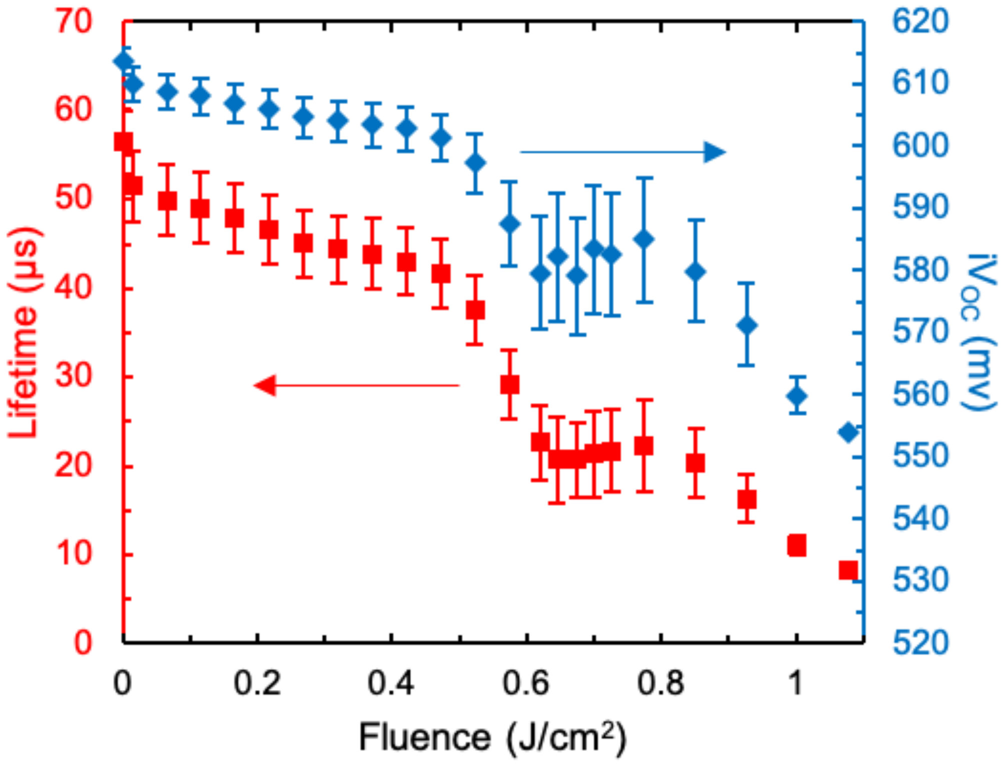

Fig. 34: Impact of laser annealing fluence on lifetime and iV_{OC} for a sample coated with symmetric 10 nm TiO_2 layers via thermal evaporation.

annealing at these conditions has an overall negative impact on device performance, even at low fluences. This could potentially be due to the high absorption of 355 nm wavelength light for amorphous TiO_2, which would limit the amount of light reaching the TiO_2/Si interface to improve the interface properties. Additional study is needed to evaluate if laser annealing can improve thermally evaporated TiO_2 carrier-selective layers for silicon solar cells.

Laser annealing was also carried out on the Al_2O_3 tunnel oxide which typically requires temperatures in the range of 350–450 °C to improve its interface with the silicon absorber and to improve its passivation. Laser annealing was found to improve a 10 nm Al_2O_3 film on a p-Si surface drastically with no detrimental impact at any of the fluences used. Repeated scans at a high fluence were also demonstrated which showed further improvement, but this improvement began to diminish after a high number of repeated scans. While the current optimization process does not

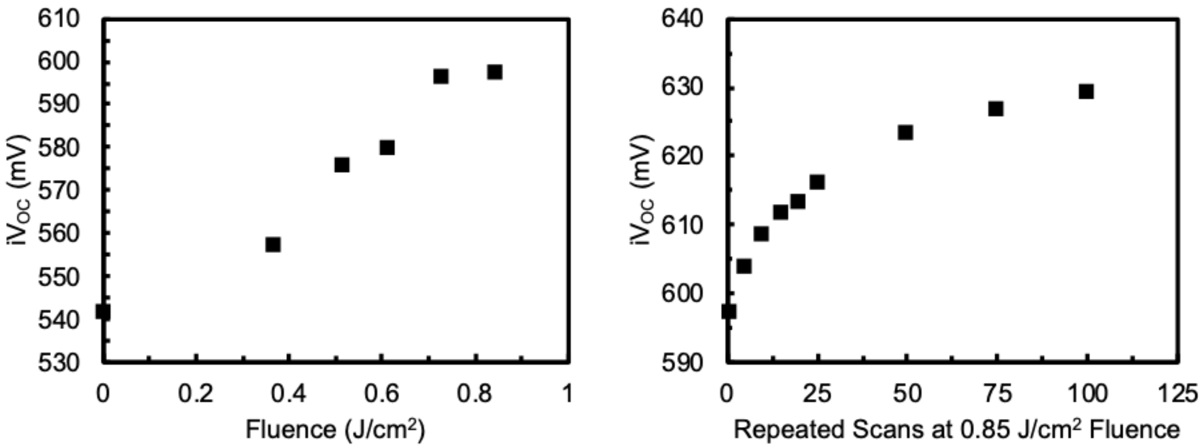

Fig. 35 Optimization of laser annealing fluence and repeated scans at the maximum 0.85 J/cm^2 fluence for 10 nm Al_2O_3 films on a p-Si wafer.

quite reach the passivation obtained by furnace annealing of Al_2O_3, further improvements to the laser annealing processes, could potentially allow it to surpass the furnace. These results are shown in Figure 35. A table summarizing different device structure used, the processing condition used, and the resultant lifetime and iV_{OC} are shown in Table II.

TABLE II

DEVICE TEST STRUCTURES, PROCESSING CONDITIONS, LIFETIME, AND IMPLIED OPEN CIRCUIT VOLTAGE

Structure	Processing Condition	τ_{fit} (μs)	iV_{OC} (mV)
10 nm Al_2O_3 / n-Si / 10 nm Al_2O_3	As-Deposited	5	520
10 nm Al_2O_3 / n-Si / 10 nm Al_2O_3	350 °C, 30 min, FGA	580	667
10 nm Al_2O_3 / n-Si / 10 nm Al_2O_3	350 °C, 60 min, FGA	622	671
10 nm Al_2O_3 / n-Si / 10 nm Al_2O_3	350 °C, 120 min, FGA	638	673
1.2 nm Al_2O_3 / n-Si / 1.2 nm Al_2O_3	As-Deposited	4	515
1.2 nm Al_2O_3 / n-Si / 1.2 nm Al_2O_3	450 °C, 60 min, FGA	627	666
1.2 nm Al_2O_3 / n-Si / 1.2 nm Al_2O_3 / 5 nm TiO_x	As-Deposited	446	656
1.2 nm Al_2O_3 / n-Si / 1.2 nm Al_2O_3 / 5 nm TiO_x	125 °C, 30 min, FGA	455	656
8 nm MoO_x / 1.2 nm Al_2O_3 / n-Si / 1.2 nm Al_2O_3 / 5 nm TiO_x	As-Deposited	583	668
1.2 nm Al_2O_3 / NatOx / n-Si / NatOx / 1.2 nm Al_2O_3	350 °C, 30 min, FGA	954	687

Lifetime and implied open-circuit voltage for the various carrier-selective and tunnel-oxide structures tested at different processing conditions. Extra spacing between rows represents different samples.

6.3 Conclusions

This section demonstrated a transition metal oxide-based heterojunction silicon solar cell that was amorphous Si-free. Laser processing of the MoO_x hole-selective contact enables low temperature annealing of the device to achieve increased passivation performance. However, laser processing of TiO_x electron-selective contacts has not yet been demonstrated to improve the passivation. The laser annealing process also improves the passivation of thin ALD-deposited Al_2O_3 substantially. This work demonstrates that laser processing of MoO_x can successfully achieve an exceptional τ_{fit} of 743 μs, iV_{OC} of 679 mV, and 1 x J_0 as low as 14 fA/cm^2. This work opens the door for fabricating low-cost, low-temperature heterojunction Si solar cells that do not require the use of PECVD or a-Si layers.

The results of the MoO_x study were published in a conference proceeding at the 47th IEEE Photovoltaics Specialist Conference in July 2020. An additional publication is in preparation for the remaining results on TiO_x, $Al2O_3$, and a complete TMO heterojunction device.

CHAPTER 7: Impact of Pulsed Laser Heating on Silicon Passivation and Defect Generation

7.1 Introduction

The use of lasers for photovoltaic fabrication has been growing in recent years particularly for dielectric opening, doping, laser annealing, and contact firing. Because of the growing use of lasers in photovoltaic fabrication, there is substantial interest in understanding how laser heating of carrier-selective or passivation layers could lead to defect generation in the silicon surface. In addition, it was evaluated if subsequent passivating layers can passivate any defects that form from laser heating. This study examines how the quasi-steady state photoconductance and micro-photoluminescence (μ-PL) change with high-fluence laser processing of a percentage of the full area of a well-passivated wafer. One state-of-the-art passivation method is to use a 5–10 nm ALD-deposited Al_2O_3 followed by a 60 nm PECVD-deposited Si_3N_4 as it can achieve surface recombination velocities below 1 cm/s [58] and iV_{OC}'s in excess of 720 mV. Typically, the contact area percentage, or the ratio of the contact area to the full device area, is a delicate balance between decreasing the series resistance and reducing the amount of contact shading on the device. Budhraja et al. have shown that the benefit of increased contact area on the series resistance are diminishing above 10%, but the Suns Voc, which takes into account current generation while ignoring series resistance loses, decreases rapidly [66]. Laser processing of 1-10% of the contact area would be necessary for dielectric opening so metal contact can be made through the dielectric or annealing of carrier-selective layers beneath the contacts to increase the conductivity and reduced interface recombination. Therefore, the impact of laser processing at a variety of high laser fluences with contact areas between 1-10% is of wide interest to the photovoltaic community.

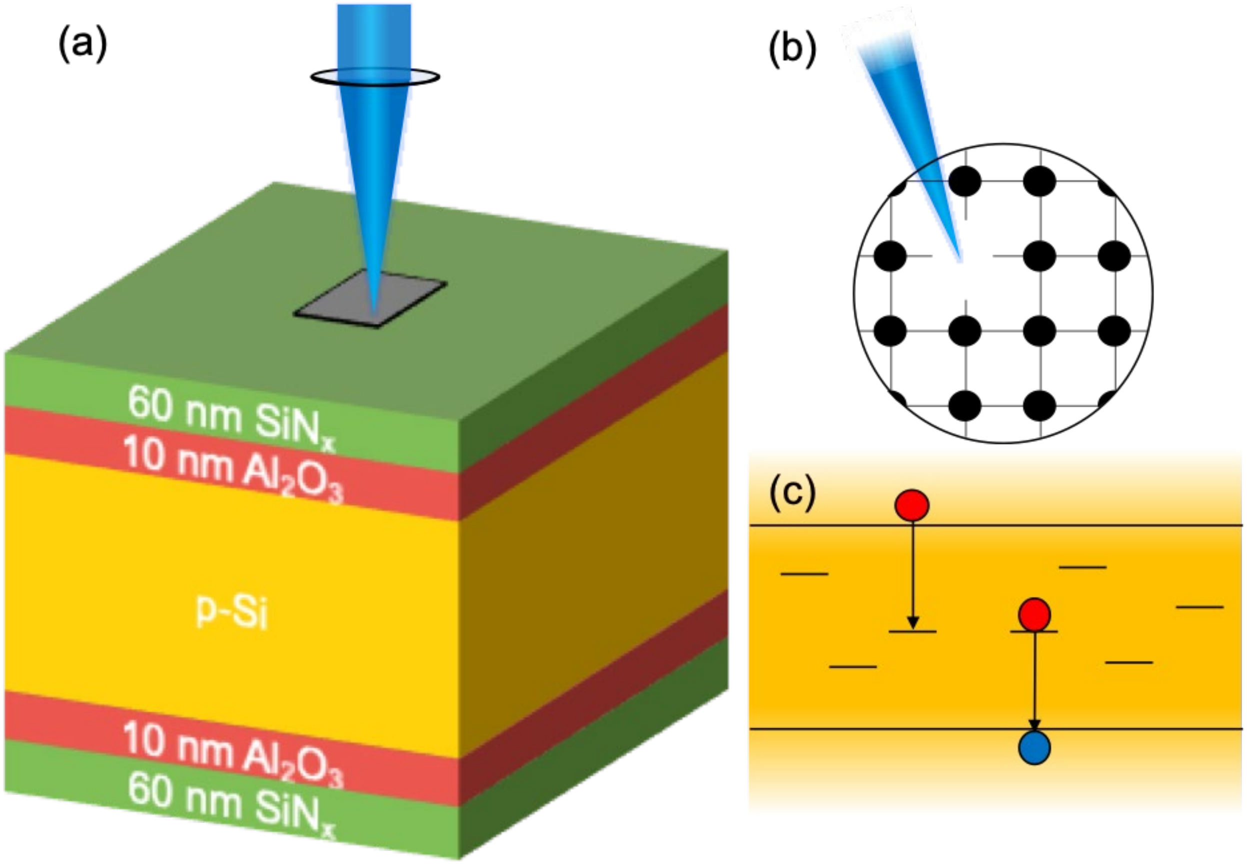

Fig. 36 (a) Device schematic showing ultraviolet laser processing of a relative percentage of the total device area, (b) diagram showing laser generated defects and dislocations in the silicon lattice, (c) band diagram showing sub-band gap recombination sites introduced from laser processing.

Depending on the laser fluence, defects in the silicon absorber, such as dislocations could be generated. The laser wavelength is also important, as green (532 nm) and ultraviolet (355 nm) wavelengths would generate defects near the surface due to silicon's high absorption coefficient, while near infrared would generate defects further in the bulk. So far, evidence of laser generated dislocations has typically been shown and characterized for near infrared wavelengths [67]. There is a surprising absence of characterization of defects caused at UV wavelength laser processing even with identical pulse energies and when clear damage to the silicon wafer can be seen via optical microscopy [68]. Since ultraviolet wavelengths are optimal for reducing bulk damage, while opening dielectrics or annealing carrier selective layers with thicknesses on the order of 10s of nm, there is strong interest in seeing if high fluence laser processing with UV wavelengths generates similar dislocations.

7.2 Device Fabrication and Laser Processing Setup

A high lifetime, single-side polished, p-Si wafer with a resistivity of 1–5 Ω·cm was used for this study as it provides the best passivation in combination with an Al_2O_3 and SiN_x stack. The wafer was laser cut to a 25 mm square shape, cleaned, dipped in HF to remove native oxide, and rinsed with DI water. Next, 10 nm of Al_2O_3 was deposited on both sides of the wafer using a plasma ALD process at 200 °C (FlexAL, Oxford Instruments). Following that, 60 nm of SiN_x was deposited on both sides of the wafer using a 350 °C PECVD process (Orion, Trion Technology) at a pressure of 600 mTorr with flow rates of 600 sccm of 2% SiH_4 balanced with N_2 and 15 sccm of NH_3. This structure was then annealed in forming gas (H_2 5%, Ar 95%) at 350°C for 30 minutes. An exceptional device iV_{OC} of 721 mV, lifetime of 940 μs, and incredibly strong PL signal at the 1150 nm Si PL peak was obtained. Additional samples were fabricated for testing the impact of incrementally spaced 50 μm-width lines at 1%, 5%, and 10% of the total area. These samples consisted of double-side polished, n-Si wafers with a 1–5 Ω·cm resistivity. The native oxide was left intact and 30 nm of Al_2O_3 was deposited via the same ALD process on both sides of the wafer. These samples were annealed in forming gas at 425 °C for 1 hour resulting in an average lifetime of 1152 μs, iV_{OC} of 710 mV, and J_0 of 5.38 fA/cm^2.

Laser processing of 1%, 5% and 10% of the total area of this device at increasing laser fluence was investigated to see how it impacts the overall passivation, μ-PL signal, and defect formation. An ultraviolet laser with a wavelength of 355 nm, repetition rate of 50 kHz, and spot size of 50 μm was used for this study (MATRIX 355-8-50, Coherent) with laser fluences between 0.11–5.67 J/cm^2. The laser was raster scanned with a 0% pulse spot overlap both from pulse-to-pulse and line-to-line due to the 2500 mm/s scan speed and 50 μm raster line spacing across 2.5, 5.6, and 7.9 mm squares on the sample, corresponding to 1%, 5% and 10% of the sample area, respectively. The full fluence range was explored with 1% of the area first, then sequentially to the 5% and 10% sample areas. Additional laser processing with 3.5 mm squares at individual laser fluences were marked along the edges of the sample after the QSSPCD measurements to allow for additional characterization. The samples used for the incrementally space line study consisted of 25 mm length, 50 μm width lines. For 1%, 5%, and 10% of the total area, 5 lines with a 4.16 mm spacing, 25 lines with a 0.96 mm spacing, and 50 lines with a 0.49 mm spacing were used respectively.

The overall device passivation was measured via the QSSPCD method described by Kane and Swanson (WCT-120, Sinton). Micro photoluminescence (μ-PL) was measured using an excitation wavelength of 405 nm to limit the measured signal to around 100 nm depth from the surface due to the shallow silicon absorption depth at this wavelength. The beam was focused onto the sample with roughly a 2 mm spot, which could be contained within 1% of the processed area (2.5 mm) to ensure signal only came from the region of interest. The spectrometer (iHR 320, Horiba Jobin-Yvon) measurements were conducted between 800–1800 nm wavelengths to include the a-Si peak (~900 nm), c-Si peak (1150 nm), and dislocation peaks (1240-1527 nm). An InGaAs photo-receiver thermoelectrically-cooled to -40 °C was used to measure the signal (Electro-Optical Systems). An optical chopper (SR540, Stanford Research Systems) operating at a 200 Hz frequency was synced to a lock-in amplifier (SR 830 DSP, Stanford Research Systems) to improve the photoluminescence signal and to reduce noise by allowing only the 200 Hz luminescence signal to be registered by the measurement software. Additionally, a long-wave pass filter (>532 nm) was used to prevent the high laser intensity from entering the spectrometer. Raman spectra were also measured with an excitation wavelength of 405 nm (TopMode 405, Toptica Photonics) and in high-confocality mode to limit signal from the surface, and for Raman shifts between 0 and 3000 cm^{-1} (InVia confocal Raman Microscope, Renishaw). Optical microscopy images were taken at 50x with an Olympus BX53MRF-S microscope.

7.3 Results and Discussion

An image of the device with 1% (red), 5% (green), and 10% (blue) marked area percentages processed at 5.647 J/cm^2 laser fluence is shown in Figure 36 (a). The additional 3.5 mm squares that were later used for further characterization are indicated, but not initially used or shown, with the dashed yellow squares in Figure 37 (a). The change in sample lifetime, iV_{OC}, and J_0 with sequentially increasing laser fluence, and later sequentially increasing in percentage are shown in Figure 37 (b), (c) and (d), respectively. After an initial, relatively small drop in passivation at low fluences, the full area device passivation remained relatively unchanged with increasing fluence, even far above the ablation fluence for Si (~0.5 J/cm^2). Increasing the processed area resulted in further reductions, but overall the device lifetime and iV_{OC} remained above 600 μs and 709 mV, respectively. Interestingly, the J_0 initially decreased and then remained around 5 fA/cm^2 regardless of laser fluence or processing area. This demonstrates that typical laser processing for dielectric opening or carrier-selective layer annealing will have minimal impact on the overall device passivation.

For dielectric opening for subsequent contact formation with the absorber, different geometries are used. Typically these consist of lines drawn at incremental spacings, that can make

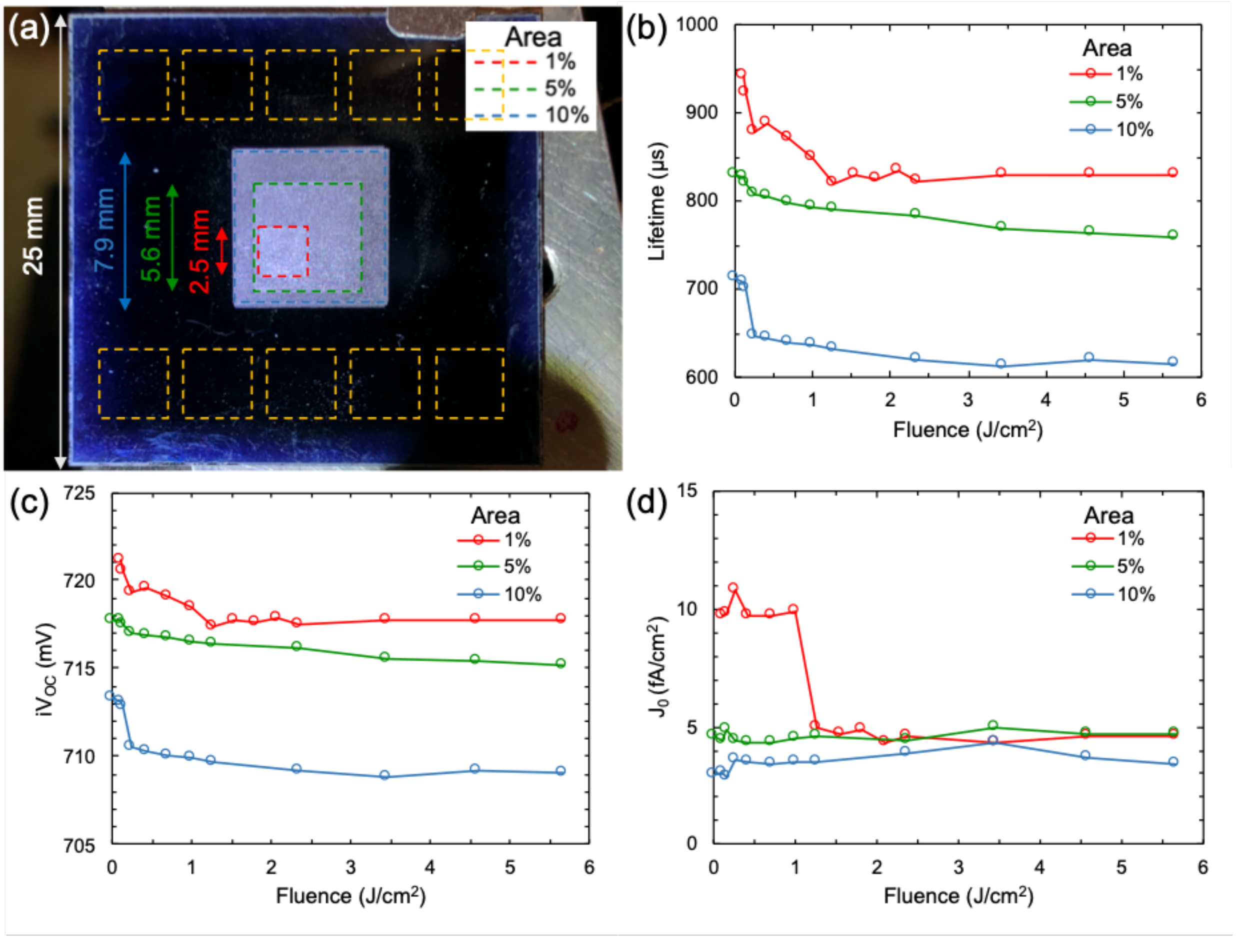

Fig. 37 (a) Image of the various laser processed areas on the sample at 5.67 J/cm^2 and (c-d) lifetime, iV_{OC}, and J_0 of the sample versus laser fluence and processing area.

up between 1–10% of the front area surface of the cell. To replicate this, 25 mm length lines with a 50 µm width were marked onto the cell at varying fluences to account for 1%, 5%, and 10% of the cell. The line densities are shown in Figure 38 (a). The impact of fluence and laser line percentage area on the sample passivation is shown in Figure 38 (b)–(d). In this case, the increased line area percentage contributes significantly to a loss in passivation. Fluences above the 0.25 J/cm^2 dielectric ablation threshold also lead to rapid degradation in the sample passivation—with the iV_{OC} of all samples above this threshold decreasing by 70 mV at a 10% line area coverage. However, the impact of increasing laser fluence above this threshold is minimal as the loss in passivation is comparable. Surprisingly, even at the 0.25 J/cm^2 threshold there is still a large loss

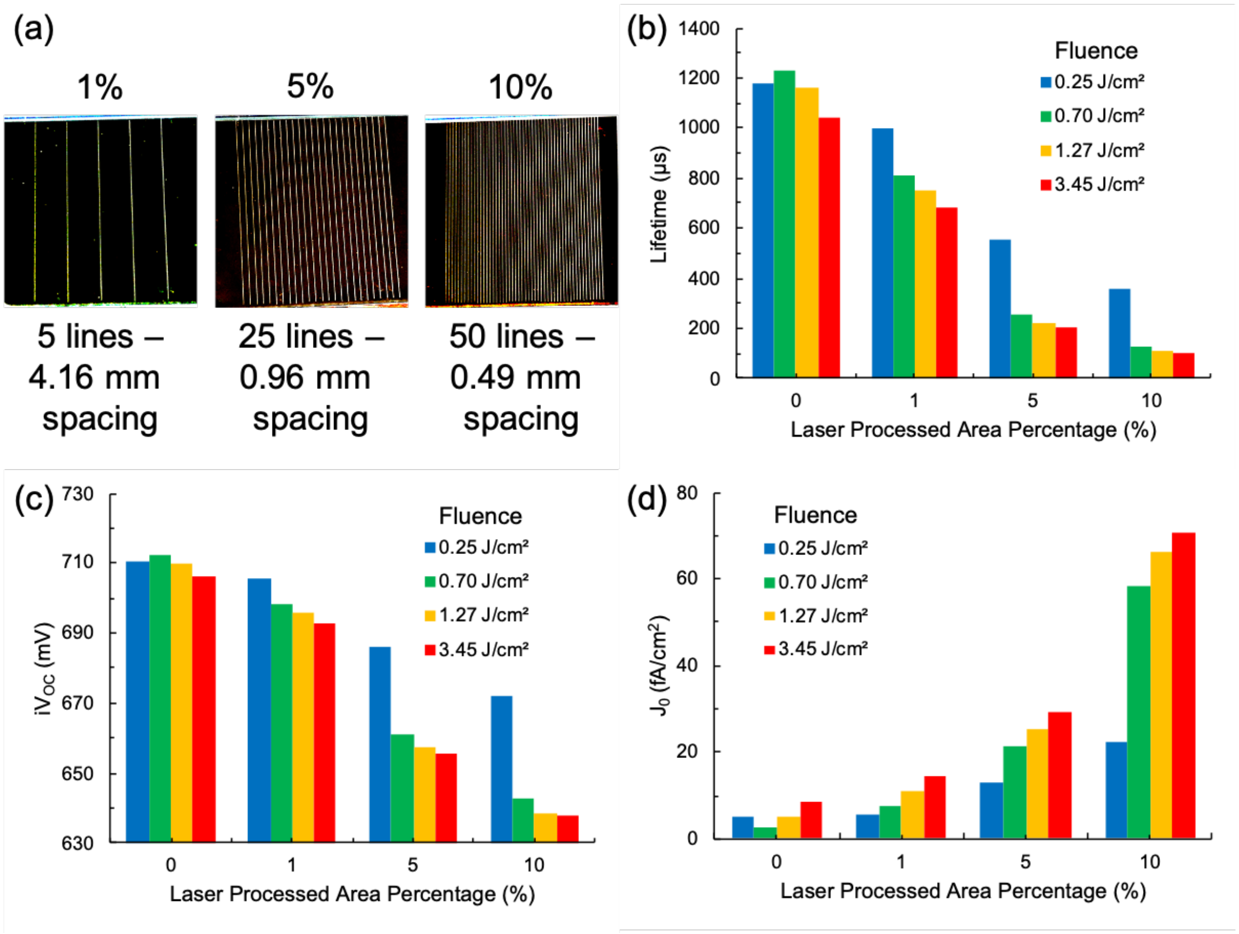

Fig. 38 (a) Image of the various laser processed line areas on the sample at 3.45 J/cm^2 and (c-d) lifetime, iV$_{OC}$, and J$_0$ of the sample versus laser fluence and laser processed line area percentage.

in passivation with the iV$_{OC}$ decreasing 38 mV from its starting value. The difference in loss between the samples in Figure 37 and Figure 38 can be explained by the larger distributed area in Figure 38 and the long 100–300 µm diffusion length of charge carriers in silicon. Because the diffusion length is on the order of the magnitude of the line spacings, there are ample sites for the free carriers to recombine at the laser damaged silicon surface that is free of dielectric.

The impact of the laser fluence can be seen in the microscope images in Figure 39 where the blue color originates from the SiN$_x$ layer while the grey color is the underlying silicon. From these images, it appears that the delamination and stress within the dielectric layers begins around 0.25 J/cm^2 while ablation of the dielectric begins occurring at 0.42 J/cm^2, just above the melting

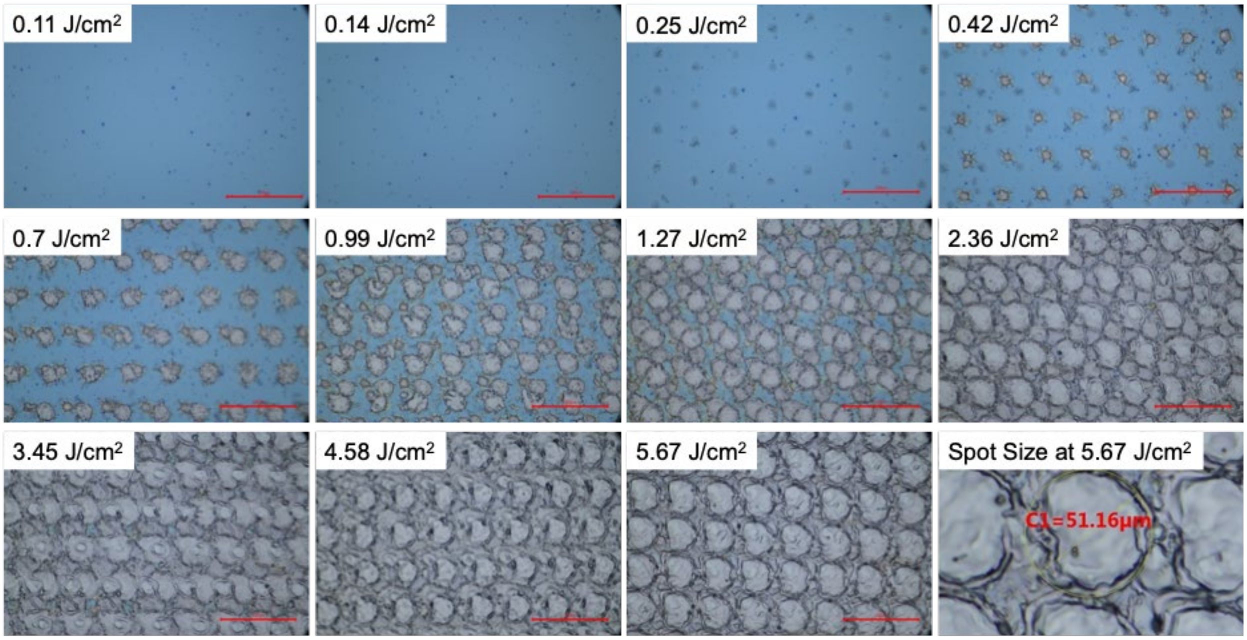

Fig. 39 Microscope images of a region of the laser processed area at increasing fluences with the effected mark area of ~50 μm at 5.67 J/cm^2 shown in the bottom right. The blue color is from SiN_x while the grey is from the underlying silicon.

fluence for silicon. Clear melting and resolidification of the silicon can be seen at a fluence of 0.7 J/cm^2. As the fluence further increases the laser effected area becomes larger, and reaches ~50 μm at 5.67 J/cm^2 as shown in the bottom right of Figure 39. At this fluence, the dielectrics are almost entirely removed from the laser processed area, so this area will no longer be passivated.

After the 10% of the area was processed at 5.67 J/cm^2, an additional 10 nm of Al_2O_3 was deposited on the laser processed side of the sample via ALD and annealed in forming gas at 350 °C for 30 minutes in an attempt to see if the laser damage could be subsequently passivated. Prior to deposition and annealing, the sample had a lifetime of 616 μs, iV_{OC} of 709 mV, and J_0 of 3.4 fA/cm^2. Afterwards, the lifetime rose to 647 μs, iV_{OC} rose to 711 mV, and strangely the J_0 also rose to 6.6 fA/cm^2. This indicates that most of the damage is likely permanent and subsequent passivation may not fix the laser damaged area. However, fluences above the melting threshold of silicon are not needed for dielectric ablation or for annealing of carrier selective layers, so it is likely that the typical laser fluences used in this work are repairable with subsequent passivating layer deposition.

Micro-photoluminescence was carried out on the 3.5 mm laser processed squares at individual fluences as shown in Figure 37 (a). The primary finding is that the silicon band-to-band peak photoluminescence degrades exponentially with increasing laser fluence, indicating localized damage to the passivation, despite the overall sample passivation remaining high. This reduction in PL with increasing fluence is shown in Figure 40 (a)–the intensity is plotted in log scale to better show this change. Besides the band-to-band transition, photoluminescence can also show the presence of defect-band transitions typically caused by dislocations and other defects. Infrared lasers operating at 1064 nm wavelength at high fluence commonly generate these dislocations [67], and due to the ~900 μm penetration depth of silicon at a 1064 nm wavelength, these dislocations propagate quite deep into the Si sample. Commonly, excitation wavelengths below the Si bandgap are used for photoluminescence, such as 532 nm lasers, which will penetrate shallower than the depth of the 1064 nm laser used for high-fluence processing, ensuring that these dislocation-related peaks show up in photoluminescence. In contrast, this study used a 355 nm laser processing wavelength, where the penetration depth into Si is roughly 10 nm and any defect

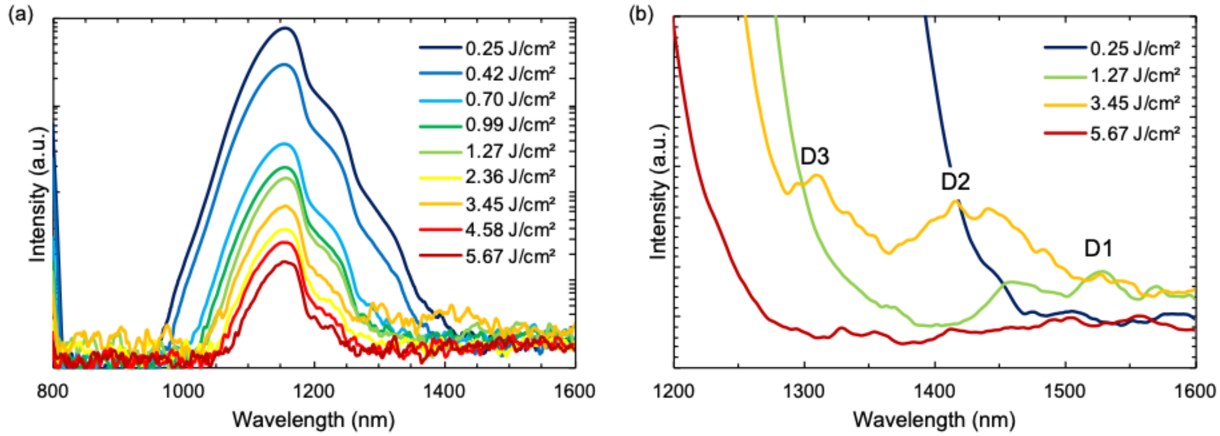

Fig. 40 (a) Log plot of the Si band-to-band photoluminescence peak exponentially decreasing with linearly increasing laser fluence and (b) linear plot of defect peaks at mid-level laser fluences.

generation, if at all, would be confined to a similar depth from the Si surface. This study used a 405 nm laser for photoluminescence excitation, which has a penetration depth of roughly 100 nm, meaning that only a partial component of the signal may come from the surface where the laser generate defects are concentrated. Additionally, these defect-band peaks are typically visible at room temperature, but their intensities increase drastically at cryogenic temperatures [69], [70]. These defect-band dislocation peaks, called D1, D2, and D3 are found at 1527 nm, 1417 nm, and 1327 nm and are typically broad at room temperature [69], [71]. There is an additional defect peak, D4, at 1240 nm, but this peak is often overshadowed by the large and broad band-to-band Si peak (1150 nm) and the shorter, but still prominent at room temperature, phonon Si peak (1200 nm), making the D4 peak difficult to observe. Despite these considerations, the D1 peak was observed above a laser fluence of 1.27 J/cm^2 and the D1 and D2 dislocation peaks were observed at a laser fluence of 3.45 J/cm^2. The defect peaks at the fluences of interest are compared with the low fluence and high fluences used to show that they are not present at low fluences and disappear at higher fluences, likely due to large scale melting and resolidification of the Si surface. Additionally the same defect peaks are not present at both the 1.27 J/cm^2 and 3.45 J/cm^2 fluences, suggesting that the laser fluence is important on the type of defect formed. These results are shown in Figure 40 (b)–note that the intensity is plotted in linear scale here.

Raman spectra of the 520 cm^{-1} wavenumber Si Raman peak for laser marked spots at increasing fluences is shown in Figure 41 (a). With increasing fluence, they show a reduction in peak height and also broadening of the peak. This indicates that high fluences are causing a loss in silicon crystallinity by forming amorphous silicon, which has a broad shallow peak. At higher fluences, the peak height begins to increase again, potentially due to the remelting of the amorphous silicon and formation of polycrystalline silicon. The full width at half maximum

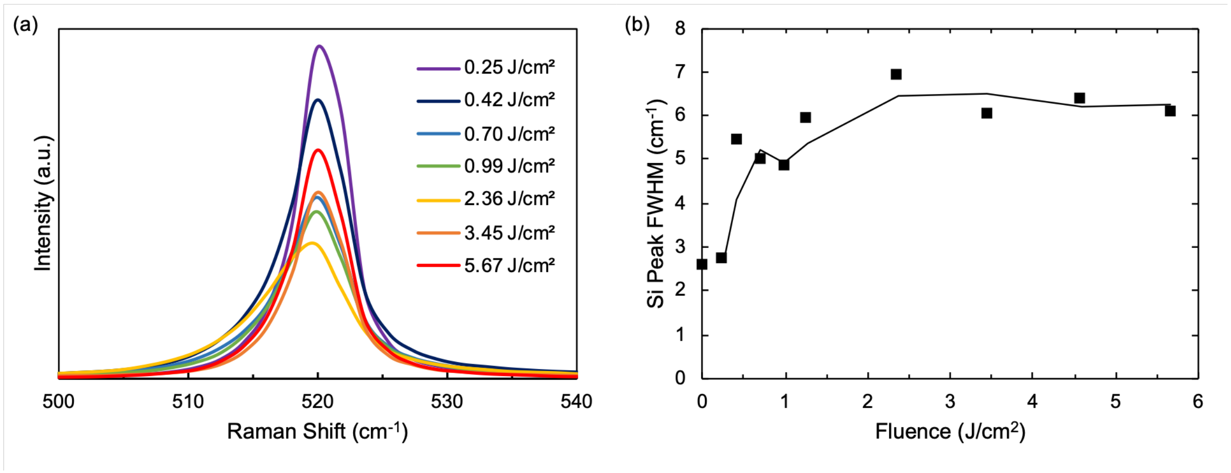

Fig. 41 (a) Raman spectra of the 520 cm^{-1} silicon peak taken for different laser fluences inside the marked spot. (b) the FWHM of the 520 cm^{-1} Si Raman peak versus laser fluence, demonstrating peak broadening with increased laser fluence.

(FWHM) of the peaks are plotted versus the laser fluence in Figure 41 (b) with a line indicating the moving average. The increase in FWHM demonstrates the broadening of the peak relative to the peak height intensity, and indicates the degree of crystallinity in the sample. Large FWHMs are indicative of a decrease in crystallinity and the formation of amorphous silicon. It can be seen in Figure 42 (b) that there is a sharp increase in FWHM at low laser processing fluences, which levels off at fluences above 2.36 J/cm^2. The formation of amorphous silicon can also be used to characterize the amount of defects because amorphous silicon has reduced crystal structure order and therefore is more likely to contain dislocations.

7.4 Conclusions

This work characterizes the impact of ultraviolet laser processing of well-passivated silicon at a variety of fluences and ratios of total sample area to laser processed area to evaluate how laser dielectric opening as well as laser annealing of carrier-selective and passivating layers can impact the overall device passivation, localized photoluminescence signal, and defect formation in the Si substrate. Excellent passivation was achieved using an Al_2O_3/SiN_x stack for an iV_{OC} of 721 mV and lifetime near 1 ms. Laser fluences below the melting fluence (0.4 J/cm^2) and far above the ablation threshold (0.5 J/cm^2) as well as area ratios of 1%, 5%, and 10% were studied to compare with the wide range of conditions used for laser processing of these devices. Overall sample passivation was found to only decrease at low fluence with no substantial decrease even at exceptionally high fluences. Increasing the laser processed area resulted in further decrease to the overall passivation, but the overall sample passivation remained excellent. Localized μ-PL of the Si band-to-band peak in the laser processed regions dropped exponentially with increasing laser fluence. Defect generation was examined through the defect-band photoluminescence peaks and was found to occur at specific laser fluences. Raman spectroscopy revealed the degree of amorphous Si generation and allowed for further characterization of defects. This findings of this study are of widespread interest to the photovoltaic community as the use of laser processing in high-efficiency photovoltaics grows.

A manuscript for this study is in preparation with the aim of submitting it for journal publication.

CHAPTER 8: Laser Direct Wafer Bonding for Solar Cell Junction Formation

8.1 Introduction

Conventional p-n junctions are formed via doping by ion implantation, dopant diffusion, or epitaxy. These methods have been thoroughly studied for applications in logic gates, diodes, and photovoltaics. However, control of dopant diffusion and limiting unwanted diffusion at higher temperatures, which are needed for solar cell fabrication, is a difficult process. Joining of two isolated pieces of Si wafer with opposite doping type, called silicon direct bonding (SDB) for silicon p-n junctions, is an underexplored area and typically needs custom pressurized chambers and temperatures in excess of 1100 °C [72], [73] to achieve bonding. Water is also typically used at the wafer interface to form Si-O-Si bonds between the wafers.

As stated earlier, laser processing of silicon has attracted growing attention in recent years. Laser wafer bonding would be of immense interest for p-n junction formation because it is able to inject heat locally without excessive heating to the rest of the device, reducing the heat affected zone and thereby reducing thermal stress [74]. The bandgap of silicon is 1.1 eV so the absorption of silicon begins to drop off at wavelengths above 1000 nm and becomes near transparent to wavelengths above 1100 nm. Therefore, near-infrared lasers can pass through silicon wafers relatively unattenuated (besides reflection loss). This has led to recent interest in in-volume silicon modification for waveguide, microchannel and microfluidic devices using non-linear absorption by ultrafast lasers. In 2017, Kämmer et al. used a 1.55 μm wavelength, picosecond pulse width laser focused through a high-NA microscope objective to achieve a sharp and short focal distance [75]. They focused this beam to the inside of a 1 mm thick Si wafer and created cavities on the order of 100 μm, due to non-linear absorption by the ultrafast 1.55 μm pulses [75]. Chambonneau et al. used a similar wavelength and pulse width to create waveguides in single crystalline silicon in 2016 [76]. Liu et al. was able to melt the rear surface of a 380 µm thick Si wafer using a ns pulsed, 1064 nm wavelength laser by passing the beam through the wafer [77]. While the absorption at 1064 nm is higher for Si than 1.55 µm used in previous demonstrations, their technique showed no marking on the front surface of wafer while the rear surface had 2–3 µm high clusters of molten silicon [77]. Wissinger et al. first demonstrated a laser wafer bonding technique by using a 1940 nm-wavelength, CW-thulium fiber laser by making use of metallic interlayers between the wafers which would absorb the 1940 nm light and melt, inducing bonding [74]. However, the use of interlayers, metallic or otherwise, induces a high number of defects at the desired p-n junction and is not suitable for solar cells.

This opens a window for the possibility of direct wafer laser bonding of two silicon wafers. By focusing a near-infrared laser at the interface between two wafers, laser induced melting can be sufficient to join the two wafers together without inducing melting at the front surface of the top wafer. If the wafers are of opposite type (n and p) and are well passivated for high lifetime and iV_{OC}, they could potentially form a p-n junction which could be used for solar cells. This would be a transformative method of solar cell fabrication, but involves the complex task of precisely

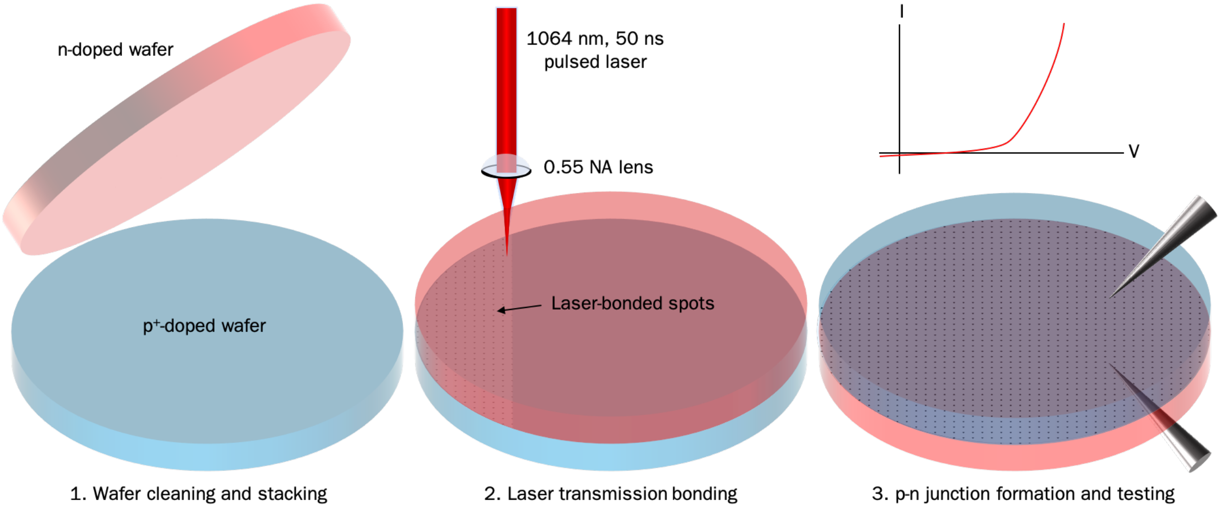

Fig. 42 Schematic overview of laser direct wafer bonding for silicon p-n junction formation.

matching the laser focal position with the wafer interface position. They would also be heavily reliant on carrier-selective layers to effectively separate the photogenerated charge and prevent recombination at the front and rear surface of the top and bottom wafer, respectively. This study investigates the use of a 50 ns pulse-width, 1064 nm wavelength laser to mark the front surface of the bottom silicon wafer without damaging the front surface of the top silicon wafer, as well as its applications for laser bonding the wafers together using this technique to form a p-n junction for low cost fabrication of Si solar cells.

8.2 Optical Properties and Laser Beam Focusing Considerations

Selecting an appropriate wavelength for laser transmission bonding of silicon wafers needs to be done carefully to ensure sufficient laser light reaches the interface between the wafers to induce melting and bond the wafers. The optical properties of silicon are shown in Figure 43 [48][78]. While reflection is of some concern for direct wafer bonding, the major concern is the absorption of the laser energy. Visible wavelengths (380–700 nm) have very shallow absorption depths (0.01–5 μm), and given that typical wafers are between 200–500 μm, these absorption depths are insufficient to reach the interface. In contrast, wavelengths above 1200 nm have absorption depths > 4.5 mm, far above the typical wafer thickness and are likely to pass through

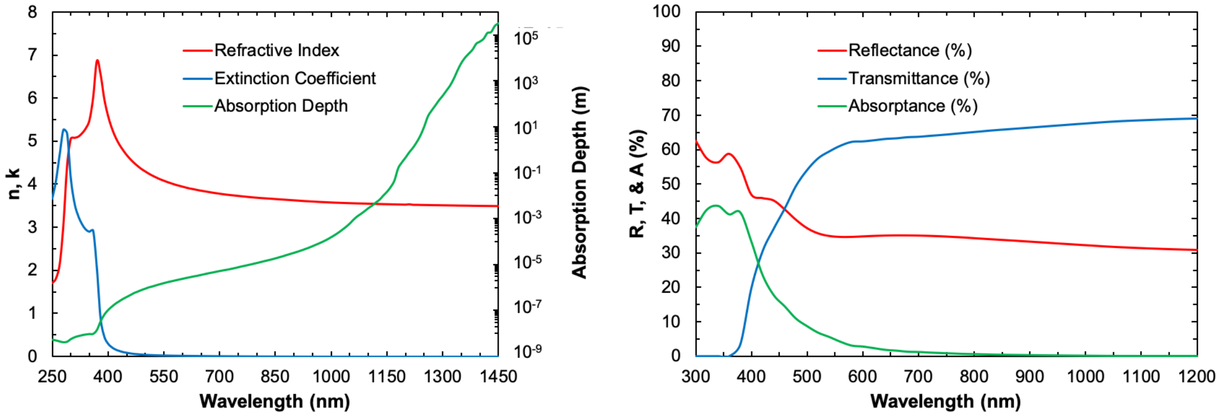

Fig. 43 Optical properties of silicon and variation of reflection, transmission and absorption versus wavelength for a 500 μm thick silicon wafer [48][73].

the silicon wafers entirely (omitting reflection) without generating significant absorption to induce melting. Ultrashort pulsed lasers are capable of in-volume marking thanks to non-linear processes such as multiphoton absorption, where the material absorption coefficient has linear or higher-order dependence as a function of the light intensity. However, these processes are typically several orders of magnitude weaker than standard, linear absorption and thus are energy- and cost-intensive for industrial fabrication processes. Additionally, metallic (or similar) interlayers, which have high infrared absorption, can be sandwiched between the two wafers to ensure adequate bonding, but they will detrimentally hinder any diode behavior by introducing numerous charge-carrier recombination defect sites at the interface.

Therefore, to ensure that the laser light reaches the interface and can still be readily absorbed, wavelengths between 1000–1200 nm should be used. Of commonly available laser wavelengths, Nd:YAG lasers operate at a fundamental wavelength of 1064 nm and are widespread, efficient and cost-effective laser systems. The semiconductor industry already makes use of Nd:YAG lasers operating at a 1064 nm wavelength for stealth wafer dicing technology which focuses these lasers through the front Si surface to induce cracking which enables subsequent dicing through a dry and clean process [77]. However, getting a 1064 nm wavelength to melt the rear surface is complicated task due to the weak Si absorption coefficient (9.55 cm^{-1} [79]) at this wavelength.

Free-carrier absorption is light absorption where the free carriers, such as electrons or holes, absorb a photon that excites them from an already-excited state to an unoccupied excited state in the same band; i.e. conduction-to-conduction band transition for electrons and valence-to-valence transition for holes. It can be described as an intraband transition rather than interband transition like typical semiconductor absorption, where an excited carrier travels from the valence to the conduction band or vice versa after absorbing light. The statistical occurrence of such transitions is typically low, but becomes increasingly prevalent with heavily doped silicon, due to the shift in Fermi level. This occurs primarily with near-bandgap photon energies, where band-to-band absorption is weakest. Typically, it is thought to be detrimental to solar cell performance because it will parasitically absorb infrared light without contributing to current generation. However, free-carrier absorption can be exploited for direct wafer laser bonding by utilizing a lowly doped top cell (~10^{16} cm^{-3}) and heavily doped bottom cell (~10^{19} cm^{-3}) and infrared laser wavelengths near the bandgap. The absorption depth at near infrared wavelengths for undoped silicon and silicon with boron and phosphorus dopants at high doping densities is shown in Figure 44. The free-carrier absorption depths for doping densities of 10^{17}–10^{20} and wavelengths between 1000 and 1450 nm are calculated from parameterized equations from Baker-Finch et al. [80]. As can be seen in Figure 44, the absorption depth for silicon at a wavelength of 1064 nm increases approximately an order of magnitude for every order of magnitude increase in the doping density

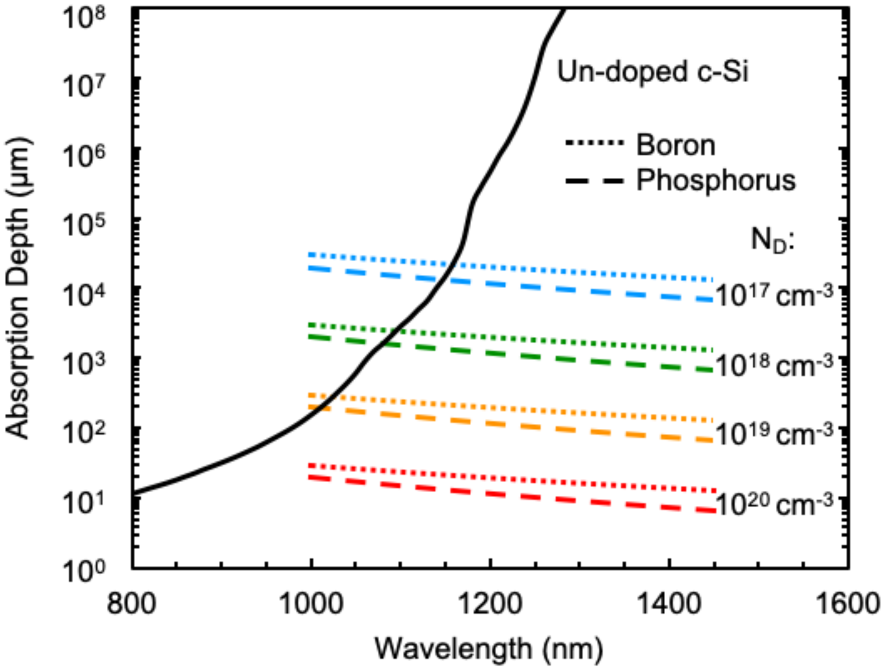

Fig. 44 Effect of dopant concentration on the absorption depth of infrared wavelengths [48], [75].

above 10^{18} cm^{-3}, meaning undoped silicon will absorb 63% of the initial intensity of 1064 nm light at 900 μm depth, much greater than the thickness of standard wafers used in the photovoltaics industry, while 10^{20} cm^{-3} boron-doped silicon will absorb the same amount of light in 25 μm, far closer to the surface of a standard wafer. With wafer thicknesses of 280 μm, the top wafer will absorb roughly 24% of the relative intensity, while the bottom wafer will absorb 99% of the remaining intensity within 120 μm of the front surface. By having absorption depths change two orders of magnitude for the same material based on the doping content, direct wafer laser bonding of silicon becomes practical without the use of absorptive interlayers.

Another factor to consider is how the refractive index of the silicon wafers induces reflection and refraction of the incident laser light. For silicon, the refractive index is 3.55 at a wavelength of 1064 nm. This results in a compounding 31.5% reflection each time the incident light crosses from air-to-silicon and vice versa, which will occur three times for light entering the bottom wafer, meaning 68% of the light entering the bottom silicon wafer will be lost to reflection. Including the absorption losses through a top wafer thickness of 280 μm, only ~25% of the incident laser intensity energy will enter the bottom wafer to be absorbed. Consequently, in order to achieve melting at the rear surface with only ~25% of the initial energy without inducing damage at the front surface, a significantly larger beam diameter is needed at the front surface to keep the energy density low. To achieve this, a high numerical aperture (NA) lens should be used, enabling a tight depth of focus, so that the energy density of the focused beam with 25% of the initial energy is significant enough to induce Si melting at the interface between wafers, while the energy density at the front surface, hundreds of microns apart, is significantly low to avoid damage. Thermally-induced red-shifting in absorption of the top wafer must also be avoided as this will result in additional beam intensity losses prior to reaching the interface [81]. Even with a high numerical

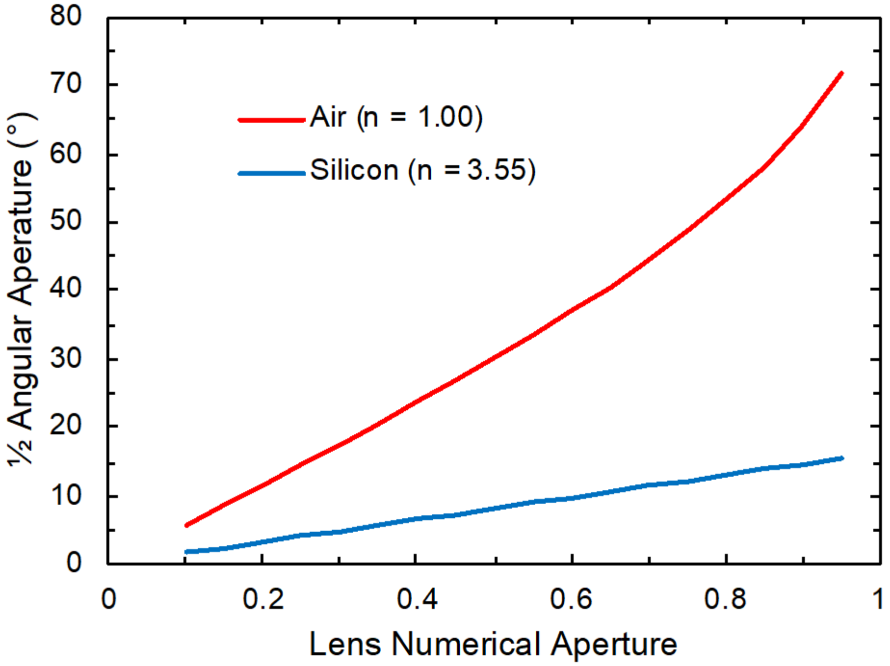

Fig. 45 Change in ½ angular aperture with lens numerical aperture for light in air after leaving the lens (red) and after entering silicon from the air (blue).

aperture lens, the refractive index of silicon at 1064 nm is 3.55, so the large ½ angular apertures (< 90°) achieved with high numerical aperture lenses will be reduced (< 16°) due to Snell's law within the silicon substrate as shown in Figure 45. The ½ angular aperture, α, first defined by Ernst Abbe, is calculated from:

$$\alpha = \sin^{-1}\left(\frac{NA}{n}\right) \tag{1}$$

where *NA* is the numerical aperture of the lens and *n* is the refractive index of the medium, which is air in this case. The change in ½ angular aperture once the beam enters silicon, β, is given by:

$$\beta = \sin^{-1}\left(\frac{n_{air}\sin(\alpha)}{n_{Si}}\right) \tag{2}$$

By passing the beam through silicon, the focal length or working distance of the lens is increased due to Snell's law. The increase in focal distance is dependent on the numerical aperture and the thickness of the silicon, but independent of the lens' initial focal length or working distance

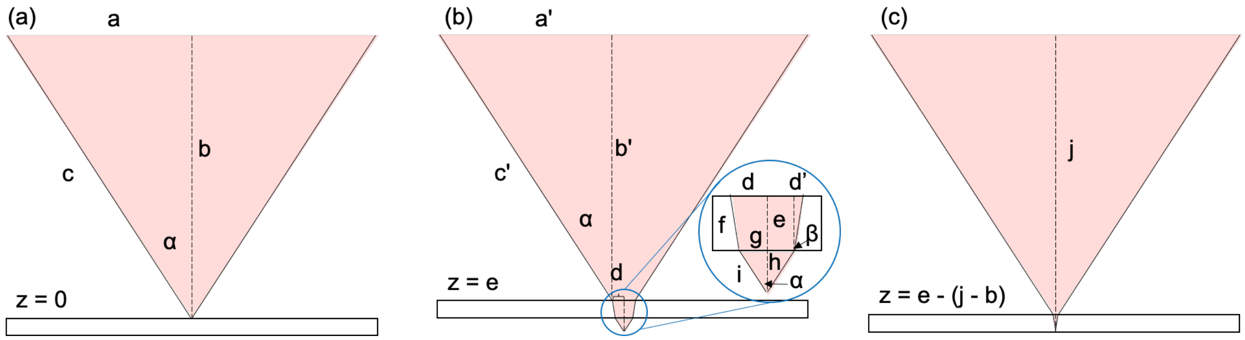

Fig. 46 Light path when (a) the laser is focused on the front surface of the sample (z = 0), (b) the focal height is changed exactly the distance of the wafer thickness, t, (z = t), and (c) where the true focal height lies for in focus marking of the rear surface (z = e – (j – b))

and can be solved through simple trigonometry, however it must be accounted for with high numerical aperture lenses with small depths of focus. Figure 46 shows how the light path would look when (a) the laser is focused on the front surface of the sample (z = 0), (b) the focal height is changed exactly the distance of the wafer thickness, t, (z = t), and (c) where the true focal height lies for in-focus marking of the rear surface (z = e – (j – b)). The sides of the triangles are labeled alphabetically, where primes indicate a side length that is modified by the presence of silicon, and the Greek letters indicate angles. The focal length is given by b and helps to define the other parameters, but the focal length shift, the difference in focal height from the front of the wafer to the rear of the wafer, and the spot size at the front of the wafer when the back of the wafer is in focus are independent of this value, and it can be set to 1 for the purposes of simplifying the calculation. For the example in Figure 46 (a), *a* and *c* are given by:

$$a = \frac{b}{\tan\alpha}, \qquad c = \frac{b}{\cos\alpha} \tag{3}$$

When the wafer height, *z*, is shifted upwards by the thickness of the wafer, *t*, as shown in the example in Figure 46 (b) (where *t* = *e*), it's sides are similarly given by:

$$b' = b - e, \qquad a' = \frac{b'}{\tan\alpha}, \qquad c' = \frac{b'}{\cos\alpha} \tag{4}$$

and the beam waist at the front of the wafer is denoted as *d* and given by:

$$d = a - a' \tag{5}$$

and β is given by equation (2). The remaining sides can be solved for in a similar fashion, noting that the angle of the triangle will change back to α once it exits the rear of the wafer. The inset of Figure 46 (b) shows the labels of the remaining sides. The shift in focal length, which is independent of the rear of the wafer's distance from the focus assuming the beam exits from or focuses at the rear surface of the wafer, is denoted j, and given by:

$$j = b' + e + h \tag{6}$$

The wafer distance necessary to have the focus position at the rear surface of the wafer, as shown in Figure 46 (c), which is also equivalent to the difference in distance from marking the front of the wafer as in Figure 46 (a) and marking the rear surface is given by:

$$z_{rear\ focus} = e - (j - b) \tag{6}$$

Lastly, the beam waist at the front surface of the wafer when the rear surface of the wafer is in focus, is given by *2d'*. This value is important when considering a fluence that is necessary to mark the rear surface after absorption and reflection losses through the wafer. If it is too small, than the energy density of the laser will be too large at the front surface causing marking of the front surface without reaching the rear. How these important parameters vary together with various lens numerical apertures and wafer thicknesses is shown in Figure 47.

While there are many choices for laser wavelength, wafer doping, lens NA and wafer thickness that could accomplish wafer bonding, the feasibility of the entire system should be evaluated with these considerations in mind.

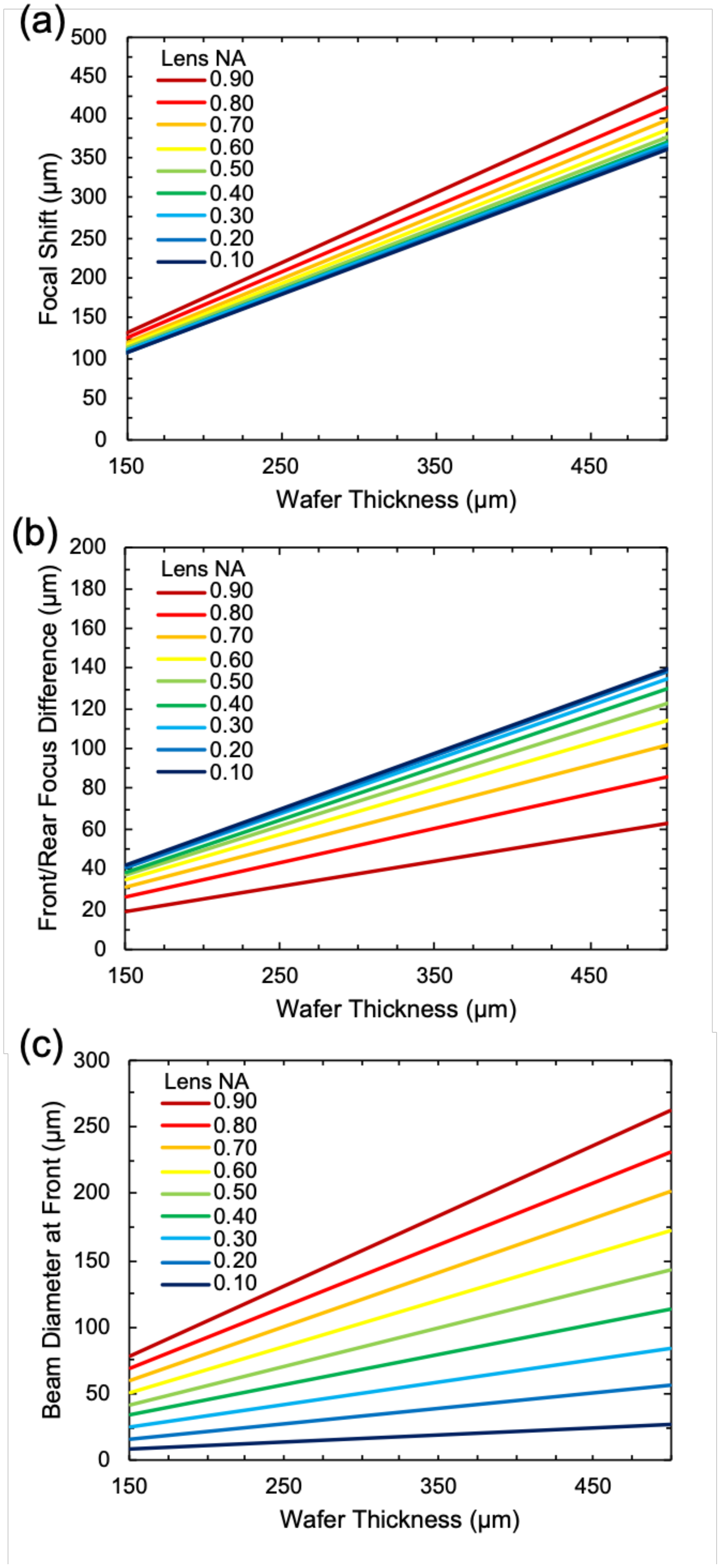

Fig. 47 Impact of wafer thickness and lens NA on the (a) shift in focal length, (b) difference between the focus spot size at the front of the wafer and rear of the wafer, (c) beam diameter at the front surface of the wafer when the rear surface is in focus.

8.3 Experimental Approach

For this study, a 1064 nm laser with a 50 ns pulse width and maximum pulse energy of 1 mJ was used (IPG, YLP RA 1-50-30-30). The pulse repetition rate was fixed at 30 kHz. The collimated beam diameter was approximately 4.5 mm before focusing. A lens with an NA of 0.55, effective focal length of 4.51 mm, working distance of 2.43 mm, and clear aperture of 5.07 mm was used (Thorlabs, C230TMD-C). The lens was coated with an infrared anti-reflective layer to reduce reflection on the lens. The lens was mounted on a Z-stage to control the focal distance from the sample. The beam was directed into the lens via tiltable infrared mirrors. A computer controlled X-Y stage with a stepper resolution of 0.24 µm was used to move the sample underneath the lens in a raster pattern (MKS Newmark, ET-50-21). A kinematic sample holder with adjustable tip and tilt was placed on the X-Y stage and used to level the sample relative to the lens. Levelness was ensured by drawing large squares on a silicon sample (via the computer controlled X-Y stage) just above the threshold marking fluence and adjusting the tip and tilt and lens z-stage position until the square pattern marked perfectly and an ablation plume could be seen along all edges and corners of the square pattern on the sample.

Two Si wafers, with thicknesses of 280 µm and opposite doping type were utilized. A double side polished n-type wafer with a resistivity of 1-5 Ω·cm (doping concentration of $1\text{–}5 \times 10^{15}$ cm^{-3}) was used as the top wafer due to its flatness on both sides and low free carrier absorption. A single side polished p^{+}-type wafer with a resistivity of 1-5 mΩ·cm (doping concentration of $2\text{–}10 \times 10^{19}$ cm^{-3}) was used as the rear wafer, with the polished side face up. The high doping concentration of this wafer enables significantly higher free carrier absorption. The wafers were cleaned to remove any debris and to ensure the wafers remained perpendicular and flush with one another. Wafers were passivated with 1.2 nm of Al_2O_3 on both sides deposited by a plasma ALD process to reduce recombination in the subsequent device after bonding and increase current capture. After Al_2O_3 deposition the wafers were annealed in forming gas for 1 hour at 350 °C. The wafers were placed on top of one another and DI water was applied between them to increase bond strength. A weight was applied to the edges of the top wafer to push it against the bottom wafer and squeeze out excess water.

8.4 Results

Initial I–V measurements were taken of each wafer individually and with both wafers stacked on top of one another without bonding and are shown in Figure 48 (a). As expected, the highly doped p-type wafer showed a higher conductivity than the lowly doped n-type wafer. It also displayed Schottky behavior most likely caused by the CuBe probe used to measure the wafer. When stacked, diodic, rectifying behavior is measured however overall current flow is quite poor most likely because current flow only is occurring from wafer contact causing high series resistance. Under AM1.5 illumination the current of the stack increases, due to the photovoltaic effect, however due to the lack of bonding this effect is significantly reduced (Figure 48 (b)).

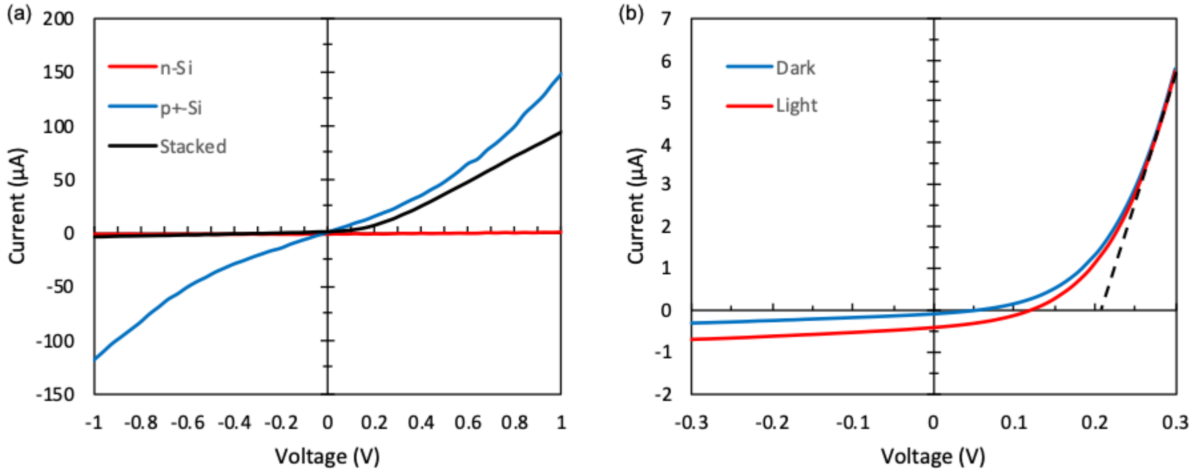

Fig. 48 (a) I–V curves of the individual wafers under darkness as well as the wafers stacked on top of one another without bonding, showing current—indicating contact between the wafers and (b) illuminated and dark I–V curves of the stacked wafers demonstrating small photocurrent generation.

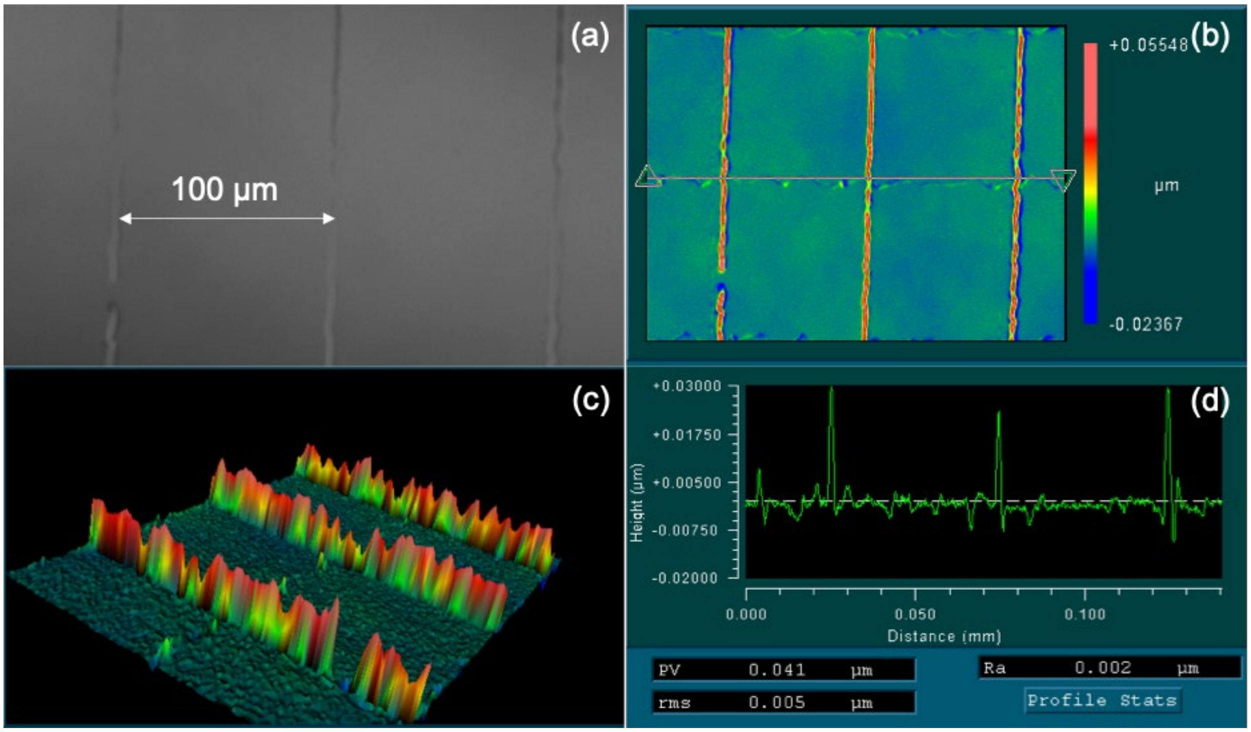

Fig. 49 (a) Microscope image showing the laser raster lines with 100 µm line spacing, (b) ejected material heat map showing the three lines, (c) 3D model of the surface profile, (d) surface profile of line drawn across the three laser marked lines shown in (b).

Laser marking of the bottom wafer through the top wafer was first attempted without DI water between the wafers in order to evaluate the amount of swollen material produced from thru-wafer marking. Height profiles of the laser marked lines were taken via optical profilometer (Zygo, NewView 7300). Depending on the laser fluence, the height profiles of the ejected material on the front of the bottom wafer ranged between 30–90 nm. On the rear surface of the front wafer, peak height profiles were on the order of 70–110 nm. This means that the space between the wafers would need to be between 100-200 nm in order to ensure sufficient silicon-to-silicon bonding through the ejected material. The height profile of the front surface of the rear wafer is shown in Figure 49.

After deposition of 1.2 nm of Al_2O_3 on via ALD each side of the wafer and subsequent 350°C anneal, the n-type wafer had an iV_{OC} of 687 mV, lifetime of 954 µs, and J_0 of 67 fA/cm^2. Due to the high doping of the p-type wafer, it was unable to be measured by the QSSPCD method from Kane and Swanson (Sinton, WCT-120). However, it is assumed that the p^+-wafer's surface passivation would also be markedly increased, but internal Auger recombination would still be significant. After raster scanning the laser at the interface between these stacked wafers at a pulse energy of 0.03 mJ (1.0 W average power), the wafers remain affixed to one another demonstrating successful bonding. Figure 50 (a) shows the rear wafer being held at a vertical angle while both wafers remain attached. Figure 50 (a) also shows that no marking of the front surface of the front wafer occurred during bonding, indicating that melting did not occur and the front surface passivation remained intact. An illuminated I–V curve of the laser bonded stack is shown in Figure 50 (b). While it showed diode behavior and photovoltaic response, the current through the device was still limited due to the high series resistance (700 Ω) of the device. However, the open circuit voltage (652 mV) remained close to the implied open circuit voltage value (687 mV) measured for the n-type wafer. The fill factor was largely limited (36.8%) by series resistance losses.

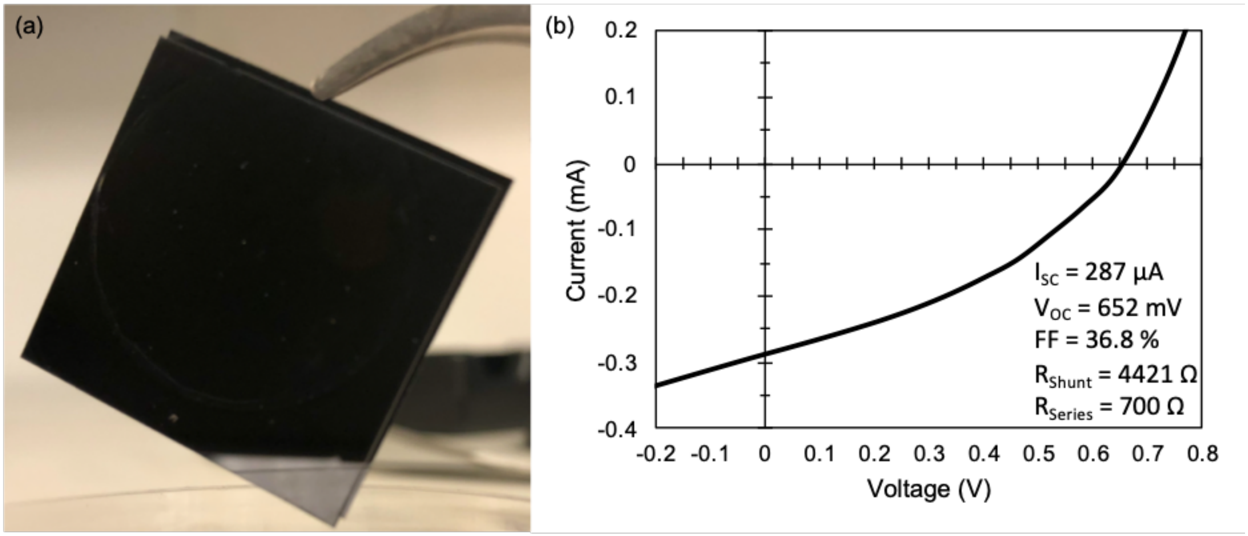

Fig. 50 (a) Picture of the laser bonded wafers being held vertically by the rear wafer and (b) AM 1.5-illuminated I–V result of the laser bonded wafers with text inset showing relevant parameters.

8.5 Conclusions

This work has demonstrated a novel method of wafer bonding and p-n junction formation at low temperatures, that relies solely on injecting laser energy significant to induce melting at exactly the interface between two wafers. All optical considerations are discussed for demonstrating laser direct-wafer bonding, including laser wavelength, lens numerical aperture, wafer thickness, and wafer doping type. An experimental setup is demonstrated and the impact of laser pulse energy is explored through the impact on the ejected molten material height profile. Direct-laser wafer bonding is also demonstrated with the assistance of water at the interface between the wafers. Dark and illuminated current-voltage characteristics are measured for the individual wafers, the wafers stacked without bonding, and the wafers bonded via laser. After bonding, diode formation occurs and the photovoltaic effect is demonstrated. The open circuit voltage is largely preserved from QSSPCD measurement, but the generated current is low. Future work will focus on optimizing the laser bonding process to reduce series resistance and increase current generation.

A manuscript for this study is in preparation with the aim of submitting it for journal publication.

CHAPTER 9: Conclusions and Future Work

9.1 Conclusions

This work entails the use of novel laser processing techniques for the fabrication of advanced solar cell concepts for high-efficiency solar cells. Of particular importance in this work were the carrier-selective and passivating layers of photovoltaic cells, which efficiently separate photogenerated charge while simultaneously preventing recombination at the absorber surface and interfaces. This includes the electron transport layer in flexible perovskite solar cells, the heavily doped polysilicon layer in TOPCon silicon solar cells, and transition metal oxide layers and tunnel oxides in amorphous Si-free, asymmetric heterojunction solar cells. In addition, the influence of laser processing parameters on defect generation was investigated. Lastly, a novel use of infrared lasers for room-temperature silicon wafer bonding and p-n junction formation with wide-ranging applications for semiconductor devices was explored.

For flexible perovskite solar cells, the traditional, high-temperature thermal annealing conditions for the sol-gel TiO_2 electron transport layer, was replaced with laser annealing of the TiO_2 layer. This laser annealing condition was optimized in terms of film morphology and device performance. Using this optimized condition, a 17.1%-efficient flexible device was fabricated and showed better performance than its rigid, furnace annealed counterpart. The laser-annealed TiO_2 layer was also characterized using optical transmission, ellipsometry, and X-ray photoelectron spectroscopy to confirm its crystallinity and high transparency. This study demonstrates a novel, low-temperature method for generating high-efficiency flexible perovskite solar cells without impacting the flexible substrate.

For state-of-the-art tunnel-oxide passivated contact (TOPCon) solar cells, the highest-temperature step of the fabrication process is the annealing of the heavily doped polysilicon on tunnel oxide stack–necessary to activate the dopants within the polysilicon, crystallize the layer for improved conductivity, and anneal the interfaces for improved passivation. Using a novel laser annealing technique, these same tasks are accomplished without heating the entire wafer through selective laser surface heating and with further control, resulting in an iV_{OC} of 718 mV and resistivity of 7.1 mΩ•cm. Optical and laser modeling are provided to give an estimated absorption depth and temperature with laser fluence, correlating well with the experimental findings. The laser fluence is optimized for both improved passivation and conductivity of the poly-Si. This work provides a rapid and novel method for low-temperature annealing of TOPCon devices.

The laser annealing concept was also applied to amorphous silicon layer-free, asymmetric carrier-selective transition metal oxide contacts in silicon solar cells, which can be deposited with far cheaper source materials and without toxic and flammable silane, phosphine, and diborane used in intrinsic and doped amorphous and polycrystalline silicon. Optimization of the laser annealing conditions is demonstrated for MoO_x, TiO_x, and Al_2O_3 and compared with the impact of traditional thermal annealing. Further study on the laser annealing process can be used to create a complete photovoltaic device.

With the growing use of laser processing for photovoltaic device fabrication and the demonstrated improvements in device performance in this work, there is widespread interest in characterizing how high fluence laser processing could impact the total and localized passivation of a device and if it could lead to defects in the silicon absorber. This chapter discussed how laser fluence and processing area impacted those factors, showing that high laser fluences processing at 10% of the device area had minimal impact on the overall device lifetime. Defects such as dislocations were discovered at particular fluences and were also characterized.

Lastly, this work discussed a novel method of wafer bonding by focusing a laser through one wafer at the interface between to wafers to inducing melting and bond the wafers. Optical considerations were carefully discussed as well as choice of laser wavelength, wafer thickness, and wafer doping. This work also demonstrated the bonding of two wafer of opposite doping to form a p-n junction and demonstrated a solar cell with a photovoltaic response using this technique. The bonded wafers also made use of passivating and carrier-selective layers to improve the device efficiency. This technique has broad applications for low temperature bonding of vertically integrated devices like multijunction photovoltaics, CMOS devices, and multi-layer structures that require low-temperatures compatible with the on wafer devices.

Overall, this work demonstrated the feasibility and benefit of utilizing pulsed laser processing for carrier-selective layers in high-efficiency hybrid organic-inorganic lead halide perovskite and silicon photovoltaics. The key implications of this work are as follows: (1) The electron transporting layer in perovskite solar cells can be laser annealed to allow for the use of flexible substrates; (2) that laser annealing allows for the fabrication of TOPCon silicon solar cells at relatively lower temperatures, under 500 °C; (3) a systematic evaluation for the scientific understanding of laser generated defects and their impact on device performance; (4) demonstration of a p-n junction device by laser bonding of two wafers, which eliminates high temperature processing and dopant diffusion processes. This work is of widespread interest to the photovoltaic community and essential to improving efficiency and reducing the fabrication cost of photovoltaic devices. By demonstrating laser annealing methods for various carrier-selective layers, characterizing them, and demonstrating an innovative method for p-n junction formation, this work provides viable avenues for further improvements to device efficiency and fabrication cost reduction.

9.2 Future Work

Perovskite solar cells could benefit from future work with laser annealing for alternative carrier-selective layers that require high temperature annealing. Inverted structures could potentially utilize this technique as it would protect the temperature-sensitive underlayer from high temperatures. Additionally, large scale roll-to-roll printing on flexible substrate could use this technique with high-speed polygon scanners to increase throughput and remove costly furnaces all-together. Any device that utilizes sol-gel precursors which need high temperatures to convert to their final layers could utilize laser annealing instead.

TOPCon devices could benefit from further optimization with laser annealing if the thickness and laser wavelength were optimized for industrially compatible solar cell fabrication. Because this process is far more rapid than conventional high temperature annealing, TOPCon devices could see reduced fabrication cost, higher throughput and potentially improved device efficiency though minimized dopant diffusion and oxide breakup. Additionally, a fundamental understanding of how tunneling and carrier-selectivity in TOPCon structures is still lacking, and a transmission electron microscopy study of this interface would lead to a complete understanding of how it could be improved. This method will be further explored as a part of NSF Grant ECCS-2005098, which is ongoing at the time of the publication of this thesis.

Transition metal oxide, amorphous silicon layer-free, asymmetric heterojunction solar cells would benefit from further study if the laser annealing process and alternate carrier-selective layers are explored. Current candidates for hole-selective layers include NiO_x, WO_x and VO_x, which may have better temperature stability than MoO_x. By coupling these layers with various tunnel oxides, the passivation of these layers could be further improved without loss of carrier selectivity. If the conductivity of the top carrier-selective layer could be improved, this device could be fabricated without costly indium tin oxide transparent conductive oxide. This activity will also be explored under NSF Grant ECCS-2005098.

Characterizing the defects generated from ultraviolet laser processing of well-passivated carrier-selective contacts is a difficult process due to the shallow absorption depth of this laser wavelength. Ultraviolet excitation wavelengths for photoluminescence and Raman spectroscopy would enable the bulk of the signal to come from the surface and allow further understanding of how these defects propagate. Additional structures which require different wavelengths or laser fluences could benefit from the understanding of how laser-induced defects impact the overall device.

Lastly, wafer laser bonding has only just been demonstrated in this work. It has a wide range of potential applications for a multitude of semiconductor devices. There is much to explore on this topic, including optimizing the wafer bonding process for reduced series resistance, increasing current flow through the wafer interface, and minimizing laser induced defects at the interface between the wafers. Besides photovoltaics, this approach could be translated to vertically integrated structures for lasers, medical applications, and 3D-chip structures.

The most impactful areas to apply this research would be further improvement in laser processing for alternative low-cost carrier-selective layers for silicon and perovskite photovoltaics. Laser treatment allows for selective energy deposition only in certain incremental areas of the carrier-selective layer—ideally where the contacts would be subsequently deposited. This would enable higher conductivity near the contacts while maintaining passivation elsewhere. While this work showed the potential of a variety of carrier-selective layers, a fundamental understanding of charge transport at these layers and the change in charge transport with furnace or laser annealing is still needed to explain how exactly these contacts work on a fundamental level. Lastly, the laser wafer bonding process has only just been demonstrated with silicon wafer bonding, but there are a multitude of applications for this type of bonding for electronics and photonics. Additional materials, laser wavelengths, pulse energies, and focusing strategies should be explored to make this technique more robust and widely applicable.

APPENDIX A: Projects on Photovoltaics in Space Applications

A.1 Encapsulated Perovskite Cells for Space Applications

Photovoltaics have long been used in space, since the first satellite launch in 1959, and have since vastly improved in their specific power. The most recently deployed photovoltaic panel, the Roll Out Solar Array (ROSA), utilizes 4-junction inverted metamorphic solar cells with an efficiency exceeding 32% (AM0) and a specific power above 1 W/g [82]. On Earth, laboratory demonstrations of triple junction III-V photovoltaics have exceeded 3 W/g [83]. Unfortunately, the fabrication of these cells is cost, energy and rare-material intensive. Perovskite solar cells have demonstrated specific powers of 29.4 W/g with a device PCE of only 12.9% [84], owing in large part to their solution processability and ultrathin active layer thicknesses, typically <500 nm which is 300 times thinner than a commercial silicon wafer (~150 μm). Perovskite solar cells have demonstrated efficiencies of over 25.2% [2], so the potential to achieve substantially higher W/g ratios is within reach. This would enable huge weight savings for NASA as current launch costs are $22,000/kg for payload sent to orbit. However, studies on the effects of micro-gravity, high ultraviolet light irradiation, cosmic radiation, atomic oxygen and drastic temperature fluctuations on perovskite solar cells are limited and have only been demonstrated on stratospheric balloons which reach an altitude of 35 km [85] or rockets reaching 240 km [86]. The International Space Station (ISS) has an orbital altitude of over 400 km, where environmental conditions are considered “real space” [86]. A unique opportunity was provided to send encapsulated perovskite solar cells to the ISS as part of the 11th Materials International Space Station Experiment (MISSE-11) mission to evaluate the durability of these cells in true space conditions. The objective of this mission is to test material samples for space qualification studies where the samples are located outside of the ISS and subjected to exposure to vacuum, cosmic radiation, enhanced ultraviolet, atomic oxygen and drastic thermal fluctuations, where the results of this mission would be helpful in evaluating the success of said materials in future space exploration missions. To date, the perovskite solar cells have not yet returned but details of this study and the mission are described.

The cells consist of the same structure and were fabricated identically to the device in Chapter 4, but the TiO_2 was thermally annealed. It consists of a glass substrate, patterned indium tin oxide transparent cathode deposited via sputtering, 500 °C thermally-annealed TiO_2 electron transporting layer, a mixed-halide mixed-cation perovskite active layer ($FA_{0.85}MA_{0.15}PbI_{2.55}Br_{0.45}$), a doped Spiro-OMeTAD hole transporting layer, a gold anode, dual side conductive copper tape attached to each pixel anode and shared cathode, and is encapsulated with microslide glass and UV-cured optical cement. Pictures of the front and rear of the device are shown in Figure A1. Four devices were fabricated simultaneously, each consisting of 6 pixel cells. The I-V result of the champion pixel as well as the average and standard deviation of all I-V parameters is shown in Figure A2. One device was sent to NASA as part of the MISSE-11 mission and the remaining three were stored in a nitrogen-filled, humidity free glovebox.

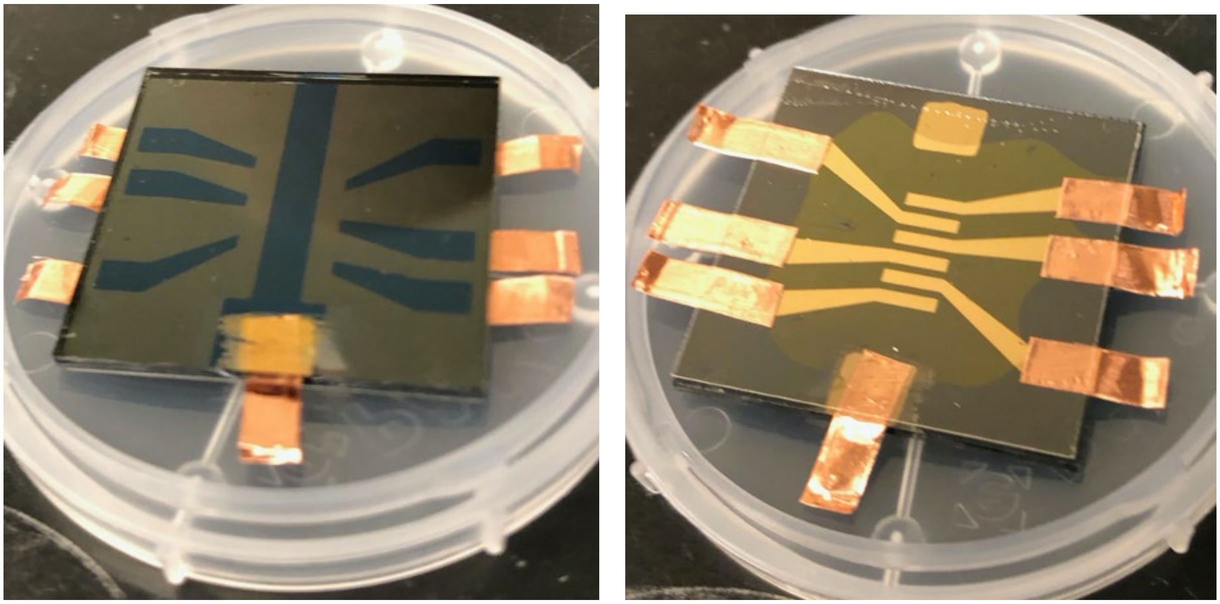

Fig. A1 Front and rear of encapsulated perovskite solar cell with conductive copper tape connected to cathode and anode.

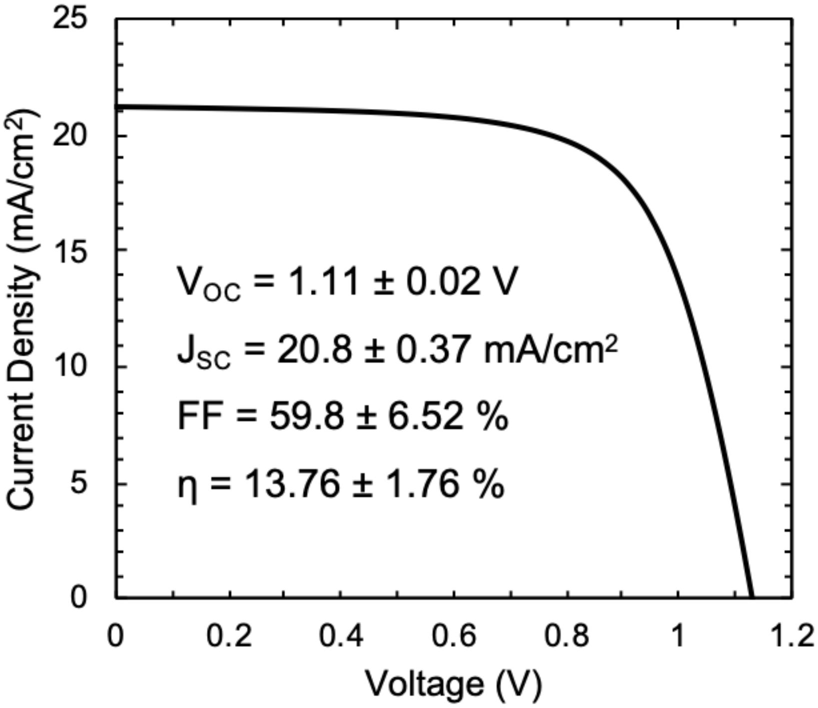

Fig. A2 Illuminated I-V result of the champion perovskite pixel. The average and standard deviation of all pixels is shown within the curve.

The sample was mounted on a Material Sample Carrier deck with various other NASA-sponsored samples by Alpha Space Test and Research Alliance of Houston, Texas in a state-of-the-art cleanroom. The location of the sample in the deck is shown in Figure A3, circled in red and was titled SQOODAM-5 [87]. The MISSE sample carrier remains closed until deployed on the ram side of the ISS, where it will remain for at least one year while exposed to the conditions of space. A camera periodically scans across the samples to provide qualitative assessment of the sample condition. The closed, open and imaging configurations are shown sequentially in Figure A4. The MISSE-11 mission was launched on April 17th, 2019 on the Northrop Grumman (NG)-11 Cygnus via x an Antares rocket. An image of this launch was capture by Brady Kenniston and is shown in Figure A5. Once at orbit with the ISS, Canadarm2 was used to grapple the NG-11 and bring it to the Node-1 “Unity” module nadir (Earth-facing) port on the ISS, shown in Figure A6.

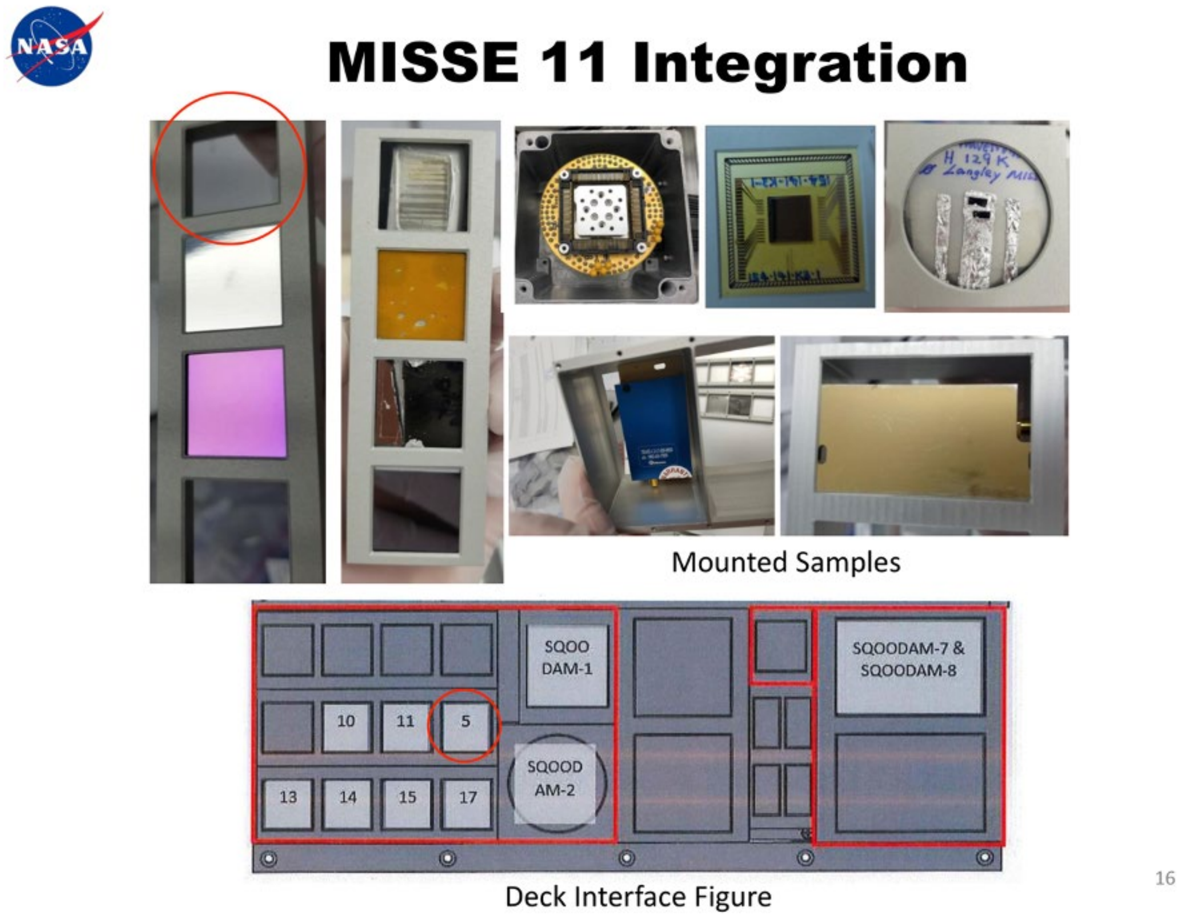

MISSE 11 Integration

Mounted Samples

Deck Interface Figure

16

Fig. A3 Sample integration on the deck and location of perovskite solar cell on sample deck indicated with a red circle (modified from N. Prasad [82]).

Figure A7 shows different views of Alpha Space Technology and Research Alliance's MISSE carrier mounted on the International Space Station. The carrier remains in place while sample decks are swapped out by Canadarm2 as shown in Figure A8. The location of our sample deck on the ram side of the ISS in its open configuration is shown in Figure A9.

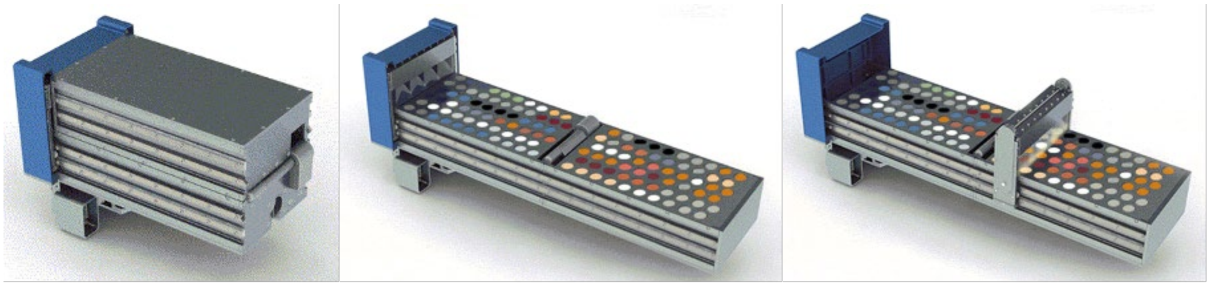

Fig. A4 MISSE sample carrier in its closed (stowing) configuration, open (exposed) configuration, and with imaging camera scanning across the samples (from Alpha Space Test & Research Alliance website).

Fig. A5 April 17th , 2019 launch of the Cygnus Northrup Grumman (NG)-11 aboard an Antares rocket (Photo credit: Brady Kenniston).

Fig. A6 Canadarm2 grappling the NG-11 to bring it to the node-1 Nadir (Earth-facing) port on of the ISS (Photo credit: NASA).

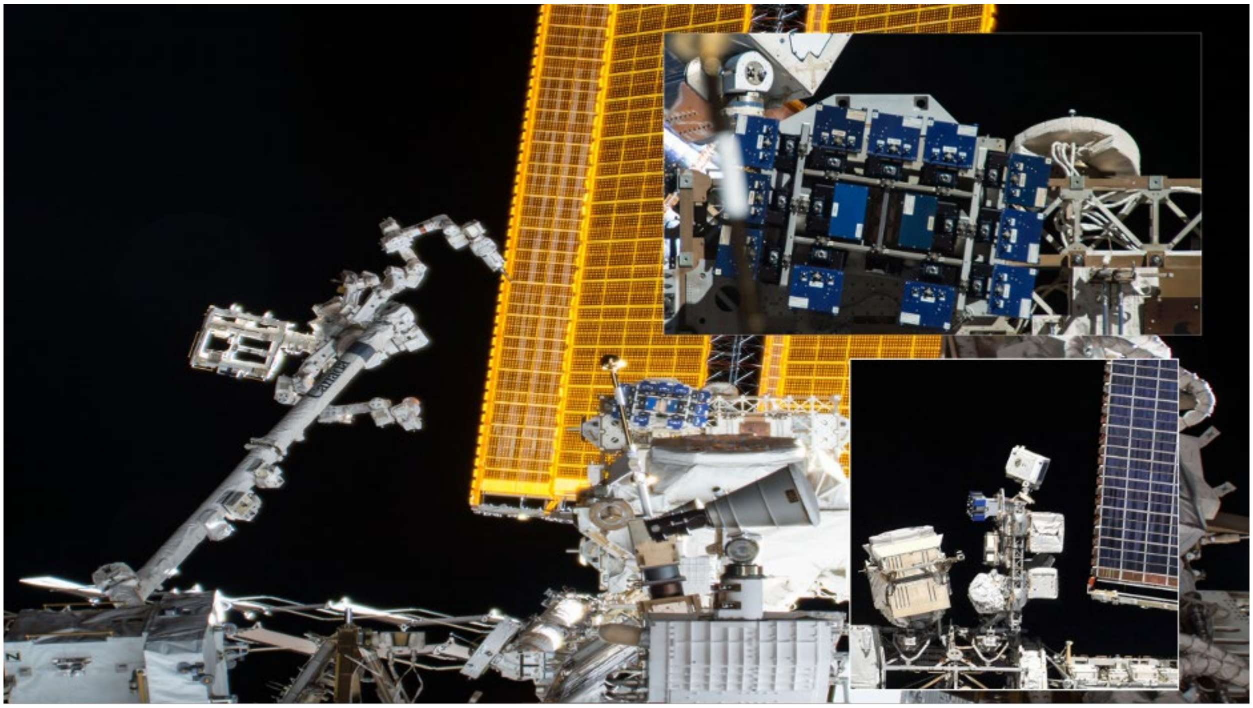

Fig. A7 Different views of the Alpha Space MISSE carrier on the ISS (Photo credit: NASA).

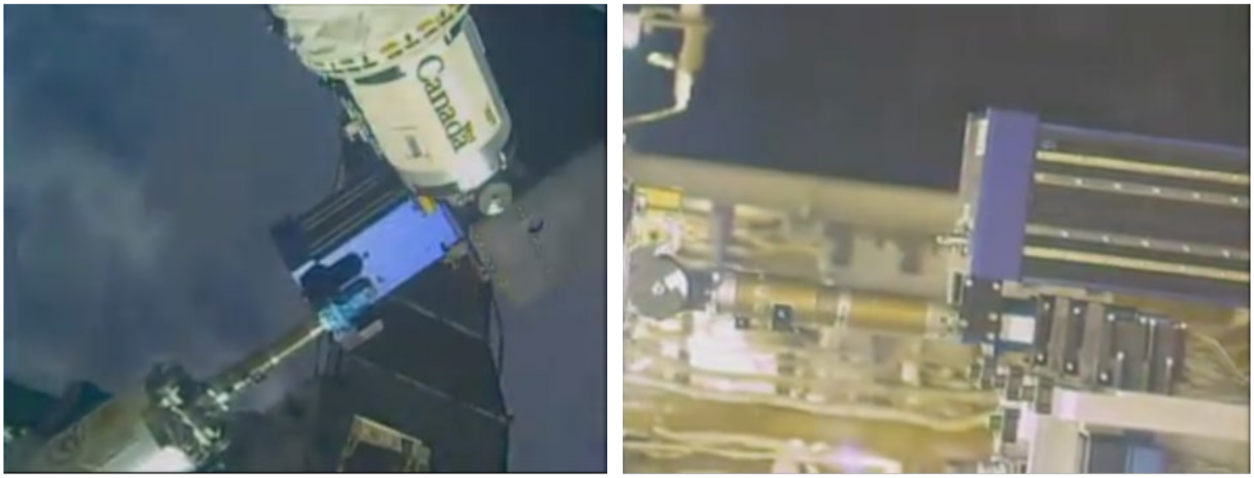

Fig. A8 Canadarm2 extracting a sample deck from the ISS and installing the deck on the MISSE sample carrier (Photo credit: NASA).

After returning from orbit, changes to pixel efficiency, surface morphology, and layer composition will be compared to the devices stored on Earth in inert nitrogen. This study will evaluate their long-term space readiness for potential power generation needs of future space exploration missions—whereby the impact of ozone, vacuum, and drastic temperature swings will be evaluated. Potential degradation over time will be demonstrated via the periodic images of this device in said conditions.

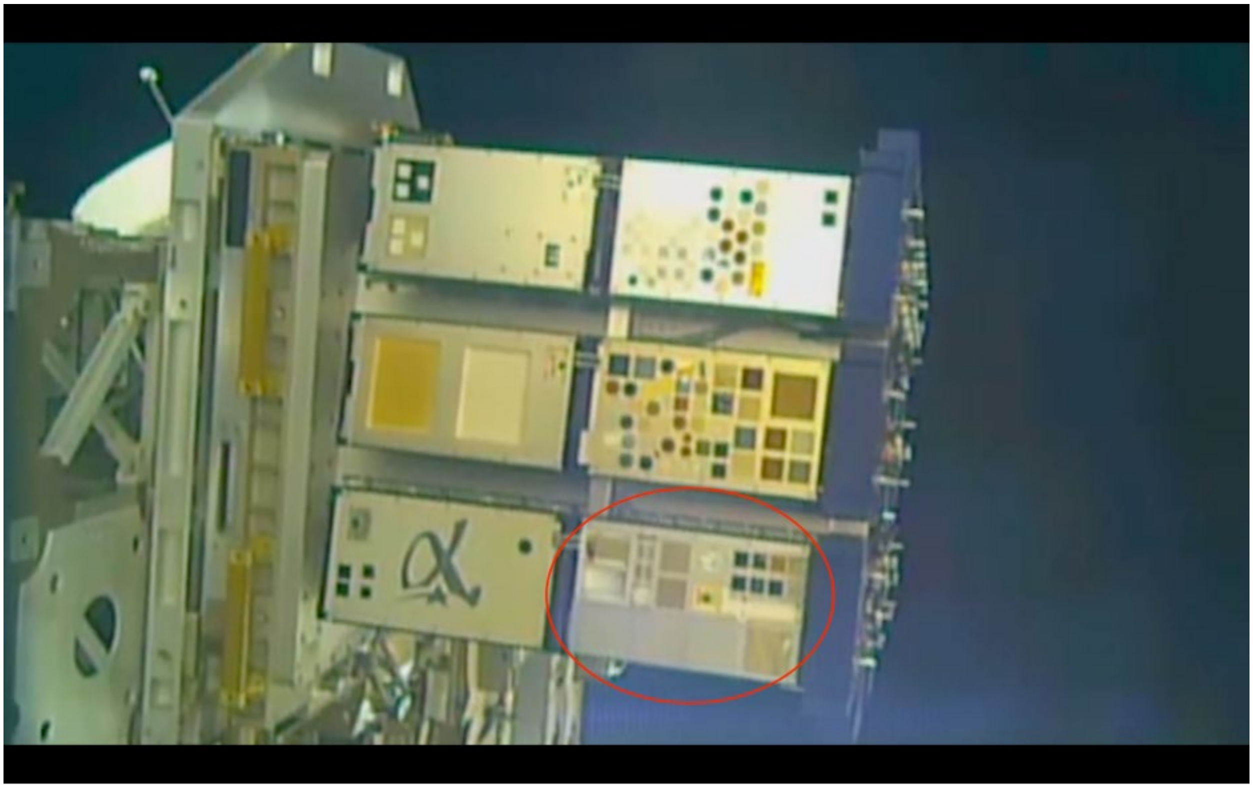

Fig. A9 The location of the opened sample deck integrated into the MISSE carrier on the ISS (Photo credit: NASA).

A.2 Photovoltaic Balloon for Energy Generation on Mars

In 2018, NASA identified a need for an energy source on Mars that would be reliable, sustainable, and autonomous as a part of the 2018 BIG Idea challenge. The Sun provides Mars with an abundance of solar energy, but the Martian climate has seasonal variations in solar intensity and fine powdery dust which impede the effectiveness of panels fixed on the ground. Additionally, the photovoltaic system would need to be deployed autonomously so that power is available before human arrival. Our proposed design utilized a spherical balloon made of a Kapton-Kevlar film with a low emissivity coating that was filled with Martian atmosphere (primarily CO_2). The top of the balloon would house 1000 m^2 of high efficiency PV cells, whereas the height of the top of the balloon would be far from the Martian surface, reducing dust accumulation on the PVs. The CO_2 could also be heated allowing the balloon to generate lift and further increase its altitude from the dusty surface.

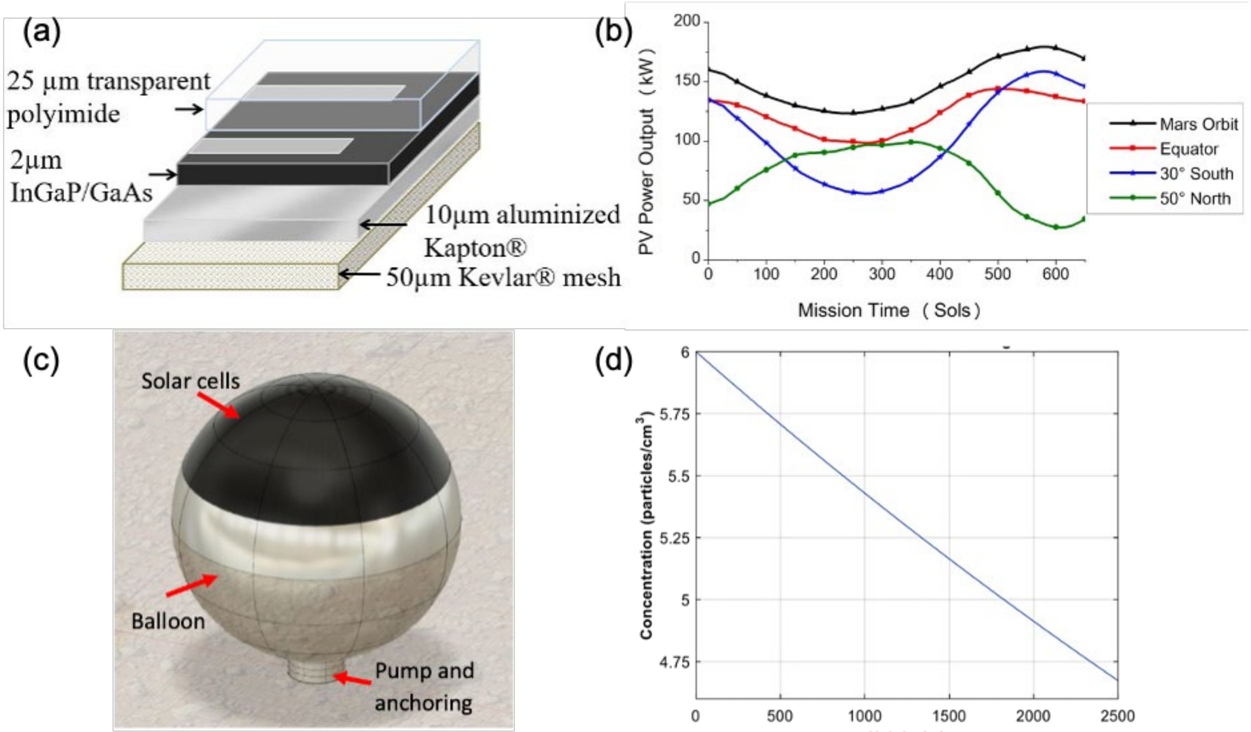

Fig. A10 (a) Balloon surface structure, (b) the estimated power output during mission time, (c) complete balloon design, and (d) the Martian dust concentration compared at various altitudes.

REFERENCES

[1] Lazard, “Lazard’s Levelised Cost of Energy Analysis - Version 14.0,” *Lazard.com*, vol. 14, October, 2020.

[2] NREL, “Best Research-Cell Efficiency Chart | Photovoltaic Research | NREL,” *National Renewable Energy Laboratory*, 2020. [Online]. Available: https://www.nrel.gov/pv/cell-efficiency.html.

[3] G. C. Wilkes, X. Deng, J. J. Choi, and M. C. Gupta, “Laser Annealing of TiO_2 Electron-Transporting Layer in Perovskite Solar Cells,” *ACS Appl. Mater. Interfaces*, vol. 10, no. 48, pp. 41312–41317, Dec. 2018.

[4] Fraunhofer, “Fraunhofer ISE: Photovoltaics Report,” 2019.

[5] K. Yamamoto, K. Yoshikawa, H. Uzu, and D. Adachi, “High-efficiency heterojunction crystalline Si solar cells,” *Jpn. J. Appl. Phys.*, vol. 57, no. 8S3, p. 08RB20, Aug. 2018.

[6] A. Richter, M. Hermle, and S. W. Glunz, “Reassessment of the Limiting Efficiency for Crystalline Silicon Solar Cells,” *IEEE J. Photovoltaics*, vol. 3, no. 4, pp. 1184–1191, Oct. 2013.

[7] M. D. Lammert and R. J. Schwartz, “The interdigitated back contact solar cell: A silicon solar cell for use in concentrated sunlight,” *IEEE Trans. Electron Devices*, vol. 24, no. 4, pp. 337–342, Apr. 1977.

[8] B. Dale and H. G. Rudenberg, “High efficiency silicon solar cells,” in *Proceedings of the 14th Annual Power Sources Conference*, 1960, p. 22.

[9] J. Zhao and M. A. Green, “Optimized antireflection coatings for high-efficiency silicon solar cells,” *IEEE Trans. Electron Devices*, vol. 38, no. 8, pp. 1925–1934, 1991.

[10] A. Goetzberger, J. Knobloch, and B. Voß, "The Physics of Solar Cells," in *Crystalline Silicon Solar Cells*, Chichester, UK: John Wiley & Sons, Ltd, 2014, pp. 67–86.

[11] Z. Song, S. C. Watthage, A. B. Phillips, and M. J. Heben, "Pathways toward high-performance perovskite solar cells: review of recent advances in organo-metal halide perovskites for photovoltaic applications," *J. Photonics Energy*, vol. 6, no. 2, p. 022001, Apr. 2016.

[12] B. W. H. van de Loo, "Atomic-layer-deposited surface passivation schemes for silicon solar cells," Technische Universiteit Eindhoven, 2017.

[13] R. Islam, "Metal Oxide Carrier Selective Contacts for On-chip Embedded Photovoltaics," Stanford University, 2017.

[14] M. C. Gupta and D. E. Carlson, "Laser processing of materials for renewable energy applications," *MRS Energy Sustain.*, vol. 2, p. E2, Apr. 2015.

[15] A. Kojima, K. Teshima, Y. Shirai, and T. Miyasaka, "Organometal Halide Perovskites as Visible-Light Sensitizers for Photovoltaic Cells," *J. Am. Chem. Soc.*, vol. 131, no. 17, pp. 6050–6051, May 2009.

[16] W. Ke, G. Fang, J. Wan, H. Tao, Q. Liu, L. Xiong, P. Qin, J. Wang, H. Lei, G. Yang, M. Qin, X. Zhao, and Y. Yan, "Efficient hole-blocking layer-free planar halide perovskite thin-film solar cells," *Nat. Commun.*, vol. 6, no. 1, p. 6700, Nov. 2015.

[17] G. Yang, H. Tao, P. Qin, W. Ke, and G. Fang, "Recent progress in electron transport layers for efficient perovskite solar cells," *J. Mater. Chem. A*, vol. 4, no. 11, pp. 3970–3990, 2016.

[18] F. Li, C. Chen, F. Tan, C. Li, G. Yue, L. Shen, and W. Zhang, "Semitransparent inverted polymer solar cells employing a sol-gel-derived TiO2 electron-selective layer on FTO and

MoO3/Ag/MoO3 transparent electrode," *Nanoscale Res. Lett.*, vol. 9, no. 1, p. 579, Dec. 2014.

[19] M. Tariq Bhatti, A. M. Rana, A. F. Khan, and M. I. Ansari, "Effect of Annealing on Electrical Properties of Indium Tin Oxide (ITO) Thin Films," *J. Appl. Sci.*, vol. 2, no. 5, pp. 570–573, May 2002.

[20] F. Di Giacomo, A. Fakharuddin, R. Jose, and T. M. Brown, "Progress, challenges and perspectives in flexible perovskite solar cells," *Energy Environ. Sci.*, vol. 9, no. 10, pp. 3007–3035, 2016.

[21] X. Deng, G. C. Wilkes, A. Z. Chen, N. S. Prasad, M. C. Gupta, and J. J. Choi, "Room-Temperature Processing of TiO_x Electron Transporting Layer for Perovskite Solar Cells," *J. Phys. Chem. Lett.*, vol. 8, no. 14, pp. 3206–3210, Jul. 2017.

[22] S. M. Sze and K. K. Ng, *Physics of Semiconductor Devices*. Hoboken, NJ, USA: John Wiley & Sons, Inc., 2006.

[23] M. Kaltenbrunner, G. Adam, E. D. Głowacki, M. Drack, R. Schwödiauer, L. Leonat, D. H. Apaydin, H. Groiss, M. C. Scharber, M. S. White, N. S. Sariciftci, and S. Bauer, "Flexible high power-per-weight perovskite solar cells with chromium oxide–metal contacts for improved stability in air," *Nat. Mater.*, vol. 14, no. 10, pp. 1032–1039, Oct. 2015.

[24] M. Kaltenbrunner, N. S. Sariciftci, and S. Bauer, "Ultrathin, air-stable perovskite solar cells for powering unmanned aircraft," *SPIE Newsroom*, Aug. 2016.

[25] Astrobotic, "Peregrine Lunar Lander Payload User's Guide," 2018. [Online]. Available: https://www.astrobotic.com/lunar-delivery.

[26] A. Nakaruk, D. Ragazzon, and C. C. Sorrell, "Anatase–rutile transformation through high-

temperature annealing of titania films produced by ultrasonic spray pyrolysis," *Thin Solid Films*, vol. 518, no. 14, pp. 3735–3742, May 2010.

[27] P. B. Nair, V. B. Justinvictor, G. P. Daniel, K. Joy, K. C. James Raju, D. Devraj Kumar, and P. V. Thomas, "Optical parameters induced by phase transformation in RF magnetron sputtered TiO2 nanostructured thin films," *Prog. Nat. Sci. Mater. Int.*, vol. 24, no. 3, pp. 218–225, Jun. 2014.

[28] A. Bendavid and P. J. Martin, "Review of thin film materials deposition by the filtered cathodic vacuum arc process at CSIRO," *Journal of the Australian Ceramic Society*. 2014.

[29] A. Pradana, C. Kluge, and M. Gerken, "Tailoring the refractive index of nanoimprint resist by blending with TiO2 nanoparticles," *Opt. Mater. Express*, vol. 4, no. 2, p. 329, Feb. 2014.

[30] V. Schmiedova, P. Dzik, M. Vesely, O. Zmeskal, M. Morozova, and P. Kluson, "Optical Properties of Titania Coatings Prepared by Inkjet Direct Patterning of a Reverse Micelles Sol-Gel Composition," *Molecules*, vol. 20, no. 8, pp. 14552–14564, Aug. 2015.

[31] F. Giordano, A. Abate, J. P. Correa Baena, M. Saliba, T. Matsui, S. H. Im, S. M. Zakeeruddin, M. K. Nazeeruddin, A. Hagfeldt, and M. Graetzel, "Enhanced electronic properties in mesoporous TiO2 via lithium doping for high-efficiency perovskite solar cells," *Nat. Commun.*, vol. 7, no. 1, p. 10379, Apr. 2016.

[32] Z. Liu, Q. Chen, Z. Hong, H. Zhou, X. Xu, N. De Marco, P. Sun, Z. Zhao, Y.-B. Cheng, and Y. Yang, "Low-Temperature TiO x Compact Layer for Planar Heterojunction Perovskite Solar Cells," *ACS Appl. Mater. Interfaces*, vol. 8, no. 17, pp. 11076–11083, May 2016.

[33] T. Blasco, M. A. Camblor, A. Corma, and J. Perez-Pariente, "The state of Ti in

titanoaluminosilicates isomorphous with zeolite .beta.," *J. Am. Chem. Soc.*, vol. 115, no. 25, pp. 11806–11813, Dec. 1993.

[34] R. Sanjinés, H. Tang, H. Berger, F. Gozzo, G. Margaritondo, and F. Lévy, "Electronic structure of anatase TiO 2 oxide," *J. Appl. Phys.*, vol. 75, no. 6, pp. 2945–2951, Mar. 1994.

[35] G. M. Ingo, S. Dirè, and F. Babonneau, "XPS studies of SiO2-TiO2 powders prepared by sol-gel process," *Appl. Surf. Sci.*, vol. 70–71, pp. 230–234, Jun. 1993.

[36] E. Yablonovitch, T. Gmitter, R. M. Swanson, and Y. H. Kwark, "A 720 mV open circuit voltage SiO x : c -Si:SiO x double heterostructure solar cell," *Appl. Phys. Lett.*, vol. 47, no. 11, pp. 1211–1213, Dec. 1985.

[37] W. Füssel, W. Henrion, and R. Scholz, "Structural, optical and electrical properties of SIPOS passivation layers," *Microelectron. Eng.*, vol. 22, no. 1–4, pp. 355–358, Aug. 1993.

[38] F. Feldmann, M. Simon, M. Bivour, C. Reichel, M. Hermle, and S. W. Glunz, "Carrier-selective contacts for Si solar cells," *Appl. Phys. Lett.*, vol. 104, no. 18, p. 181105, May 2014.

[39] R. Peibst, U. Romer, Y. Larionova, H. Schulte-Huxel, T. Ohrdes, M. Haberle, B. Lim, J. Krugener, D. Stichtenoth, T. Wutherich, C. Schollhorn, J. Graff, and R. Brendel, "Building blocks for back-junction back-contacted cells and modules with ion-implanted poly-Si junctions," in *2014 IEEE 40th Photovoltaic Specialist Conference (PVSC)*, 2014, pp. 0852–0856.

[40] P. Stradins, S. Essig, W. Nemeth, B. G. Lee, D. Young, A. Norman, Y. Liu, J. Luo, E. Warren, A. Dameron, V. Lasalvia, M. Page, and Y. Ok, "Passivated Tunneling Contacts to

N-Type Wafer Silicon and Their Implementation into High Performance Solar Cells Preprint," *6th World Conf. Photovolt. Energy Convers.*, 2014.

[41] A. D. Upadhyaya, Y.-W. Ok, E. Chang, V. Upadhyaya, K. Madani, K. Tate, B. Rounsaville, C.-J. Choi, V. Chandrasekaran, V. Yelundur, A. Gupta, and A. Rohatgi, "Ion-Implanted Screen-Printed n-Type Solar Cell With Tunnel Oxide Passivated Back Contact," *IEEE J. Photovoltaics*, vol. 6, no. 1, pp. 153–158, Jan. 2016.

[42] B. Nemeth, D. L. Young, M. R. Page, V. LaSalvia, S. Johnston, R. Reedy, and P. Stradins, "Polycrystalline silicon passivated tunneling contacts for high efficiency silicon solar cells," *J. Mater. Res.*, vol. 31, no. 6, pp. 671–681, Mar. 2016.

[43] S. Reiter, N. Koper, R. Reineke-Koch, Y. Larionova, M. Turcu, J. Krügener, D. Tetzlaff, T. Wietler, U. Höhne, J.-D. Kähler, R. Brendel, and R. Peibst, "Parasitic Absorption in Polycrystalline Si-layers for Carrier-selective Front Junctions," *Energy Procedia*, vol. 92, pp. 199–204, Aug. 2016.

[44] Z. Sun and M. C. Gupta, "Laser annealing of silicon surface defects for photovoltaic applications," *Surf. Sci.*, vol. 652, pp. 344–349, Oct. 2016.

[45] L. Wei, M. Vaudin, C. S. Hwang, G. White, J. Xu, and A. J. Steckl, "Heat conduction in silicon thin films: Effect of microstructure," *J. Mater. Res.*, vol. 10, no. 8, pp. 1889–1896, Aug. 1995.

[46] G. R. Wolstenholme, N. Jorgensen, P. Ashburn, and G. R. Booker, "An investigation of the thermal stability of the interfacial oxide in polycrystalline silicon emitter bipolar transistors by comparing device results with high-resolution electron microscopy observations," *J. Appl. Phys.*, vol. 61, no. 1, pp. 225–233, Jan. 1987.

[47] D. Sands, "Pulsed Laser Heating and Melting," in *Heat Transfer - Engineering*

Applications, 2011.

[48] S. A. Sopra, “Optical Data from Sopra SA,” 2000. [Online]. Available: http://www.sspectra.com/sopra.html.

[49] A. Fell and G. P. Willeke, “Fast simulation code for heating, phase changes and dopant diffusion in silicon laser processing using the alternating direction explicit (ADE) method,” *Appl. Phys. A*, vol. 98, no. 2, pp. 435–440, Feb. 2010.

[50] A. Fell, “Modelling and Simulation of Laser Chemical Processing (LCP) for the Manufacturing of Silicon Solar Cells,” Universität Konstanz, 2010.

[51] D. E. Kane and R. M. Swanson, “Measurement of the Emitter Saturation Current by a Contactless Photoconductivity Decay Method,” in *Conference Record of the IEEE Photovoltaic Specialists Conference*, 1985.

[52] K. Yoshikawa, W. Yoshida, T. Irie, H. Kawasaki, K. Konishi, H. Ishibashi, T. Asatani, D. Adachi, M. Kanematsu, H. Uzu, and K. Yamamoto, “Exceeding conversion efficiency of 26% by heterojunction interdigitated back contact solar cell with thin film Si technology,” *Sol. Energy Mater. Sol. Cells*, vol. 173, pp. 37–42, Dec. 2017.

[53] A. Richter, J. Benick, F. Feldmann, A. Fell, B. Steinhauser, J.-I. Polzin, N. Tucher, J. N. Murthy, M. Hermle, and S. W. Glunz, “Both Sides Contacted Silicon Solar Cells: Options for Approaching 26% Efficiency,” *36th Eur. PV Sol. Energy Conf. Exhib.*, 2019.

[54] J. Bullock, Y. Wan, Z. Xu, S. Essig, M. Hettick, H. Wang, W. Ji, M. Boccard, A. Cuevas, C. Ballif, and A. Javey, “Stable Dopant-Free Asymmetric Heterocontact Silicon Solar Cells with Efficiencies above 20%,” *ACS Energy Lett.*, vol. 3, no. 3, pp. 508–513, Mar. 2018.

[55] H. Mehmood, H. Nasser, T. Tauqeer, S. Hussain, E. Ozkol, and R. Turan, “Simulation of

an efficient silicon heterostructure solar cell concept featuring molybdenum oxide carrier-selective contact," *Int. J. Energy Res.*, vol. 42, no. 4, pp. 1563–1579, Mar. 2018.

[56] R. Islam and K. C. Saraswat, "Metal/insulator/semiconductor carrier selective contacts for photovoltaic cells," in *2014 IEEE 40th Photovoltaic Specialist Conference, PVSC 2014*, 2014.

[57] C. Battaglia, S. M. De Nicolás, S. De Wolf, X. Yin, M. Zheng, C. Ballif, and A. Javey, "Silicon heterojunction solar cell with passivated hole selective MoO x contact," *Appl. Phys. Lett.*, 2014.

[58] Z. Sun, X. Deng, J. J. Choi, and M. C. Gupta, "Silicon Surface Passivation by Laser Processing a Sol–Gel TiO_x Thin Film," *ACS Appl. Energy Mater.*, p. acsaem.8b01043, Sep. 2018.

[59] C. Battaglia, X. Yin, M. Zheng, I. D. Sharp, T. Chen, S. McDonnell, A. Azcatl, C. Carraro, B. Ma, R. Maboudian, R. M. Wallace, and A. Javey, "Hole Selective MoO_x Contact for Silicon Solar Cells," *Nano Lett.*, vol. 14, no. 2, pp. 967–971, Feb. 2014.

[60] J. Bullock, A. Cuevas, T. Allen, and C. Battaglia, "Molybdenum oxide MoOx: A versatile hole contact for silicon solar cells," *Appl. Phys. Lett.*, 2014.

[61] J. Geissbühler, J. Werner, S. Martin de Nicolas, L. Barraud, A. Hessler-Wyser, M. Despeisse, S. Nicolay, A. Tomasi, B. Niesen, S. De Wolf, and C. Ballif, "22.5% efficient silicon heterojunction solar cell with molybdenum oxide hole collector," *Appl. Phys. Lett.*, vol. 107, no. 8, p. 081601, Aug. 2015.

[62] I. Irfan, A. James Turinske, Z. Bao, and Y. Gao, "Work function recovery of air exposed molybdenum oxide thin films," *Appl. Phys. Lett.*, vol. 101, no. 9, p. 093305, Aug. 2012.

[63] L. Neusel, M. Bivour, and M. Hermle, "Selectivity issues of MoOx based hole contacts,"

Energy Procedia, vol. 124, pp. 425–434, Sep. 2017.

[64] OpenSim, “SPIM Optics 101/Theoretical basics.” [Online]. Available: https://openspim.org/SPIM_Optics_101/Theoretical_basics.

[65] J. Bullock, M. Hettick, J. Geissbühler, A. J. Ong, T. Allen, C. M. Sutter-Fella, T. Chen, H. Ota, E. W. Schaler, S. De Wolf, C. Ballif, A. Cuevas, and A. Javey, “Efficient silicon solar cells with dopant-free asymmetric heterocontacts,” *Nat. Energy*, vol. 1, no. 3, p. 15031, Mar. 2016.

[66] V. Budhraja, S. Devayajanam, and P. Basnyat, “Simulation Results: Optimization of Contact Ratio for Interdigitated Back-Contact Solar Cells,” *Int. J. Photoenergy*, vol. 2017, pp. 1–10, 2017.

[67] Z. Sun and M. C. Gupta, “A study of laser-induced surface defects in silicon and impact on electrical properties,” *J. Appl. Phys.*, vol. 124, no. 22, p. 223103, Dec. 2018.

[68] L. Bounaas, N. Auriac, B. Grange, R. Monna, M. Pirot, S. De Vecchi, J. Jourdan, S. Mialon, M. Pasquinelli, and D. Barakel, “Laser Ablation of Dielectric Layers and Formation of Local Al-BSF in Dielectric back Passivated Solar Cells,” *Energy Procedia*, vol. 38, pp. 670–676, 2013.

[69] T. Arguirov, W. Seifert, M. Kittler, and J. Reif, “Temperature behaviour of photoluminescence and electron-beam-induced current recombination behaviour of extended defects in solar grade silicon,” *J. Phys. Condens. Matter*, vol. 14, no. 48, pp. 13169–13177, Dec. 2002.

[70] H. T. Nguyen, Y. Han, M. Ernst, A. Fell, E. Franklin, and D. Macdonald, “Dislocations in laser-doped silicon detected by micro-photoluminescence spectroscopy,” *Appl. Phys. Lett.*, vol. 107, no. 2, p. 022101, Jul. 2015.

[71] R. Sauer, J. Weber, J. Stolz, E. R. Weber, K.-H. K�sters, and H. Alexander, “Dislocation-related photoluminescence in silicon,” *Appl. Phys. A Solids Surfaces*, vol. 36, no. 1, pp. 1–13, Jan. 1985.

[72] M. Shimbo, K. Furukawa, K. Fukuda, and K. Tanzawa, “Silicon-to-silicon direct bonding method,” *J. Appl. Phys.*, vol. 60, no. 8, pp. 2987–2989, Oct. 1986.

[73] R. Wiget, E. P. Burte, J. Gyulai, H. Ryssel, and P. O. Box, “Silicon to silicon direct bonding-characterization of the interface and manufacture of p-i-n diodes,” *1993 Fifth Eur. Conf. Power Electron. Appl.*, pp. 63–68, 1993.

[74] A. Wissinger, A. Olowinsky, A. Gillner, and R. Poprawe, “Laser transmission bonding of silicon to silicon with metallic interlayers for wafer-level packaging,” *Microsyst. Technol.*, vol. 19, no. 5, pp. 669–673, May 2013.

[75] H. Kämmer, G. Matthäus, S. Nolte, M. Chanal, O. Utéza, and D. Grojo, “In-volume structuring of silicon using picosecond laser pulses,” *Appl. Phys. A*, vol. 124, no. 4, p. 302, Apr. 2018.

[76] M. Chambonneau, Q. Li, M. Chanal, N. Sanner, and D. Grojo, “Writing waveguides inside monolithic crystalline silicon with nanosecond laser pulses,” *Opt. Lett.*, vol. 41, no. 21, p. 4875, Nov. 2016.

[77] N. Liu, “Processing of Back Surface of Si Wafers With a Pulsed Nd:YAG Laser,” *J. Laser Micro/Nanoengineering*, vol. 11, no. 2, pp. 232–238, Jul. 2016.

[78] M. A. Green and M. J. Keevers, “Optical properties of intrinsic silicon at 300 K,” *Prog. Photovoltaics Res. Appl.*, vol. 3, no. 3, pp. 189–192, 1995.

[79] C. Schinke, P. Christian Peest, J. Schmidt, R. Brendel, K. Bothe, M. R. Vogt, I. Kröger, S. Winter, A. Schirmacher, S. Lim, H. T. Nguyen, and D. MacDonald, “Uncertainty analysis

for the coefficient of band-to-band absorption of crystalline silicon," *AIP Adv.*, vol. 5, no. 6, p. 067168, Jun. 2015.

[80] S. C. Baker-Finch, K. R. McIntosh, D. Yan, K. C. Fong, and T. C. Kho, "Near-infrared free carrier absorption in heavily doped silicon," *J. Appl. Phys.*, vol. 116, no. 6, p. 063106, Aug. 2014.

[81] H. A. Weakliem and D. Redfield, "Temperature dependence of the optical properties of silicon," *J. Appl. Phys.*, vol. 50, no. 3, pp. 1491–1493, Mar. 1979.

[82] M. O'Neill, A. J. McDanal, H. Brandhorst, K. Schmid, P. LaCorte, M. Piszczor, and M. Myers, "Recent space PV concentrator advances: More robust, lighter, and easier to track," in *2015 IEEE 42nd Photovoltaic Specialist Conference (PVSC)*, 2015, pp. 1–6.

[83] D. Cardwell, A. Kirk, C. Stender, A. Wibowo, F. Tuminello, M. Drees, R. Chan, M. Osowski, and N. Pan, "Very High Specific Power ELO Solar Cells (>3 kW/kg) for UAV, Space, and Portable Power Applications," in *2017 IEEE 44th Photovoltaic Specialist Conference (PVSC)*, 2017, pp. 3511–3513.

[84] S. Kang, J. Jeong, S. Cho, Y. J. Yoon, S. Park, S. Lim, J. Y. Kim, and H. Ko, "Ultrathin, lightweight and flexible perovskite solar cells with an excellent power-per-weight performance," *J. Mater. Chem. A*, vol. 7, no. 3, pp. 1107–1114, 2019.

[85] I. Cardinaletti, T. Vangerven, S. Nagels, R. Cornelissen, D. Schreurs, J. Hruby, J. Vodnik, D. Devisscher, J. Kesters, J. D'Haen, A. Franquet, V. Spampinato, T. Conard, W. Maes, W. Deferme, and J. V. Manca, "Organic and perovskite solar cells for space applications," *Sol. Energy Mater. Sol. Cells*, 2018.

[86] L. K. Reb, M. Böhmer, B. Predeschly, S. Grott, C. L. Weindl, G. I. Ivandekic, R. Guo, C. Dreißigacker, R. Gernhäuser, A. Meyer, and P. Müller-Buschbaum, "Perovskite and

Organic Solar Cells on a Rocket Flight," *Joule*, vol. 4, no. 9, pp. 1880–1892, Sep. 2020.

[87] N. S. Prasad, "Optoelectronic Devices and Nanocomposite materials for testing on ISS Under MISSE 11 Mission," in *ISS R&D Conference*, 2019, pp. 1–21.

LIST OF PUBLICATIONS, CONFERENCES, AND AWARDS

List of Publications

1. X. Deng, **G. C. Wilkes,** A. Chen, N. Prasad, M. C. Gupta, and J. J. Choi, **Room Temperature Processing of TiOx Electron Transporting Layer for Perovskite Solar Cells.** *J. Phys. Chem. Lett.*, 8 (14), **2017**, pp. 3206–3210.
2. **G. C. Wilkes,** X. Deng, J. J. Choi, and M. C. Gupta, **Laser Annealing of TiO_2 Electron-Transporting Layer in Perovskite Solar Cells.** *ACS Appl. Mater. Interfaces*, 10 (48), **2018**, pp. 41312–41317.
3. F. Peixun, Z. Sun, **G. C. Wilkes,** and M. C. Gupta, **Low-temperature Laser Generated Ultrathin Aluminum Oxide Layers for Effective c-Si Surface Passivation.** *Appl. Surf. Sci.*, 480, **2019**, pp. 35–42.
4. **G. C. Wilkes,** A. D. Upadhyaya, A. Rohatgi, and M. C. Gupta, **Laser Crystallization and Dopant Activation Process for a-Si:H Film in Carrier-Selective Contacts for Si Solar Cells.** *2019 IEEE 46th Photovoltaic Specialist Conference (PVSC) Proceedings,* pp, 2709–2712.
5. **G. C. Wilkes,** A. D. Upadhyaya, A. Rohatgi, and M. C. Gupta, **Laser Crystallization and Dopant Activation of a-Si:H Carrier Selective Layer in TOPCon Si Solar Cell.** *IEEE Journal of Photovoltaics,* 10 (5), **2020**, pp. 1283–1289.
6. **G. C. Wilkes** and M. C. Gupta, **Laser Annealing of Carrier-Selective MoO_x Layers for Silicon Solar Cells.** *2020 IEEE 47th Photovoltaic Specialist Conference (PVSC) Proceedings,* Accepted June 2020.
7. Expected publication on the impact of laser annealing on passivation.
8. Expected publication on direct wafer laser bonding for junction formation.

List of Conference Presentations:

1. Hisiro, W.; Julian, M.; Pantoja, E.; Sinha, A.; **Wilkes, G. C.** (Team Leader); Gupta, M. C.; **Photovoltaic Balloon for Autonomous Energy Generation on Mars.** *2018 NASA BIG Idea Competition,* NASA Glenn Research Center, Cleveland, OH, March, 2018.
2. **G. C. Wilkes** and M. C. Gupta, **Laser Processing for Low-Cost, High-Efficiency Solar Cells.** *6th International School on Lasers in Materials Science (SLIMS),* Venice, Italy, July, 2018.
3. K. Fisher, X. Meng, S. Mony, **G. C. Wilkes**, M. C. Gupta, M. Bertoni, and Z. Holman, **Novel Al Conductive Backsheets and Interconnects for Back-Contact Silicon Solar Cells.** *8th Metallization and Interconnection Workshop*, Konstanz, Germany, May, 2019.
4. **G. C. Wilkes,** A. D. Upadhyaya, A. Rohatgi, and M. C. Gupta, **Laser Crystallization and Dopant Activation Process for a-Si:H Film in Carrier-Selective Contacts for Si Solar Cells.** *IEEE 46th Photovoltaic Specialist Conference (PVSC)*, Chicago, IL., June, 2019.
5. **G. C. Wilkes** and M. C. Gupta, **Laser Annealing of Carrier-Selective MoO_x Layers for Silicon Solar Cells.** *IEEE 47th Photovoltaic Specialist Conference (PVSC),* Virtual Meeting, June, 2020.
6. K. Radhakrishnan, J. Rudy, R. Serpe, J. St. Martin, **G. C. Wilkes** and M. C. Gupta, **Beaming of Energy via Laser for Lunar Exploration (BELLE)**. *2020 NASA BIG Idea Competition*, Virtual Forum, January, 2021.

List of Awards, Funding, and Other Notable Activities:

1. National Institute of Aerospace Best Student Paper Award 2019, for **G. Wilkes,** X. Deng, J. J. Choi, and M. C. Gupta, **Laser Annealing of TiO_2 Electron-Transporting Layer in Perovskite Solar Cells.** *ACS Appl. Mater. Interfaces*, 10 (48), **2018**, pp. 41312–41317

2. Contributions to the NSF Grant Award 2005098 in the ECCS Organization under EPMD Program for: **Collaborative Research: Fundamental Studies of Carrier-Selective Passivating Contacts for Efficient Photovoltaic Devices using Laser Processing and Atomic Resolution Interfaces** *(Total Award: $249,976.00)* June 1 2020 – May 31, 2020.
3. Encapsulated laser-annealed TiO_2 perovskite solar cell sample selected for the Materials Science International Space Station (MISSE)-11 experiment, aboard the International Space Station for a year-long study on space exposure.
4. Team Finalist in the 2018 NASA BIG Idea Competition for **Photovoltaic Balloon for Autonomous Energy Generation on Mars**.
5. Team Finalist in the 2020 NASA BIG Idea Competition for **Beaming of Energy via Laser for Lunar Exploration (BELLE)**.
6. Outreach including guest lectures on photovoltaics to Charlottesville High School in Fall 2018 and informative poster display at Jefferson-Madison Regional Library (Charlottesville City Public Library).

COLLECTION OF PUBLISHED WORKS

THE JOURNAL OF PHYSICAL CHEMISTRY Letters

Letter

pubs.acs.org/JPCL

Room-Temperature Processing of TiO_x Electron Transporting Layer for Perovskite Solar Cells

Xiaoyu Deng,[†,∥] George C. Wilkes,[‡,∥] Alexander Z. Chen,[†] Narasimha S. Prasad,[§] Mool C. Gupta,[*,‡] and Joshua J. Choi[*,†]

[†]Department of Chemical Engineering, University of Virginia, Charlottesville, Virginia 22904, United States
[‡]Department of Electrical and Computer Engineering, University of Virginia, Charlottesville, Virginia 22904, United States
[§]NASA Langley Research Center, Hampton, Virginia 23681, United States

Supporting Information

ABSTRACT: In order to realize high-throughput roll-to-roll manufacturing of flexible perovskite solar cells, low-temperature processing of all device components must be realized. However, the most commonly used electron transporting layer in high-performance perovskite solar cells is based on TiO_2 thin films processed at high temperature (>450 °C). Here, we demonstrate room temperature solution processing of the TiO_x layer that performs as well as the high temperature TiO_2 layer in perovskite solar cells, as evidenced by a champion solar cell efficiency of 16.3%. Using optical spectroscopy, electrical measurements, and X-ray diffraction, we show that the room-temperature processed TiO_x is amorphous with organic residues, and yet its optical and electrical properties are on par with the high-temperature TiO_2. Flexible perovskite solar cells that employ a room-temperature TiO_x layer with a power conversion efficiency of 14.3% are demonstrated.

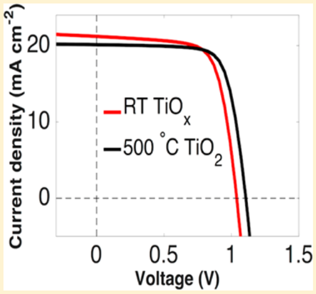

Metal halide perovskite (MHP) solar cells have demonstrated the most rapid improvement in power conversion efficiency (PCE) among all photovoltaic technologies to date. With a record PCE of 22.1%,[1] MHP solar cells are now on par with silicon solar cells in terms of efficiency. Moreover, MHP solar cells can be fabricated entirely using low-cost solution processing methods and earth-abundant compositions. Therefore, they can combine high efficiency with low cost and have a great potential for realizing more economically competitive solar power.

What is particularly exciting about MHPs is that they can be deposited on various substrates at low temperature (<150 °C) and enable roll-to-roll manufacturing of low-cost, lightweight and flexible devices.[2] Lead halide-based MHPs have been shown to possess a large extinction coefficient greater than 10^4 cm^{-1}, and a long electron−hole diffusion length in the range of hundreds of nanometers to microns in polycrystalline thin films.[3] This means that a film only about 500 nm thick can harvest most of the sunlight and efficiently transport the photogenerated charges into the external circuit. Such a thin MHP film is highly flexible and corresponds to only 2 g m^{-2} of weight, which is 2 orders of magnitude lighter than a silicon solar cell. Successful development of MHP solar cells that simultaneously combine high efficiency, low cost, lightweight, and flexibility can enable novel portable power generation capabilities in situations where conventional rigid and heavy solar cells are not feasible, such as wearable electronics, solar aviation, automobiles, building integrated photovoltaics, and more.

While the quest for achieving high PCE has shown exceptional progress, a majority of the high-performance MHP solar cell structures rely on a titanium dioxide (TiO_2) electron transporting layer (ETL) processed at high temperatures (>450 °C). The high temperature requirement prohibits the use of flexible plastic substrates such as polyethylene terephthalate (PET) and polyethylene naphthalate (PEN) that cannot withstand temperatures greater than 150 °C. Due to the high performance of metal oxide-based ETLs for MHP solar cells, it is of great interest to achieve low-temperature processing of metal oxide thin films with favorable optical and electrical properties. Indeed, among all flexible MHP solar cell results to date, device architectures that employ metal oxide ETLs currently hold the best PCE records of between 15% and 18%.[4−6] Previous efforts to deposit metal oxide ETLs on flexible substrates at low temperature have been based on solution processing of nanoparticles,[5,7−13] sputter deposition,[4,14,15] spray coating,[16,17] e-beam evaporation,[18] atomic layer deposition (ALD),[19,20] and electrodeposition.[21,22] Despite the encouraging device performance, these methods require vacuum processing steps, nanoparticle formulations, etc., that can significantly increase the cost while reducing the throughput. Therefore, there is a need for developing low-temperature solution processing of metal oxide films starting from simple and low-cost commercially available precursors.

Here, we demonstrate that room temperature processing of simple solution formulation (titanium(IV) isopropoxide ($Ti(OiPr)_4$) in isopropanol) can result in a TiO_x layer with high

Received: June 9, 2017
Accepted: June 28, 2017
Published: June 28, 2017

DOI: 10.1021/acs.jpclett.7b01466
J. Phys. Chem. Lett. 2017, 8, 3206−3210

performance in MHP solar cells, as evidenced by a champion solar cell efficiency of 16.3%. Using optical spectroscopy, electrical measurements, and X-ray diffraction, we show that the room-temperature processed TiO_x is amorphous with organic residues and yet its optical and electrical properties are on par with the high temperature TiO_2. Flexible MHP perovskite solar cells with a power conversion efficiency of 14.3% were achieved with the room temperature processed TiO_x layer. The power conversion efficiency could potentially be increased further through process optimization.

The room-temperature (RT) processed thin films from the $Ti(OiPr)_4$ solution, from here on referred to as "$Ti(OiPr)_4$ RT", were prepared on top of glass/indium−tin-oxide (ITO) substrates as described in the Supporting Information. The thickness of $Ti(OiPr)_4$ RT film was measured to be 20 nm using ellipsometry (Table S1). Scanning electron microscopy (SEM) images show pinhole free surface morphology (Figure S1) and PbI_2 in DMF solution shows good wetting behavior on the $Ti(OiPr)_4$ RT film (Figure S2). Hydrolysis and condensation of precursor $Ti(OiPr)_4$ is the key to forming solid thin film.[23] Once the $Ti(OiPr)_4$ precursor solution is spin coated on the ITO slide, the isopropanol solvent evaporates quickly, and $Ti(OiPr)_4$ makes contact with moisture in the air. Subsequently, hydrolysis and condensation reactions form Ti−O−Ti linkages.[24] Incomplete condensation will result in OH groups left in the thin film,[25] as is the case with our $Ti(OiPr)_4$ RT film (*vide infra*).

We fabricated and tested perovskite solar cells with $Ti(OiPr)_4$ RT films deposited in different relative humidity (RH) to investigate the impact of RH on solar cell efficiency. The device structure is shown in Figure 1a,b. On top of the $Ti(OiPr)_4$ RT film, a methylammonium lead iodide ($MAPbI_3$) layer (∼300 nm), (2,2′,7,7′-tetrakis N, N-di-*p*-methoxyphenyl-amine)-9,9′-spirobi-fluorine (Spiro-OMeTAD) layer (100 nm), and silver anode layer (60 nm) were deposited as described in the Supporting Information. The cells with $Ti(OiPr)_4$ RT films fabricated in 40% to 55% RH resulted in the highest efficiency (Figure S3), so all the following $Ti(OiPr)_4$ films were made in 55% RH. Next, to check for the impact of thermal annealing on solar cell efficiency, $Ti(OiPr)_4$ films were annealed immediately after the spin-coating step at various temperatures ranging from room temperature up to 500 °C. Our results show that the temperature at which the $Ti(OiPr)_4$ thin film is annealed has no significant impact on the solar cell efficiency (Figure 1c). Specifically, the unannealed film (RT) and 500 °C annealed films result in comparable open-circuit voltages (V_{OC}), short-circuit current densities (J_{SC}), fill factors (FF), and efficiencies (η) as shown in Figure 1d.

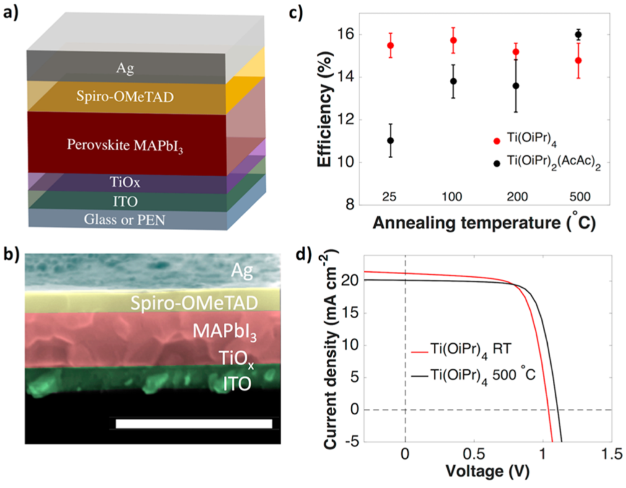

Figure 1. Device structures and their performance. (a) Perovskite solar cell structure. (b) SEM image of device cross-section. Scale bar represents 1 μm. (c) Impact of annealing temperature of ETL on performance of solar cells when two different precursor solutions were used, $Ti(OiPr)_4$ and $Ti(OiPr)_2(AcAc)_2$. The statistics are based on six devices at each annealing temperature. (d) J−V curves of champion devices using ETL of $Ti(OiPr)_4$ film fabricated at room temperature (red line) and annealed at 500 °C (black line). The substrates for these devices were glass.

Additionally, we examined the impact of thermal annealing temperature on the performance of TiO_2 thin films made from titanium diisopropoxide bis(acetylacetonate) in butanol, from here on referred to as "$Ti(OiPr)_2(AcAc)_2$". This is the most commonly employed TiO_2 precursor solution for high-efficiency perovskite solar cells[26−28] and is typically annealed at high temperatures (>450 °C). Our results show that, indeed, when varying the annealing temperature from 25 to 500 °C, the solar cell efficiency changes from 11% to 16% (Figure 1c), mostly due to an increase in the J_{SC} (Figure S4). We attribute the starkly different dependence of $Ti(OiPr)_4$ and $Ti(OiPr)_2(AcAc)_2$ performance on the annealing temperature to slower hydrolysis of the acetylacetone groups.[29] $Ti(OiPr)_2(AcAc)_2$ has an octahedral coordination with two isopropoxide and two acetylacetone (AcAc) groups around a central titanium atom. Previous literature has shown that the labile isopropoxide groups can easily hydrolyze compared to AcAc groups.[29,30] In fact, the AcAc groups have been used to stabilize the solution formulation by suppressing uncontrolled precipitation since hydrolysis of the AcAc groups is significantly more suppressed.[31] Therefore, when $Ti(OiPr)_2(AcAc)_2$ is used as the precursor solution to form the titania ETL, pyrolysis at high temperature is needed rather than just hydrolysis. By contrast, we show in this work that $Ti(OiPr)_4$ can readily form a titania layer at room temperature that performs well in perovskite solar cells.

To better understand the nature of the $Ti(OiPr)_4$ RT film, we performed optical, electrical, and X-ray diffraction characterization. The absorbance spectra of the $Ti(OiPr)_4$ RT film and $Ti(OiPr)_2(AcAc)_2$ 500 °C film were measured using a spectrophotometer equipped with an integrating sphere (Figure 2a). The band gap of $Ti(OiPr)_4$ RT film was determined to be 3.69 eV using a Tauc plot, which matches the band gap of TiO_x reported in the literature.[32,33] The absorbance onset of precursor $Ti(OiPr)_4$ solution is 3.89 eV, which is higher than the deposited $Ti(OiPr)_4$ RT film. The band gap of $Ti(OiPr)_2(AcAc)_2$ 500 °C film was determined to be 3.57 eV, which is slightly lower than the band gap of the $Ti(OiPr)_4$ RT film. Fourier Transform Infrared (FTIR) spectroscopy results are shown in Figure 2b. Both samples show absorption in the region below 1000 cm^{-1}, which corresponds to a vibration peak of Ti−O−Ti bonds,[25] suggesting that Ti−O−Ti bonds have formed in both cases.

In higher wavenumber regions, the spectrum from the $Ti(OiPr)_4$ sample shows several peaks that are missing in the spectrum from the $Ti(OiPr)_2(AcAc)_2$ sample. These peaks are associated with O−H groups (2450−3600 cm^{-1} and 1600−1700 cm^{-1}), C−O stretching (1050−1180 cm^{-1}), C−H bending (1350−1410 cm^{-1}), and C−H stretching (2850−3000 cm^{-1}). These peaks indicate the presence of an OH group

DOI: 10.1021/acs.jpclett.7b01466
J. Phys. Chem. Lett. 2017, 8, 3206−3210

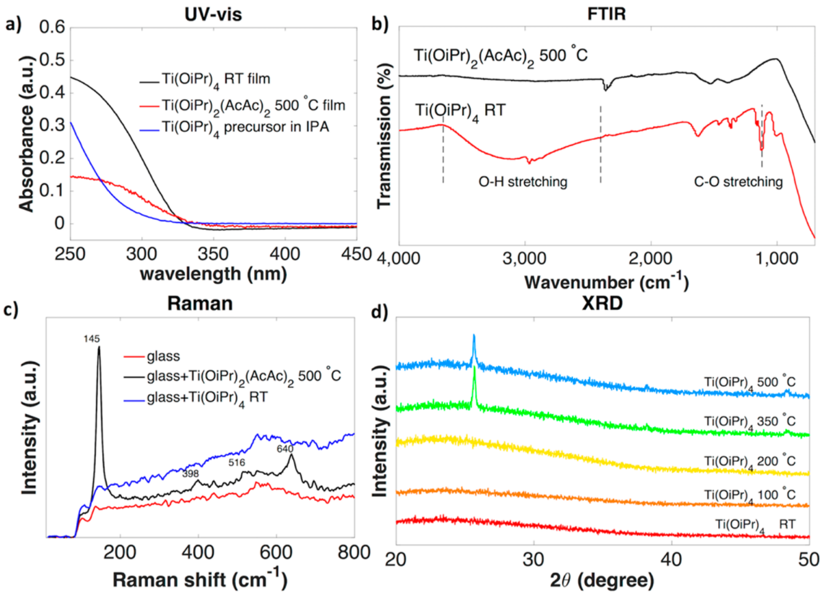

Figure 2. Characterization for $Ti(OiPr)_4$ film. (a) UV−vis absorbance spectra for $Ti(OiPr)_4$ RT film, $Ti(OiPr)_2(AcAc)_2$ 500 °C film, and $Ti(OiPr)_4$ RT precursor solution. (b) FTIR transmission spectra of $Ti(OiPr)_2(AcAc)_2$ 500 °C and $Ti(OiPr)_4$ powder. (c) Raman spectra of substrate glass, $Ti(OiPr)_4$ RT film, and $Ti(OiPr)_2(AcAc)_2$ 500 °C film. (d) XRD of $Ti(OiPr)_4$ film without annealing, annealed at 100 °C, 200 °C, 350 °C, and 500 °C.

as well as organic residues in the $Ti(OiPr)_4$ sample.[34] In a pH neutral condition such as $Ti(OiPr)_4$ in isopropanol (IPA), a significant fraction of the product will form weaker olation bonds, which consist of metal ions bridged through hydroxide, rather than condensation bonds.[35] FTIR spectra indicates the occurrence of a terminal type of OH groups,[25] which passivates the dangling bond of the TiO_x film. Therefore, our FTIR results suggest that some of the $Ti(OiPr)_4$ did not completely go through the hydrolysis and condensation steps.

X-ray diffraction (XRD) patterns show no peaks from thin films deposited from $Ti(OiPr)_4$ and annealed below 350 °C (Figure 2d). If annealed at temperatures above 350 °C, XRD patterns show peaks that correspond to anatase TiO_2. The transition temperature of ∼350 °C observed in our work is consistent with the transition from the amorphous to the anatase phase of TiO_2.[36] Our Raman spectroscopy results also present a consistent picture that the $Ti(OiPr)_4$ RT sample is completely amorphous since there are no obvious peaks that correspond to crystalline TiO_2 as shown previously in the literature[37] (Figure 2c). In comparison, the $Ti(OiPr)_2(AcAc)_2$ 500 °C show peaks at 145, 398, 516, and 640 cm^{-1} Raman shift that correspond agreeably to the anatase phase of TiO_2.[37]

The electrical resistivity was determined using a two-terminal measurement with ITO and thermally evaporated silver as the electrical contacts with TiO_x thin film sandwiched in the middle. The measured resistivities for the TiO_x thin films annealed at different temperatures are shown in Table 1. They are in the range of 60−150 × 10^5 Ω·cm, which lies between that of metals (10^{-6} Ω·cm) and insulators (10^{14} Ω·cm), indicating semiconducting behavior. TiO_2 has a resistivity of 10^8 Ω cm making it electrically insulating, but as the titanium ratio increases relative to the oxide it becomes more like an n-type semiconductor and its resistivity decreases.[38] This indicates that our film is partially suboxidized due to the resistivity being 3 orders of magnitude lower than pure TiO_2. This further indicates that the titanium/oxygen ratio in our films will drastically affect our electrical properties.[38] As the film is annealed at higher temperatures, the observed slight increase in two-terminal resistivity is likely due to the increase in sheet resistance of ITO thin films at temperatures greater than 300 °C. Our TiO_x resistivity measurements are on the same order of magnitude as those obtained from magnetron sputtering at varying substrate temperatures by Su et al.[39] Additionally, this high resistivity ensures us that our film is complete and pinhole-free; otherwise short paths would arise and dramatically reduce the measured resistance.

Table 1. Electrical Resistivity of TiO_x Thin Films Prepared from $Ti(OiPr)_4$ Solution

anneal temperature [°C]	two terminal resistivity [10^5 Ω·cm]
25	61.88
110	78.75
300	101.3
500	144.0

Refractive indices of the $Ti(OiPr)_4$ and $Ti(OiPr)_2(AcAc)_2$ thin films prepared at room temperature, and annealed at 110 and 500 °C on ITO coated glass, were measured using ellipsometry (Figure S6). The measured spectral refractive indices were obtained in the range of 250−750 nm. At 633 nm, our films have a refractive index of 1.75, which is much lower than the value of anatase TiO_2 (2.55),[40] but more close to amorphous TiO_2 (2.03).[40] This is consistent with our Raman, XRD, and FT-IR results that indicate our film being amorphous TiO_x. The lower refractive indices also indicate that the $Ti(OiPr)_4$ thin films processed at room temperature may be a low density film with organic residues as shown by FT-IR. The refractive index of TiO_2 is known to correlate positively with annealing temperature and titanium oxide density.[41,42]

By employing the room-temperature processed TiO_x layer, we have fabricated and tested flexible perovskite solar cells using ITO-coated PEN substrates (Figure 3). The device architecture is shown in Figure 1a. The champion device

DOI: 10.1021/acs.jpclett.7b01466
J. Phys. Chem. Lett. 2017, 8, 3206−3210

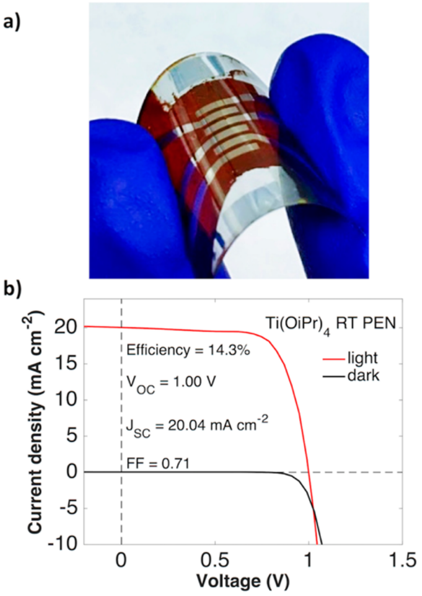

Figure 3. Flexible solar cell. (a) Picture of flexible perovskite solar cell with device architecture shown in Figure 1a. (b) J−V curves for device fabricated on ITO-coated PEN substrate with ETL fabricated using Ti(OiPr)$_4$ as precursor solution at 25 °C. Efficiency, V_{OC} (V), J_{SC} (mA cm^{-2}), and FF are shown in inset.

achieved 14.3% efficiency, with V_{OC} of 1.00 V, J_{SC} of 20.04 mA cm^{-2}, and FF of 0.71 (Figure 3b). This is close to the record for efficiency of a flexible solar cell based on MAPbI$_3$, 15% to 16%. The highest record efficiency so far by Wang et al. of 18% efficiency has been achieved with alloyed perovskites.[6] We emphasize that all of these previous record efficiency results have relied on either vacuum processing (ALD or sputter deposition) or colloidal nanoparticles, whereas our flexible solar cells are based on room-temperature and nonvacuum processing with a simple sol−gel precursor. To check for the stability of our flexible solar cells, we monitored the device performance over a time period in nitrogen glovebox storage and found that the device maintained ∼90% of its original efficiency after 2 weeks (Figure S7). We have also performed mechanical durability testing by bending the device with a radius of curvature of 5 mm (Figure S8). After 300 bending cycles, the device maintained ∼85% of its original efficiency. The decrease in efficiency was caused mainly by the reduced J_{SC} and increased series resistance.

In summary, we demonstrated room-temperature solution processing of amorphous TiO$_x$ thin film with high-performance TiO$_x$ ETL in MHP solar cells. We showed that the solar cell efficiency of cells with the TiO$_x$ film annealed at a temperature in the range of room temperature to 500 °C is similar, suggesting that thermal annealing at high temperature is not necessary to achieve high solar cell performance. Flexible MHP solar cells that employ the room temperature processed TiO$_x$ layer achieved a PCE of 14.3% and show promising stability and mechanical durability. Our work highlights the potential of flexible, lightweight, and high-efficiency MHP solar cells fabricated all through low-cost, high-throughput, and low thermal budget processing steps.

■ ASSOCIATED CONTENT

Supporting Information

The Supporting Information is available free of charge on the ACS Publications website at DOI: 10.1021/acs.jpclett.7b01466.

> Experimental details, SEM images for TiO$_x$ film, impact of humidity and temperature on performance of solar cells fabricated with TiO$_x$ film, spectral refractive indices, and stability of flexible solar cell (PDF)

■ AUTHOR INFORMATION

Corresponding Authors

*E-mail: jjc6z@virginia.edu (J.J.C.).
*E-mail: mgupta@virginia.edu (M.C.G.).

ORCID

Joshua J. Choi: 0000-0002-9013-6926

Author Contributions

‖These authors contributed equally.

Notes

The authors declare no competing financial interest.

■ ACKNOWLEDGMENTS

J.J.C. acknowledges support from an Early Career Faculty Award grant from NASA's Space Technology Research Grants Program (NNX15AU43G). M.C.G. acknowledges support from the NASA Langley Professor Program and IRAD.

■ REFERENCES

(1) NREL. Research Cell Record Efficiency Chart http://www.nrel.gov/ncpv/images/efficiency_chart.jpg (accessed June 10th, 2017).

(2) Di Giacomo, F.; Fakharuddin, A.; Jose, R.; Brown, T. M. Progress, challenges and perspectives in flexible perovskite solar cells. *Energy Environ. Sci.* **2016**, *9*, 3007−3035.

(3) Stranks, S. D.; Eperon, G. E.; Grancini, G.; Menelaou, C.; Alcocer, M. J. P.; Leijtens, T.; et al. Electron-hole diffusion lengths exceeding 1 micrometer in an organometal trihalide perovskite absorber. *Science* **2013**, *342*, 341−344.

(4) Mali, S. S.; Hong, C. K.; Inamdar, A. I.; Im, H.; Shim, S. E. Efficient planar n-i-p type heterojunction flexible perovskite solar cells with sputtered TiO$_2$ electron transporting layers. *Nanoscale* **2017**, *9*, 3095−3104.

(5) Heo, J. H.; Lee, M. H.; Han, H. J.; Patil, B. R.; Yu, J. S.; Im, S. H. Highly efficient low temperature solution processable planar type CH$_3$NH$_3$PbI$_3$ perovskite flexible solar cells. *J. Mater. Chem. A* **2016**, *4*, 1572−1578.

(6) Wang, C.; Zhao, D.; Yu, Y.; Shrestha, N.; Grice, C. R.; Liao, W.; Cimaroli, A. J.; Chen, J.; Ellingson, R. J.; Zhao, X.; et al. Compositional and morphological engineering of mixed cation perovskite films for highly efficient planar and flexible solar cells with reduced hysteresis. *Nano Energy* **2017**, *35*, 223−232.

(7) Wojciechowski, K.; Saliba, M.; Leijtens, T.; Abate, A.; Snaith, H. J. Sub-150 °C processed meso-superstructured perovskite solar cells with enhanced efficiency. *Energy Environ. Sci.* **2014**, *7*, 1142−1147.

(8) Yella, A.; Heiniger, L. P.; Gao, P.; Nazeeruddin, M. K.; Grätzel, M. Nanocrystalline rutile electron extraction layer enables low-temperature solution processed perovskite photovoltaics with 13.7% efficiency. *Nano Lett.* **2014**, *14*, 2591−6.

(9) Wang, J. T.-W.; Ball, J. M.; Barea, E. M.; Abate, A.; Alexander-Webber, J. A.; Huang, J.; Saliba, M.; Mora-Sero, I.; Bisquert, J.; Snaith, H. J.; et al. Low-temperature processed electron collection layers of graphene/TiO$_2$ nanocomposites in thin film perovskite solar cells. *Nano Lett.* **2014**, *14*, 724−730.

(10) Dkhissi, Y.; Huang, F.; Rubanov, S.; Xiao, M.; Bach, U.; Spiccia, L.; Caruso, R. A.; Cheng, Y.-B. Low temperature processing of flexible

planar perovskite solar cells with efficiency over 10%. *J. Power Sources* **2015**, *278*, 325−331.

(11) Das, S.; Gu, G.; Joshi, P. C.; Yang, B.; Aytug, T.; Rouleau, C. M.; Geohegan, D. B.; Xiao, K. Low thermal budget, photonic-cured compact TiO_2 layers for high-efficiency perovskite solar cells. *J. Mater. Chem. A* **2016**, *4*, 9685−9690.

(12) Liu, D.; Kelly, T. L. Perovskite solar cells with a planar heterojunction structure prepared using room-temperature solution processing techniques. *Nat. Photonics* **2014**, *8*, 133−138.

(13) Shin, S. S.; Yang, W. S.; Noh, J. H.; Suk, J. H.; Jeon, N. J.; Park, J. H.; Kim, J. S.; Seong, W. M.; Seok, S. I. High-performance flexible perovskite solar cells exploiting Zn_2SnO_4 prepared in solution below 100 degrees C. *Nat. Commun.* **2015**, *6*, 7410.

(14) Yang, D.; Yang, R.; Zhang, J.; Yang, Z.; Liu, S.; Li, C. High efficiency flexible perovskite solar cells using superior low temperature TiO_2. *Energy Environ. Sci.* **2015**, *8*, 3208−3214.

(15) Kogo, A.; Iwasaki, S.; Ikegami, M.; Miyasaka, T. An Ultrathin sputtered TiO_2 compact layer for mesoporous brookite-based plastic $CH_3NH_3PbI_{3-x}Cl_x$ solar cells. *Chem. Lett.* **2017**, *46*, 530−532.

(16) Huang, A.; Zhu, J.; Zhou, Y.; Yu, Y.; Liu, Y.; Yang, S.; Ji, S.; Lei, L.; Jin, P. One step spray-coated TiO_2 electron-transport layers for decent perovskite solar cells on large and flexible substrates. *Nanotechnology* **2017**, *28*, 01LT02.

(17) Zhou, P.; Li, W.; Li, T.; Bu, T.; Liu, X.; Li, J.; He, J.; Chen, R.; Li, K.; Zhao, J.; Huang, F. Ultrasonic spray-coating of large-scale TiO_2 compact layer for efficient flexible perovskite solar cells. *Micromachines* **2017**, *8*, 55.

(18) Qiu, W.; Paetzold, U. W.; Gehlhaar, R.; Smirnov, V.; Boyen, H.-G.; Tait, J. G.; Conings, B.; Zhang, W.; Nielsen, C. B.; McCulloch, I.; et al. An electron beam evaporated TiO_2 layer for high efficiency planar perovskite solar cells on flexible polyethylene terephthalate substrates. *J. Mater. Chem. A* **2015**, *3*, 22824−22829.

(19) Chandiran, A. K.; Yella, A.; Mayer, M. T.; Gao, P.; Nazeeruddin, M. K.; Grätzel, M. Sub-nanometer conformal TiO_2 blocking layer for high efficiency solid-state perovskite absorber solar cells. *Adv. Mater.* **2014**, *26*, 4309−12.

(20) Kim, B. J.; Kim, D. H.; Lee, Y.-Y.; Shin, H.-W.; Han, G. S.; Hong, J. S.; Mahmood, K.; Ahn, T. K.; Joo, Y.-C.; Hong, K. S.; et al. Highly efficient and bending durable perovskite solar cells: toward a wearable power source. *Energy Environ. Sci.* **2015**, *8*, 916−921.

(21) Chen, J.-Y.; Chueh, C.-C.; Zhu, Z.; Chen, W.-C.; Jen, A. K. Y. Low-temperature electrodeposited crystalline SnO_2 as an efficient electron-transporting layer for conventional perovskite solar cells. *Sol. Energy Mater. Sol. Cells* **2017**, *164*, 47−55.

(22) Zhang, J.; Juárez-Pérez, E. J.; Mora-Seró, I.; Viana, B.; Pauporté, T. Fast and low temperature growth of electron transport layers for efficient perovskite solar cells. *J. Mater. Chem. A* **2015**, *3*, 4909−4915.

(23) Danks, A. E.; Hall, S. R.; Schnepp, Z. The evolution of 'sol−gel' chemistry as a technique for materials synthesis. *Mater. Horiz.* **2016**, *3*, 91−112.

(24) Park, S. H.; Roy, A.; Beaupré, S.; Cho, S.; Coates, N.; Moon, J. S.; Moses, D.; Leclerc, M.; Lee, K.; Heeger, A. J. Bulk heterojunction solar cells with internal quantum efficiency approaching 100%. *Nat. Photonics* **2009**, *3*, 297−302.

(25) Nakamura, M.; Kato, S.; Aoki, T.; Sirghi, L.; Hatanaka, Y. Role of terminal OH groups on the electrical and hydrophilic properties of hydro-oxygenated amorphous TiO_x:OH thin films. *J. Appl. Phys.* **2001**, *90*, 3391−3395.

(26) Jeon, N. J.; Noh, J. H.; Yang, W. S.; Kim, Y. C.; Ryu, S.; Seo, J.; Seok, S. I. Compositional engineering of perovskite materials for high-performance solar cells. *Nature* **2015**, *517*, 476−80.

(27) Liu, M.; Johnston, M. B.; Snaith, H. J. Efficient planar heterojunction perovskite solar cells by vapour deposition. *Nature* **2013**, *501*, 395−8.

(28) Bi, D.; Tress, W.; Dar, M. I.; Gao, P.; Luo, J.; Renevier, C.; Schenk, K.; Abate, A.; Decoppet, J.-D.; Zakeeruddin, S. M.; et al. Efficient luminescent solar cells based on tailored mixed-cation perovskites. *Sci. Adv.* **2016**, *2*, e1501170.

(29) Sanchez, C.; Livage, J.; Henry, M.; Babonneau, F. Chemical modification of alkoxide precursors. *J. Non-Cryst. Solids* **1988**, *100*, 65−76.

(30) Caulton, K. G.; Hubert-Pfalzgraf, L. G. Synthesis, structural principles, and reactivity of heterometallic alkoxides. *Chem. Rev.* **1990**, *90*, 969−995.

(31) Duoss, E. B.; Twardowski, M.; Lewis, J. A. Sol-gel inks for direct-write assembly of functional oxides. *Adv. Mater.* **2007**, *19*, 3485−3489.

(32) Kim, J. Y.; Lee, K.; Coates, N. E.; Moses, D.; Nguyen, T.-Q.; Dante, M.; Heeger, A. J. Efficient tandem polymer solar cells fabricated by all-solution processing. *Science* **2007**, *317*, 222−225.

(33) Nakamura, M.; Korzec, D.; Aoki, T.; Engemann, J.; Hatanaka, Y. Characterization of TiO_x film prepared by plasma enhanced chemical vapor deposition using a multi-jet hollow cathode plasma source. *Appl. Surf. Sci.* **2001**, *175−176*, 697−702.

(34) Wang, Y.; Qin, Y.; Li, G.; Cui, Z.; Zhang, Z. One-step synthesis and optical properties of blue titanium suboxide nanoparticles. *J. Cryst. Growth* **2005**, *282*, 402−406.

(35) Kallala, M.; Sanchez, C.; Cabane, B. Structures of inorganic polymers in sol-gel processes based on titanium oxide. *Phys. Rev. E: Stat. Phys., Plasmas, Fluids, Relat. Interdiscip. Top.* **1993**, *48*, 3692−3704.

(36) Khatim, O.; Amamra, M.; Chhor, K.; Bell, A. M. T.; Novikov, D.; Vrel, D.; Kanaev, A. Amorphous−anatase phase transition in single immobilized TiO_2 nanoparticles. *Chem. Phys. Lett.* **2013**, *558*, 53−56.

(37) Ji, Y. Growth mechanism and photocatalytic performance of double-walled and bamboo-type TiO_2 nanotube arrays. *RSC Adv.* **2014**, *4*, 40474−40481.

(38) Ju, Y.; Wang, M.; Wang, Y.; Wang, S.; Fu, C. Electrical properties of amorphous titanium oxide thin films for bolometric application. *Adv. Condens. Matter Phys.* **2013**, *2013*, 365475.

(39) Su, H. X.; Peng, Z. J.; Fu, X. L. Composition, structure and electrical resistivity of TiO_x thin films deposited by RF magnetron sputtering at varied substrate temperatures. *Key Eng. Mater.* **2014**, *602−603*, 1039−1042.

(40) Loper, P.; Stuckelberger, M.; Niesen, B.; Werner, J.; Filipic, M.; Moon, S. J.; Yum, J. H.; Topic, M.; De Wolf, S.; Ballif, C. Complex fefractive index spectra of $CH_3NH_3PbI_3$ perovskite thin films determined by spectroscopic ellipsometry and spectrophotometry. *J. Phys. Chem. Lett.* **2015**, *6*, 66−71.

(41) Ayieko, C. O.; Musembi, R. J.; Waita, S. M.; Aduda, B. O.; Jain, P. K. Structural and optical characterization of nitrogen-doped TiO_2 thin films deposited by spray pyrolysis on fluorine doped tin oxide (FTO) coated glass slides. *International Journal of Energy and Engineering* **2012**, *2*, 67−72.

(42) Mergel, D.; Buschendorf, D.; Eggert, D.; Grammes, R.; Samset, B. Density and refractive index of TiO_2 films prepared by reactive evaporation. *Thin Solid Films* **2000**, *371*, 218−224.

ACS APPLIED MATERIALS & INTERFACES

Research Article

Cite This: ACS Appl. Mater. Interfaces 2018, 10, 41312−41317

www.acsami.org

Laser Annealing of TiO_2 Electron-Transporting Layer in Perovskite Solar Cells

George C. Wilkes,[†] Xiaoyu Deng,[‡] Joshua J. Choi,[‡] and Mool C. Gupta*,[†]

[†]Department of Electrical and Computer Engineering and [‡]Department of Chemical Engineering, University of Virginia, Charlottesville, Virginia 22904, United States

Supporting Information

ABSTRACT: Solution-processed TiO_2 and other metal-oxide electron-transporting layers (ETLs) for perovskite solar cells commonly require high-temperature annealing (>450 °C), causing the underlying indium-tin oxide (ITO) to degrade and inhibiting the use of flexible plastic substrates, such as poly(ethylene naphthalate). Laser-based solar cell manufacturing is attracting increased interest and can enable rapid and low-temperature fabrication of perovskite solar cells. By using novel pulsed ultraviolet laser processing on the solution-processed TiO_2, we demonstrate a champion 17.1% efficient flexible perovskite solar cell. We can independently control the annealing of the ETL without affecting the underlying ITO or substrate due to the shallow absorption depth and short pulse duration of the laser. Ellipsometry and X-ray photoelectron spectroscopy verify that the laser-annealed TiO_2 thin film is stoichiometric and relatively denser than the thermally annealed control sample. The efficiencies of the laser-processed devices exceeded those fabricated via hot plate, but with the added benefit of a high-throughput, low-temperature, and flexible-substrate-friendly process.

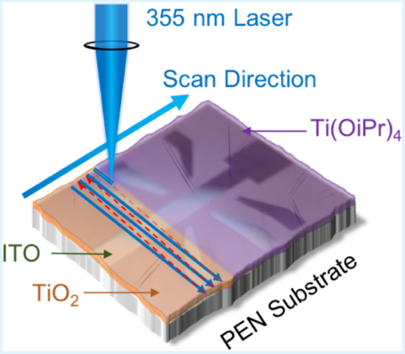

KEYWORDS: *perovskites, solar cells, TiO_2, laser processing, flexible, electron-transporting layer*

1. INTRODUCTION

Perovskite solar cells are the fastest-developing photovoltaic technology in the industry. Rising from a 3.4% efficiency at their inception in 2009, single-junction perovskite solar cells have recently reached a power conversion efficiency of 22.7%.[1] A variety of relatively low-cost methods exist to fabricate perovskite solar cells, which will culminate in their competitive commercialization with traditional photovoltaics. Perovskite solar cells depend on an electron-transporting layer (ETL), which is necessary to prevent charge recombination at the indium-tin oxide (ITO) and perovskite interface by introducing a layer with favorable energy levels that enable efficient electron extraction while simultaneously preventing hole transport. Without an ETL, perovskite device efficiencies are limited to 14%.[2]

TiO_2 is the most-employed inorganic ETL material, with numerous synthesis and deposition methods, and some of the most highly efficient architectures built on top of it. Although other materials like SnO_2 and ZnO have been investigated as alternative metal-oxide ETLs, they have issues with hysteresis and chemical instability, respectively, as well as large conduction band maximum mismatches of ∼0.6 and ∼0.3 eV, respectively, which can cause electron injection offsets.[3] TiO_2 has an excellent band gap with only a ∼0.2 eV conduction band maximum mismatch with perovskite, highly stable electronic properties, high optical transmittance, high durability, and ultra-thin uniformity and homogeneity which enables high-performance perovskite solar cells.[3]

Unfortunately, the majority of high-efficiency perovskite solar cells utilize a TiO_2 ETL that requires high-temperature (>450 °C) annealing. Not only does this hinder scalability and throughput because of the increased thermal budget of the solar cell processing, but it also limits the available substrates that perovskite devices can use, namely flexible transparent plastics and ITO-coated glass. Despite ITO's low surface roughness which makes it an ideal candidate for subsequent layer deposition, high-temperature (>300 °C) annealing negatively affects electrical conductivity. When annealing ITO in air at temperatures of 500 °C, the sheet resistance can increase by 500% due to a filling of oxygen vacancies and consequent decrease in current carrier density.[4,5] A doubling in sheet resistance can negatively impact the normalized power conversion efficiency of the finished device by as much as ∼20%. Fortunately, laser annealing of ITO can decrease the surface roughness and slightly decrease the sheet resistance of high-melting temperature oxides on low-melting temperature substrates.[6]

Since perovskite films are typically grown and annealed at low temperatures (<150 °C), there is considerable interest in developing perovskite solar cell fabrication techniques that are compatible with flexible substrates such as poly(ethylene terephthalate) (PET) and poly(ethylene naphthalate) (PEN).

Received: August 10, 2018
Accepted: November 13, 2018
Published: November 13, 2018

DOI: 10.1021/acsami.8b13740
ACS Appl. Mater. Interfaces 2018, 10, 41312−41317

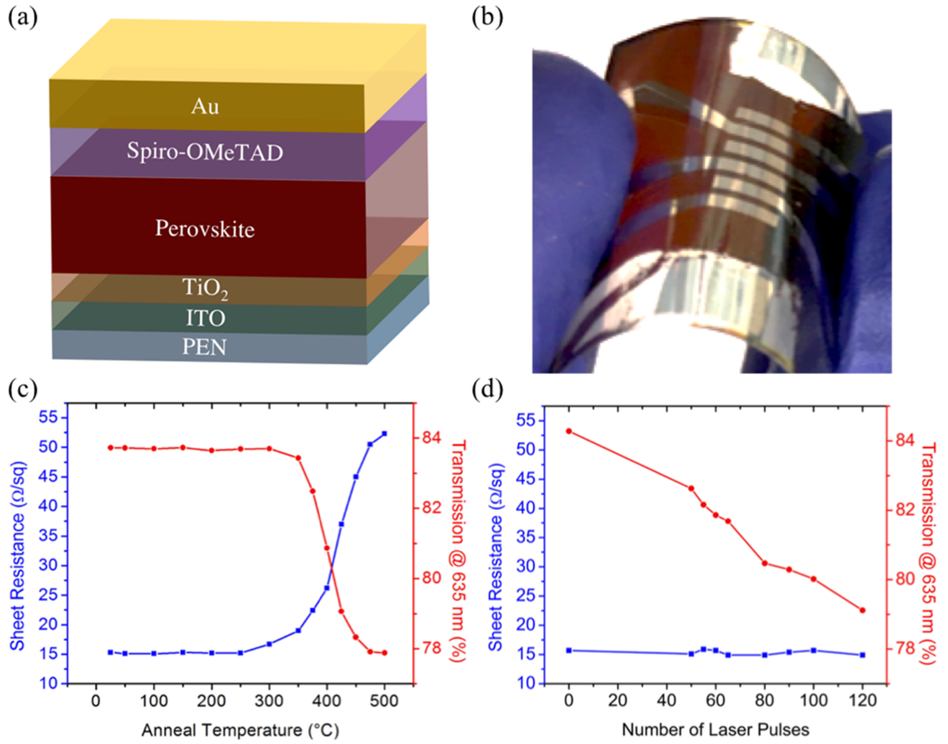

Figure 1. (a) Perovskite solar cell structure and (b) a photo of the flexible perovskite solar cell. (c) Effect of annealing temperature and (d) number of laser pulses on the sheet resistance and light transmission at a wavelength of 635 nm for TiO_2 films on ITO-coated glass (TiO_2 + ITO + glass).

These substrates are low cost and enable perovskite solar cells to be lightweight, flexible, and roll-to-roll processable.[7] Flexible substrates make perovskite solar cell manufacturing attractive by decreasing the weight while increasing the production throughput and volume, reducing overall manufacturing cost.[8] They also make the market for perovskite solar cells more attractive by enabling high power per gram ratios, flexibility, storability, and low weight all at a lower cost than traditional photovoltaics (PV) and even current flexible thin-film PV. Previously used techniques to deposit low-temperature electron transport layers consist of vacuum deposition techniques[9] or nanoparticle processing,[10] which can lower manufacturing throughput while drastically increasing manufacturing cost. Thus, to develop commercially viable and efficient low-temperature-processed ETLs, vacuum-free, nanoparticle-free techniques are needed.

Laser-based processing opens a window of opportunity for low-temperature solar cell manufacturing and has garnered enormous interest in recent years.[11−14] Lasers allow for superior processing control by replacing furnaces with a rapid process that independently controls the application of heat to localized regions. Ultraviolet (355 nm), pulsed-laser processing enables us to control the annealing of the ETL without affecting the underlying ITO or substrate, due to the shallow absorption depth (~100 nm) and ultrashort pulse duration (25 ns). This allows us to use a common and robust sol−gel titanium diisopropoxide bis(acetylacetonate), from here on referred to as $Ti(OiPr)_2(AcAc)_2$, in butanol, which generates high power conversion efficiencies of 15−18% on flexible substrates without any of the damaging effects normally found from high-temperature (>450 °C) thermal processing.

In this work, we introduce the novel laser annealing method for hydrolysis and densification of sol−gel TiO_2 films on glass ITO substrates, which can result in a stable ITO sheet resistance and a champion 17.1% efficient perovskite solar cell, with slightly enhanced performance over its 16.6% efficient, hot plate-annealed TiO_2 counterpart. We verify the laser-annealed TiO_2 structure and composition via vis−NIR spectrometry, variable angle spectroscopic ellipsometry (VASE), and X-ray photoelectron spectroscopy (XPS) while demonstrating its performance with four-point probe measurements and illuminated current−voltage scans of completed devices. We show that film hydrolysis, condensation reactions, removal of moisture, removal of hydroxyl groups, and Ti−O−Ti linkages occur within tens of nanoseconds, on the order of the laser pulse width. Future efforts can utilize this process for other metal-oxide ETLs, which require high-temperature processing and further optimization of ITO/TiO_2 devices for increased power conversion efficiency.

2. RESULTS

2.1. ITO Investigation. The thickness and surface roughness of the ITO films on glass, commercially prepared by KINTEC Company, were 919.2 ± 0.4 and 24.1 ± 0.4 Å, respectively, using spectroscopic ellipsometry. A scanning electron microscopy (SEM) investigation of the ITO topography has good visual qualitative agreement with the ellipsometric surface roughness measurement. The patterned ITO has a sheet resistance of 19 Ω/sq, which rose to 90.2 Ω/sq after annealing at 500 °C for 5 min on a hot plate. Additionally, the ITO has an optical band gap of 3.55 eV, which dropped to 3.29 eV after the hot plate annealing due to film degradation.

2.2. Laser Parameter Optimization. We investigated the effect of 355 nm wavelength, ultraviolet laser raster scanning on ITO sheet resistance and TiO_2 thin-film annealing for

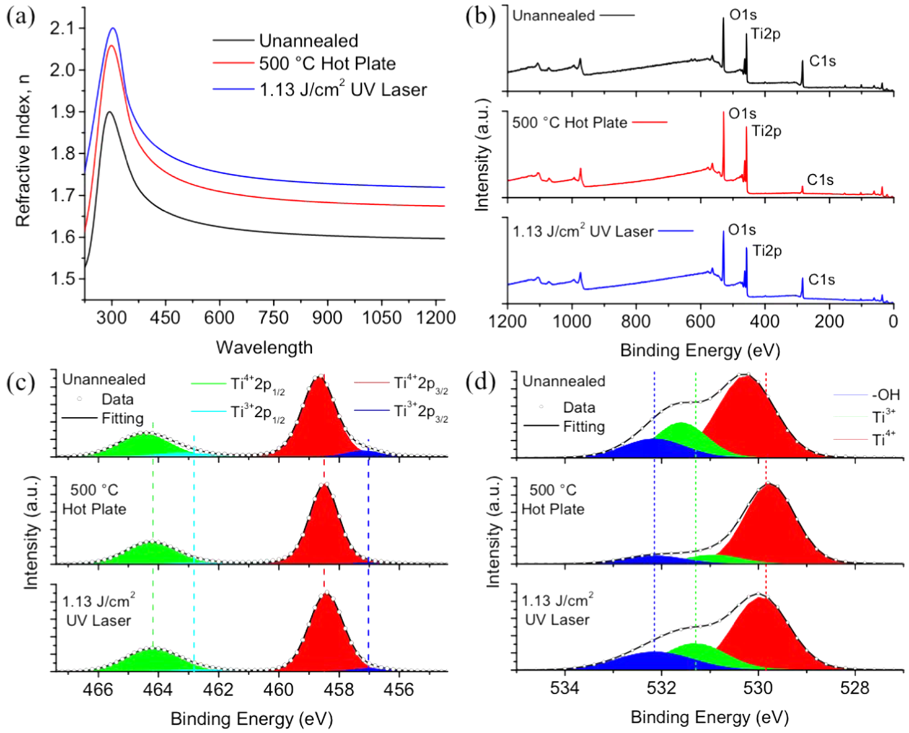

Figure 2. (a) Spectral refractive index, (b) XPS survey spectra and high-resolution XPS spectra of the (c) Ti 2p and (d) O 1s peaks of unannealed, 500 °C thermally annealed, and 1.13 J/cm^2 laser-annealed TiO_2.

perovskite solar cells. Perovskite solar cell devices consisting of glass or PEN/ITO/TiO_2/perovskite/Spiro-OMeTAD/Ag or Au were fabricated and tested in the dark and under illumination with different laser scan and raster characteristics for the TiO_2 layer. Figure 1a,b shows a schematic of the device structure and a picture of the flexible perovskite device, respectively. All devices had an area of 0.03 cm^2 defined by the overlap between the bottom and top contacts. For the 355 nm UV laser, with a 25 ns pulse width, Gaussian beam profile, and a ~20 μm focused spot diameter (determined via the heat-affected zone from a single laser pulse), we found that the film became uniformly annealed with a spot overlap at 25% (or a 15 μm spacing between pulses) using a scan speed of 750 mm/s at a laser repetition rate of 50 kHz. The raster line spacing is identical to the spot overlap (15 μm) for two-dimensional consistency. The laser fluence was chosen to be 1.13 J/cm^2 because it is capable of rapid film conversion and compatible with both flexible and glass substrates without damaging them. At this fluence, the laser has no impact on the ITO's sheet resistance or optical band gap and is compatible with flexible substrates due to its short pulse and shallow absorption depth.

2.3. Effect of Thermal and Laser Annealing on Resistivity and Optical Transmittance. TiO_2 films were prepared on top of the ITO substrates via either 500 °C thermal annealing or pulsed UV laser processing of a spin-coated $Ti(OiPr)_2(AcAc)_2$ in butanol precursor solution, which is the most commonly employed TiO_2 precursor.[9,15] A topographical SEM investigation of the hot plate-annealed TiO_2 and laser-annealed TiO_2 films shows that both films are smooth and uniform. The hot plate-treated films were annealed at various temperatures from 25 to 500 °C for 1 min, and the sheet resistance and optical transmission spectra were measured. Similarly, films were raster-scanned via laser with a varying number of pulses from 50 to 120, and the sheet resistance and optical transmission spectra were measured via four-point probe and vis−NIR spectrometry, respectively. Figure 1 shows a summary of these results for a transmission spectral wavelength of 635 nm. Although the thermally processed films showed a large increase in the sheet resistance and a drop in the visible transmission at high temperatures, the laser-processed film showed a similar shift in the visible spectra without any increase in the sheet resistance. Morphological changes in the film due to phase transition to crystalline TiO_2 and crystalline grain boundary improvement from annealing contribute to a change in the photon mean free path due to increased light scattering at the grain boundaries causing a slight decrease in the visible transparency.[16,17] The gradual changes for the thermally annealed films are attributed to the kinetics of the 5 min annealed increments at each given temperature, which would likely be steeper for longer anneal times.

2.4. Film Characterization. TiO_2 films were prepared via laser annealing and thermal annealing and characterized using VASE and XPS to better understand their structure and composition. A summary of the data is in Figure 2. TiO_2 films have a refractive index peak around 300 nm between 2.0 and 3.3 and a band gap between 3.2 and 3.6 eV, which correlates positively with film phase[18] and density.[19,20] Voids in the film have refractive indices near 1.0 and decrease the overall refractive index of the film, indicating that denser films with fewer voids will have higher index. Our unannealed films have a band gap of 3.35 eV and a peak refractive index of 1.9, which increases to E_g = 3.51 eV and n_{peak} = 2.05 after thermal annealing at 500 °C for 5 min, demonstrating an increase in film density and transition to crystalline phase. After laser processing of unannealed films, the band gap increases to 3.56

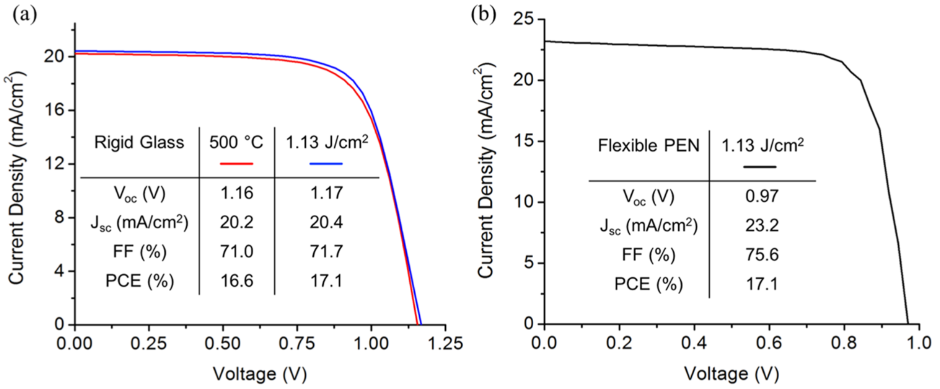

Figure 3. Current−voltage curve and corresponding parameters for the (a) rigid champion laser-processed device, its reference 500 °C thermally annealed champion device and (b) laser-processed flexible device and device statistics for other flexible devices.

eV and our refractive index peak increases to 2.1, suggesting that laser processing has improved film density and equivalent phase. Our film thicknesses were measured to be 45, 24, and 27 nm for the unannealed, hot plate-annealed, and laser-annealed samples via ellipsometry, respectively.

XPS survey spectra for unannealed, hot plate-annealed, and laser-annealed samples, shown in Figure 2b, reveal peaks for O 1s, Ti 2p, and C 1s consistent with results in the literature for Ti(OiPr)$_2$(AcAc)$_2$ films fabricated via thermal annealing.[21,22] Figure 2c,d shows high-resolution XPS spectra for the Ti 2p peaks and O 1s peaks, respectively. Between the laser-annealed TiO$_2$ and the 500 °C thermally annealed TiO$_2$, the Ti 2p$_{3/2}$ and Ti 2p$_{1/2}$ peaks (458.4 and 464.3 eV, respectively) are well aligned with each other and match values found in the literature.[22,23] The unannealed Ti 2p peaks have a higher binding energy than films that have been thermal or laser annealed, due to their structural difference from the annealed forms. The Ti^{4+} 2p peaks correspond predominantly with stoichiometric TiO$_2$. Additionally, since the Ti^{4+} 2p$_{3/2}$ values are all within the 458.4−459.3 eV range and the Ti^{3+} peak intensity reduces with both thermal and laser annealing, we can conclude that our layer is stoichiometric TiO$_2$ and not TiO (455 eV) or TiO$_x$.[24] The Ti^{4+}−O 1s peaks (Figure 2d) correspond with the Ti^{4+} 2p peaks and indicate stoichiometric TiO$_2$. The O 1s peaks (Ti^{4+}, Ti^{3+}, and −OH) show a shift in binding energy between the unannealed and annealed conditions, which arises from their decreased oxidation states from annealing. For instance, the Ti^{4+} O 1s peaks for anatase and sol−gel derived TiO$_2$ are at 529.85[25] and 530.6 eV,[26] respectively. From this we infer that our unannealed Ti^{4+} O 1s peaks match well with sol−gel TiO$_2$, whereas our laser- and hot plate-annealed Ti^{4+} peaks match with anatase TiO$_2$. Residual organic compounds and hydroxyl groups contribute to the other observed O 1s peaks. However, presence of these species does not impact subsequent device performance.[8] Hydrolysis of the precursor film and Ti−O−Ti linkage formation occurs on the order of the 25 ns laser pulse, demonstrating nanosecond formation of TiO$_2$ films.

2.5. Device Performance. Devices were fabricated and tested using TiO$_2$ films that were processed with varying laser processing conditions, which include the number of pulses per area, the number of repeated raster scans, and the amount of adjacent line overlap. Reference devices utilized TiO$_2$ films processed on a hot plate at 500 °C. On top of the TiO$_2$ films, a two-step mixed-halide alloyed perovskite (FA$_{0.85}$MA$_{0.15}$PbI$_{2.55}$Br$_{0.45}$) layer, a 2,2′,7,7′-tetrakis(*N*,*N*-di-*p*-methoxyphenylamine)-9,9′-spiro bifluorine (Spiro-OMeTAD) layer (100 nm), and a gold anode layer (60 nm) were deposited. These layers are described in detail within the experimental section. The champion 1.13 J/cm^2-fluence UV laser-processed device and its thermally annealed reference device's current−voltage curve and parameters are shown in Figure 3.

An additional advantage of our low-temperature UV laser processing is that it can be used on flexible ITO-coated PEN substrates to create flexible perovskite solar cells with the rest of the structure the same as stated above without any degradation to the underlying substrate or ITO. The 500 °C high-temperature annealing, normally required for the Ti(OiPr)$_2$(AcAc)$_2$ solution to form TiO$_2$, is incompatible with PEN and PET substrates, as temperatures that high will melt and degrade PEN and PET. The champion flexible device achieved an efficiency of 17.1%, with a V_{oc} of 0.97 V, J_{sc} of 23.2 mA/cm^2, and fill factor of 75.6% (Figure 3b). Parameters for devices fabricated on flexible substrates were also very consistent, demonstrating the uniformity achieved by sol−gel laser processing on flexible substrates.

3. CONCLUSIONS

For the first time, we have demonstrated the novel laser processing concept for the TiO$_2$ ETL for fabricating high-performance perovskite solar cells. By utilizing laser processing, we can obtain a 17.1% device power conversion efficiency on rigid and flexible substrates. We demonstrate that device parameters and composition of the laser-processed TiO$_2$ are similar to those of 500 °C thermally annealed TiO$_2$, suggesting that we can utilize our laser processing technique to replace the high-temperature thermal annealing normally required for TiO$_2$ ETLs. As an added benefit, our laser processing technique is compatible with flexible PEN substrates, which cannot withstand 500 °C thermal annealing. We demonstrate that our laser processing does not impact the sheet resistance of the ITO, while still achieving the same effect as thermal annealing. These results indicate that a dense, uniform, crystalline, stoichiometric, and conductive TiO$_2$ thin film can be formed in hundreds of nanoseconds in standard atmosphere via pulsed-laser annealing without the need for sustained 500 °C thermal annealing. Our work opens the door for high-throughput and low-temperature laser processing in high-performance perovskite solar cells and has the potential to bring the efficiencies of flexible and rigid perovskite devices toward parity.

4. EXPERIMENTAL SECTION

4.1. TiO_2 Film. Compact TiO_2 thin films were fabricated by spin-coating a solution of 146.6 μL $Ti(OiPr)_2(AcAc)_2$ in 2 mL of butanol for 40 s at 4000 rpm. Hot plate-processed devices were annealed at 500 °C for 5 min on a hot plate. Laser-processed devices were raster-scanned with a Coherent (Matrix 355-8-50), 355 nm wavelength ultraviolet laser using a mirrored XY-galvanometer to control the beam direction and speed. The laser has a ~20 μm focused spot size and was systematically optimized to a pulse duration of 25 ns, a repetition rate of 50 kHz, a scan speed of 750 mm/s, a line spacing of 15 μm (25%), and a fluence of 1.13 J/cm^2.

4.2. Solar Cell Fabrication. The patterned ITO glass and PEN substrates were cleaned sequentially in Hellmanex III detergent for 10 min, deionized water for 5 min, and ethanol for 5 min in an ultrasonic cleaner and cleaned with an ultraviolet ozone plasma cleaner for 10 min. The patterned ITO glass and PEN substrates (25.4 mm^2 in area) were purchased from KINTEC Company. Scotch tape was used to cover the end of the ITO contact to protect it from being coated during spin-coating. After the TiO_2 films were deposited using the above methods, $FA_{0.85}MA_{0.15}PbI_{2.55}Br_{0.45}$ perovskite was deposited using a method developed by Saliba et al.[27] A $FA_{0.85}MA_{0.15}PbI_{2.55}Br_{0.45}$ solution (1.8 M) was prepared by mixing PbI_2 (99.9985%, Alfa Aesar), PbBr (TCI), MABr (Greatcell Solar), and FAI (Greatcell Solar) with 0.425, 0.075, 0.075, and 0.425 part ratios and adding a 1-to-4 ratio of dimethyl sulfoxide (Sigma-Aldrich) and dimethylformamide (Sigma-Aldrich), stirring at 60 °C for 2 h, and filtering the solution with a 0.45 μm filter. Utilizing the timing-dependent deposition method, the $FA_{0.85}MA_{0.15}PbI_{2.55}Br_{0.45}$ solution was statically dispensed onto the substrate, and then the substrate was spun in a two-step program: spun at 1000 rpm for 10 s and 6000 rpm for 30 s. During the second step, the substrate was dynamically solvent-washed with anhydrous chlorobenzene (Sigma-Aldrich) for 20 s prior to the end of the program, and then the perovskite was annealed at 150 °C for 15 min.[27] Spiro-OMeTAD (Luminescence Technology Corp.) was prepared with anhydrous chlorobenzene in a 72 mg/mL concentration and doped with 28.8 μL of 4-*tert*-butylpuridine (anhydrous, Sigma-Aldrich) and 17.5 μL of a solution of lithium-bis(trifluoromethane)sulfonamide (Li-TFSI, 99.95%, Sigma-Aldrich) in acetonitrile (anhydrous, Sigma-Aldrich) and left to dissolve. The Spiro-OMeTAD solution was spin-coated at 4000 rpm for 30 s in a nitrogen-filled glovebox and left to oxidize in a humidity-controlled dry air box overnight with 10 min of 50% humidity exposure. The rear contact was deposited by evaporating silver (Ag) or gold (Au) evaporation pellet (Kurt J. Lesker, 99.999%) via thermal evaporation for a 60−70 nm layer of silver or gold at a vacuum of 1×10^{-6} mbar.

4.3. Solar Cell Characterization. The devices were tested under reference cell (PVM551, 8 mm Si KG5 Window from PV Measurements)-calibrated AM 1.5 illumination from a solar simulator (PV measurements) using a Keithley source meter operating at a reverse scan direction at a rate of 1 V/s. Additionally, an optical mask was used to limit exposure to the 3 mm^2 active device area.

4.4. XPS. Survey spectra were captured with a 100 μm spot, 15 kV accelerating voltage, and a 224 eV pass energy, whereas the high-resolution spectra were captured at a 55 eV pass energy. The chamber was at ultrahigh vacuum pressure of 6×10^{-8} Pa, and the XPS utilized a monochromated Al Kα as the excitation source (PHI VersaProbe III). Peak fitting was done using MultiPak software using the Gauss−Lorentz fitting with all peaks shifted so that the C 1s peak was located at 484.80 eV binding energy.

4.5. SEM. Topographical SEM images were captured in secondary electron mode at an accelerating voltage between 3 and 5 kV, with a 5.0 spot, the Everhart−Thornley Detector, and a horizontal field width between 6 and 12 μm (FEI Quanta 650).

4.6. Electrical Resistivity. A four-point probe with a linear 1.00 mm probe spacing and a 25 μm tip radius was used to verify sheet resistances of the ITO-coated glass substrates before and after laser and thermal treatments (Jandel Multiposition Probe).

4.7. Vis−NIR. Spectra of the laser and thermally processed TiO_2 films on ITO glass were taken with a Cary 5E spectrophotometer in a wavelength range of 300−3300 nm with a 1 nm resolution.

4.8. Ellipsometry. The ITO and TiO_2 films on glass were measured with a J. A. Woollam M2000 spectroscopic ellipsometer in a wavelength range between 250 and 1700 nm at a 50, 60, 70, 75, 80, and 85° angle of incidence. Fitting was done using CompleteEASE software from J. A. Woollam. For the ITO, the Kramers−Kronig consistent general oscillator model was used to fit the measured psi and delta values. The TiO_2 films used the Tauc−Lorentz dispersion model to fit the measured psi and delta values and provide the optical band gap values. Modeled film thicknesses were 45, 24, and 27 nm for the unannealed, hot plate-annealed, and laser-annealed samples.

4.9. X-ray Diffraction. Bragg−Brentano and grazing-incidence X-ray diffraction were conducted with a PANalytical X'Pert Series 2 for unannealed, hot plate-annealed, and laser-annealed films on ITO-coated glass (TiO_2 + ITO + glass). This data can be found in Figure S4.

■ ASSOCIATED CONTENT

Ⓢ Supporting Information

The Supporting Information is available free of charge on the ACS Publications website at DOI: 10.1021/acsami.8b13740.

> Laser fluence and shot spacing optimization for glass and PEN substrates; SEM images of TiO_2 film before annealing, after hot plate annealing, and after laser annealing; X-ray diffraction data, device histograms, and statistics; device hysteresis; and laser setup schematic (PDF)

■ AUTHOR INFORMATION

Corresponding Author

*E-mail: mgupta@virginia.edu.

ORCID

George C. Wilkes: 0000-0001-9450-6253
Joshua J. Choi: 0000-0002-9013-6926
Mool C. Gupta: 0000-0002-1782-5354

Notes

The authors declare no competing financial interest.

■ ACKNOWLEDGMENTS

M.C.G. acknowledges support from the NASA Langley Professor Program and the NSF I/UCRC Center. J.J.C. acknowledges support from an Early Career Faculty Award grant from NASA's Space Technology Research Grants Program (NNX15AU43G). The authors thank Shelby Fields for assistance with X-ray diffraction measurements.

■ REFERENCES

(1) NREL. https://www.nrel.gov/pv/assets/images/efficiency-chart.png, 2018.

(2) Ke, W.; Fang, G.; Wan, J.; Tao, H.; Liu, Q.; Xiong, L.; Qin, P.; Wang, J.; Lei, H.; Yang, G.; Qin, M.; Zhao, X.; Yan, Y. Efficient Hole-Blocking Layer-Free Planar Halide Perovskite Thin-Film Solar Cells. *Nat. Commun.* **2015**, *6*, No. 6700.

(3) Yang, G.; Tao, H.; Qin, P.; Ke, W.; Fang, G. Recent Progress in Electron Transport Layers for Efficient Perovskite Solar Cells. *J. Mater. Chem. A* **2016**, *4*, 3970−3990.

(4) Li, F.; Chen, C.; Tan, F.; Li, C.; Yue, G.; Shen, L.; Zhang, W. Semitransparent Inverted Polymer Solar Cells Employing a Sol-Gel-Derived TiO_2 Electron-Selective Layer on FTO and MoO_3/Ag/MoO_3 Transparent Electrode. *Nanoscale Res. Lett.* **2014**, *9*, No. 579.

(5) Tariq Bhatti, M.; Rana, A. M.; Khan, A. F.; Ansari, M. I. Effect of Annealing on Electrical Properties of Indium Tin Oxide. *J. Appl. Sci.* **2002**, *2*, 570−573.
(6) Chen, M.; Lin, K.; Ho, Y. Laser Annealing Process of ITO Thin Films Using Beam Shaping Technology. *Opt. Lasers Eng.* **2012**, *50*, 491−495.
(7) Di Giacomo, F.; Fakharuddin, A.; Jose, R.; Brown, T. M. Progress, Challenges and Perspectives in Flexible Perovskite Solar Cells. *Energy Environ. Sci.* **2016**, *9*, 3007−3035.
(8) Deng, X.; Wilkes, G. C.; Chen, A. Z.; Prasad, N. S.; Gupta, M. C.; Choi, J. J. Room-Temperature Processing of TiO_x Electron Transporting Layer for Perovskite Solar Cells. *J. Phys. Chem. Lett.* **2017**, *8*, 3206−3210.
(9) Wojciechowski, K.; Saliba, M.; Leijtens, T.; Abate, A.; Snaith, H. J. Sub-150 °C Processed Meso-Superstructured Perovskite Solar Cells with Enhanced Efficiency. *Energy Environ. Sci.* **2014**, *7*, 1142−1147.
(10) Chandiran, A. K.; Yella, A.; Mayer, M. T.; Gao, P.; Nazeeruddin, M. K.; Grätzel, M. Sub-Nanometer Conformal TiO_2 Blocking Layer for High Efficiency Solid-State Perovskite Absorber Solar Cells. *Adv. Mater.* **2014**, *26*, 4309−4312.
(11) Gupta, M. C.; Carlson, D. E. Laser Processing of Materials for Renewable Energy Applications. *MRS Energy Sustainability* **2015**, *2*, No. 1101.
(12) Hsu, L. S.; Solanki, R.; Collins, G. J.; She, C. Y. Raman Study of Structural Transformations of Titania Coatings Induced by Laser Annealing. *Appl. Phys. Lett.* **1984**, *45*, No. 1065.
(13) Mincuzzi, G.; Palma, A. L.; Di Carlo, A.; Brown, T. M. Laser Processing in the Manufacture of Dye-Sensitized and Perovskite Solar Cell Technologies. *ChemElectroChem* **2016**, *3*, 9.
(14) Palneedi, H.; Park, J. H.; Maurya, D.; Peddigari, M.; Hwang, G.-T.; Annapureddy, V.; Kim, J.-W.; Choi, J.-J.; Hahn, B.-D.; Priya, S.; Lee, K. J.; Ryu, J. Laser Irradiation of Metal Oxide Films and Nanostructures: Applications and Advances. *Adv. Mater.* **2018**, *30*, No. e1705148.
(15) Jeon, N. J.; Noh, J. H.; Yang, W. S.; Kim, Y. C.; Ryu, S.; Seo, J.; Seok, S. I. Compositional Engineering of Perovskite Materials for High-Performance Solar Cells. *Nature* **2015**, *517*, 476−480.
(16) Nakaruk, A.; Perera, D. S.; Sorrel, C. C. Anatase-Rutile Transformation Through High-Temperature Annealing of Titania Films Produced by Ultrasonic Spray Pyrolysis. *Thin Solid Films* **2010**, *518*, 3735−3742.
(17) Nair, P. B.; Justinvictor, V. B.; Daniel, G. P.; Joy, K.; Raju, K. C. J.; Kumar, D. D.; Thomas, P. V. Optical Parameters Induced by Phase Transformation in RF Magnetron Sputtered TiO_2 Nanostructured Thin Films. *Prog. Nat. Sci.: Mater. Int.* **2014**, *24*, 218−225.
(18) Bendavid, A.; Martin, P. J. Review of Thin Film Materials Deposition by the Filtered Cathodic Vacuum Arc Process at CSIRO. *J. Aust. Ceram. Soc.* **2014**, *50*, 86−101.
(19) Pradana, A.; Kluge, C.; Gerken, M. Tailoring the Refractive Index of Nanoimprint Resist by Blending with TiO_2 Nanoparticles. *Opt. Mater. Express* **2014**, *4*, 329−337.
(20) Schmiedova, V.; Dzik, P.; Vesely, M.; Zmeskal, O.; Morozova, M.; Kluson, P. Optical Properties of Titania Coatings Prepared by Inkjet Direct Patterning of Reverse Micelles Sol-Gel Composition. *Molecules* **2015**, *20*, 14552−14564.
(21) Giordano, F.; Abate, A.; Baena, J. P. C.; Saliba, M.; Matsui, T.; Im, S. H.; Zakeeruddin, S. M.; Nazeeruddin, M. K.; Hagfeldt, A.; Graetzel, M. Enhanced Electronic Properties in Mesoporous TiO_2 via Lithium Doping for High-Efficiency Perovskite Solar Cells. *Nat. Commun.* **2016**, *7*, No. 10379.
(22) Liu, Z.; Chen, Q.; Hong, Z.; Zhou, H.; Xu, X.; De Marco, N.; Sun, P.; Zhao, Z.; Cheng, Y.; Yang, Y. Low-Temperature TiO_x Compact Layer for Planar Heterojunction Perovskite Solar Cells. *ACS Appl. Mater. Interfaces* **2016**, *8*, 11076−11083.
(23) Blasco, T.; Camblor, M. A.; Corma, A.; Perez-Pariente, J. The State of Ti in Titanoaluminosilicates Isomorphous with Zeolite β. *J. Am. Chem. Soc.* **1993**, *115*, 11806−11813.
(24) Moulder, J. F.; Stickle, W. F.; Sobol, P. E.; Bomben, K. D. *Handbook of X-Ray Photoelectron Spectroscopy, a Reference Book of Standard Spectra for Identification and Interpretation of XPS Data*; Physical Electronics Division, Perkin-Elmer Corp., 1992.
(25) Sanjinés, R.; Tang, H.; Berger, H.; Gozzo, F.; Margaritondo, G.; Lévy, F. Electronic Structure of Anatase TiO_2 Oxide. *J. Appl. Phys.* **1994**, *75*, 2945−2951.
(26) Ingo, G. M.; Dirè, S.; Babonneau, F. XPS Studies of SiO_2-TiO_2 Powders Prepared by Sol-Gel Process. *Appl. Surf. Sci.* **1993**, *70−71*, 230−234.
(27) Saliba, M.; Matsui, T.; Seo, J.; Domanski, K.; Correa-Baena, J.; Nazeeruddin, M. K.; Zakeeruddin, S. M.; Tress, W.; Abate, A.; Hagfeldt, A.; Grätzel, M. Cesium-Containing Triple Cation Perovskite Solar Cells: Improved Stability, Reproducibility and High Efficiency. *Energy Environ. Sci.* **2016**, *9*, 1989−1997.

Applied Surface Science 480 (2019) 35–42

Contents lists available at ScienceDirect

Applied Surface Science

journal homepage: www.elsevier.com/locate/apsusc

Full length article

Low-temperature laser generated ultrathin aluminum oxide layers for effective c-Si surface passivation

Peixun Fan, Zeming Sun, George C. Wilkes, Mool C. Gupta*

Department of Electrical and Computer Engineering, University of Virginia, Charlottesville, VA 22904, United States

A R T I C L E I N F O

Keywords:
Silicon
Surface passivation
Minority carrier lifetime
Aluminum oxide
Laser processing

A B S T R A C T

In this paper, we propose and experimentally demonstrate a new laser processing method for low-temperature formation of effective aluminum oxide passivation layers on crystalline silicon. An aluminum film with a thickness of only several nm is evaporated on the silicon surface, after which a long pulse laser is utilized to convert the metal film to oxide. Laser processing parameters, especially laser energy fluence, are systematically optimized to get the critical condition to realize carrier lifetime similar to that of the bulk wafer, which we consider good passivation, while causing no damage to its surface. An effective surface recombination velocity below 25 cm s^{-1} is obtained right after the proper laser treatment of the Al metal film. After further annealing in forming gas, a 1.02 millisecond effective carrier lifetime as well as an effective surface recombination velocity below 13 cm s^{-1} is achieved for 1.4 Ω·cm n-type Si wafer.

1. Introduction

Surface passivation of silicon is essential to achieve higher conversion efficiencies in various optoelectronic devices and crystalline silicon (c-Si) solar cells in particular [1–6]. In past decades, a variety of materials have been utilized for passivation layers, including hydrogenated amorphous silicon (a-Si:H) [7], silicon oxide (SiO_x) [2,3], silicon nitride (SiN_x) [2,3], silicon carbide (SiC_x) [2,3], aluminum oxide (Al_2O_3) [8,9], titanium oxide (TiO_2) [10], organic materials [11], etc. Among them, aluminum oxide exhibits an extraordinary capability in yielding excellent surface passivation properties through a combination effect of chemical passivation, low interface defect density, and high negative charge accumulation located at the Si/Al_2O_3 interface, and thus has attracted increasing research interest [12–20].

Currently, high-quality Al_2O_3 passivation layers are mainly prepared by various chemical vapor deposition techniques, such as thermal or plasma atomic layer deposition (ALD) [8,9], plasma-enhanced chemical vapor deposition (PECVD) [12], atmospheric-pressure chemical vapor deposition (APCVD) [13], etc. Landmark solar cell efficiencies have been achieved via the Al_2O_3 passivation layers produced by these techniques, especially by the ALD method [14]. Surface passivation of crystalline silicon, giving very high effective minority carrier lifetimes (τ_{eff}), has been demonstrated by aluminum oxide layers produced via ALD, even with a very small layer thickness ≤ 5 nm [15,16]. Correspondingly, very low effective surface recombination velocity (S_{eff}) < 1 cm s^{-1} has been reported [16]. In the past few years, significant progress was further realized by a high-speed spatial ALD technique, which can preserve the excellent passivation effect while increasing throughput, and thus shows potential as an industrial approach [17,18]. However, in spite of these inspiring developments, a chemical precursor such as trimethylaluminum (TMA) is required for these chemical vapor deposition techniques, which is highly pyrophoric. Alternatively, physical vapor deposition techniques, reactive sputtering deposition in particular, have also been recently developed for producing aluminum oxide passivation layers, which show the capability to provide moderate surface passivation for crystalline silicon wafers with layer thicknesses of 20–30 nm [19,20]. These techniques usually require post annealing at around 425–500 °C, and the obtained lifetimes are not as good as the ALD method.

Laser materials processing has garnered widespread implementation in the field of photovoltaics, with a variety of specific techniques being developed for the manufacture of crystalline silicon solar cells, such as laser isolation, laser scribing, laser firing, laser transfer, laser doping, laser annealing, laser texturing, etc. [21–25]. Within these techniques, laser materials processing has exhibited distinct advantages as a highly flexible, non-contact, maskless and scalable approach. More importantly, the light-matter interaction during laser processing can be delicately controlled at specified surface areas and within limited surface depths, which makes it a promising low-temperature technology, and thus compatible with high-throughput manufacturing of

---

* Corresponding author.
E-mail address: mgupta@virginia.edu (M.C. Gupta).

https://doi.org/10.1016/j.apsusc.2019.02.023
Received 9 August 2018; Received in revised form 1 February 2019; Accepted 4 February 2019

photovoltaic devices. However, in spite of these advantages, the potential of a laser processing approach in preparing Al_2O_3 passivation layers on silicon wafers remains elusive, and the corresponding techniques have been seldom developed. Here in this paper, we propose and experimentally demonstrate a new laser processing approach for preparing effective aluminum oxide passivation layers on crystalline silicon. A 1.02 millisecond effective minority carrier lifetime as well as a low effective surface recombination velocity below 13 cm s^{-1} has been achieved by an ultrathin Al_2O_3 layer of only several nanometers for 1.4 Ω·cm n-type Si wafers.

2. Experimental section

2.1. E-beam evaporation of Al film

Aluminum layers were evaporated on double-side polished n-type float-zone Si (100) wafers (1.4 Ω·cm) using electron-beam evaporation (CHA six crucible E-beam Evaporator). Before evaporation, the native oxide layer on the wafers was removed by 2% HF for 10 min, after which all wafers were cleaned by 3% HCl and 2% HF for 10 min to react with ionic contaminants, 65% HNO_3 for 10 min to remove any organic contaminants, and lastly 2% HF for 10 min to dissolve the formed silicon oxide from the high concentration of HNO_3 [10,25]. The final wafer thickness is 280 µm. During evaporation, the chamber pressure was $\sim 1.7 \times 10^{-7}$ Pa, and the thickness of the Al layer is ~7 nm. For the infrared transmittance measurement, the aluminum layers were evaporated on only one side of the silicon wafers. For investigating the surface passivation quality, the aluminum evaporation as well as the following laser treatment was implemented on both sides of the silicon wafers to get symmetrical test structures.

2.2. Laser treatment

The conversion of aluminum metal layers to oxide was conducted using an IPG YLP-150/1500-QCW-AC long pulse laser system, which can generate variable duration (0.1–10 ms) pulses at a central wavelength of 1070 nm. An x-y galvo was used to focus and scan the laser beam on Si wafer surfaces in a pattern of parallel lines, with the diameter of focused spot on the sample surfaces to be around 1.5 mm. Through systematical optimization, the pulse duration, pulse repetition rate, laser scanning speed, and scanning line spacing were set to be 0.1 ms, 500 Hz, 50 mm s^{-1}, and 100 µm, respectively. Then, the metal to oxide conversion process was carefully investigated by adapting the laser energy fluence in a range of 0.68–1.36 J/cm^2 and controlling the time durations of laser scanning treatment from 0 min to 90 min on each sample surface with an area of 20×16 mm^2. In order to further enhance the metal-oxygen reaction, the laser processing was done in an ozone chamber.

2.3. Characterization and measurements

The surface morphologies of Si wafer surfaces after different laser treatments were observed by a Zeiss Axio Imager.A2 optical microscope. A Zygo NewView 7300 white light interferometer was utilized for imaging and measuring the 3D topography and roughness of the sample surfaces. The thicknesses and optical constants of the E-beam evaporated Al films and those treated by laser were examined via a J. A. Woollam M2000 spectroscopic ellipsometer in the wavelength range of 200–900 nm. For data acquisition and analysis, the CompleteEASE software from Woollam was used. X-ray photoelectron spectroscopy (XPS, PHI5000*VersaProbe* III) was used to check the composition and chemical bonding of the film. Raman spectra were taken by a Renishaw inVia Raman Microscope under an excitation source with a wavelength of 514 nm. Sheet resistance of the film was measured by a Jandel four-point-probe system. The wavelength dependence of transmittance for Si wafers in the infrared spectrum (1000–2500 nm) was characterized with a Cary 5E UV–Vis-NIR spectrophotometer.

The injection-level-dependent minority carrier lifetimes were measured by a Sinton WCT-120 wafer lifetime tester via a Quasi-Steady-State Photoconductance (QSSPC) method, which is preferred for small samples. The measurement was carried out using a non-conductive aperture of fixed size (10×10 mm^2) to mask off the edges of the samples and lessen inversion effects at the edge [26,27], while different aperture sizes showed limited variation. This method is described by Sinton Instruments in their Application Notes for the WCT-120 tester. However, some edge inversion may still affect the injection-dependent lifetime due to the sample size [26], which suggests large-area samples utilizing our passivation method will have further improved lifetime than our extracted values for small samples. The passivation quality of the laser generated Al_2O_3 layers was quantified in terms of both the effective lifetime (τ_{eff}) and effective surface recombination velocity (S_{eff}), which is calculated from τ_{eff} by the expression [10,18]:

$$\frac{1}{\tau_{eff}} = \frac{1}{\tau_{bulk}} + \frac{2S_{eff}}{W} \tag{1}$$

with τ_{bulk} being the intrinsic bulk lifetime of Si, which is calculated to be around 12.3 ms for n-type crystalline silicon with a doping concentration of 3.5×10^{15} cm^{-3} using the procedure outlined by Richter et al. [28] and Veith-Wolf et al. [29], and W being the wafer thickness which is 280 µm. However, the measured bulk lifetime of our samples was 2.2 ms using an iodine-methanol solution coated on both sides, far lower than the 12.3 ms calculated value, suggesting that the true S_{eff} of our passivation method is even lower.

3. Results and discussions

As schematically illustrated in Fig. 1a, the entire strategy starts from E-beam evaporation of an Al metal layer onto bare silicon wafer surface. Through this procedure, smooth and high-quality aluminum layers with desired thicknesses can be prepared on silicon substrates. Subsequently, the silicon wafers with aluminum surface layers are put into an ozone chamber, where laser treatment is conducted for converting the metal films to oxide. During this procedure, the amount of heat input onto silicon surfaces via laser irradiation can be flexibly controlled by tuning the laser energy fluences as well as the laser irradiation time, and thus the aluminum metal layers can significantly oxidize to form passivating films, while avoiding any damage to the bottom silicon substrate.

As shown in Fig. 1b, the Si surfaces remain smooth and preserve a mirror look after both the Al film evaporation and the subsequent laser treatment, indicating that no obvious surface damage has been induced during both procedures. The microscopic observations (Fig. S1) also confirmed this, except that some tiny spots were found after laser treatment. These tiny spots were speculated to be certain local roughness induced by the laser treatment. There was already some local roughness after evaporation of the Al metal layer, as indicated by the surface morphology measurement shown in Fig. S2. Although the laser treatment induced more local roughness, i.e., these small spots, the whole roughness of the sample surface showed only a slight increase. On this basis, it is demonstrated that the laser treatment has been well controlled to minimize, if there is any, morphological changes on the film or the silicon sample surface. The intrinsic bare Si surface is dark. After evaporating the Al film, the Si surface becomes bright, resulting from the highly reflective nature of Al metal. Then after laser treatment, the Si surface darkens, indicating that chemical composition change on the surface film has taken place. Since aluminum and oxygen are the only species involved during the whole process, it is suggested that the Al metal film has been partially converted to oxide, which can act as a passivation layer for silicon wafer surfaces.

As can be seen from the injection-level-dependent effective lifetimes in Fig. 1c, effective surface passivation is realized right after proper

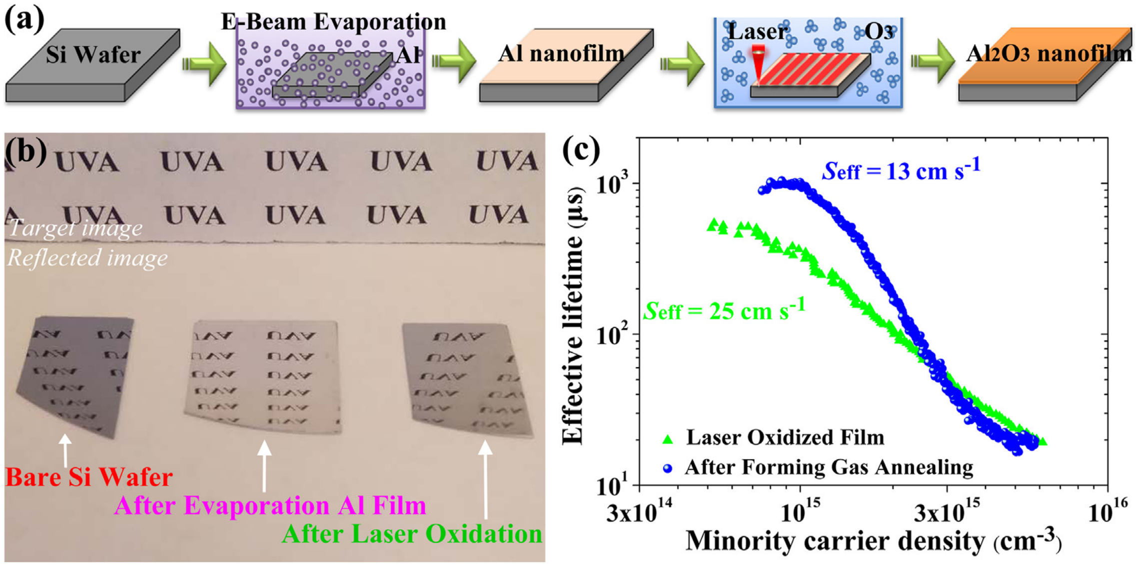

Fig. 1. (a) Schematic for preparing the Al_2O_3 passivation layers by laser on Si wafers; (b) optical images of bare Si wafer, Si wafer after evaporating Al film, and after laser oxidation treatment; projection of letters "UVA" was made as a clearer indicator of the change in surface brightness; (c) injection-level-dependent effective lifetimes of Si wafers after different treatment. The calculated effective surface recombination velocities are also shown.

laser treatment of the Al metal film, with the effective lifetime being significantly increased to 545 μs, giving a S_{eff} below 25 cm s^{-1}. To further improve the passivation effect, the laser treated silicon surface films were forming gas annealed at 400 °C for 10 min, which more than doubled the effective lifetime, reaching a value of 1020 μs. Correspondingly, a surface recombination velocity as lower than 13 cm s^{-1} is achieved at a minority carrier density of 10^{15} cm^{-3}, providing high-quality passivation of the silicon surface.

Generally, it is known that post deposition annealing at around 400–450 °C for the activation of surface passivation must be made in order to obtain any passivation effect for the aluminum oxide layers prepared by various chemical vapor deposition as well as reactive sputtering techniques. In contrast, our results demonstrate that effective surface passivation with industrially-acceptable low surface recombination velocities can be realized right after the proper laser oxidation treatment of the Al metal films. In addition, no bulk heating at high temperatures over 400 °C is needed for either the E-beam evaporation or the laser oxidation procedures. Thus, the degradation of bulk lifetime of silicon wafers during surface passivation treatment can be minimized, offering processing superiority for practical applications.

In order to obtain optimized laser processing conditions for achieving the high-quality aluminum oxide passivation layer, we carried out systematic investigation on the evolution of aluminum films with laser conditions, during which the infrared light transmittance of silicon wafers was utilized as an indicator, as shown in Fig. 2. The bare silicon wafers have intrinsic transmittance about 50–55% in the studied infrared spectrum of 1000–2500 nm (see Fig. S3). When aluminum films are evaporated on silicon surfaces, the transmittance decreases significantly to a level around 30–35% caused by the enhanced reflection and absorption within the metal layer. Subsequently, when laser irradiation is done on the aluminum films at different laser energy fluences, different evolution trends of transmittance with laser processing time duration are induced.

Specifically, when a wafer is treated with a low laser energy fluence, e.g., 1.13 J/cm^2, the transmittance of the aluminum coated silicon wafer increases gradually as the laser continues scanning on the aluminum surface layer (Fig. 2a). However, the rate of transmission increase diminishes, indicating that the ongoing oxidation of the metal layer is slowed. After 30 min of laser treatment, the transmittance tends to reach a steady level. Almost no further increase can be induced in the transmittance even after double laser irradiation time is applied. The transmittance spectra for aluminum films treated by lower laser energy fluence, e.g., 0.68 J/cm^2 and 0.91 J/cm^2, keep the same evolution trend, as presented in Fig. S3. This is a reasonable result, given that the aluminum-oxygen reaction in this research is a diffusion-dependent process. As aluminum is oxidized, the diffusion of oxygen atoms to the underlying unoxidized aluminum layer needs to pass through the already formed oxide, which becomes exceedingly difficult as the oxidation continues.

When a high laser energy fluence is applied, e.g., 1.36 J/cm^2, the transmittance of silicon wafer increases continuously with laser irradiation time, with no obvious change in the increasing rate (Fig. 2c). When irradiation time is doubled, there is an approximate doubling in the transmission. This evolution trend keeps constant for even longer time durations, as shown in Fig. S4. Therefore, it is suggested that a different laser process mechanism rather than laser oxidation dominates at high laser fluence conditions. In consideration of the nearly linear increase of transmittance with laser irradiation time, it is speculated to be laser ablation combined with oxidation, which normally happens at laser power intensities higher than those needed for the oxidation reaction.

The above differences in the laser induced transmittance evolution trends of silicon wafers can be more clearly understood through the comparison at a specific wavelength, as shown in Fig. 3. The increase of transmittance is faster at the beginning stage at low laser energy fluence, and then levels off. In contrast to that, a nearly constant and linear increase of transmittance is displayed under the high laser fluence condition. Based on these analysis, a moderate laser fluence is desired, which is expected to provide stronger driving force for oxygen diffusion and thus for the oxidation reaction, while causing negligible ablation of the surface material.

For testing this, a laser fluence of 1.25 J/cm^2 is used. From Fig. 2b, it can be observed that the increase of transmittance with time is more pronounced compared to the condition of 1.13 J/cm^2 laser fluence, suggesting that the metal-oxygen reaction is enhanced and accelerated. Despite that a decline in the increasing transmittance rate still exists, the growth does not level off after laser irradiation for 30 min, and a further transmittance increase can be expected. After laser irradiation for 60 min, the transmittance increases to a higher level and finally stabilizes. Such an evolution is also verified in Fig. 3, with a steeper rate of increase being displayed during initial laser irradiation under a laser fluence of 1.25 J/cm^2. Due to the enhanced and prolonged oxidation

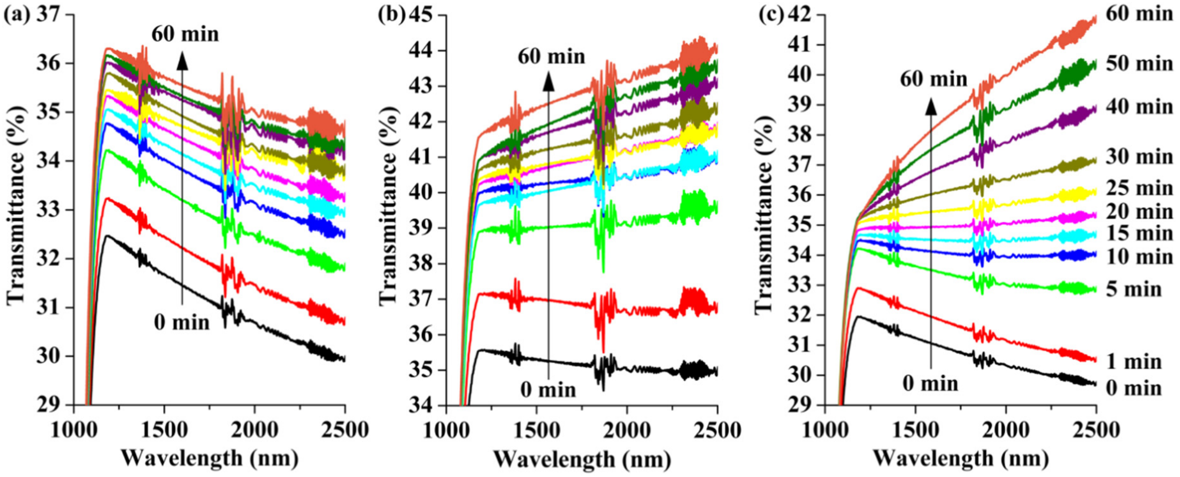

Fig. 2. Laser-induced evolution of transmittance spectra of Si wafers with aluminum surface layers at different laser energy fluences and for different time durations: (a) at laser fluence of 1.13 J/cm^2; (b) at laser fluence of 1.25 J/cm^2; (c) at laser fluence of 1.36 J/cm^2. Bottom black lines (referred as 0 min) are the curves for silicon wafers with as-evaporated aluminum films. The curve labels are consistent in all three figures. Fluctuations in the spectra are caused by switching light sources and detectors within the spectrophotometer for measurement in different wavelength regions.

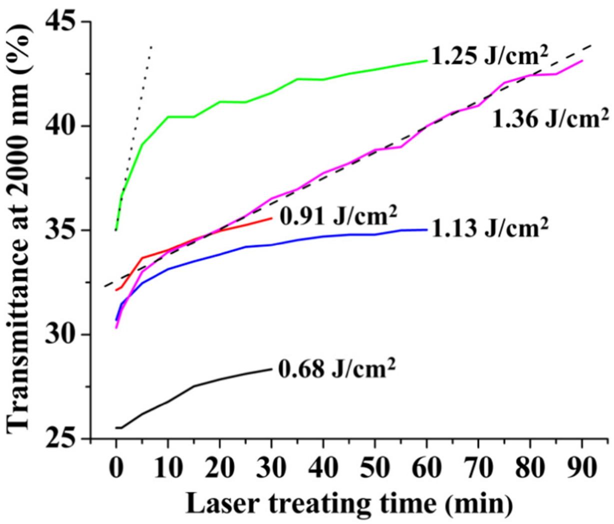

Fig. 3. Evolution of transmittance of silicon wafers at the wavelength of 2000 nm with time durations of laser oxidation treatment at different laser fluences. The dashed and doted lines indicate the increasing slopes of transmittance with respect to time at laser fluences of 1.36 J/cm^2 and 1.25 J/cm^2, respectively.

reaction, a larger portion part of the evaporated aluminum metal layers can be converted to oxide, also evidenced by the good passivation effect shown above.

Through XPS characterization, the chemical change on the film can be further examined, as shown in Fig. 4. For the Al 2p spectra, the peaks at around 73 and 75 eV belong to metallic aluminum and aluminum oxide, respectively [30,31]. The peak for metallic Al is the major peak in the Al 2p spectrum before laser treatment, as shown in Fig. 4a. The peak for Al_2O_3 is also detected before laser treatment, which could result from the natural oxidation of metallic Al in air during storage. After laser treatment, the peak for metallic Al almost disappeared and the peak for Al_2O_3 dominates the Al 2p spectrum (Fig. 4d), confirming that partial conversion of the film from Al metal to oxide has occurred.

It can be noticed that an obvious peak for silicon appeared after laser treatment in the Si 2p spectrum (Fig. 4f), which did not show up before laser treatment (Fig. 4c). A possible reason is that it is easier for the photoelectrons of Si to escape from the oxide film and then be detected. The obvious increase in the Si 2p signal results in the decrease in relative intensity of the Al 2p peaks. Meanwhile, the relative intensity of O 1s increases slightly (Fig. 4b, e), suggesting that significantly more oxide has been formed. This evolution can also be seen from the atomic ratios of Al, O, and Si in the film, as shown in Table 1.

More detailed analysis is conducted via angle resolved XPS (AR-XPS, Fig. 5), with the corresponding atomic ratio results of Al, O, and Si being shown in Fig. 6a. The AR-XPS spectra can give the sample composition information at different depths. As larger incident angles are used, namely, the XPS measurement penetrates deeper into the film and the content of oxygen in the film both before and after laser treatment decreases gradually, which indicates that the metallic Al to oxide conversion is a diffusion-dependent process. At the initial step of the aluminum-oxygen reaction, the active oxygen atom, produced in the ozone chamber and driven.

by laser heating, can diffuse through the thin nanofilm to the aluminum-silicon interface where metallic Al to oxide conversion occurs. Once some oxide is formed in the film, the oxygen diffusion slows down obviously since the diffusion coefficient of oxygen in aluminum oxide is very low [32]. As a result, a gradually changing distribution of oxygen content along the depth of the film is induced, which in turn results in a gradually changing oxide distribution. More investigation in the aluminum-oxygen reaction mechanism during our laser processing is being conducted.

In spite of the gradual decrease of oxygen content in the film, it can be seen that the film after laser treatment has a higher oxygen content at all depth positions, confirming that more oxide has been grown by our laser treatment throughout the film. For the sake of comparison, we calculated the relative atomic ratio of oxygen to aluminum, as shown in Fig. 6b. It is illustrated that the O/Al ratio within the film before laser treatment is smaller than 3:2 even under the shallowest incident angle condition, i.e., 5°, indicating only the existence of limited amount of naturally formed oxide. As a contrast, the O/Al ratio within the film after laser treatment is larger than 3:2 even in the highest incident angle condition, i.e., 90°, demonstrating that the metallic Al film has been partially converted to oxide.

The chemical composition change in the film can also be confirmed from the Raman spectra, as shown in Fig. S5. The characteristic peaks in the Raman spectra of the bare silicon wafer correspond to the different optical and acoustical modes of silicon. When the Al metal film is deposited on the silicon wafer surface, most of these peaks disappear except for the major peak of Si at around 520 cm^{-1}, which is a reasonable result because the metal layer blocks the signal from the silicon substrate. After laser oxidation treatment, these peaks for the silicon

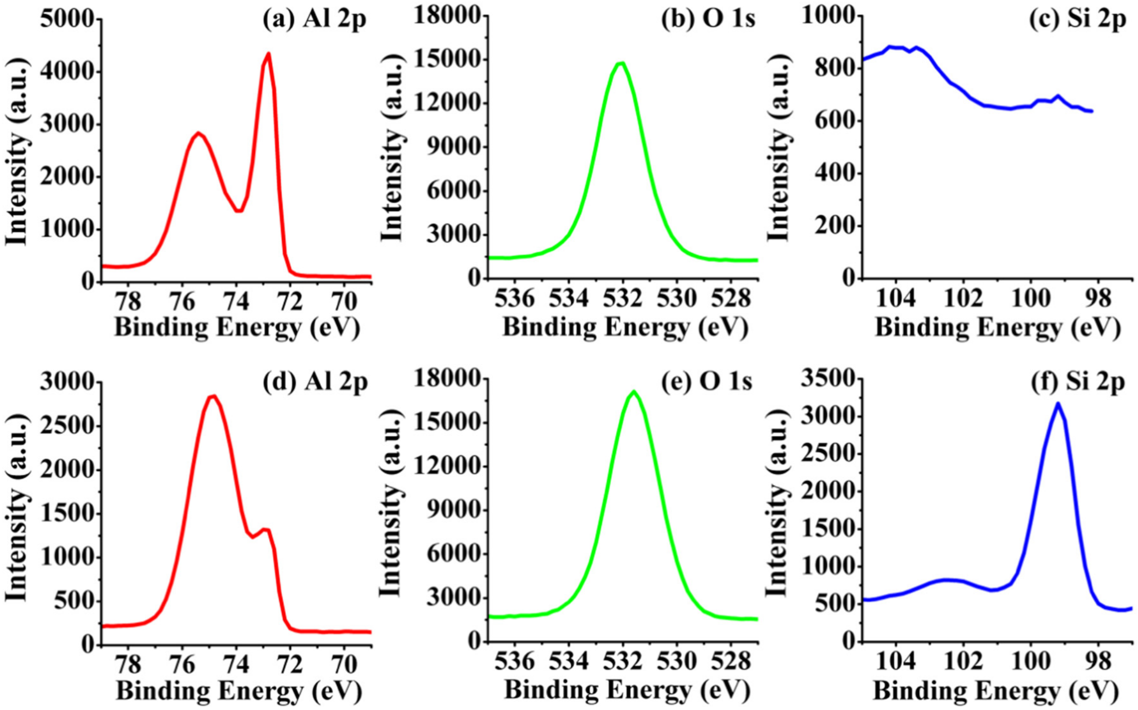

Fig. 4. XPS spectra of (a) (d) Al 2p, (b) (e) O 1s, and (c) (f) Si 2p signals derived from the evaporated Al film (a)–(c) before and (d)–(f) after laser oxidation and forming gas annealing treatment.

Table 1
Atomic ratios of Al, O, and Si in the film according to the XPS spectra in Fig. 4.

Element	Al 2p	O 1s	Si 2p
Before laser treatment	45.6	53.6	0.8
After laser treatment	29.8	61.2	9

modes show up again, indicating that a chemical change on the metal film has occurred. Additionally, three new peaks at around 632, 645, and 656 cm^{-1} are also detected, which are assigned to aluminum oxide. Thus, the partial transition of Al metal film to oxide is verified after the laser treatment.

We also tested the change in thickness as well as optical constants of the Al films after laser treatment by spectroscopic ellipsometry measurement. The thickness of the as-evaporated aluminum metal film was measured to be around 6.9–7.8 nm, as given by Fig. 7a. After laser treatment, the film thickness was increased to be around 7.8–8.4 nm as shown in Fig. 7b, which is consistent with the surface morphology measurement shown in Fig. S2 and resulted from the mass growth during the oxidation reaction. Although it is difficult to get an accurate measurement for the absolute thickness of such thin films by ellipsometry, we can see that the variance in the film thickness was below 1 nm both before and after laser treatment. This indicates that the as-evaporated film was uniform and stayed uniform after laser treatment.

The ellipsometry measurement also detects the change in optical constants of the film, as plotted in Fig. 7c, d. For ultrathin films ($<$ 10 nm thickness), the optical constants differ greatly from the bulk material, which is evidenced when we compare our results to bulk film optical properties [33,34]. However, when we compare our optical constants to that of a 5 nm thick Al film deposited by molecular beam epitaxy, our results for both refractive index and extinction coefficient are complemented by the literature [35]. It was also reported that the refractive index at a wavelength of 635 nm rapidly increased above 2.0 for sub-10-nm Al_2O_3 films [36], which shows agreement with our measured refractive index. On this basis, the optical constant n increases while the optical constant k decreases after laser treatment in our approach, which suggests a chemical change in the film from metal to dielectric. The dielectric-type property of the film after laser treatment can also be evidenced by its electrical characteristics. The sheet resistance of the film increased from below 1 Ω/□ before laser treatment to over 100 Ω/□ after laser treatment. Such an obvious increase indicates the formation of a dielectric. However, we note that both the ellipsometry and sheet resistance measurements could be quite rough and qualitative, because great difficulties exist in discerning optical constant data for ultrathin films and the influence from the substrate as well as the contact of the film with probes could be high on measuring the resistance.

To further confirm the capability of laser treatment in converting aluminum metal films to oxide, we also conducted E-beam evaporation and laser treatment procedures on glass substrate, with its transmittance being measured, as shown in Fig. S6. Glass is intrinsically transparent material in the visible wavelength range, possessing a high transmittance value of about 90%. When an aluminum layer is evaporated onto its surface, its transmittance drops to around 50%, as shown in Fig. S6a. Correspondingly, the transparent glass darkens, as can be seen in Fig. S6b. The laser treatment was applied with identical processing conditions to those used for treating silicon wafers but at a fixed laser energy fluence of 0.68 J/cm^2. Displaying a similar evolution trend, the transmittance of glass with an aluminum layer shows a rapid increase to $>$ 70% at the beginning of laser treatment, after which the increase subsides. After laser treatment for a certain period, a very slight increase can be further induced in the transmittance of glass even with much longer laser irradiation time, indicating that the aluminum metal layer has been obviously oxidized. In addition, the earlier darkly tinted glass becomes more transparent. Therefore, the capability of laser treatment in converting aluminum metal films to oxide films is verified for multiple substrates, indicating its flexibility.

Traditional furnace heating techniques can also grow thin aluminum oxide films using Al metal, although they require 500 °C annealing for several hours to obtain an ~5 nm thick layer [37]. Our laser processing method, however, can lead to a transient high temperature (~900 °C) at the interface between aluminum oxide film and silicon

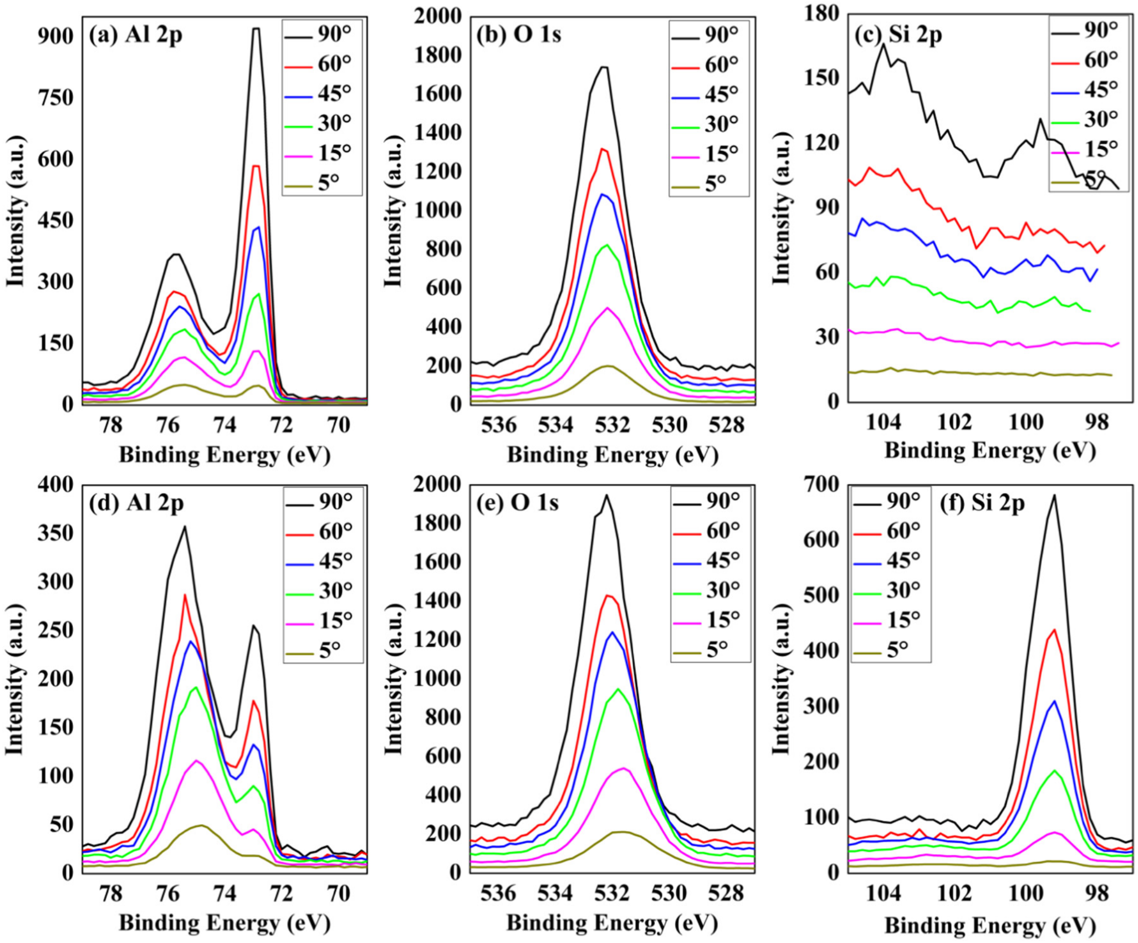

Fig. 5. AR-XPS spectra of (a) (d) Al 2p, (b) (e) O 1s, and (c) (f) Si 2p signals derived from (a)–(c) as-evaporated and (d)–(f) laser-oxidized Al metal films.

substrate, which is beneficial for generating a significant amount of chemical bonding and greatly decreases the interface state density. With these advantages, laser generated aluminum oxide films can realize an excellent chemical passivation effect for silicon surfaces. High-efficiency c-Si solar cells generally require excellent surface passivation with a S_{eff} below 13 cm s^{-1} [3,4]. Here, the < 13 cm s^{-1} S_{eff} in the laser generated aluminum oxide film can successfully satisfy this requirement. In addition, with current availability of high power (> 10 kW) laser systems and high speed (> 10 m s^{-1}) scanners, the laser processing approach developed in this research could be extended for high-

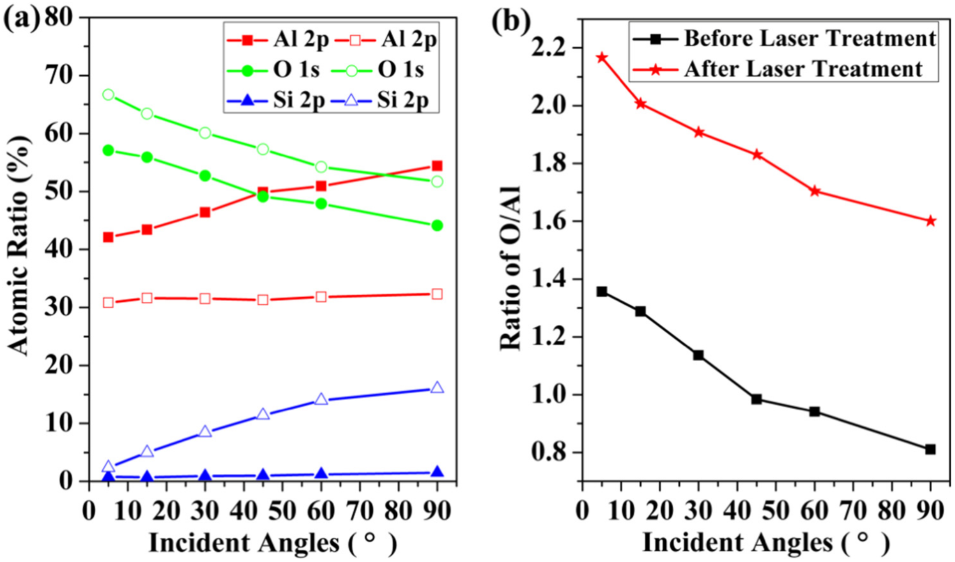

Fig. 6. (a) Atomic ratios of Al, O, and Si in the film obtained from AR-XPS spectra. Solid and open symbols refer the results before and after laser treatment, respectively; (b) Relative ratio of O atoms to Al atoms in the film derived from (a).

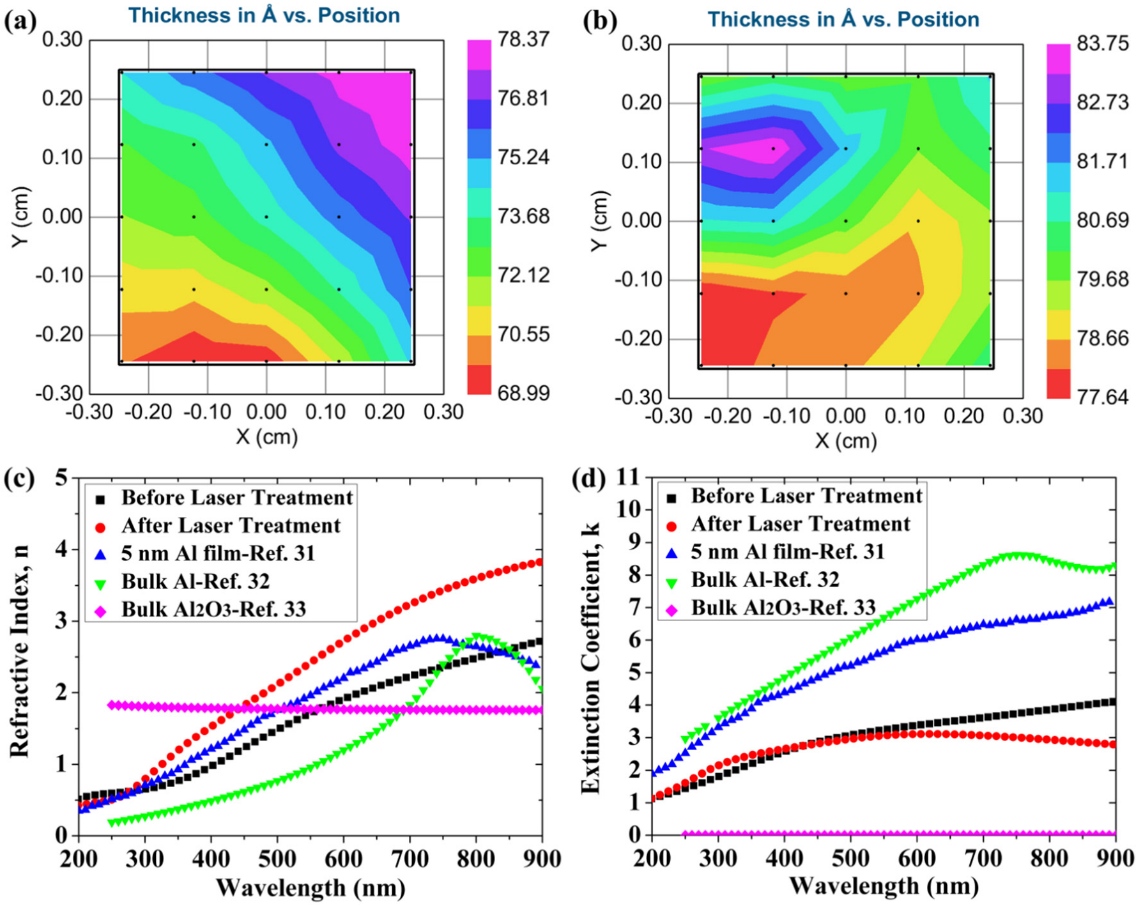

Fig. 7. Ellipsometry measurement for thickness and optical constants of the prepared films on silicon wafer. (a) and (b) are mapping results of film thickness over an area of 0.5 × 0.5 cm^2 before and after laser treatment, respectively. Wavelength dependence of (c) refractive index n and (d) extinction coefficient k of the films before and after laser treatment. The optical constants from three references are also shown for comparison.

throughput production. On this basis, the approach can find direct application in the silicon solar cell industry. Moreover, we believe the demonstrated laser processing technique can also be instructive for the preparation of thin films of other kinds of metal oxides, which are broadly utilized in optoelectronic and energy devices [38,39].

4. Conclusions

We propose and experimentally demonstrate a new laser processing method for low-temperature formation of effective aluminum oxide passivation layers on crystalline silicon. Aluminum films with a thickness of only several nm are evaporated on the silicon surface, after which a long pulse laser is utilized to convert the metal film to oxide. We find that in order to realize good passivation on silicon while causing no damage to its surface, the laser processing parameters, especially laser energy fluence, need to be optimized to get the critical condition. An effective surface recombination velocity below 25 cm s^{-1} is obtained right after the proper laser treatment of the Al metal film. After further annealing in forming gas, a 1.02 millisecond effective carrier lifetime as well as an effective surface recombination velocity below 13 cm s^{-1} is achieved for a 1.4 Ω·cm n-type Si wafer.

Acknowledgements

The authors greatly thank the funding support by NSF IUCRC Program (IIP 1338917). We would also like to acknowledge the help from Catherine Dukes in the Nanoscale Materials Characterization Facility (NMCF) at the University of Virginia for the use of XPS, and the assistance of James Hilfiker from J.A. Woollam Co. for discussion on ellipsometry measurements.

Appendix A. Supplementary data

Comparison of optical microscope images of silicon surfaces; Comparison of surface morphology images and surface roughness of silicon wafers measured by white light interferometer; Evolution of optical transmittance of Si wafer with evaporated Al metal layers induced by laser fluences of 0.68 J/cm^2 and 0.91 J/cm^2; Evolution of optical transmittance of Si wafer with evaporated Al metal layers induced by laser fluence of 1.36 J/cm^2 for 0–90 min process time durations; Raman spectra of different samples; Evolution of transmittance spectra of glass with Al layers induced by laser oxidation treatment. Supplementary data to this article can be found online at https://doi.org/10.1016/j.apsusc.2019.02.023.

References

[1] A.G. Aberle, Surface passivation of crystalline silicon solar cells: a review, Prog. Photovolt. Res. Appl. 8 (2000) 473–487.
[2] M.Z. Rahman, S.I. Khan, Advances in surface passivation of c-Si solar cells, Mater. Renew. Sustain. Energy 1 (2012) 1–11.
[3] M.Z. Rahman, Advances in surface passivation and emitter optimization techniques of c-Si solar cells, Renew. Sust. Energ. Rev. 30 (2014) 734–742.
[4] T. Dullweber, J. Schmidt, Industrial silicon solar cells applying the passivated emitter and rear cell (PERC) concept—a review, IEEE J. Photovolt. 6 (2016) 1366–1381.
[5] J. Bullock, D. Kiriya, N. Grant, A. Azcatl, M. Hettick, T. Kho, P. Phang, H.C. Sio, D. Yan, D. Macdonald, M.A. Quevedo-Lopez, R.M. Wallace, A. Cuevas, A. Javey, Superacid passivation of crystalline silicon surfaces, ACS Appl. Mater. Interfaces 8

(2016) 24205–24211.

[6] Y. Tao, R. Hauert, C.L. Degen, Exclusively gas-phase passivation of native oxide-free silicon(100) and silicon(111) surfaces, ACS Appl. Mater. Interfaces 8 (2016) 13157–13165.

[7] F. Wang, X. Zhang, L. Wang, Y. Jiang, C. Wei, J. Sun, Y. Zhao, Role of hydrogen plasma pretreatment in improving passivation of the silicon surface for solar cells applications, ACS Appl. Mater. Interfaces 6 (2014) 15098–15104.

[8] B. Hoex, S.B.S. Heil, E. Langereis, M.C.M. van de Sanden, W.M.M. Kessels, Ultralow surface recombination of c-Si substrates passivated by plasma-assisted atomic layer deposited Al_2O_3, Appl. Phys. Lett. 89 (2006) 042112.

[9] G. Agostinelli, A. Delabie, P. Vitanov, Z. Alexiev, H.F.W. Dekkers, S. De Wolf, G. Beaucarn, Very low surface recombination velocities on p-type silicon wafers passivated with a dielectric with fixed negative charge, Sol. Energy Mater. Sol. Cells 90 (2006) 3438–3443.

[10] Z. Sun, X. Deng, J.J. Choi, M.C. Gupta, Silicon surface passivation by laser processing a sol-gel TiOx thin film, ACS Appl. Energy Mater. 1 (2018) 5474–5481.

[11] R. Yang, T. Buonassisi, K.K. Gleason, Organic vapor passivation of silicon at room temperature, Adv. Mater. 25 (2013) 2078–2083.

[12] G. Dingemans, M.C.M. van de Sanden, W.M.M. Kessels, Influence of the deposition temperature on the c-Si surface passivation by Al_2O_3 films synthesized by ALD and PECVD, Electrochem. Solid State Lett. 13 (2010) H76–H79.

[13] L.E. Black, T. Allen, A. Cuevas, K.R. McIntosh, B. Veith, J. Schmidt, Thermal stability of silicon surface passivation by APCVD Al_2O_3, Sol. Energy Mater. Sol. Cells 120 (2014) 339–345.

[14] H. Huang, J. Lv, Y. Bao, R. Xuan, S. Sun, S. Sneck, S. Li, C. Modanese, H. Savin, A. Wang, J. Zhao, 20.8% industrial PERC solar cell: ALD Al_2O_3 rear surface passivation, efficiency loss mechanisms analysis and roadmap to 24%, Sol. Energy Mater. Sol. Cells 161 (2017) 14–30.

[15] J. Schmidt, B. Veith, R. Brendel, Effective surface passivation of crystalline silicon using ultrathin Al_2O_3 films and Al_2O_3/SiN_x stacks, Phys. Status Solidi Rapid Res. Lett. 3 (2009) 287–289.

[16] G. Dingemans, R. Seguin, P. Engelhart, M.C.M. van de Sanden, W.M.M. Kessels, Silicon surface passivation by ultrathin Al_2O_3 films synthesized by thermal and plasma atomic layer deposition, Phys. Status Solidi Rapid Res. Lett. 4 (2010) 10–12.

[17] P. Poodt, A. Lankhorst, F. Roozeboom, K. Spee, D. Maas, A. Vermeer, High-speed spatial atomic-layer deposition of aluminum oxide layers for solar cell passivation, Adv. Mater. 22 (2010) 3564–3567.

[18] B. Vermang, A. Rothschild, A. Racz, J. John, J. Poortmans, R. Mertens, P. Poodt, V. Tiba, F. Roozeboom, Spatially separated atomic layer deposition of Al_2O_3, a new option for high-throughput Si solar cell passivation, Prog. Photovolt. Res. Appl. 19 (2011) 733–739.

[19] T.T. Li, A. Cuevas, Effective surface passivation of crystalline silicon by rf sputtered aluminum oxide, Phys. Status Solidi Rapid Res. Lett. 3 (2009) 160–162.

[20] X. Zhang, A. Cuevas, A. Thomson, Process control of reactive sputter deposition of AlO_x and improved surface passivation of crystalline silicon, IEEE J. Photovolt. 3 (2013) 183–188.

[21] M.C. Gupta, D.E. Carlson, Laser processing of materials for renewable energy applications, MRS Energy Sustain. 2 (2015) 1–15.

[22] Z. Sun, M.C. Gupta, Laser annealing of silicon surface defects for photovoltaic applications, Surf. Sci. 652 (2016) 344–349.

[23] P. Ortega, I. Martín, G. Lopez, M. Colina, A. Orpella, C. Voz, R. Alcubilla, p-Type c-Si solar cells based on rear side laser processing of Al_2O_3/SiC_x stacks, Sol. Energy Mater. Sol. Cells 106 (2012) 80–83.

[24] I. Martín, P. Ortega, M. Colina, A. Orpella, G. López, R. Alcubilla, Laser processing of Al_2O_3/a-SiC_x:H stacks: a feasible solution for the rear surface of high-efficiency p-type c-Si solar cells, Prog. Photovolt. Res. Appl. 21 (2013) 1171–1175.

[25] Z. Sun, M.C. Gupta, Laser processing of silicon for photovoltaics and structural phase transformation, Appl. Surf. Sci. 456 (2018) 342–350.

[26] B. Veith, T. Ohrdes, F. Werner, R. Brendel, P.P. Altermatt, N. Harder, J. Schmidt, Injection dependence of the effective lifetime of n-type Si passivated by Al_2O_3: an edge effect? Sol. Energy Mater. Sol. Cells 120 (2014) 436–440.

[27] B.A. Veith-Wolf, J. Schmidt, Unexpectedly high minority-carrier lifetimes exceeding 20 ms measured on 1.4-Ω cm n-type silicon wafers, Phys. Status Solidi Rapid Res. Lett. 11 (2017) 1700235.

[28] A. Richter, S.W. Glunz, F. Werner, J. Schmidt, A. Cuevas, Improved quantitative description of Auger recombination in crystalline silicon, Phys. Rev. B 86 (2012) 165202.

[29] B.A. Veith-Wolf, S. Schafer, R. Brendel, J. Schmidt, Reassessment of intrinsic lifetime limit in n-type crystalline silicon and implication on maximum solar cell efficiency, Sol. Energy Mater. Sol. Cells 186 (2018) 194–199.

[30] K. Djebaili, Z. Mekhalif, A. Boumaza, A. Djelloul, XPS, FTIR, EDX, and XRD analysis of Al_2O_3 scales grown on PM2000 alloy, J. Spectrosc. 16 (2015) 868109.

[31] M. Okoshi, K. Iwai, H. Nojiri, N. Inoue, F_2-laser-induced modification of aluminum thin films into transparent aluminum oxide, Jpn. J. Appl. Phys. 51 (2012) 122701.

[32] A.H. Heuer, Oxygen and aluminum diffusion in α-Al_2O_3: how much do we really understand, J. Eur. Ceram. Soc. 28 (2008) 1495–1507.

[33] E.D. Palik, Handbook of Optical Constants of Solids, 2 Elsevier, 1991, pp. 397–400.

[34] T. Lichtenstein, Handbook of Thin Film Materials, College of Engineering and Applied Science, University of Rochester, 1979.

[35] S. Gao, J. Lian, P. Song, P. Li, Z. Ma, X. Wang, S. Wu, Study on optical constant of ultrathin aluminum films deposited by molecular beam epitaxy, 2011 Symposium on Photonics and Optoelectronics (SOPO), Wuhan, 2011, pp. 1–4.

[36] C. Barbos, D. Blanc-Pelissier, A. Fave, E. Blanquet, A. Crisci, E. Fourmond, D. Albertini, A. Sabac, K. Ayadi, P. Girard, M. Lemiti, Characterization of Al_2O_3 thin films prepared by thermal ALD, Energy Procedia 77 (2015) 558–564.

[37] L.P.H. Jeurgens, W.G. Sloof, F.D. Tichelaar, E.J. Mittemeijer, Growth kinetics and mechanisms of aluminum-oxide films formed by thermal oxidation of aluminum, J. Appl. Phys. 92 (2002) 1649–1656.

[38] L.G. Gerling, S. Mahato, A. Morales-Vilches, G. Masmitja, P. Ortega, C. Voz, R. Alcubilla, J. Puigdollers, Transition metal oxides as hole-selective contacts in silicon hetero junctions solar cells, Sol. Energy Mater. Sol. Cells 145 (2016) 109–115.

[39] J. Meyer, S. Hamwi, M. Kröger, W. Kowalsky, T. Riedl, A. Kahn, Transition metal oxides for organic electronics: energetics, device physics and applications, Adv. Mater. 24 (2012) 5408–5427.

Laser Crystallization and Dopant Activation for a-Si:H Film in Carrier-Selective Contacts for Silicon Solar cells

George C. Wilkes,[1] Ajay D. Upadhyaya,[2] Ajeet Rohatgi,[2] and Mool C. Gupta[1*]

[1]University of Virginia, Charlottesville, VA, 22903, USA, [2]Georgia Institute of Technology, Atlanta, Georgia 30332, USA

***Abstract* — Herein we present a pulsed laser processing method for crystallization and dopant activation of a highly n-doped amorphous silicon (a-Si:H) carrier selective layer for high conductivity, high carrier lifetime, low emitter saturation current and limited surface layer heating as opposed to high temperature furnace annealing induced heating of the bulk Si wafer. We demonstrate increased crystallinity and reduced layer resistivity, without impacting surface passivation quality. Additionally, we examine the role of forming gas annealing (FGA) on further improving the passivation of laser-processed polysilicon layers to achieve a <2 mΩ·cm film resistivity, 2.1 ms effective carrier lifetime, 685 mV implied open-circuit voltage (iV_{OC}), and 27 fA/cm^2 recombination current density (J_0) with the potential for further passivation improvement via laser process optimization.**

***Index* — laser annealing, laser processing, silicon crystallization, dopant activation, surface passivation, carrier-selective contacts.**

I. INTRODUCTION

Carrier recombination in high-efficiency silicon solar cells can be greatly reduced by using passivating and carrier-selective interlayers between silicon and its metal electrodes to enhance cell efficiency. Highly-doped a-Si:H, well studied as an interlayer in various Si devices, is receiving increasing interest as a carrier selective layer for Si solar cells [1–7]. When coupled with a thin (< 2 nm) passivating layer (such as SiO_2), surface passivation can be achieved without negatively impacting carrier transport. Additionally, tunnel-oxide passivating contacts are one of few viable methods to eradicate diffusion and metal-contact-induced recombination because they relocate heavily-doped diffused regions and metallized contacts outside of the absorbing base. The band alignment of the base, thin passivation layer, and carrier selective layer work together to create a high barrier for one carrier and low barrier for the other, providing carrier selectivity for low minority carrier recombination and efficient majority carrier transport. The energy diagram of this system is shown in Fig. 1.

Typically, the highly-doped amorphous or nanocrystalline silicon layer is deposited via PECVD or LPCVD at low temperatures between 200-600 °C and a subsequent 30-minute high-temperature anneal between 800-1000 °C is used to further crystallize the as-deposited layer [1–3,5–7], increase structural and electrical stability [2–4,6,7], activate dopants within the layer [1,6,7], reduce short wavelength parasitic absorption by increasing crystallinity [8], and possibly generate pinholes in the interfacial oxide for carrier transport [3,4]. Amorphous Si can reduce short-circuit current density values by as much as 9 mA/cm^2 for a 100 nm thick layer, which is reduced to 4 mA/cm^2 for poly-Si [8], emphasizing the need for layer crystallization. Dopant activation will decrease the sheet resistance of the poly-Si enabling a low series resistance for subsequent metallization. However, high-temperature anneals lead to several problems: (1) degradation of the tunnel oxide and its interfaces [3], (2) dopant diffusion from the poly-Si into the base which increases Auger recombination, (3) incomplete dopant activation in the poly-Si, and (4) degradation of the absorber lifetime due to prolonged high-temperature exposure.

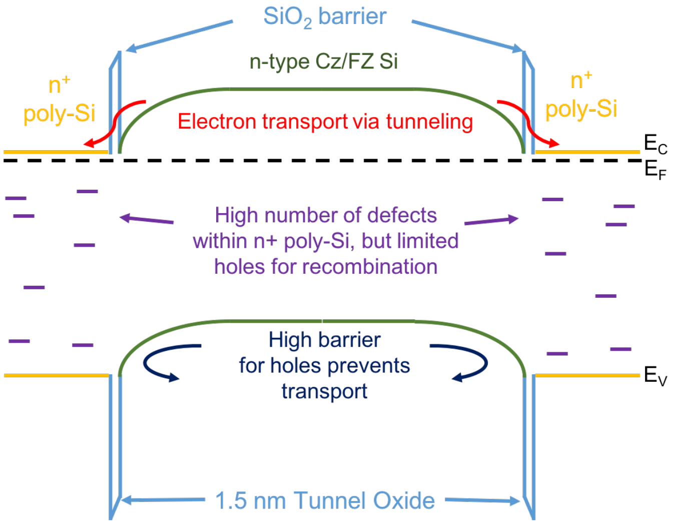

Fig. 1. Test structure energy diagram showing carrier transport.

To alleviate these issues and grant further control over the processing, we investigate the use of ultraviolet pulsed-laser annealing to replace the secondary furnace-based high-temperature anneal. Laser based solar cell manufacturing has gained increased interest in recent years, allowing for easy adoption [9,10]. Pulsed laser annealing allows for selective control over dopant activation and crystallization of the poly-Si layer while preventing oxide degradation, absorber degradation, and excessive diffusion. This is due to the short laser pulse (25 ns) which can activate dopants and crystallize the poly-Si in nanoseconds and the shallow absorption depth (13 nm for Si) enabling the processing to only affect the desired layer. Coupled with the low thermal diffusivity of amorphous (0.10 cm^2/s) and polycrystalline silicon (0.14 cm^2/s) when compared to crystalline silicon (0.90 cm^2/s) [11], it is unlikely that temperatures required for oxide break-up (900 °C) [12] will reach the interface oxide or c-Si through the 200 nm poly-Si

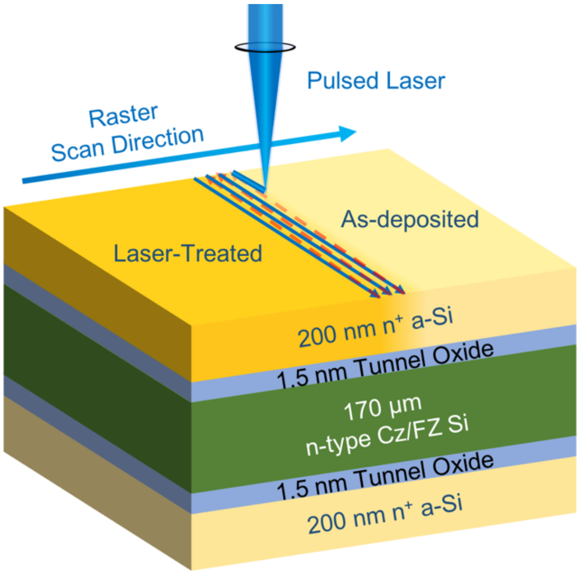

Fig. 2. Schematic drawing of the device test structure showing laser raster scan pattern and laser processing on n+ poly-Si layers.

layer under nanosecond pulsed laser heating [13]. This gives us a unique advantage in preventing oxide break-up while annealing the poly-Si layer. Herein, we investigate the change in passivation and resistance of laser processed a-Si:H carrier-selective passivating contacts and the impact of forming gas annealing (FGA) to replace the furnace-based high temperature anneal for a-Si:H carrier-selective layers for high efficiency Si solar cells.

II. Device Fabrication and Testing

This study used high-lifetime, large-area, 76 Ω-cm resistivity, 170 µm thick, textured, n-type Cz wafers so that the J$_0$ variation better reflects the change in surface passivation and sheet resistance measurements reflect the change in resistivity. The wafers are planarized and etched using a KOH solution and then cleaned in an RCA solution. Next, we grow a 1.5 nm thick tunnel oxide symmetrically on both sides of the wafer using a HNO$_3$ solution at 100 °C. After this, we deposit a ~200 nm thick phosphorus-doped a-Si:H layer at ~600 °C on both sides of the structure using an LPCVD furnace with a mixture of SiH$_4$ and PH$_3$ gas. This layer is subjected to a furnace anneal at 875 °C for 30 minutes or pulsed laser annealing to further crystallize the layer and improve its properties [6]. Using a 355 nm wavelength, 25 ns pulse width, diode-pumped solid-state laser with a focal spot size of 20 µm and a computer-controlled galvanometric scan head, we optimized the laser fluence. The pulsed laser is raster scanned across the substrate with a repetition rate of 50 kHz, a scan speed of 100 mm/s, a raster line spacing of 9 µm, and a 2 µm x-y galvanometric wobble. Fig. 2. shows a schematic of the device structure and laser raster pattern. Afterwards, we treated samples to a FGA at 450 °C to investigate the effect of passivation by the reintroduction of hydrogen. The structures are symmetric to better test their passivation properties. We measured passivation parameters of the structure shown in figure 1 with the method developed by Kane and Swanson [14] using a Sinton Instruments WCT-120 QSSPCD at a specified minority carrier density of 1.0×10^{16} cm^{-3} in quasi-steady state analysis mode. We divided J$_0$ values by two to reflect the saturation current of one of the two layers in the symmetric structure. We measured sheet resistances of the deposited films with a Jandel Multiposition Probe with a linear 1.00 mm probe spacing and a 25 µm tip radius.

III. Results and Discussion

After deposition of 200 nm of n$^+$ a-Si:H film but before the subsequent anneal, the sheet resistance, effective carrier lifetime, iV$_{OC}$, and J$_0$ of the symmetric structure shown in figure 1 was determined as 649 Ω/sq, 1762 µs, 0.683 V, and 29 fA/cm^2, respectively. Next, pulsed laser processing was conducted using the laser parameters stated in the experimental section at varied laser fluences on both sides of the symmetric sample. The sheet resistances and passivation parameters were remeasured, and the results of this are shown in Table I. At first, laser fluence appears to have little effect on either sheet resistance and the passivation parameters, suggesting that there is incomplete crystallization of the polysilicon.[4,7] As laser fluence increases, the sheet resistance decreases while passivation parameters are mostly unaffected, which is

TABLE I

Summary Of Sheet Resistance And Passivation Parameters As A Function Of Increasing Laser Fluence, Repeated Scans At The Optimal[†] Laser Fluence, Champion Device[‡], And 450°C FGA Time For CSPC.

Sample Condition	**R$_S$ (Ω/sq)**	**Tau fit (µs)**	**iVoc (mV)**	**J$_0$ (fA/cm^2)**
As-Deposited	649	1762	683	29
0.96 J/cm^2 Fluence	639	1739	683	28
1.09 J/cm^2 Fluence[†]	495	1680	683	29
1.15 J/cm^2 Fluence	352	1209	680	29
1.22 J/cm^2 Fluence	257	742	674	28
1.09 J/cm^2 Scan 2	409	1672	684	27
1.09 J/cm^2 Scan 3	347	1616	684	27
1.09 J/cm^2 Scan 4	292	1598	684	27
1.09 J/cm^2 Scan 5	260	1534	684	26
1.09 J/cm2 Scan 6	230	1425	683	27
1.09 J/cm2 Scan 7	206	1269	682	27
1.09 J/cm2 Scan 8	145	1260	682	27
1.09 J/cm2 Scan 9	112	1187	681	27
Laser Annealed Champion[‡]	98	1628	680	33
Champion w/ 5 min FGA	100	1813	677	40
Champion w/ 10 min FGA	102	2095	683	27
Champion w/ 15 min FGA	98	2125	685	27

attributed to increased dopant activation and layer crystallization [3,6]. Above laser fluences of 1.22 J/cm^2, passivation parameters begin to rapidly degrade suggesting damage to the underlying tunnel oxide, loss of dopant, or possible laser ablation of a-Si [6]. Therefore, a laser fluence of 1.09 J/cm^2 is capable of decreasing the sheet resistance without appreciably impacting the effective lifetime, the iV_{OC}, or the J_0, and is therefore selected as the optimal fluence for repeated scans. Since low sheet resistances in the poly-Si are required for ohmic contact for later metallization, repeated scans are necessary to further lower the sheet resistance without impacting passivation parameters. The second section of Table I shows the dependence of device sheet resistance and passivation parameters on the number of repeated scans, demonstrating that repeated laser scans at the optimal fluence can bring the device sheet resistance below 100 Ω/sq for ohmic metal contact. Our champion test structure was achieved using repeated scans at 1.09 J/cm^2 laser fluence, and its sheet resistance and passivation parameters are shown in the third section of Table I. Thus, we have demonstrated a laser fluence condition which improves the electrical and structural properties of the polysilicon layer for subsequent metallization, with minimal impact to that layer's passivation. The slow decline in passivation parameters with repeated scans is attributed to a loss in hydrogen from the a-Si:H, which increases the defect density and subsequently impacts the passivation quality. After laser processing, the champion test structure was subjected to an FGA at 450 °C in 5 minute increments, to examine if reintroducing hydrogen to the annealed layer would improve its passivation parameters. Improvements in the passivation parameters increased only marginally after 15 minutes. These results are shown in the fourth section of Table I. After 15 minutes of FGA, the effective carrier lifetime of the champion test structure increased above its initial state to 2125 µs, had an improved iV_{OC} of 0.685 V, and a low 27 fA/cm^2 J_0 while the sheet resistance remained under 100 Ω/sq, demonstrating the viability of FGA in conjunction with laser processing.

IV. CONCLUSIONS

We have demonstrated a novel laser processing concept to replace the high-temperature furnace anneal for carrier-selective a-Si:H passivating layers for silicon solar cells. By utilizing laser processing, the polysilicon layer increases in crystallinity, increases in electrical conductivity due to dopant activation, and maintains passivation qualities due to the shallow absorption depth of the laser wavelength and the nano-timescale from the laser pulse width, with minimal thermal impact on the interfacial oxide. Combined with FGA, we demonstrate a passivating poly-Si/tunnel oxide/Si structure with a low 98 Ω/sq sheet resistivity, over 2.1 ms effective carrier lifetime, 27 fA/cm^2 J_0, and 685 mV iV_{OC} demonstrating the viability of our approach. By adapting the laser processing to a solar cell device, high-efficiency and well-passivated carrier selective silicon solar cells could be fabricated at a reduced thermal budget and without the detrimental effects of furnace annealing.

ACKNOWLEDGMENT

We acknowledge the support of the NASA Langley Professor Program.

REFERENCES

[1] E. Yablonovitch, T. Gmitter, R. M. Swanson, and Y. H. Kwark, "A 720 mV open circuit voltage SiO_x:c-Si:SiO_x double heterostructure solar cell." *Appl. Phys. Lett.,* vol. 47, 1211, 1985.

[2] W. Füssel, W. Henrion, and R. Scholz, "Structural, optical and electrical properties of SIPOS passivation layers." Microelectron. Eng., vol. 22, pp. 355-358, 1993.

[3] F. Feldmann, M. Simon, M. Bivour, C. Reichel, M. Hermle, and S. W. Glunz, "Carrier-selective contacts for Si solar cells." *Appl. Phys. Lett.*, vol. 104, 181105, 2014.

[4] R. Peibst, U. Römer, Y. Larionova, H. Schulte-Huxel, T. Ohrdes, M. Häberle, B. Lim, J. Krügener, D. Stichtenoth, T. Wütheruch, C. Schöllhorn, J. Graff, and R. Brendel, "Building blocks for back-junction back-contacted cells and modules with ion-implanted poly-Si junctions." In *IEEE 40th Photovoltaic Specialist Conference (PVSC)*, 2014, p. 8-13.

[5] P. Stradins, A. Rohatgi, S. Glunz, J. Benick, F. Feldmann, S. Essig, W. Nemeth, A. Upadhyaya, B. Rounsaville, Y.-W. Ok, B. G. Lee, D. Young, A. Norman, Y. Liu, J.-W. Luo, E. Warren, A. Dameron, V. LaSalvia, M. Page, M. Hermle, "Passivated tunneling contacts to n-type wafer silicon and their implementation into high performance solar cells: Preprint." In *Proc. 6th World Conf. Photovolt. Energy Convers.*, Kyoto, Japan, 2014, p. 1-4.

[6] A. D. Upadhyaya, Y.-W. Ok, E. Chang, V. Upadhyaya, K. Madini, K. Tate, B. Rounsaville, C.-J. Choi, V. Chandrasekaran, V. Yelundur, A. Gupta, and A. Rohatgi, "Ion-implanted screen-printed n-type solar cell with tunnel oxide passivated back contact." IEEE J. Photovoltaics, vol. 6, pp. 153-158, 2016.

[7] B. Nemeth, D. L. Young, M. R. Page, V. LaSalvia, S. Johnston, R. Reedy, and P. Stradins, "Polycrystalline silicon passivated tunneling contacts for high efficiency silicon solar cells." J. Mater. Res., vol. 31, pp. 671-791, 2016.

[8] S. Reiter, N. Koper, R. Reinke-Koch, Y. Larionova, M. Turcu, J. Krügener, D. Tetzlaff, T. Wietler, U. Höhne, J. D. Kähler, R. Brendel, and R. Peibst, "Parasitic absorption in polycrystalline Si-layers for carrier-selective front junctions." *Energy Procedia*, vol. 92, pp. 199-204, 2016.

[9] M. C. Gupta and D. E. Carlson, "Laser processing of materials for renewable energy applications." *MRS Energy & Sustainability*, vol. 2, E2, 2015.

[10] Z. Sun and M. C. Gupta, "Laser annealing of silicon surface defects for photovoltaics applications." *Surf. Sci.*, vol. 652, pp. 344-349, 2016.

[11] L. Wei, M. Vaudin, C. S. Hwang, G. White, J. Xu, and A. J. Steckl, "Heat conduction in silicon thin films: Effects of microstructure." *J. Mater. Res.,* vol. 10, pp. 1889-1896, 1995.

[12] G.R. Wolstenholme, N. Jorgensen, P. Ashburn, and G.R. Booker "An investigation of the thermal stability of the interfacial oxide in polycrystalline silicon emitter bipolar transistors by comparing device results with high - resolution electron microscopy observations." *J. Appl. Phys.,* vol. 61, pp. 225-233, 1987.

[13] D. Sands, “Heat Transfer: Pulsed laser heating and melting.” Engineering Applications, InTech, Vyacheslav Vikhrenko (Ed.), 2011.

[14] D. E. Kane and R. M. Swanson “Measurement of the emitter saturation current by a contactless photoconductivity decay method,” *Proc. 18th IEEE Photovoltaic Spec. Conf.*, Las Vegas, NV, USA, 1985, p. 578.

Laser Crystallization and Dopant Activation of a-Si:H Carrier-Selective Layer in TOPCon Si Solar Cells

George C. Wilkes, *Graduate Student Member, IEEE*, Ajay D. Upadhyaya, *Member, IEEE*,
Ajeet Rohatgi, *Life Fellow, IEEE*, and Mool C. Gupta, *Fellow, IEEE*

***Abstract*—Herein, we present a pulsed-laser processing method for crystallization and dopant activation of a highly n-doped amorphous silicon (a-Si:H) carrier-selective layer in a tunnel oxide passivated contact (TOPCon) Si solar cell structure. The laser method provides enhanced conductivity and implied open circuit voltage while reducing emitter saturation current density and surface heating, as opposed to conventional high-temperature furnace annealing of the bulk Si wafer with a TOPCon structure. We identify an appropriate laser wavelength, fluence, and layer thickness using modeling and simulations. Raman and Hall effect measurements demonstrate increased crystallinity and dopant activation, whereas photoconductive decay shows enhanced surface and interface passivation quality. Additionally, we examine the role of subsequent SiN_x deposition on further improving the passivation of laser-processed TOPCon layers to achieve a 5.9 kΩ/sq film sheet resistance, 2 ms effective carrier lifetime, 718 mV implied open-circuit voltage (iV_{OC}), and 8.6 fA/cm^2 one-side recombination current density (J_0) with the potential for further passivation improvement via laser process and a-Si layer thickness optimization.**

***Index Terms*—Carrier-selective contact, dopant activation, laser annealing, laser processing, silicon crystallization, surface passivation, tunnel oxide passivated contact (TOPCon).**

I. INTRODUCTION

CARRIER recombination in silicon solar cells can be greatly reduced by using passivating and carrier-selective interlayers between silicon and its metal electrodes to enhance cell efficiency. Highly doped amorphous silicon (a-Si:H), well studied as an interlayer in various Si devices, is receiving increasing interest as a carrier-selective layer for high-efficiency Si solar cells [1]–[7]. When coupled with a thin (<2 nm) passivating layer (such as SiO_2), surface passivation can be achieved without negatively impacting carrier transport. Additionally, tunnel-oxide passivating contacts are one of the few viable methods for eradicating diffusion and metal-contact-induced recombination because they relocate heavily doped diffused regions and metallized contacts outside of the absorbing base. The band alignment of the base, thin passivation layer, and carrier selective layer work together to create a high barrier for one carrier and low barrier for the other, providing carrier selectivity for low minority carrier recombination and efficient majority carrier transport [8], [9]. The energy diagram of this system is shown in Fig. 1.

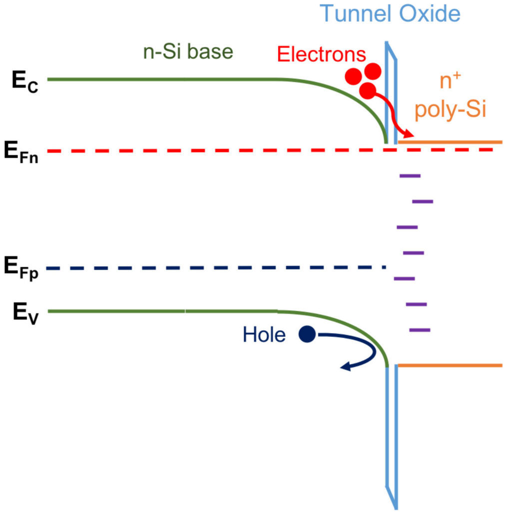

Fig. 1. Energy diagram showing carrier transport.

Typically, the highly doped a-Si or nanocrystalline silicon layer is deposited via plasma-enhanced chemical vapor deposition (PECVD) or low-pressure chemical vapor deposition (LPCVD) at low temperatures (between 200° and 600 °C) and a subsequent 30-min high-temperature anneal between 800° and 1000 °C is used to further crystallize the as-deposited layer [1]–[3], [5]–[7], increase structural and electrical stability [2]–[4], [6], [7], activate dopants within the layer [1], [6], [7], reduce short wavelength parasitic absorption by increasing crystallinity [10], and possibly generate pinholes in the interfacial oxide for carrier transport [3], [4]. Amorphous Si can reduce short-circuit current density values by as much as 9 mA/cm^2 for a 100 nm thick layer, which is reduced to 4 mA/cm^2 for poly-Si [10], emphasizing the need for layer crystallization. Dopant activation will decrease the sheet resistance of the poly-Si, enabling a low series resistance for subsequent metallization. However, high-temperature furnace anneals lead to several problems: first, degradation of the tunnel oxide and its interfaces [3]; second,

Manuscript received April 8, 2020; revised May 28, 2020; accepted June 22, 2020. Date of publication July 9, 2020; date of current version August 20, 2020. This work was supported by the NASA Langley Professor Program and the National Science Foundation (NSF) under Grant ECCS-2005098 and Grant I/UCRC-1338917. *(Corresponding author: Mool C. Gupta.)*

George C. Wilkes and Mool C. Gupta are with the University of Virginia, Charlottesville, VA 22904 USA (e-mail: gcw5qu@virginia.edu; mgupta@virginia.edu).

Ajay D. Upadhyaya and Ajeet Rohatgi are with the Georgia Institute of Techology, Atlanta, GA 30332 USA (e-mail: ajay.upadhyaya@ece.gatech.edu; ajeet.rohatgi@ece.gatech.edu).

Color versions of one or more of the figures in this article are available online at https://ieeexplore.ieee.org.

Digital Object Identifier 10.1109/JPHOTOV.2020.3006273

dopant diffusion from the poly-Si into the base which increases Auger recombination; third, incomplete dopant activation in the poly-Si; and finally, degradation of the absorber lifetime due to prolonged high-temperature exposure.

To alleviate these issues and grant further control over the processing, we investigated the use of ultraviolet pulsed-laser annealing to replace the secondary furnace-based high-temperature anneal. Laser-based solar cell manufacturing has gained increased interest in recent years, allowing for easy adoption [11], [12]. Pulsed-laser annealing allows for selective control over dopant activation and crystallization of the poly-Si layer while preventing oxide degradation, absorber degradation, and excessive diffusion. This is due to the short laser pulse (25 ns), which can activate dopants and crystallize the poly-Si in nanoseconds, and the shallow absorption depth (10 nm for Si) enabling the processing to only affect the desired layer. Coupled with the low thermal diffusivity of amorphous (0.10 cm^2/s) and polycrystalline silicon (0.14 cm^2/s) when compared to crystalline silicon (0.90 cm^2/s) [13], it is possible to reach the high temperatures required for activation and crystallization while preventing tunnel oxide break-up at 900 °C [14] under nanosecond pulsed-laser heating [15]. This gives us a unique advantage in preventing oxide break-up while annealing the poly-Si layer.

Herein, we investigate the change in passivation, crystallization, and dopant concentration of laser-processed a-Si:H, carrier-selective passivating contacts, and the impact of subsequent SiN_x deposition to replace the furnace-based high temperature anneal for tunnel oxide passivated contact (TOPCon) for high efficiency Si solar cells. This work enhances our earlier conference proceeding [16] by providing modeling and simulation results, Raman and Hall effect studies, and improved passivation of a 718 mV implied open circuit voltage. The investigations were carried out with a 355 nm laser wavelength. We also report the results of the effect of passivating layer thickness (12 and 200 nm), as the 355 nm wavelength will have a different impact on these layers given the fixed absorption depth. Due to the short absorption depth (∼10 nm) of the ultraviolet laser wavelength, the temperature of c-Si/SiO_2/a-Si interface may not be high enough to improve the passivation. Thicker films can be used if a longer wavelength laser is utilized.

II. OPTICAL MODELING AND LASER SIMULATION

In order to understand the impact of the laser wavelength and fluence on the absorption and resultant temperature increase in the TOPCon structure, the spectral optical properties of amorphous and crystalline silicon were modeled and the laser-material interaction was simulated to provide a conceptual background for the study.

A. *Choice of Laser Wavelength From Optical Modeling*

The optical properties of amorphous and crystalline silicon were modeled to assess an appropriate wavelength for laser annealing using Essential Macleod optical modeling software. While laser wavelengths can vary greatly, high-power lasers based on Nd:YAG are typically restricted to 1064, 532, 355, and 266 nm wavelengths based on the first, second, third, and fourth harmonic generation. We looked at the absorption properties of silicon with varying degrees of crystallinity from amorphous to single crystal using data from Sopra SA [17]. Throughout the visible spectrum, the absorption coefficient can shift by an order of magnitude across the aforementioned allotropes, but is relatively constant belowmentioned 360 nm and abovementioned 940 nm. A constant absorption depth across allotropes ensures consistent laser energy absorption regardless of the crystallinity of the Si, and is therefore desired to ensure film homogeneity. However, abovementioned 940 nm the absorption depth reaches 100 μm, indicating the majority of the laser energy will be absorbed in the bulk wafer and not in the film. Therefore, a laser wavelength of 355 nm was chosen to ensure sufficient energy absorption in the a-Si film without large amounts of c-Si substrate absorption. Fig. 2 shows a log plot of the absorption depth of silicon with various states of crystallinity from amorphous to single crystal for ultraviolet wavelengths.

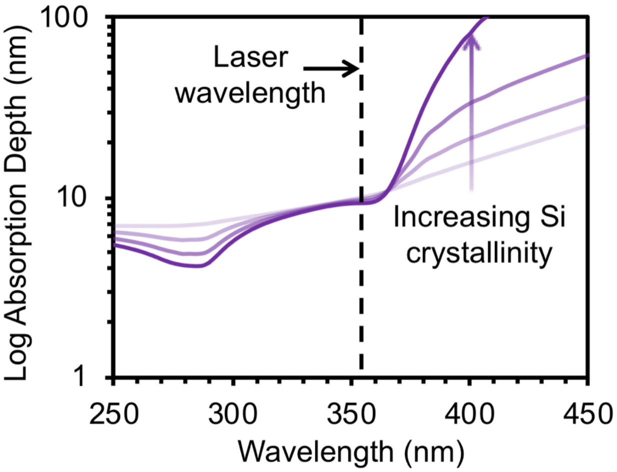

Fig. 2. Log plot of the ultraviolet absorption depth of silicon of various degrees of crystallinity from amorphous to single crystal [17]. The arrow direction indicates the trend of increasing crystallinity. The dashed line indicates the selected laser wavelength, which will have identical absorption regardless of the silicon's degree of crystallinity.

B. *Simulation of Laser-Si Interaction*

LCPSim, a finite differences code programmed in MATLAB and developed by Andreas Fell at Fraunhofer ISE, can simulate laser optical effects such as reflection and absorption as well as thermodynamic effects such as heat transport and phase change within various materials [18], [19]. This simulation was used to assess the effect of laser fluence on the temperature versus depth within silicon to support our experimental results. Only the laser interaction with crystalline silicon could be reliably modeled, because the varying film density of a-Si means it does not have consistent thermal diffusivity or optical properties. An enthalpy-based heat transfer model was used along with the laser wavelength set to 355 nm, pulse width to 25 ns, and pulse shape to Gaussian. Fig. 3 shows the simulated temperature versus depth in crystalline silicon for single laser pulses of increasing fluence. Additionally, the substrate temperature after times of 20, 10, and 7 μs, which correspond to the time between pulses for repetition rates of 50, 100, and 150 kHz, respectively, were investigated.

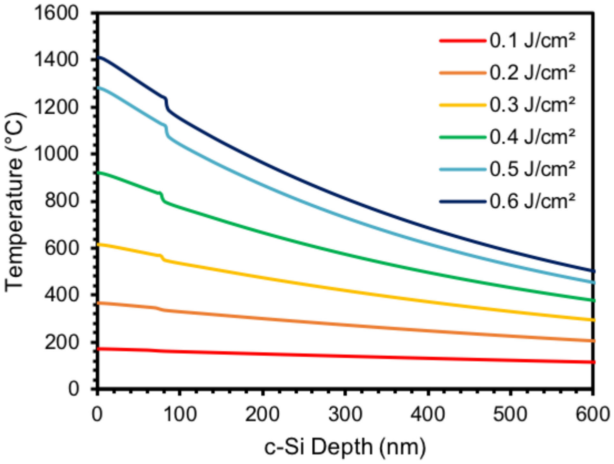

Fig. 3. Modeled results of temperature versus crystalline silicon depth for increasing laser fluences of a single laser pulse. The simulated laser had a 355 nm wavelength and 25 ns pulse width and was modeled using LCPSim from Fraunhofer ISE with permission from Andreas Fell [18].

We found that despite the high repetition rates (50–150 kHz) used in laser raster processing, substrate temperature returns to near 25 °C between pulses for the fluences assessed, suggesting that there is no thermally induced increase in absorption between pulses and each pulse has its own discrete, isolated effect on the sample. The thermal diffusivities for crystalline, polycrystalline, and a-Si are 0.90, 0.10–0.14, and <0.10 cm^2/s, respectively [13]. Therefore, the true temperatures at increasing depths in our a-Si may be lower.

III. DEVICE FABRICATION AND LASER PROCESSING

This study used high lifetime, 100 mm, 500 Ω-cm resistivity, 298 μm thick, textured, n-type FZ wafers so that the J_0 variation better reflects the change in surface passivation, and sheet resistance measurements reflect the change in film resistivity. The wafers are planarized and etched using a KOH solution and then cleaned in an RCA solution. Next, a 1.4–1.5 nm-thick tunnel oxide is grown symmetrically on both sides of the wafer using an HNO_3 solution at 100 °C, verified by ellipsometry. After this, we deposit a 12 nm-thick phosphorus-doped a-Si:H layer on both sides of the structure using a UNAXIS PECVD at a deposition temperature of 300 °C. Deposition details can be found in Rohatgi *et al.* [9]. This layer is subjected to a furnace anneal at 875 °C for 30 min or pulsed laser annealing to further crystallize the layer, activate dopants, and improve its interface with SiO_2 [6]. Using a 355 nm wavelength, 25 ns pulse width, Coherent MATRIX-355, diode-pumped solid-state laser with a spot size of 160 μm, and a computer-controlled galvanometric scan head, we optimized the laser fluence and pulse overlap. The pulsed laser is raster scanned across the entire surface of the 25 × 25 mm sample with a repetition rate of 50 kHz, a scan speed between 2–8 m/s, and a raster line spacing of 40–160 μm. Fig. 4 shows a schematic of the laser setup, device structure, and laser raster pattern.

Due to the 12 nm film thickness and sample roughness, characterization with Raman and Hall effect measurement becomes difficult because the majority of the Raman signal would come from the bulk Si substrate, and Hall effect measurements on rough samples with ultrathin films leads to inconsistent results. Therefore, 200 nm a-Si films were deposited and similarly furnace or laser annealed to characterize the crystallization and dopant activation via those methods. Due to the increased film thickness, the ultraviolet laser wavelength was unable to reach the c-Si/SiO_2/a-Si interface and influence the passivation, but Raman and Hall effect characterization was simplified.

To examine how SiNx further improves the passivation properties, 60 nm of SiN_x was deposited symmetrically on a prelaser processed sample with a Trion Orion PECVD system. Films were deposited at a substrate temperature of 350 °C and pressure of 600 mTorr using 600 sccm of 2% SiH_4 balanced with N_2 and 15 sccm of NH_3. The films were annealed at 350 °C for 30 min after deposition to ensure suitable film adhesion.

IV. LASER PARAMETER OPTIMIZATION

To evaluate the passivation parameters of the symmetric structures shown in Fig. 4(b), we used the method developed by Kane and Swanson [20] using a Sinton Instruments WCT-120 quasi-steady-state photoconductance decay (QSSPCD) measurement at a specified minority carrier density of 1.0×10^{15} cm^{-3} in generalized (1/1) analysis mode. We divided J_0 values by two to reflect the saturation current of one of the two layers in the symmetric structure which is designated by $1 \times J_0$. We measured sheet resistances of the deposited films with a Jandel multiposition probe with a linear 1.00 mm probe spacing and a 25 μm tip radius.

After deposition of the 12 nm n^+ a-Si:H films but before any subsequent anneal, the as-deposited films had an average sheet resistance exceeding 10 kΩ/sq, active dopant concentration on the order of 10^{16} cm^{-3}, lifetime fit of 733 μs, implied open circuit voltage (iV_{OC}) of 679 mV, and $1 \times J_0$ of 25.6 fA/cm^2. One sample was conventionally annealed in a furnace at 875 °C for 30 min in inert nitrogen to activate the dopants, crystallize the a-Si, and improve the interface it shares with SiO_2. After annealing, the sheet resistance dropped to 0.6 kΩ/sq and the active dopant concentration increased to 7.7×10^{19} cm^{-3}, indicating phosphorus moving from interstitial to substitutional lattice sites and solid-phase crystallization of the n^+ a-Si. The lifetime and iV_{OC} increase to 3586 μs and 719 mV, respectively, whereas the $1 \times J_0$ decreased to 5.2 fA/cm^2, indicating excellent surface passivation.

To reduce the thermal budget for this process and the amount of time at which the structure stays at elevated temperatures, as-deposited samples were laser-processed across a variety of laser fluences and pulse overlap percentages on both sides of the symmetric structure. The process optimization results are shown in Fig. 5 and do not include subsequent SiN_x deposition. Initially, as the laser fluence increases, the film sheet resistance decreases and the iV_{OC} increases, suggesting simultaneous dopant activation and passivation improvement. The iV_{OC} peaks at 703 mV at a fluence of 0.34 J/cm^2, which corresponds to a temperature range near 800 °C from the simulation and coincides well with conventional furnace annealing temperatures at

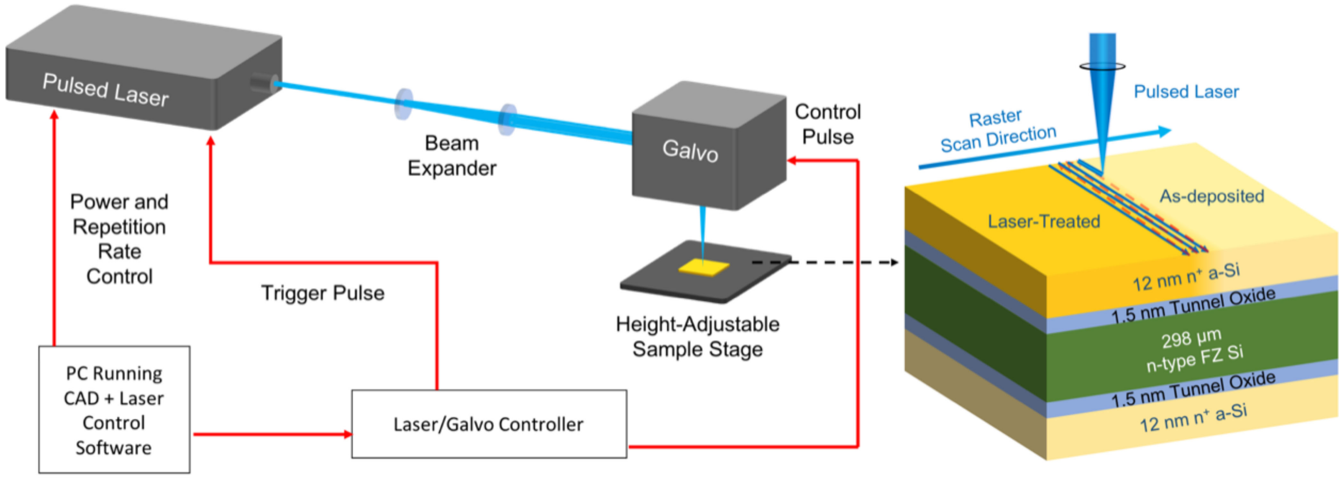

(a) (b)

Fig. 4. (a) Schematic of pulsed-laser processing setup with scanning galvanometer. (b) Symmetric carrier-selective passivating-contact device structure for QSSPCD evaluation of passivation showing laser raster scan pattern.

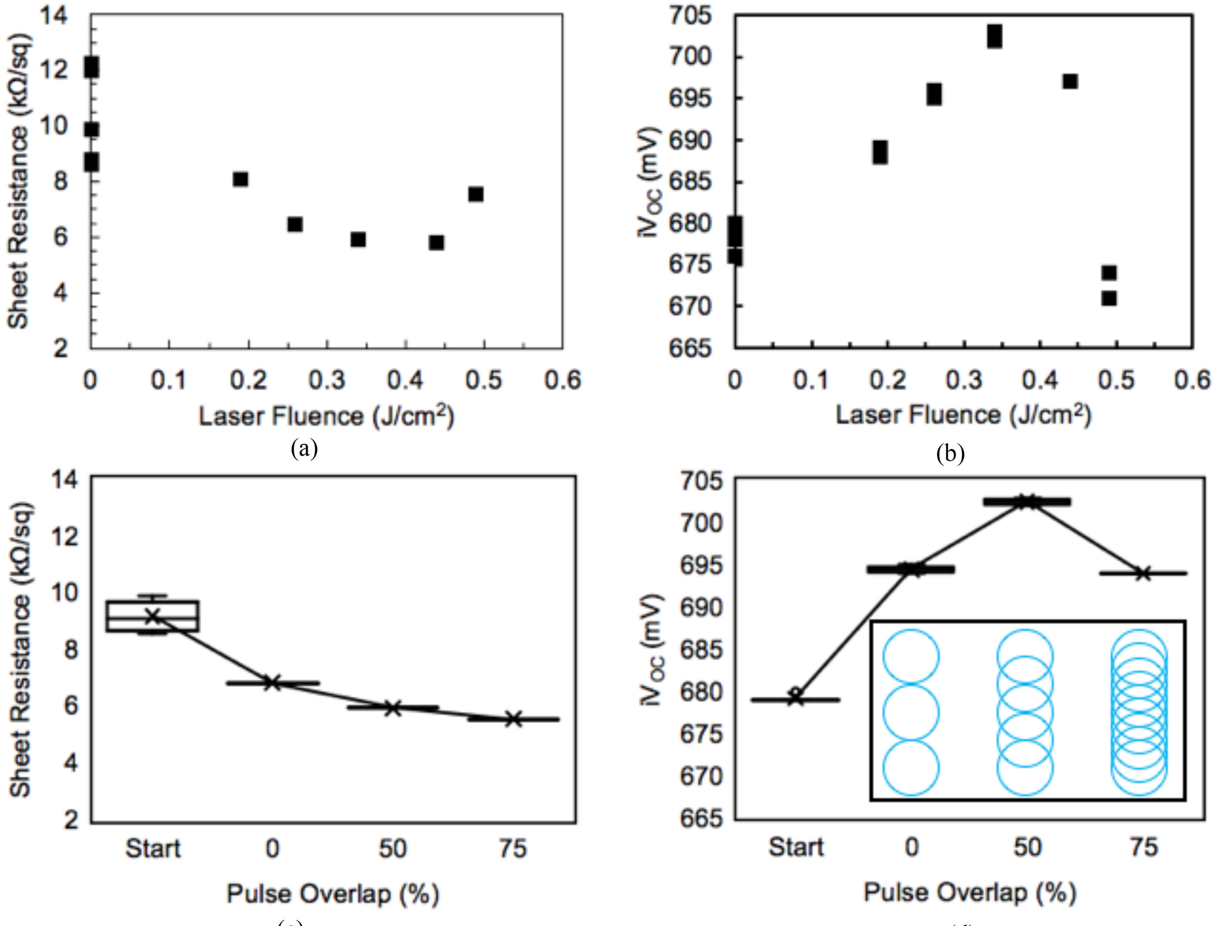

(a) (b)

(c) (d)

Fig. 5. (a) Fluence of a single laser pulse versus film sheet resistance. (b) Device iV_{OC}. The optimal fluence occurs at 0.34 J/cm^2 based on low sheet resistance and high iV_{OC}. (c) Percentage of pulse overlap at the optimal laser fluence versus film sheet resistance. (d) Device iV_{OC}. While greater overlap resulted in a lower sheet resistance, the peak device iV_{OC} occurred at a pulse overlap of 50%. (d, inset) A top-down illustration of how pulse overlap of a Gaussian beam influences the number of pulses per area. All poly-Si films used in this figure were 12 nm thick. Optimization data does not include subsequent SiN_x deposition.

TABLE I
ELECTRICAL PARAMETERS OF TOPCON TEST STRUCTURES

Sample	R_{Sheet} (kΩ/sq)	N_D (cm^{-3})	τ_{fit} (µs)	iV_{OC} (mV)	$1\times J_0$ (fA/cm^2)
As-Deposited, Pre-annealing	> 10[a]	~10^{16}	733	679	25.6
875 °C, 30 min, N_2 Furnace anneal	0.6	7.7×10^{19}	3586	719	5.2
Optimal Laser Processed[b] Sample	5.9	7.1×10^{18}	1333	703	15.5
Laser Processed Sample with Post-Deposition of SiN_x	5.9	7.1×10^{18}	2001	718	8.6

Sheet resistance, active dopant concentration, lifetime fit, implied open-circuit voltage, and one side recombination current density for the starting as-deposited, furnace annealed, champion laser annealed, and laser annealed with subsequent SiN_x deposition samples. All poly-Si films used in this table were 12 nm thick.

[a] Sheet resistance is unmeasurable above 10 kΩ/sq.

[b] Optimal condition is at a laser fluence of 0.34 J/cm^2.

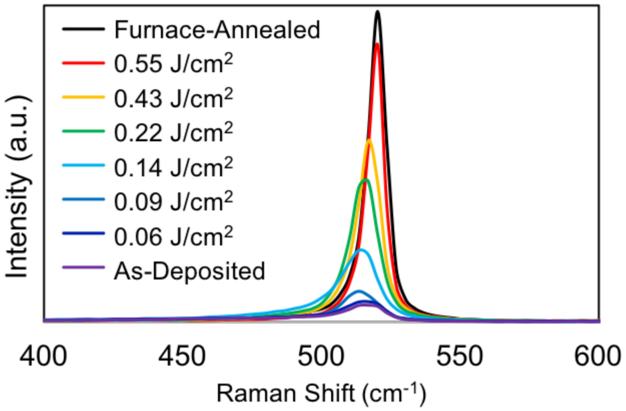

Fig. 6. Raman spectra of 200 nm thick as-deposited, furnace annealed and a-Si films that were laser processed under a single pulse at increasing laser fluence. As the laser fluence increases, the intensity of the 520 cm^{-1} Si peak increases, demonstrating increased crystallinity under increasing laser fluence. Thicker films were used to ensure the Raman signal only comes from the deposited film and not the wafer.

800 °C. For instance, Rohatgi *et al.* [9] obtained a 702 mV iV_{OC} when furnace annealing at 800 °C for 1 h, whereas their iV_{OC} increased to 720 mV at 875 °C. Above this fluence, the drop in sheet resistance flattens out with a minimum of 5.8 kΩ/sq and begins to increase again at even higher fluences. This suggests that laser activation of dopants may saturate at this density for 12 nm n^+ poly-Si films and the sheet resistance increase at fluences abovementioned 0.45 J/cm^2 may indicate dopant loss or a-Si film ablation. Similarly, the drop in iV_{OC} at higher fluences could indicate damage to the underlying tunnel oxide interfaces and reduced band bending as a result of dopant or film loss. The laser fluence has to be very precisely controlled to achieve the higher 720 mV iV_{OC} demonstrated at 875 °C annealing, which is difficult with a Gaussian beam profile due to the nonconstant intensity throughout the beam area. Therefore, the optimal fluence was chosen as 0.34 J/cm^2 for laser annealing and was used to optimize the pulse overlap. The pulse overlap was adjusted by changing the galvanometer scanning speed to 2, 4, and 8 m/s and the scan line spacing to 40, 80, and 160 μm, respectively, at a fixed repetition rate of 50 kHz and laser spot size of 160 μm. The pulse and scan line spacing were kept identical for simplicity. The inset of Fig. 5(d) shows a top-down illustration of the pulse overlap. The film sheet resistance continued to decrease with increasing overlap, reaching a minimum value of 5.5 kΩ/sq at an overlap percentage of 75%. However, the iV_{OC} peaked at an overlap percentage of 50% and decreased at higher overlap percentages. This indicates that while a higher overlap percentage could grant increased dopant activation, it may cause minor damage to the tunnel oxide interfaces from photomechanical stress. Therefore, 50% (4000 mm/s scan speed and 80 μm scan line spacing) was selected as the optimal pulse overlap.

Table I summarizes the dopant activation and passivation of the as-deposited, furnace annealed, optimally laser-processed sample, and optimally laser-processed sample with 60 nm of SiN_x symmetrically deposited on both sides of the sample.

V. CHARACTERIZATION OF A-SI:H LAYER CRYSTALLIZATION AND DOPANT ACTIVATION

To assess the degree to which ultraviolet laser annealing of n^+ a-Si activates dopants and crystallizes the a-Si, thicker, 200 nm films were deposited via a Tystar tube furnace LPCVD tool at 588 °C on top of a 1.4–1.5 nm HNO_3 grown tunnel oxide. Details of this process are published elsewhere by Upadhyaya *et al.* [6]. Raman spectra were taken with a Renishaw inVia confocal Raman microscope with an 1800 lines/mm grating (2.93 cm^{-1} resolution) at an excitation wavelength of 405 nm to reduce the signal coming from the substrate. Fig. 6 shows the Si Raman peak for as-deposited, furnace annealed, and laser annealed samples at increasing laser fluence where each laser annealed spectra is from a single laser pulse on an as-deposited sample. Amorphous Si has a broad Raman band based on the wide variety of different bond lengths in its amorphous state, whereas c-Si has a sharp Raman peak centered at 520.5 cm^{-1} corresponding to a high count of similar short-length bonds. With increasing fluence, the peak intensity increases and the peak width decreases indicating increased crystallinity. Part of the signal intensity increase with crystallinity will be the result of an increased interaction volume with an increased absorption depth of c-Si (100 nm) versus a-Si (11 nm) at 405 nm as shown in Fig. 2. While the high 0.55 J/cm^2 fluence spectra shows crystallinity on par with that of the furnace annealed poly-Si, that fluence is too high for thinner 12 nm a-Si samples, as it causes a large drop in iV_{OC} from oxide interface disruption. The thickness of the deposited a-Si layer could potentially be optimized to allow for a higher fluence without impacting the tunnel oxide interface.

Carrier concentration and sheet resistance were calculated from the Hall mobility, measured at room temperature with an Ecopia HMS-3000 hall measurement system using a 0.55 T permanent magnet and spring probes configured to the van der Pauw arrangement on square samples and the results are shown

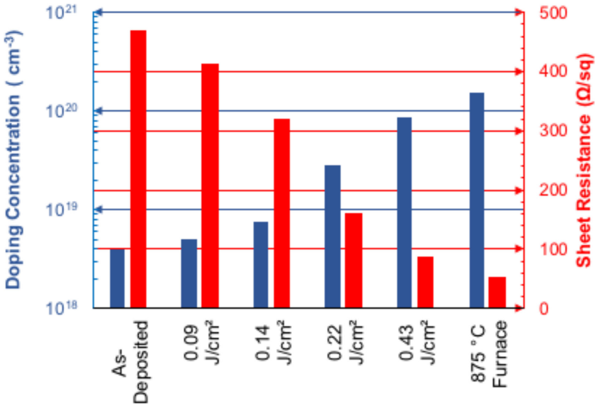

Fig. 7. Hall-effect measurement of doping concentration (left axis, blue bars) and sheet resistance (right axis, red bars) for 200 nm thick as-deposited, furnace annealed, and laser annealed a-Si films, showing an increase in doping concentration and decrease in sheet resistance with increasing laser fluence that is comparable to furnace annealing.

in Fig. 7. As-deposited samples begin with a carrier concentration of 4.0 × 10^{18} cm^{-3} and sheet resistance of 470 Ω/sq. Since most of the phosphorus dopant is in interstitial sites and few lattice sites exist in the amorphous state, it contributes little to the electrical properties of the film. As the laser fluence increases, dopant activation continues to rise, increasing the measured dopant concentration and decreasing the film sheet resistance as the amorphous film crystallizes and the phosphorus dopant enters the crystalline lattice. The highest fluence evaluated, 0.43 J/cm^2, has a measured dopant concentration of 8.7 × 10^{19} cm^{-3} and sheet resistance of 87 Ω/sq comparable to the furnace annealed 200 nm poly-Si sample's 1.5 × 10^{20} cm^{-3} concentration and 52 Ω/sq sheet resistance, indicating successful activation of dopant and film crystallization with room for future improvement through laser annealing optimization. Dopant concentration profiles for thermally annealed films can be found in Upadhyaya *et al.* [6].

The a-Si:H film thickness must be carefully chosen for improved performance at a given laser wavelength. Thicker a-Si:H films, in the range of 100–200 nm, will absorb the laser light in the upper part of the film and the thermal annealing of interface defects does not occur due to the temperature gradient in the film. If the a-Si:H film thickness is too low (∼10 nm), then part of the laser light will be absorbed by the Si substrate, inducing defects. For a 355 nm wavelength laser, an optimum a-Si:H film thickness appears to be around 20–40 nm to achieve higher performance from laser annealing. Poly-Si layers with a 20–40 nm thickness may be suitable for front surface TOPCon, but is currently not suitable for screen printing applications on the rear surface, which require 100–200 nm thick poly-Si layers for firing. However, by using a longer pulse width of 50–100 ns or a longer laser wavelength of 400–450 nm, effective and uniform annealing of a thicker poly-Si for screen printing becomes feasible [6]. We have demonstrated the feasibility of laser crystallization and dopant activation of a-Si:H in TOPCon carrier-selective contacts, and further improvements can be made by optimizing the layer thickness and corresponding annealing fluence.

VI. CONCLUSION

We have demonstrated a novel laser processing concept to replace the high-temperature furnace anneal for n-type TOPCon carrier-selective passivating contacts for silicon solar cells. By utilizing laser processing, the polysilicon layer increases in crystallinity, electrical conductivity due to dopant activation, and passivation due to the shallow absorption depth of the laser wavelength and the nano-timescale from the laser pulsewidth, with minimal thermal impact on the interfacial oxide. Optical modeling and LCPSim simulations help shape our knowledge of the laser-material interaction process and provide a foundation for experimental work. Combined with a SiN$_x$ layer, we demonstrate a well-passivated SiN$_x$/poly-Si/tunnel oxide/Si structure with a low 5.9 kΩ/sq poly-Si sheet resistivity, over 2001 ms effective carrier lifetime, 718 mV iV$_{OC}$, and 8.6 fA/cm^2 J$_0$ demonstrating the viability of our approach. Raman and Hall effect characterization of 200-nm laser-annealed a-Si films show that a degree of crystallinity and dopant activation comparable to 875 °C furnace-annealed films can be achieved.

A thicker a-Si film, potentially in the range of 20–40 nm would allow for a higher fluence to be used, granting increased crystallinity and dopant activation but reducing damage to the tunnel oxide interfaces due to the temperature decrease at increased thickness. By adapting the laser processing to a solar cell device, high-efficiency and well-passivated carrier selective silicon solar cells could be fabricated at a reduced thermal budget and without the heating of the entire wafer under furnace annealing. Thicker a-Si films and use in a full device structure will be the subject of future study.

ACKNOWLEDGMENT

The authors would like to thank A. Fell and Fraunhofer ISE for provision of and assistance with LCPSim software.

REFERENCES

[1] E. Yablonovitch, T. Gmitter, R. M. Swanson, and Y. H. Kwark, "A 720 mV open circuit voltage SiO$_x$:c-Si:SiO$_x$ double heterostructure solar cell," *Appl. Phys. Lett.*, vol. 47, 1985, Art. no. 1211.

[2] W. Füssel, W. Henrion, and R. Scholz, "Structural, optical and electrical properties of SIPOS passivation layers," *Microelectron. Eng.*, vol. 22, pp. 355–358, 1993.

[3] F. Feldmann *et al.*, "Carrier-selective contacts for Si solar cells." *Appl. Phys. Lett.*, vol. 104, 2014, Art. no. 181105.

[4] R. Peibst *et al.*, "Building blocks for back-junction back-contacted cells and modules with ion-implanted poly-Si junctions," in *Proc. IEEE 40th Photovolt. Specialist Conf.*, 2014, pp. 8–13.

[5] P. Stradins *et al.*, "Passivated tunneling contacts to n-type wafer silicon and their implementation into high performance solar cells: Preprint," in *Proc. 6th World Conf. Photovolt. Energy Convers.*, Kyoto, Japan, 2014, pp. 1–4.

[6] A. D. Upadhyaya *et al.*, "Ion-implanted screen-printed n-type solar cell with tunnel oxide passivated back contact," *IEEE J. Photovolt.*, vol. 6, no. 1, pp. 153–158, Jan. 2016.

[7] B. Nemeth *et al.*, "Polycrystalline silicon passivated tunneling contacts for high efficiency silicon solar cells," *J. Mater. Res.*, vol. 31, pp. 671–791, 2016.

[8] Y. Tao *et al.*, "Carrier selective tunnel oxide passivated contact enabling 21.4% efficient large-area N-type silicon solar cells," in *Proc. IEEE 43rd Photovolt. Specialists Conf.*, 2016, pp. 2531–2535.

[9] A. Rohatgi *et al.*, "Fabrication and modeling of high-efficiency front junction N-type silicon solar cells with tunnel oxide passivating back contact," *IEEE J. Photovolt.*, vol. 7, no. 5, pp. 1236–1243, Sep. 2017.

[10] S. Reiter *et al.*, "Parasitic absorption in polycrystalline Si-layers for carrier-selective front junctions." *Energy Procedia*, vol. 92, pp. 199–204, 2016.

[11] M. C. Gupta and D. E. Carlson, "Laser processing of materials for renewable energy applications." *MRS Energy Sustain.*, vol. 2. E2, pp. 1–15, 2015.
[12] Z. Sun and M. C. Gupta, "Laser annealing of silicon surface defects for photovoltaics applications." *Surf. Sci.*, vol. 652, pp. 344–349, 2016.
[13] L. Wei *et al.*, "Heat conduction in silicon thin films: Effects of microstructure." *J. Mater. Res.*, vol. 10, pp. 1889–1896, 1995.
[14] G. R. Wolstenholme, N. Jorgensen, P. Ashburn, and G. R. Booker, "An investigation of the thermal stability of the interfacial oxide in polycrystalline silicon emitter bipolar transistors by comparing device results with high-resolution electron microscopy observations." *J. Appl. Phys.*, vol. 61, pp. 225–233, 1987.
[15] D. Sands, "Pulsed laser heating and melting," *Heat Transfer Engineering Applications*, V. Vikhrenko, Ed. Rijeka, Croatia: InTech, 2011.
[16] G. C. Wilkes, A. D. Upadhyaya, A. Rohatgi, and M. C. Gupta, "Laser crystallization and dopant activation for a-Si:H film in carrier-selective contacts for silicon solar cells," in *Proc. IEEE 46th Photovolt. Specialists Conf.*, 2019, pp. 2709–2712.
[17] Optical Data from Sopra SA. [Online]. Available: http://sspectra.com/sopra.html, Accessed: Feb. 18, 2020.
[18] A. Fell and G. P. Willeke, "Fast simulation code for heating, phase changes and dopant diffusion in silicon laser processing using the alternating direction explicit (ADE) method," *Appl. Phys. A*, vol. 98, no. 2, pp. 435–440, 2010.
[19] A. Fell, "Modelling and simulation of laser chemical processing (LCP) for the manufacturing of silicon solar cells," Ph.D. Dissertation, Dept. Physik, Univ. Konstanz, Konstanz, Germany, 2010.
[20] D. E. Kane and R. M. Swanson, "Measurement of the emitter saturation current by a contactless photoconductivity decay method," in *Proc. 18th IEEE Photovolt. Specialists Conf.*, Las Vegas, NV, USA, 1985, pp. 578–583.

George C. Wilkes (Graduate Student Member, IEEE) received the B.S. degree in physics with a minor in mathematics from James Madison University in Harrisonburg, Harrisonburg, VA, USA, in 2015. Since 2015, he has been working toward the Ph.D. degree with National Institute of Aerospace and the University of Virginia, Charlottesville, VA, USA.

He is currently a Graduate Research Assistant with the National Institute of Aerospace, University of Virginia. He has written and co-authored four publications on low-temperature and laser applications for perovskite and silicon solar cells. His research interests include selective carrier transport and passivation layers for solar cells and how laser processing can enable increased performance with selective energy deposition at low temperatures, increasing throughput, and reducing manufacturing costs.

Mr. Wilkes was a finalist in the 2018 NASA Big Idea competition for his work on a photovoltaic balloon for energy generation on Mars. He also received the award for Best Student Paper at the National Institute of Aerospace, in 2019.

Ajay D. Upadhyaya (Member, IEEE) received the B.S. degree in electrical and computer engineering with an emphasis on semiconductors from the Georgia Institute of Technology in Atlanta, Atlanta, GA, USA, in August 2001, and the MBA degree with a focus in marketing from Mercer University, Atlanta, GA, USA, in 2006.

He has been with the Georgia Institute of Technology since 2001 in many capacities. He a Senior Research Engineer and Operations Manager with the University Center of Excellence for Photovoltaics Research and Education, Georgia Institute of Technology. He has authored or co-authored more than 50 publications in journals and conference proceedings. His current interests are to make large-area, high-efficiency n- and p-type monocrystalline silicon solar cells at lower cost through technology innovations such as passivating contact, selective emitter, laser processes, and plating. In the past, he has worked to enhance lower quality silicon materials such as multicrystalline, ribbon, and Edge-defined film-fed growth (EFG) silicon to enhance the quality and performance of solar cells through existing processing steps.

Mr. Upadhyaya was the recipient of the Best Researcher Award at Georgia Tech. He is on award committees at Georgia Tech and has chaired several sessions at the IEEE Photovoltaic Specialist Conference.

Ajeet Rohatgi (Life Fellow, IEEE) received the Ph.D. degree in metallurgy and material science from Lehigh University, Bethlehem, PA, USA, in 1977.

He is a Regents Professor and John H. Weitnauer, Jr., Chair with the College of Engineering and a Georgia Research Alliance Eminent Scholar. He is the Founding Director of the University Center of Excellence for Photovoltaic Research and Education, Georgia Institute of Technology, Atlanta, GA, USA, in 1982 and the Founder and CTO of Suniva Inc., in 2008. He has authored more than 500 technical papers in this field and has been awarded 17 patents. His current research interests include the development of cost and efficiency roadmaps for attaining grid parity with silicon photovoltaics (PV), the design and fabrication of low-cost high- efficiency cells on mono and multicrystalline silicon, and the performance and economics of PV systems.

Prof. Rohatgi is very active on various award committees with the Georgia Institute of Technology. He was the recipient of the IEEE PVSC William Cherry Award, the NREL's Department of Energy Rappaport Award, the Outstanding Research Program Development Award, and the Hoyt Clark Hottel Award for outstanding educator and innovator in the field of PV from the American Solar Energy Society.

Mool C. Gupta (Fellow, IEEE) received his Ph.D. degree in physics from Washington State University, Pullman, WA, USA, in 1973.

He was a Postdoctoral Fellow with Cornell University and a Senior Research Fellow with the California Institute of Technology. From 1998 to 2005, he was the Director of the Applied Research Center with Old Dominion University. Since 2005, he has been the Langley Distinguished Professor with the Electrical and Computer Engineering Department with the University of Virginia. He is the Founding Director of the NSF Industry/University Cooperative Research Center for Lasers and Plasmas at the University of Virginia. He has authored 250 scientific publications in various technical journals and has been awarded 28 US and international patents. His current research interests include the applications of high-powered lasers for solar cell manufacturing, thermophotovoltaics, photonic devices, laser microtexturing of surfaces, and infrared detectors.

Prof. Gupta is the Editor-in-Chief of the *Handbook of Photonics*, CRC Press, 1st and 2nd edition. He is a Fellow of the Optical Society of America, an Inductee of the Kodak Inventor's Gallery, Chair of the NRC NASA Technology Roadmap Materials Panel, and Principal Investigator for DARPA, ARO, NASA, NSF, DOE, and NRL.

Laser Annealing of Carrier-Selective MoO$_x$ Layers for Silicon Solar Cells

George C. Wilkes
Electrical and Computer Engineering
Univesity of Virginia
Charlottesville, USA
gcw5qu@virginia.edu

Mool C. Gupta
Electrical and Computer Engineering
Univesity of Virginia
Charlottesville, USA
mgupta@virginia.edu

***Abstract*—Carrier-selective contacts based on dopant-free, transition metal oxides are attracting increased interest for silicon heterojunction solar cells. Sub-stoichiometric molybdenum trioxide (MoO$_x$) has been demonstrated as one of the most promising candidates to replace a-Si, however it has poor temperature stability upon furnace annealing in a completed device. Herein, we demonstrate a pulsed laser annealing method for substantially improving the passivation of carrier-selective MoO$_x$ layers for silicon solar cells and compare it to a furnace annealing approach, facilitating future investigations.**

Keywords—laser annealing, laser processing, surface passivation, carrier-selective contacts, silicon solar cells.

I. Introduction

Efficient photovoltaics have two essential functions: (1) converting light into electron-hole pairs, and (2) effectively separating these pairs and extracting them at the electrodes before they recombine. Carrier-selective contacts have received increased interest in recent years because of their ability to collect one type of carrier (e.g. holes) while blocking the other (e.g. electrons). Additionally, these layers also provide passivation of the absorber surfaces making them the most promising method for reducing recombination at the interfaces of crystalline-Si (c-Si) photovoltaics while enabling effective carrier transport.

Current top candidates for high efficiency include solar cells with heterojunction with intrinsic thin layer (HIT)-based contacts and tunnel-oxide passivating contacts (TOPCon) and have achieved power conversion efficiencies of 26.7% [1] and 25.8% [2], respectively, however they require costly deposition techniques like PECVD or high-temperature (>800 °C) thermal treatments. To reduce fabrication complexity, temperature, and cost, transition metal oxides (TMO) carrier-selective contacts have generated increased interest and demonstrated device efficiencies of 20.7% [3] with simulated device structures reaching efficiencies of 25.3%–27.95% [4], [5]. TMO contacts can be deposited with simple techniques like thermal evaporation [3], [6] at low temperatures and without dopants while retaining ideal optical characteristics, carrier-selectivity, and passivation. Removal of hydrogenated amorphous silicon (a-Si:H) entirely would reduce the amount of toxic and flammable process gases used and fabrication complexity. Due to a-Si low band gap of 1.7 eV, there is also interest in removing them entirely to reduce parasitic absorption.

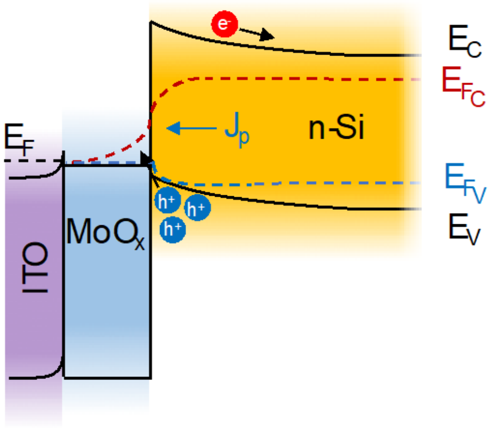

Fig. 1. Energy diagram showing carrier transport of MoO$_x$ hole-selective contact, based on induced band bending.

High-work function transition metal oxides, such as sub-stoichiometric molybdenum trioxide (MoO$_x$, x <3), have shown promise in recent years as hole-selective layers [3], [4], [6], [8], [9]. Depending on the exact stoichiometry, MoO$_x$ has a high band gap of ~3 eV [10], reducing parasitic absorption, and a high work function 5.5–6.8 eV [11], enabling effective hole selectivity. The high work function induces upward band-bending at the Si surface causing inversion, reducing the electron surface concentration and increasing the hole current density to the contact [12]. Therefore, carrier selectivity is obtained, not from induced band-bending, but by the minimal valence band offset and high conduction band offset with c-Si. The energy band diagram for MoO$_x$-based carrier-selective contacts is shown in Fig. 1. This layer can be used with thin tunnel oxides consisting of SiO$_2$ or Al$_2$O$_3$ for enhanced passivation.

Commonly, moderate temperature (250–350 °C) annealing is needed to improve layer interfaces and cure screen printed contacts. Unfortunately, Neusel et al. noted that MoO$_x$, irrespective of the presence of an a-Si:H (i) buffer layer, has a loss in carrier selectivity and fill factor with annealing temperatures above 150°C [13]. Therefore, there is a need to accomplish annealing without detrimental impact to the MoO$_x$ layer carrier-selectivity, its passivation ability, and potentially improve those properties. In this work, we investigate pulsed laser annealing of MoO$_x$. With laser annealing, the duration of

---

We acknowledge the support of the NASA Langley Professor Program, NSF Grant No. ECCS-2005098 and NSF I/UCRC Center.

time the layer of interest is heated is exceedingly low and the laser wavelength can be selected to anneal only the layer of interest without bulk heating. This prevents the detrimental effects experience from conventional furnace annealing.

II. DEVICE FABRICATION AND ANNEALING

A. *Device fabrication*

Double-side polished, 1–5 Ω cm resistivity, high-lifetime silicon wafers of both p- and n-type were used for this study. Starting wafer passivation is measured with native oxide intact. Afterwards, they are dipped in HF to remove any native oxide and rinsed with DI water. They were then placed in a thermal evaporator with a molybdenum boat containing stoichiometric MoO_3 pellets. The chamber is brought down to a pressure of 5×10^{-6} hPa, and 10 nm of MoO_x is evaporated at a rate of 0.1–0.2 Å/s by monitoring the deposition rate with a quartz crystal monitor. Afterwards, the wafers are flipped and a symmetric layer is deposited on the opposite side for characterization with QSSPCD at a minority carrier density of 1×10^{16} cm^{-3} in quasi-steady stage analysis mode (Sinton, WCT-120). The measured J_0 values are divided by two to reflect the single-side J_0 of one of the layers. Additionally, a 10 nm MoO_x film was single-side coated onto a glass slide to monitor the change in optical transmission with increasing annealing temperature.

B. *Furnance annealing and optical transmission*

As a reference, thermal annealing was done in an ambient air-filled furnace at increasing temperatures in increments of 100 °C for 10 minutes for MoO_x films on p-type wafers and a single side film on glass. Between each 10 minute anneal, the passivation properties of the MoO_x/p-Si/MoO_x structure was measured using QSSPCD. Similarly, the optical transmission of the single-side film on glass was measured in a wavelength range from 300–600 nm (Varian Cary, 5E UV-Vis-NIR Spectrophotometer). The glass was first measured without the film for comparison.

C. *Laser annealing setup*

Laser annealing was done using a 355 nm wavelength, 25 ns pulse width, diode-pumped solid-state laser (Coherent, MATRIX 355-8-50) by passing the beam through a computer-controlled galvanometer scan head (Sino-Galvo, SG7210) in a raster scan pattern. The beam was defocused while annealing MoO_x/n-Si/MoO_x samples, in order to more evenly distribute the beam energy across the beam waist and to avoid reaching the ablation threshold for MoO_x near the Gaussian peak of the beam [14]. The focused beam size is approximately 20 µm in diameter while the defocused beam size is approximately 280 µm in diameter, which was measured by optical microscopy of a laser ablated spot at varying sample focal heights. The scan speed and raster line spacing was set so that there was a 140 µm spacing between spots in both the x and y dimensions (50% overlap). The entire sample area (25 mm x 25 mm) is annealed and the substrates are flipped over to anneal the opposite side symmetrically. Laser fluence was varied to examine the effect on the passivation of this structure. Fig. 2 shows a schematic of the laser raster annealing process.

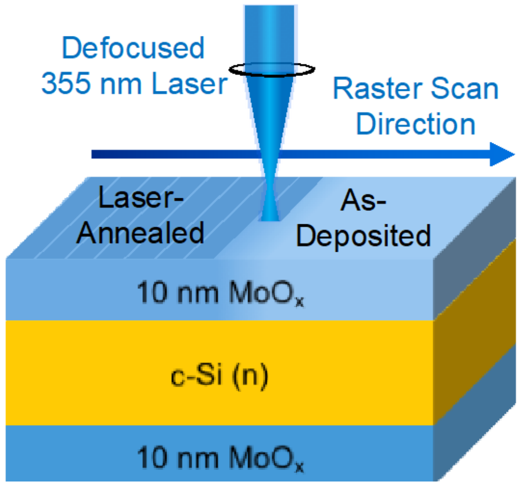

Fig. 2. Schematic of laser raster annealing process and device structure.

III. ANNEALING RESULTS

A. *Furnace annealing*

With furnace annealing of the single side-coated MoO_x on glass samples, the optical transmission of the glass samples starts at approximately 90% in the range of 350–600 nm. After deposition of the MoO_x, the transmission drops in the violet range of the spectrum. Upon thermal annealing in air, the transmission increases in that range until a temperature of 300 °C. Upon, annealing at higher temperatures (≥400 °C), this transmission begins to decrease. The increase in transmission can be explained by an oxidation reaction of the MoO_x, while the decrease by a reduction reaction [15]. Increased transmission of the MoO_x film is desirable to reduce parasitic absorption. These results are shown in Fig 3.

After an HF dip and deposition of MoO_x on p-Si samples, the symmetric, as-deposited 10 nm MoO_x passivates the wafer modestly. However, upon furnace annealing at any temperature in ambient air, the passivation performance degrades due to a shift in work function and complete loss of carrier-selectivity. Similar thermal annealing impacts have been noted in the literature [13]. The impact of thermal annealing on the device effective lifetime (τ_{eff}), implied open-circuit voltage (iV_{OC}), and one-side recombination current density ($1 \times J_0$) is shown in Table I.

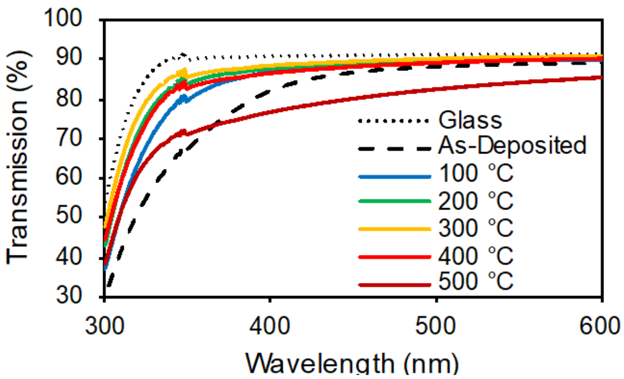

Fig. 3. Transmission spectra for thermally annealed MoO_x on glass.

TABLE I. FURNACE ANNEALING RESULTS

Sample Condition	QSSPCD at MCD of 1E16 cm^{-3}		
	Lifetime (µs)	*iV_{OC} (mV)*	*1 × J_0 (fA/cm^2)*
Starting Wafer	2	550	3438
As-Deposited	232	639	34
100 °C[a]	9	570	653
200 °C	5	554	1204
300 °C	6	558	932
400 °C	5	555	1142
500 °C	5	552	1267

[a] The sample was annealed at increasing temperatures for 10 min increments in ambient air.

TABLE II. LASER ANNEALING RESULTS

Sample Condition	QSSPCD at MCD of 1E16 cm^{-3}		
	Lifetime (µs)	*iV_{OC} (mV)*	*1 × J_0 (fA/cm^2)*
Starting Wafer	2	553	>10,000
As-Deposited	137	677	45
Laser-Annealed[b]	167	679	28

[b] Champion fluence of 0.52 J/cm^2.

B. Laser annealing

Laser annealing was carried out on n-Si samples symmetrically coated with 10 nm of MoO_x. In contrast to furnace annealing in air, a wide range of laser fluences improved the lifetime of the structures from the as-deposited state, while also decreasing the 1 × J_0. This demonstrates the large laser processing window available to improve the passivation of MoO_x passivated silicon shown in Fig. 4.

The largest improvement was demonstrated at a laser fluence of 0.52 J/cm^2, with a 22% relative increase in lifetime, < 1% relative increase in iV_{OC}, and a 37% relative decrease in 1× J_0. Table II summarizes these results. Interestingly, the iV_{OC} did not demonstrate as much improvement suggesting limitations from Auger recombination in the samples. However, the lifetime and 1 × J_0 suggest that laser annealed MoO_x has a marked improvement in the passivation of Shockley-Read-Hall recombination.

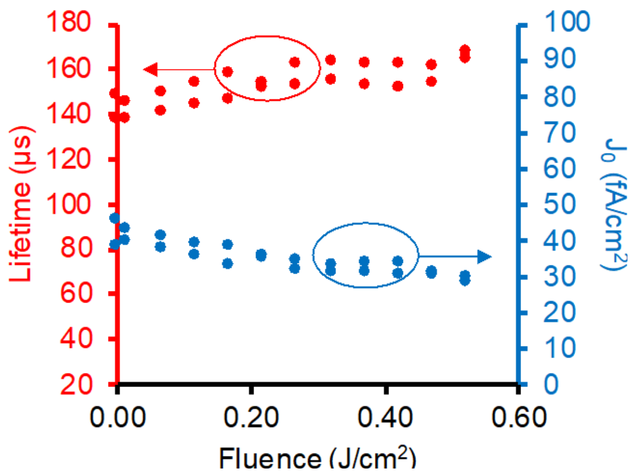

Fig. 4. Impact of UV laser annealing fluence on symmetric device lifetime (left) and 1 × J_0 (right).

IV. CONCLUSIONS

We have demonstrated an ultraviolet laser annealing approach for passivation improvement of hole-selective MoO_x contacts in silicon solar cells. When compared with ineffective thermal annealing, the laser annealing approach demonstrates substantial improvement, with the lowest J_0, and highest iV_{OC} of any a-Si interlayer-free MoO_x passivation to our knowledge.

ACKNOWLEDGMENT

We acknowledge the support of the NASA Langley Professor Program and NSF Grant No. ECCS-2005098.

REFERENCES

[1] K. Yoshikawa, W. Yoshida, T. Irie, H. Kawasaki, K. Konishi, H. Ishibashi, T. Asatani, D. Adachi, M. Kanematsu, H. Uzu, and K. Yamamoto, “Exceeding conversion efficiency of 26% by heterojunction interdigitated back contact solar cell with thin film Si technology,” *Sol. Energy Mater. Sol. Cells*, vol. 173, pp. 37–42, Dec. 2017.

[2] A. Richter, J. Benick, F. Feldmann, A. Fell, B. Steinhauser, J.-I. Polzin, N. Tucher, J. N. Murthy, M. Hermle, and S. W. Glunz, “Both Sides Contacted Silicon Solar Cells: Options for Approaching 26% Efficiency,” *36th Eur. PV Sol. Energy Conf. Exhib.*, 2019.

[3] J. Bullock, Y. Wan, Z. Xu, S. Essig, M. Hettick, H. Wang, W. Ji, M. Boccard, A. Cuevas, C. Ballif, and A. Javey, “Stable Dopant-Free Asymmetric Heterocontact Silicon Solar Cells with Efficiencies above 20%,” *ACS Energy Lett.*, vol. 3, no. 3, pp. 508–513, Mar. 2018.

[4] H. Mehmood, H. Nasser, T. Tauqeer, S. Hussain, E. Ozkol, and R. Turan, “Simulation of an efficient silicon heterostructure solar cell concept featuring molybdenum oxide carrier-selective contact,” *Int. J. Energy Res.*, vol. 42, no. 4, pp. 1563–1579, Mar. 2018.

[5] R. Islam and K. C. Saraswat, “Metal/insulator/semiconductor carrier selective contacts for photovoltaic cells,” in *2014 IEEE 40th Photovoltaic Specialist Conference, PVSC 2014*, 2014.

[6] C. Battaglia, S. M. De Nicolás, S. De Wolf, X. Yin, M. Zheng, C. Ballif, and A. Javey, “Silicon heterojunction solar cell with passivated hole selective MoO x contact,” *Appl. Phys. Lett.*, 2014.

[7] C. Battaglia, X. Yin, M. Zheng, I. D. Sharp, T. Chen, S. McDonnell, A. Azcatl, C. Carraro, B. Ma, R. Maboudian, R. M. Wallace, and A. Javey, “Hole Selective MoO x Contact for Silicon Solar Cells,” *Nano Lett.*, vol. 14, no. 2, pp. 967–971, Feb. 2014.

[8] J. Bullock, A. Cuevas, T. Allen, and C. Battaglia, “Molybdenum oxide MoOx: A versatile hole contact for silicon solar cells,” *Appl. Phys. Lett.*, 2014.

[9] J. Geissbühler, J. Werner, S. Martin de Nicolas, L. Barraud, A. Hessler-Wyser, M. Despeisse, S. Nicolay, A. Tomasi, B. Niesen, S. De Wolf, and C. Ballif, “22.5% efficient silicon heterojunction solar cell with molybdenum oxide hole collector,” *Appl. Phys. Lett.*, vol. 107, no. 8, p. 081601, Aug. 2015.

[10] I. Irfan, A. James Turinske, Z. Bao, and Y. Gao, “Work function recovery of air exposed molybdenum oxide thin films,” *Appl. Phys. Lett.*, vol. 101, no. 9, p. 093305, Aug. 2012.

[11] B. W. H. van de Loo, “Atomic-layer-deposited surface passivation schemes for silicon solar cells,” Technische Universiteit Eindhoven, 2017.

[12] L. Neusel, M. Bivour, and M. Hermle, “Selectivity issues of MoOx based hole contacts,” *Energy Procedia*, vol. 124, pp. 425–434, Sep. 2017.

[13] OpenSim, “SPIM Optics 101/Theoretical basics.” [Online]. Available: https://openspim.org/SPIM_Optics_101/Theoretical_basics.

[14] J. Werner, J. Geissbühler, A. Dabirian, S. Nicolay, M. Morales-Masis, S. De Wolf, B. Niesen, and C. Ballif, “Parasitic Absorption Reduction in Metal Oxide-Based Transparent Electrodes: Application in Perovskite Solar Cells,” *ACS Appl. Mater. Interfaces*, vol. 8, no. 27, pp. 17260–17267, Jul. 2016.